# Improving the Speed and Performance of Point-of-Care Diagnostics with Microfluidics

Thesis by

Travis Stratton Schlappi

In Partial Fulfillment of the Requirements for

the degree of

Doctor of Philosophy

**Caltech**

CALIFORNIA INSTITUTE OF TECHNOLOGY

Pasadena, California

2018

(Defended August 9, 2017)

© 2017

Travis Stratton Schlappi
ORCID: 0000-0001-6132-6459

# ACKNOWLEDGEMENTS

I would like to acknowledge and thank several people who were instrumental in helping me progress to this stage in my life of defending a thesis for a doctorate degree in chemical engineering. First, I thank my extended and immediate family, and particularly my parents, who gave me ample opportunity and motivation to succeed in academics. Even though they couldn't help (content-wise) with studies or homework past middle school, they helped me achieve my academic dreams by supporting me in all other aspects of life and providing me a stable environment in which I could focus and thrive in education.

From the support and mentorship of my parents, childhood teachers, and collegiate professors, I arrived at Caltech a dedicated and effective learner. However, I was not a scientist nor did I have the skills necessary to do independent, valuable, and successful research. I am indebted to my advisor Rustem Ismagilov for his mentorship and all the time, effort, and money he invested in me over the past five years as I learned how to *do* science instead of just *learn* scientific principles. He gave me countless opportunities to learn and grow as a scientist, while also stepping in to mentor and teach me along the way. I also thank my classmates and other Caltech professors who helped me gain a solid theoretical foundation of chemical engineering principles in my first year of doctorate work.

Next, I would like to thank the members of the Ismagilov lab. While this thesis will be credited to my name, it would not have been possible without the innumerable hours that lab members spent helping me learn experimental and scientific skills. I gained knowledge and expertise from them and then built on it to do the work that is presented here. Co-authors on publications include Nathan Schoepp, Stephanie McCalla, Matthew Curtis, Eugenia Khorosheva, Shencheng Ge, Weishan Liu, and Slava Butkovich. Other lab members that helped train me in various stages of my doctorate include Justin Rolando, David Selck, Stefano Begalo, Erik Jue, Mikhail Karymov, Natasha Shelby, Bing Sun, Jesus Rodriguez-Manzano, Dmitriy Zhukov, and Daan Witters. I particulary want to highlight two people: Stephanie McCalla, who trained me in my first year and was very patient as I went through the growing pains of becoming a scientist; Nathan Schoepp, who I have formed a very

effective team with in the last few years of my research. It has been very enjoyable working with him and a large portion of my recent success has come from collaborations with him.

External collaborations have also been instrumental in helping me do effective research. First, I want to thank my collaborators at the University of British Colombia—Christian Kastrup, Ju Hun Yeon, Nima Mazinani, and James Baylis—who enabled me to learn and develop my simulation skills as a part of their blood clotting work. I also thank our collaborators at UCLA (Romney Humphries, Shelley Miller, Janet Hindler), who provided clinical microbiology expertise and clinical samples, which were important to help us show the clinical utility of our rapid antibiotic susceptibility testing method. Lastly, I want to thank my thesis committee (Rustem Ismagilov, Mikhail Shapiro, Julie Kornfield, Dave Tirrell) for providing support and direction as I achieved this degree.

# ABSTRACT

Microfluidic devices play an important role in improving global health because they reduce the study of biological phenomena into physiological scales and lay the foundation for point-of-care (POC) diagnostics. Health is improved and lives are saved because POC diagnostics can enable earlier diagnosis of diseases and therefore more effective treatment. Accurate and available diagnostics also prevent accelerated drug resistance that stems from overtreatment or mistreatment with antibiotics, which is projected to cause up to $100 trillion in lost economic output and 10 million deaths by 2050. This work details new diagnostic assays and theoretical analysis of microfluidic devices that can be implemented at the point-of-care to improve global health.

# PUBLISHED CONTENT AND CONTRIBUTIONS

**Chapter II**: Nathan G. Schoepp[†], Eugenia M. Khorosheva[†], Travis S. Schlappi, Matthew S. Curtis, Romney M. Humphries, Janet A. Hindler and Rustem F. Ismagilov. 2016. "Digital Quantification of DNA Replication and Chromosome Segregation Enables Determination of Antimicrobial Susceptibility After Only 15 Minutes of Antibiotic Exposure." Angewandte Chemie. 55(33):9557–9561. DOI: 10.1002/anie.201602763

This article was co-first authored by Schoepp and Khorosheva. This paper describes a method for using digital PCR (dPCR) to determine phenotypic susceptibility or resistance of *E. coli* isolates to an antibiotic after 15 minutes of antibiotic exposure. The role that I held in the project was fabricating and using microfluidic devices (SlipChips) to quantify nucleic acid concentrations with dPCR after 15 min of antibiotic exposure. I also developed the statistical methods necessary to determine susceptibility based on dPCR nucleic acid concentrations quantified with Poisson statistics.

**Chapter III**: Nathan G. Schoepp[†], Travis S. Schlappi[†], Matthew S. Curtis, Slava S. Butkovich, Shelley Miller, Romney H. Humpries, and Rustem Ismagilov. "Rapid pathogen-specific phenotypic antibiotic susceptibility testing using digital LAMP quantification in clinical samples", doi: 10.1126/scitranslmed.aal3693.

This article was co-first authored by Schlappi and Schoepp. The paper describes a sample-to-answer antibiotic susceptibility testing (AST) method that can be performed in 30 minutes or less directly from a clinical urinary tract infection (UTI) sample. The roles that I held in the project were the following: developing a theortical framework to analyze tradeoffs for key parameters in phenotypic AST; helping to build upon and further optimize the dAST method shown in Chapter II (and developed by Nathan Schoepp) to determine antibiotic susceptibility from clinical UTI samples after 15 min of antibiotic exposure with digital PCR; testing digital LAMP as a rapid nucleic acid measurement method and statistically evaluating its performance and consistency in determining correct AST calls; developing necessary

protocols for determining susceptibility in less than 30 min directly from a clinical sample; writing the manuscript.

**Chapter IV**: Travis S. Schlappi[†], Stephanie E. McCalla[†], Nathan G. Schoepp, and Rustem F. Ismagilov. 2016 "Flow-through Capture and in Situ Amplification Can Enable Rapid Detection of a Few Single Molecules of Nucleic Acids from Several Milliliters of Solution." Analytical Chemistry. 88 (15): 7647–765. DOI: 10.1021/acs.analchem.6b01485

This article was co-first authored by Schlappi and McCalla. The paper describes a method for rapidly capturing and detecting zeptomolar nucleic acid concentrations (a few copies of DNA per mL) from large volumes. The roles that I held in the paper were theoretical framework and analysis, experimental design and execution, contribution to the development of one of the two methods for chitosan functionalization, and prinicipal writer of the paper.

**Chapter V**: Shencheng Ge[†], Weishan Liu[†], Travis Schlappi and Rustem Ismagilov. "Digital, ultrasensitive, end-point protein measurements with large dynamic range via Brownian trapping with drift", *J. Am. Chem. Soc.*, 2014, 136, 14662–14665. DOI: 10.1021/ja507849b

This article was co-first authored by Ge and Liu. The paper describes a microfluidic device that increases the dynamic range of protein measurement by applying drift to a standard digital assay. The role that I held in the paper was developing a theoretical understanding of the transport and capture parameters to ensure proper experimental design and parameters. I also applied the theory of Brownian trapping with drift from semiconductor physics to this digitial protein assay that Ge and Liu had designed and fabricated.

**Chapter VI**: Ju Hun Yeon[†], Nima Mazinani[†], Travis S. Schlappi, Karen Y. T. Chan, James R. Baylis, Stephanie A. Smith, Alexander J. Donovan, Damien Kudela, Galen D. Stucky, Ying Liu, James H. Morrissey, Christian J. Kastrup. "Localization of short-chain polyphosphate enhances its ability to clot flowing blood plasma". *Scientific Reports*, 2017, 7, 42119. DOI: 10.1038/srep42119

This article was co-first authored by Yeon and Mazinani. The paper describes a study of the localization of polyphosphate on the wall of a microfluidic device and how it affects blood clotting. The role that I held in the paper was developing a theoretical understanding of the transport and reaction parameters involved in this blood clotting process and numerical simulations to predict clotting times as a function of shear rate.

[†]These authors contributed equally.

# TABLE OF CONTENTS

*C h a p t e r   I*


# Introduction


The main objective of the research in this thesis is to improve global health, with an emphasis on making these innovations applicable limited-resource settings. Microfluidic devices play an important role in improving global health because they can reduce the study of biological phenomena into physiological scales and lay the foundation for point-of-care (POC) diagnostics.

The improvement of global health centers around two interdependent factors: treatment and diagnosis. Treatment receives a majority of the attention paid to healthcare, but if there is no accurate or reliable diagnosis of the infirmity, then treatment can become ineffective and expensive [1]. For example, a new POC malaria test with 90% sensitivity and specificity would prevent 447 million unnecessary treatments per year, in addition to saving 2.2 million adjusted lives [2]. A POC diagnostic test for Chlamydia and Gonorrhoea in sub-Saharan Africa, China, and southeast Asia would save ~4 million disability-adjusted life years, avert >16.5 million incident gonorrheoa and chlaymadia infections and prevent >212,000 HIV infections [2]. These lives are improved and saved because POC diagnostics enable earlier diagnosis of diseases, which increases life expectancy and treatment success [1]-[4]. Accurate and available diagnostics also prevent accelerated drug resistance that stems from overtreatment, which is projected to cause up to $100 trillion in lost economic output and 10 million deaths by 2050 [5].

Chapters II and III of this thesis address the challenge of drug resistance by demonstrating how microfluidics can be used to rapidly test bacteria for their susceptibility or resistance to antibiotics. Gold-standard antibiotic susceptibility testing (AST) methods currently used in clinical laboratories take several days to obtain a result [6]. Because knowing the phenotypic AST result of an organism in less than 30 min is crucial for appropriate treatment and antibiotic stewardship [7]-[8], the goal for our AST method was to provide susceptibility information with comparable accuracy to gold-standard methods,

but in much shorter times (30 min or less). In Chapter II, previously published work on which I am a contributing author is presented which develops an AST method to determine the phenotypic susceptibility of *E. coli* to several classes of antibiotics commonly prescribed for urinary tract infections (UTI). Schoepp and Khorosheva show that this digital antibiotic susceptibility testing (dAST) method correctly determines antibiotic susceptibility or resistance for UTI E. coli isolates after only 15 min of antibiotic exposure, which is a dramatic reduction in time from the traditionally required overnight or 24-hour cultures.

Chapter III of this thesis details unpublished work on which I am a co-first author where we build upon the work from Chapter II and make several important advances to achieve our goal of a phenotypic AST in less than 30 min. First, we further developed the dAST method to test antibiotic susceptibility from clinical UTI urine samples instead of isolates grown in media. Second, we used microfluidic devices (SlipChips [9]) and isothermal nucleic acid amplification (LAMP, ref) to precisely measure the nucleic acid concentrations and decrease the measurement time from 2 hours (necessary for digital PCR in the method of Chapter II) to less than 10 min. Third, we optimized the workflow to enable an antibiotic susceptibility call to be determined directly from a clinical UTI sample in less than 30 min, with all sample handling and image analysis steps included. This achievement—obtaining an AST call in less than 30 min—is a world-record for phenotypic AST and introduces a new dAST method that can potentially be used to address many of the drug-resistance diagnostic challenges the world is encountering today.

In Chapter IV of this thesis, previously published work on which I am a co-first author demonstrates the use of a porous matrix to rapidly (< 10 min) capture zeptomolar amounts of nucleic acids (~1 copy/mL) from large volumes (> 1 mL). Low concentration detection of nucleic acids is important in many fields: for infectious diseases, latent infections and drug effectiveness studies can only be done with a high sensitivity diagnostic device; in environmental monitoring, low pathogen concentrations are present in water and diagnostics are necessary to ensure safe drinking water [10]-[11]. Microfluidic point-of-care (POC) devices have been designed to address these needs, but they are not able to detect NAs present in zeptomolar concentrations in short time frames because they require slow flow rates and/or they are unable to handle milliliter-scale volumes. This paper evaluates the reaction and

transport tradeoffs theoretically and demonstrates a new method using microfluidic principles in a porous nylon matrix that can successfully detect zeptomolar concentrations.

In Chapter V of this thesis, previously published work on which I am a contributing author expands the dynamic range of a quantitative protein assay by incorporating Brownian trapping with drift into a digital protein assay. Typically, digital protein measurements are very precise, but with a limited dynamic range. This work contributes an understanding of the transport and capture processes in a digital protein assay with flow and uses this understanding to dictate the optimal parameters that result in an exponential decay of positive signal over the length of the microfluidic channel. Achieving this exponential decay was essential to improving the dynamic range, which is desired in assays testing for a traumatic brain injury biomarker, glial fibrillary acidic protein (GFAP).

In Chapter VI of this thesis, previously published work on which I am a contributing author studies the effect that various forms of polyphosphate (polyP) have on blood clotting. The principal hypothesis tested was whether localizing polyP onto a surface would trigger blood clotting in the presence of various shear rates. This question was analyzed with microfluidics mimicking a capillary both theoretically and experimentally. Although the physiological mechanisms for polyP localization onto platelet or vascular surfaces remain unknown, this study gives insight into the clotting mechanisms, their dependence on various forms of polyP, and potential therapeutic applications.

**References**

[1] E. Fu, P. Yager, P. N. Floriano, N. Christodoulides and J. T. McDevitt, IEEE Pulse, 2011, 2, 40–50.

[2] M. Urdea, L. A. Penny, S. S. Olmsted, M. Y. Giovanni, P. Kaspar, A. Shepherd, P. Wilson, C. A. Dahl, S. Buchsbaum, G. Moeller, and D. C. Hay Burgess, "Requirements for high impact diagnostics in the developing world," Nature, vol. 444, suppl. 1, pp. 73–79, 2006.

[3] P. Yager, G. J. Domingo and J. Gerdes, Annu. Rev. Biomed. Eng., 2008, 10, 107–144.

[4] Nakagawa F, Lodwick RK, Smith CJ, Smith R, Cambiano V, et al. (2012) Projected life expectancy of people with HIV according to timing of diagnosis. AIDS 26: 335–343.

[5] R. Laxminarayan, A. Duse, C. Wattal, A. K. Zaidi, H. F. Wertheim, N. Sumpradit, E. Vlieghe, G. L. Hara, I. M. Gould, H. Goossens, C. Greko, A. D. So, M. Bigdeli, G. Tomson, W. Woodhouse, E. Ombaka, A. Q. Peralta, F. N. Qamar, F. Mir, S. Kariuki, Z. A. Bhutta, A. Coates, R. Bergstrom, G. D. Wright, E. D. Brown, O. Cars. Antibiotic resistance--the need for global solutions. *Lancet Infect Dis* **13**, 1057-1098 (2013).

[6] K. Gupta, T. M. Hooton, K. G. Naber, B. Wullt, R. Colgan, L. G. Miller, G. J. Moran, L. E. Nicolle, R. Raz, A. J. Schaeffer, D. E. Soper, A. Infectious Diseases Society of, M. European Society for, D. Infectious. International clinical practice guidelines for the treatment of acute uncomplicated cystitis and pyelonephritis in women: A 2010 update by the Infectious Diseases Society of America and the European Society for Microbiology and Infectious Diseases. *Clinical infectious diseases : an official publication of the Infectious Diseases Society of America* 52, e103-120 (2011).

[7] H. D. Marston, D. M. Dixon, J. M. Knisely, T. N. Palmore, A. S. Fauci. Antimicrobial Resistance. JAMA 316, 1193-1204 (2016).

[8] J. M. Hicks, R. Haeckel, C. P. Price, K. Lewandrowski, A. H. B. Wu. Recommendations and opinions for the use of point-of-care testing for hospitals and primary care: summary of a 1999 symposium. Clin Chim Acta 303, 1-17 (2001).

[9] Feng Shen, Wenbin Du, Jason E. Kreutz, Alice Fok, and Rustem F. Ismagilov, "Digital PCR on a SlipChip," Lab Chip **2010** 10: 2666-2672

[10] Fearon, M.; Scalia, V.; Lane, D.; Bigham, M.; Hawes, G.; O'Brien, S.; Kadkhoda, K. Transfusion 2016, 56, 994-995.

[11] Castillo, I.; Bartolome, J.; Quiroga, J.; Barril, G.; Carreño, V. Aliment. Pharmacol. Ther. 2009, 30, 477-486.

*Chapter II*

# Digital Quantification of DNA Replication and Chromosome Segregation Enables Determination of Antimicrobial Susceptibility After Only 15 Minutes of Antibiotic Exposure[1]

**Abstract**

Rapid antimicrobial susceptibility testing (AST) would decrease misuse and overuse of antibiotics. To achieve the "holy grail" of AST, a phenotype-based test that can be performed within a doctor visit, requires determining a pathogen's susceptibility after a short antibiotic exposure. We used digital PCR (dPCR) to test whether assessing DNA replication of the target pathogen via digital single-molecule counting would shorten the required antibiotic exposure. Partitioning bacterial chromosomal DNA into many small volumes during dPCR enabled AST via (i) precise quantification and (ii) a measure of how antibiotics affect the states of macromolecular assembly of bacterial chromosomes. This digital AST (dAST) determined susceptibility of clinical isolates from urinary tract infections (UTI) after 15 min of exposure for all four antibiotic classes relevant to UTI. This work lays the foundation to develop a rapid, point-of-care AST and strengthen global antibiotic stewardship.

**Introduction**

The increasingly liberal use and misuse of antibiotics (ABX) has led to widespread development of antibiotic resistance.[1] To address this crisis, we need rapid and reliable tests of a pathogen's susceptibility to the drugs available (antimicrobial susceptibility test, AST) to provide correct, life-saving treatment, facilitate antibiotic stewardship[2] and drastically decrease hospital costs.[1a,3] Having a rapid AST that provides results within the

---

period of a doctor visit would lead to improved patient outcomes and reduced spread of antibiotic resistance.[4] Development of a rapid AST is currently the focus of significant research efforts[5] that aim to supplant traditional clinical methods. To reduce the spread of resistance, one urgently needed AST is for urinary tract infections (UTIs), which are among the most common bacterial infections, yet can progress to pyelonephritis or sepsis.[6]

Two types of ASTs are currently used in clinical settings: traditional culture-based methods and genotypic methods. Culture-based tests remain the gold standard for determining antibiotic susceptibility because they detect phenotypic susceptibility to a drug, however these tests require a long period of antibiotic exposure (typically 16–24 h).[7] We[8] and others[5a,5b,5k,9] have proposed using confinement of single, or a small number of, bacterial cells in small volumes to reduce the duration of antibiotic exposure required to read out the phenotype of the target pathogen. However, these methods typically do not differentiate between the pathogen and the potential contamination of the sample with commensal bacteria. Alternative genotypic methods (detecting genes responsible for known mechanisms of resistance) are more rapid than culture-based approaches.[10] However, these resistance genes constitute only a fraction of all possible mechanisms of resistance,[11] and new forms of resistance evolve quickly.[12] Therefore, predicting resistance by analyzing a few known resistance genes is not a general solution.[13]

To develop more rapid and specific phenotypic tests, hybrid approaches have been proposed that use quantification of nucleic acids to determine the susceptibility or resistance phenotype after a short antibiotic exposure. These tests do not rely on detecting specific resistance genes.[5g,5i] For example, quantification of RNA has allowed determination of susceptibility to ciprofloxacin (cip) and rifampin,[5i] which impair transcription, after exposures as short as 15 min. However, these methods require longer incubation times when using antibiotics with different mechanisms of action. Using quantitative PCR (qPCR), quantification of DNA after 2–9 h of antibiotic exposure was used to detect bacterial growth and determine susceptibility,[5d,5e] however an ideal exposure time would be shorter than one cell division.

Here we tested the hypothesis that digital methods of nucleic acid quantification,[14] such as digital PCR (dPCR), would enable use of DNA markers to perform a phenotypic AST after short antibiotic exposure. Digital methods partition bacterial chromosomal DNA into thousands of compartments and then use targeted amplification to determine the number of "positive" compartments containing DNA carrying one or more copies of the target gene. This partitioning should enable more precise and robust measurements of concentrations of bacterial DNA, achieving higher statistical power with fewer replicates relative to qPCR.[14c,15] Further, we hypothesized that this partitioning would provide unique capabilities for AST when analyzing target genes present in a macromolecular assembly, such as a bacterial chromosome during replication. In contrast to qPCR, dPCR results should reflect the state of the macromolecular assembly, providing a different count for a pair of segregated chromosomes (two positives) vs the chromosomal assembly just prior to segregation (one positive). We test our hypotheses in the context of four of the main antibiotics used in UTI treatment: ciprofloxacin (cip), nitrofurantoin (nit), sulfamethoxazole/trimethoprim (sxt), and amoxicillin/clavulanic acid (amc).[6a,7b,16]

**Results and Discussion**

We first determined the minimum antibiotic exposure time necessary to differentiate susceptible and resistant clinical UTI isolates using qPCR analysis of DNA after incubation in the presence ("treated") or absence ("control") of antibiotics (see SI). Cycle thresholds were used to calculate relative fold change

compared to t = 0 min (Fig. 2-1). When treated with cip, DNA replication in susceptible isolates was significantly inhibited, resulting in an increasing difference in fold change between target concentration in treated and control samples. If the isolate was resistant, DNA replication continued regardless of exposure. To align with FDA requirements for very major errors[17] we used a conservative alpha, 0.02 (see SI). Susceptibility to cip could be determined after 15 min of exposure. We obtained similar results using isolates pre-cultured in media and in urine (SI Fig. 2-S1), and chose to conduct all subsequent experiments in media in order to reduce the work with human samples and to ensure reproducibility. The focus of this work is to evaluate the differences in minimum antibiotic exposure time necessary to determine susceptibility when quantification of changes in DNA is performed with qPCR vs dPCR.
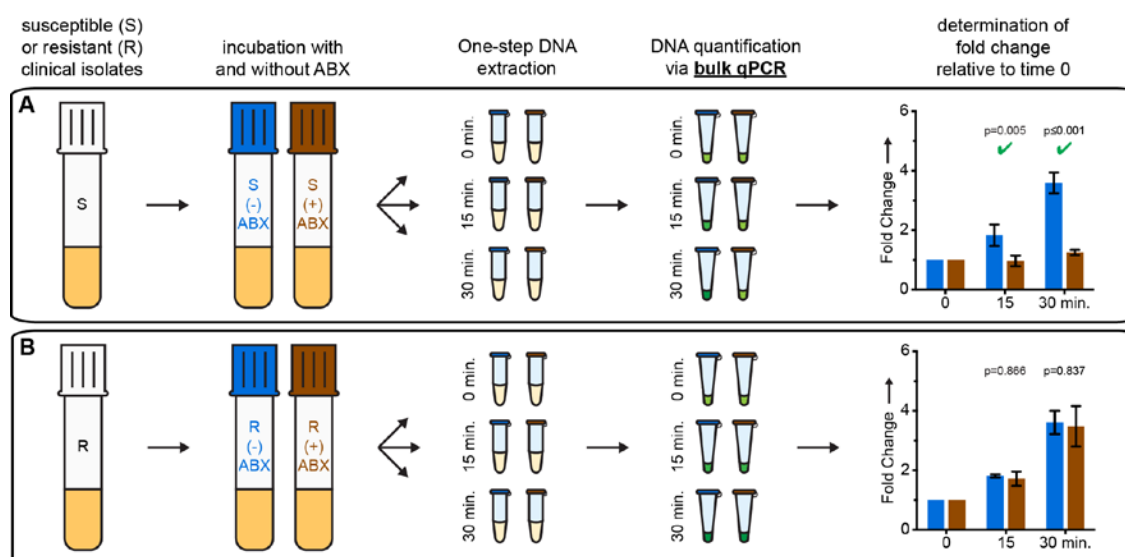


**Figure 2-1.** Quantitative PCR (qPCR) time course for exposure of (A) susceptible and (B) resistant UTI *E. coli* isolates to ciprofloxacin. For cycle thresholds (Ct) error bars are 2.8 S.D. (see SI), N=3. Fold change values represent change from t = 0 min; error bars represent the upper and lower bounds of the 98% C.I. (see SI), N=2. Significant differences (p-value ≤ 0.02) are marked with a green check.

These results are the first evidence of detection of phenotypic susceptibility based on DNA quantification after only 15 min of antibiotic exposure. The rapid effect of cip on DNA replication is logical because the drug's mechanism of action is to inhibit DNA-gyrase and

topoisomerase IV, producing double stranded breaks in DNA and directly inhibiting DNA replication.[18] To test generality, we evaluated AST with three other antibiotics: nit,[19] sxt,[20] and amc (which is not known to specifically affect DNA replication) (see SI). Using qPCR, 15 min of exposure to these three antibiotics was not sufficient to detect a significant difference in DNA replication in susceptible isolates (Fig. 2-2 B–D), while statistically significant differences were detectable with cip treatment (Fig. 2-2 A).
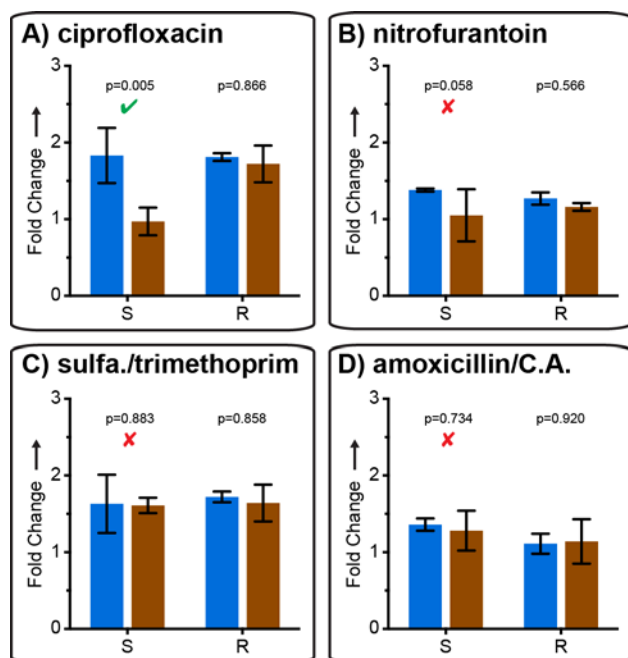


**Figure 2-2.** Comparison of susceptible and resistant isolates from UTI samples after a 15 min exposure with each of four antibiotics, analyzed by quantitative PCR. Fold change values represent change from t = 0 min; error bars are 98% C.I. (see SI), N=3. Significant (p-value ≤ 0.02) and nonsignificant differences detected using the susceptible isolate are marked with a green check and red x respectively.

We then tested AST with digital quantification by quantifying the same DNA samples using digital PCR (Fig. 2-3). For cip, we observed a more statistically significant difference (smaller p value) between target concentrations in treated and control susceptible isolates (Figure 2-3A), while target concentrations did not differ between treated and control resistant isolates (Figure 2-3B). A significant difference was also detected after 15 min exposures to nit (Figure 2-3C) or sxt (Fig. 2-3C).

Interestingly, neither qPCR or dPCR detected susceptibility after exposure to amc when samples were denatured and treated with protease during extraction (SI Figure 2-S2). This confirmed that genome replication proceeded (resulting in an increase in the total number of amplifiable targets) during incubation with amc regardless of phenotype. We therefore tested the hypothesis that dPCR would be sensitive not only to the total gene copy number, but also to the state of macromolecular assembly of chromosomal DNA. If exposure to amc causes changes in chromosome segregation, even without affecting replication, dPCR should still be able to differentiate susceptible and resistant phenotypes. To preserve chromosome structure and macromolecular complexes, we performed DNA extraction in non-denaturing conditions without protease treatment. Under these conditions, dPCR provided susceptibility phenotype after 15 min of exposure to amc (Figure 2-3D).
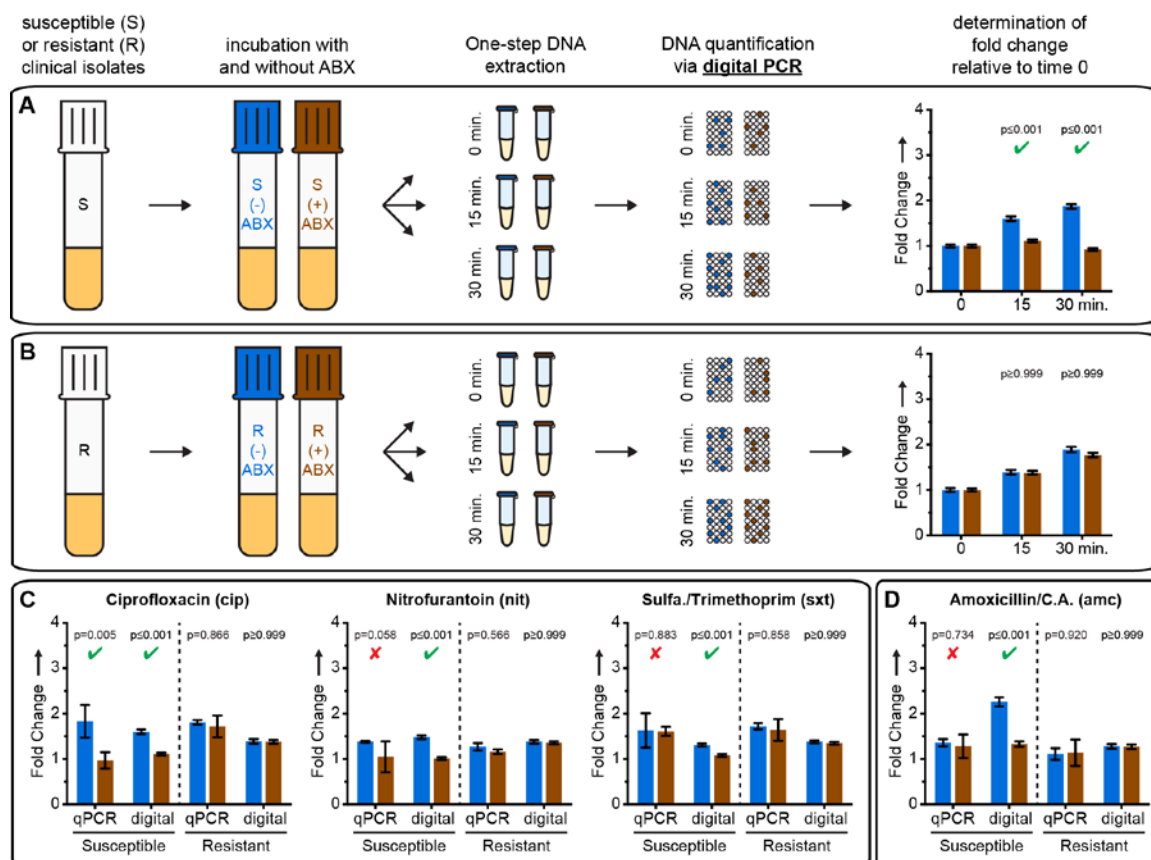
**Figure 2-3.** AST results using dPCR. (A,B) Time course results for exposure of susceptible (A) and resistant (B) UTI *E. coli* isolates to ciprofloxacin. (C,D) Fold changes after treatment with all four antibiotics tested. Significant (p-value ≤ 0.02) and nonsignificant p-values for susceptible isolates are denoted with a green check and red x respectively. Samples treated with amoxicillin/clavulanic acid (D) were extracted using a non-denaturing protocol. Concentrations are calculated using Poisson statistics. Fold change values represent change from t = 0 min; all error bars are 98% C.I. (see SI), N=3 for qPCR, N=2 for dPCR.

To test whether dPCR differentiated susceptible and resistant isolates via quantifying macromolecular assemblies, we designed control experiments in which all assemblies were sheared into ~1000 bp DNA fragments, much smaller than the average distance between 23S genes within the genome (see SI). As expected, shearing caused an increase in measured target concentration when quantified using dPCR, but not using qPCR (Fig. 2-4 A–B). In samples that were not sheared, dPCR detected the susceptible phenotype after 15 min of amc exposure (Fig. 4C). Shearing these samples to disrupt macromolecular assemblies eliminated

the ability to detect susceptibility (Fig. 4D); qPCR measurements confirmed this was not due to loss of DNA. This suggests that in amc-susceptible isolates short exposure to amc does not result in a change of the total number of target gene copies, but does change the macromolecular assembly of these copies.
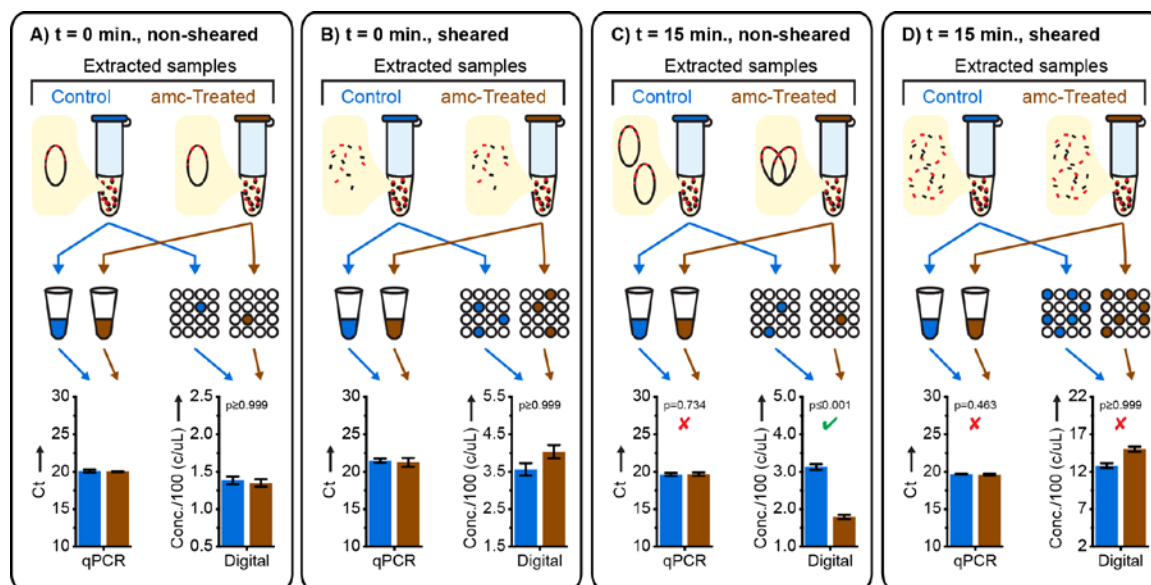


**Figure 2-4.** A mechanistic investigation of AST by digital PCR (dPCR) after beta lactam exposure and non-denaturing DNA extraction using shearing to disrupt macromolecular assemblies; error bars for qPCR are 2.8 S.D. (see SI), N=3; error bars are 98%C.I. for dPCR (see SI), N=2. Significant (p-value $\leq$ 0.02) and nonsignificant p-values for susceptible isolates quantified using dPCR are denoted with a green check and red x respectively (see SI).

Our results suggest a previously unknown effect of brief beta-lactam antibiotic exposure: a delay in chromosome segregation. Using dPCR (but not qPCR) this effect can be quantified by counting the number of macromolecular DNA assemblies containing 23S target genes, and used for AST. The high resolution of digital quantification enables measuring small (less than two-fold) changes in chromosome replication and segregation after antibiotic exposure shorter than the average time of cell division. The dAST approach developed here adds chromosome segregation to the list of the phenotypic markers suitable for rapid antibiotic susceptibility detection. The ability to partition macromolecular assemblies allows dAST to be used even when genome replication proceeds on the timescale

of antibiotic exposure, while the high precision of digital quantification allows accurate determination of susceptibility after shorter exposure times than would be required using less-precise methods such as qPCR.

**Conclusion**

These dAST results warrant a follow-up study with a wide range of Gram-positive and Gram-negative bacterial isolates from urine, blood, and other sample types, and then a clinical study comparing dAST directly from patient samples to the gold standard culture-based methods. Elucidating the effects of using variable clinical samples with a range of background matrices is a critical next step in the development of a rapid, sample-to-answer AST. Ultimately, a sample-to-answer AST at the point of care must be robust, rapid, and require minimal sample handling and instrumentation. Ideally, such a workflow will integrate sample handling, antibiotic exposure, and quantification into a single device. We anticipate that digital isothermal amplification chemistries will replace dPCR in dAST.[15a,21] When integrated with sample preparation[22] and combined with simple readouts,[23] we envision that digital quantification will establish a new paradigm in rapid point of care AST.

**References**

[1]   a) CDC, *Antibiotic Resistance Threats in the United States*, U. S. Department of Health and Human Services, Centers for Disease Control and Prevention, **2013**, p. pp. 114; b) R. Laxminarayan*, et al.*, *Lancet Infect. Dis.* **2013**, *13*, 1057-1098.
[2]White House, *National Action Plan for Combating Antibiotic-Resistant Bacteria*, Washington D.C., **2015**, p. 62.
[3]R. R. Roberts*, et al.*, *Clin. Infect. Dis.* **2009**, *49*, 1175-1184.
[4]B. Spellberg*, et al.*, *Clin. Infect. Dis.* **2011**, *52 Suppl 5*, S397-428.
[5]    a) J. D. Besant, E. H. Sargent, S. O. Kelley, *Lab Chip* **2015**, *15*, 2799-2807; b) Y. Lu, J. Gao, D. D. Zhang, V. Gau, J. C. Liao, P. K. Wong, *Anal. Chem.* **2013**, *85*, 3971-3976; c) C. Zhu, Q. Yang, L. Liu, S. Wang, *Angew. Chem. Int. Ed. Engl.* **2011**, *50*, 9607-9610; d) J.

R. Waldeisen, T. Wang, D. Mitra, L. P. Lee, *PLoS One* **2011**, *6*, e28528; e) J. M. Rolain, M. N. Mallet, P. E. Fournier, D. Raoult, *J. Antimicrob. Chemother.* **2004**, *54*, 538-541; f) A. Mezger, E. Gullberg, J. Goransson, A. Zorzet, D. Herthnek, E. Tano, M. Nilsson, D. I. Andersson, *J. Clin. Microbiol.* **2015**, *53*, 425-432; g) K. E. Mach, R. Mohan, E. J. Baron, M. C. Shih, V. Gau, P. K. Wong, J. C. Liao, *J. Urol.* **2011**, *185*, 148-153; h) V. Ivančić, *et al.*, *J. Clin. Microbiol.* **2008**, *46*, 1213-1219; i) C. Halford, R. Gonzalez, S. Campuzano, B. Hu, J. T. Babbitt, J. Liu, J. Wang, B. M. Churchill, D. A. Haake, *Antimicrob. Agents Chemother.* **2013**, *57*, 936-943; j) A. K. Barczak, *et al.*, *Proc. Natl. Acad. Sci. U. S. A.* **2012**, *109*, 6217-6222; k) I. Sinn, P. Kinnunen, T. Albertson, B. H. McNaughton, D. W. Newton, M. A. Burns, R. Kopelman, *Lab Chip* **2011**, *11*, 2604-2611; l) T. S. Mann, S. R. Mikkelsen, *Anal. Chem.* **2008**, *80*, 843-848; m) Y. Tang, L. Zhen, J. Liu, J. Wu, *Anal. Chem.* **2013**, *85*, 2787-2794.

[6]a) T. M. Hooton, *N. Engl. J. Med.* **2012**, *366*, 1028-1037; b) F. M. Wagenlehner, A. Pilatz, W. Weidner, *Int. J. Antimicrob. Agents* **2011**, *38 Suppl*, 51-57.

[7]     a) J. M. Andrews, *J. Antimicrob. Chemother.* **2001**, *48 Suppl 1*, 5-16; b) Clinical and Laboratory Standards Institute (CLSI), *Performance Standards for Antimicrobial Susceptibility Testing; Seventeenth Informational Supplement*, **2007**.

[8]J. Q. Boedicker, L. Li, T. R. Kline, R. F. Ismagilov, *Lab Chip* **2008**, *8*, 1265-1272.

[9]C. H. Chen, Y. Lu, M. L. Sin, K. E. Mach, D. D. Zhang, V. Gau, J. C. Liao, P. K. Wong, *Anal. Chem.* **2010**, *82*, 1012-1019.

[10]   a) S. G. Beal, J. Ciurca, G. Smith, J. John, F. Lee, C. D. Doern, R. M. Gander, *J. Clin. Microbiol.* **2013**, *51*, 3988-3992; b) O. Altun, M. Almuhayawi, M. Ullberg, V. Özenci, *J. Clin. Microbiol.* **2013**, *51*, 4130-4136; c) A. J. Blaschke, *et al.*, *Diagn. Microbiol. Infect. Dis.* **2012**, *74*, 349-355; d) T. Spanu, *et al.*, *J. Clin. Microbiol.* **2012**, *50*, 2783-2785; e) T. Kostic, M. Ellis, M. R. Williams, T. M. Stedtfeld, J. B. Kaneene, R. D. Stedtfeld, S. A. Hashsham, *Appl. Microbiol. Biotechnol.* **2015**, *99*, 7711-7722.

[11]a) C. Walsh, *Nature* **2000**, *406*, 775; b) M. A. Webber, L. J. V. Piddock, *J. Antimicrob. Chemother.* **2003**, *51*, 9-11.

[12]R. T. Cirz, J. K. Chin, D. R. Andes, V. de Crecy-Lagard, W. A. Craig, F. E. Romesberg, *PLoS Biol.* **2005**, *3*, e176.

[13]     a) N. Tuite, K. Reddington, T. Barry, A. Zumla, V. Enne, *J. Antimicrob. Chemother.*

**2014**, *69*, 1729-1733; b) M. R. Pulido, M. Garcia-Quintanilla, R. Martin-Pena, J. M. Cisneros, M. J. McConnell, *J. Antimicrob. Chemother.* **2013**, *68*, 2710-2717.

[14]     a) M. Baker, *Nature Methods* **2012**, *9*, 541-544; b) J. F. Huggett, *et al.*, *Clin. Chem.* **2013**, *59*, 892-902; c) A. S. Whale, J. F. Huggett, S. Cowen, V. Speirs, J. Shaw, S. Ellison, C. A. Foy, D. J. Scott, *Nucleic Acids Res.* **2012**, *40*, e82.

[15]a) D. A. Selck, M. A. Karymov, B. Sun, R. F. Ismagilov, *Anal. Chem.* **2013**, *85*, 11129-11136; b) B. Vogelstein, K. W. Kinzler, *Proc. Natl. Acad. Sci. U. S. A.* **1999**, *96*, 9236-9241; c) S. Weaver, S. Dube, A. Mir, J. Qin, G. Sun, R. Ramakrishnan, R. C. Jones, K. J. Livak, *Methods* **2010**, *50*, 271-276.

[16]K. Gupta, *et al.*, *Clin. Infect. Dis.* **2011**, *52*, e103-120.

[17]     FDA, *Class II Special Controls Guidance Document: Antimicrobial Susceptibility Test (AST) Systems*, **2007**.

[18]A. Fàbrega, S. Madurga, E. Giralt, J. Vila, *Microb Biotech* **2009**, *2*, 40-61.

[19]D. R. Guay, *Drugs* **2001**, *61*, 353-364.

[20]     P. A. Masters, T. A. O'Bryan, J. Zurlo, D. Q. Miller, N. Joshi, *Arch. Intern. Med.* **2003**, *163*, 402-410.

[21]    a) A. Gansen, A. M. Herrick, I. K. Dimov, L. P. Lee, D. T. Chiu, *Lab Chip* **2012**, *12*, 2247-2254; b) J. Jarvius, J. Melin, J. Goransson, J. Stenberg, S. Fredriksson, C. Gonzalez-Rey, S. Bertilsson, M. Nilsson, *Nature Methods* **2006**, *3*, 725-727; c) F. Shen, E. K. Davydova, W. Du, J. E. Kreutz, O. Piepenburg, R. F. Ismagilov, *Anal. Chem.* **2011**, *83*, 3533-3540; d) B. Sun, J. Rodriguez-Manzano, D. A. Selck, E. Khorosheva, M. A. Karymov, R. F. Ismagilov, *Angew. Chem. Int. Ed. Engl.* **2014**, *53*, 8088-8092.

[22]     J. R. Buser, A. Wollen, E. K. Heiniger, S. A. Byrnes, P. C. Kauffman, P. D. Ladd, P. Yager, *Lab Chip* **2015**, *15*, 1994-1997.

[23]     J. Rodriguez-Manzano, M. A. Karymov, S. Begolo, D. A. Selck, D. V. Zhukov, E. Jue, R. F. Ismagilov, *ACS Nano* **2016**, *10*, 3102-3113.

**Supporting Information**


**Experimental Section**

*Materials and reagents*

All reagents purchased from commercial sources were used as received unless otherwise stated. BBL Trypticase Soy Agar plates with 5% Sheep Blood and Bacto Brain Heart Infusion (BHI) media were purchased from BD (Franklin Lakes, NJ, USA). BHI was dissolved in deionized water at the manufacturers recommended concentration and autoclaved prior to use. All antibiotic stock solutions and PCR reactions were prepared using sterile, nuclease-free water (NF-$H_2O$) purchased from Thermo Fisher (Waltham, MA, USA).

All antibiotics and clavulanic acid were purchased from Sigma-Aldrich (St. Louis, MO, USA), with the exception of amoxicillin, which was purchased from Alfa-Aesar (Ward Hill, MA, USA). Ciprofloxacin and clavulanic acid were prepared as a 1 mg/mL stock solutions in NF-$H_2O$. Nitrofurantoin was prepared as a 10 mg/mL stock solution in dimethylformamide (DMF). Sulfamethoxazole was prepared as a 10 mg/mL stock solution in dimethyl sulfoxide (DMSO). Trimethoprim was prepared as a 1 mg/mL stock solution in DMSO. All antibiotic stock solutions were stored at -20 °C. Amoxicillin was prepared fresh as a 1 mg/mL stock solution in NF-$H_2O$ before each experiment.

QuickExtract DNA Extraction Solution and QuickExtract RNA Extraction Kit were purchased from Epicentre (Madison, WI, USA). SsoFast EvaGreen Supermix (2X) and QX200 ddPCR EvaGreen Supermix was purchased from Bio-Rad Laboratories (Hercules, CA, USA) and used for all qPCR and dPCR experiments respectively.

Pooled human urine (catalog no. 991-03-P) was obtained from Lee Biosolutions (Maryland Heights, MO, USA).

*Isolate maintenance*

Ten *E. coli* isolated from the urine of 10 unique patients were obtained from the University of California Los Angeles (UCLA) Clinical Microbiology Laboratory with approval from the UCLA and Veterans Affairs Institutional Review Boards and appropriate Health

Insurance Portability and Accountability Act exemptions. All isolates were identified as
*E. coli* using the Vitek2 GNID panel (bioMerieux, Durham, NC, USA), and chosen for use
based on their determined MICs. Urine cultures were performed by routine semi-quantitative
methods, by inoculating 1 µL of urine to a BBL Trypticase Soy Agar plate with 5% Sheep
Blood (BAP, BD, Sparks MD) and a MacConkey plate followed by overnight incubation at
35 +/-2 °C in ambient air. In all cases, the *E. coli* grew in pure culture at >100,000 colony
forming units. Minimum inhibitory concentrations (MIC) for each isolate was determined by
UCLA for ciprofloxacin (cip), nitrofurantoin (nit), sulfamethoxazole/trimethoprim (sxt), and
amoxicillin/clavulanic acid (amc) using the Clinical and Laboratory Standards Institute
(CLSI) reference broth microdilution method,[1] in panels prepared by UCLA with cation-
adjusted Mueller-Hinton broth (MHB). BMD tests were incubated at 35 +/- 2 ºC in ambient
air conditions for 16-20 h. MICs were interpreted using CLSI M100S 26th edition
breakpoints.[1]  *E. coli* isolates were stored at -80 °C in Brucella broth with 20% glycerol
(Becton, Dickinson, Sparks, MD, USA). Isolates were subcultured twice on BAP and well-
isolated colonies were used for antibiotic exposure time course experiments.

*Antibiotic exposure time course experiments*
In order to generate liquid culture for use in experiments, *E. coli* isolates were cultured
overnight (10-12 hours) after scraping a small portion of the plate and inoculating in 4 mL
BHI. Overnight cultures were re-inoculated into 4 mL of fresh BHI and grown for an
additional 4–6 h until early logarithmic phase. Cultures were then diluted 10 fold into pre-
warmed BHI, and optical density (600 nm) was measured using a portable spectrophotometer
(GE Healthcare Ultrospec 10). OD was converted to approximate cell count using the
correlation factor OD600 1.0 = 8.0*10^8 cells/mL). The dilutions prepared for OD
measurements were then immediately diluted a second time into 2 mL polypropylene tubes
to a final volume of 500 µL (dilution factor dependent on desired final cell concentration).
These tubes were incubated for 5 min at 37 °C with shaking at 500 rpm in a heating/shaking
block (Thermo Fisher Digital Heating Shaking Drybath) to ensure thorough mixing. During
this time, separate 2 mL polypropylene tubes containing 450 µL of BHI with and without
antibiotics were prepared. All exposure time courses were conducted with antibiotic

concentrations above the minimum inhibitory concentration (MIC) of the susceptible isolate and below the MIC of the resistant isolate being tested. Ciprofloxacin exposure in media and urine was conducted at a final antibiotic concentration of 2.00 and 0.75 μg/mL respectively. Nitrofurantoin experiments were performed at 64.00 μg/mL. Sulfamethoxazole/trimethoprim experiments were performed at 76.00/4.00 μg/mL. For amoxicillin experiments, susceptible isolates were exposed to a final concentration of 12.00 μg/mL, and resistant isolates were exposed to a final concentration of 14.00 μg/mL. Cultures were then diluted a final 10 fold (50 µL culture into 450 µL) into single tubes containing media with or without antibiotics, and time was started. 10 µL aliquots were removed at 0, 15, and 30 min., and immediately mixed with 90 µL of a one-step extraction buffer suitable for direct use in PCR. Denaturing extraction conditions used Epicentre QuickExtract DNA Extraction Solution. Cells were mixed with Epicentre QuickExtract DNA Extraction Solution, pipette mixed, incubated at 65 °C for 6 min., 98 °C for 4 min., then chilled on ice. Non-denaturing extraction conditions used Epicentre Quick Extract RNA Extraction solution. Aliquots were mixed with RNA extraction immediately via pipette, gently vortexed to ensure thorough mixing, and chilled on ice. All samples were stored at -20 °C for several days during use before being moved to -80 °C for long-term storage.

*DNA fragmentation*

DNA was fragmented to a predicted 1000 bp fragment size using a Covaris 220M ultrasonicator. Samples were diluted 10 fold into a 130 µL microTUBE AFA Fiber Snap-Cap, and sheered for 90 seconds at 20 °C with a Peak Incident Power of 50 W, duty factor of 2%, and 200 cycles per burst. This size was chosen to ensure that all copies of the 23S gene will be separated from each other. Based on an analysis of 11 *E.coli* strains isolated from UTIs, the average distance between 23S genes is 1,169 kb with the closest genes being 38 kb apart. These genomes may be accessed with the following accession numbers: CP011018.1; HG941718.1; CP007265.1; CP007391.1; CP002797.2; CP002212.1; CP001671.1; CU928163.2; CP000247.1; CP000243.1; CP011134.1.

*DNA quantification*

All qPCR reactions were performed using a Roche LightCycler 96. All reactions contained only SsoFast EvaGreen Supermix at a final concentration of 1X, forward and reverse primers (forward primer TGCCGTAACTTCGGGAGAAGGC, reverse primer TCAAGGCTCAATGTTCAGTGTC) specific for Enterobacteriaceae[2] at a final concentration of 500 nM, template DNA at variable concentrations, and NF-H$_2$O. A single master mix containing supermix, primers, and NF-H$_2$O was prepared and aliquoted into PCR tubes. Template was then added, bringing the final volume to 30 µL. Each tube was then mixed thoroughly via pipette and technical triplicates (9 µL each) were aliquoted into the 96 well plate. Cycling conditions consisted of an initial denaturation step at 95 °C for 3 min. followed by 30 cycles of 95 °C for 20 s, 62 °C for 20 s, and 72 °C for 20 s. Following amplification a continuous melt curve was obtained between 55 and 95 °C. Total cycling time (including melt analysis) was 60 min.

Digital PCR reactions were carried out in a BioRad QX200 Droplet Digital PCR system according to the manufacturer's instructions. Samples were prepared in identical fashion as those prepared for qPCR. For each sample, two wells of the droplet generation chip and well plate were used to generate and thermocycle droplets, respectively. This resulted in approximately 40,000 droplets being analyzed for each sample. Cycling conditions consisted of an initial denaturation step at 95 °C for 5 min followed by 40 cycles of 95 °C for 30 s, 60 °C for 30 s, and 72 °C for 30 s. Following initial thermocycling, the sample was cooled to 4 °C for 5 min followed by a final heating step at 95 °C for 5 min. All thermocycling steps were performed with a 2 °C/s ramp rate. Total cycling time was 115 min.

*Statistical analyses*

Raw Ct values are not normally distributed; therefore, a typical plot showing the mean Ct +/- 2·SD does not mean that the true mean will lie in the confidence interval 95% of the time. Understanding this fact, we would still like to represent the variability in qPCR measurements for the raw Ct plot. We did this with a standard confidence interval calculation:

$$Ct_{U/L} = Ct_{avg} \pm t_{crit} \cdot \frac{S_{Cq}}{\sqrt{n}} \qquad (1)$$

The critical $t$ value ($t_{crit}$) for a 98% confidence interval with 2 degrees of freedom is 4.85; with $n = 3$ replicates, this results in the SD being multiplied by 2.80 for the confidence intervals. This does not mean that the true Ct is within this interval 98% of the time, but it does give a representation of the variability in Ct measurements.

In order to calculate the p-value for comparing treated and untreated samples, the raw Ct values (which are exponential) were linearized into a relative quantity ($FC$) with t = 0 min as the reference point using $FC = 2^{Ct(t)-Ct(0)}$. The log ratio of these linearized quantities was compared to $\ln(1.1)$ using a one-tailed $t$ test. A one-tailed test was chosen because the untreated sample should have a higher concentration than the treated sample; if by some random event the treated sample has a statistically significant higher concentration than untreated, we don't want to draw the false conclusion that the isolate is susceptible. To account for pipetting variation (the treated sample could have randomly had 10% more bacteria pipetted into its media at time = 0 than the untreated sample), the null hypothesis is $\ln\left(\frac{FC_{ut}}{FC_t}\right) - \ln(1.1) = 0$ instead of $\ln\left(\frac{FC_{ut}}{FC_t}\right) = 0$. This makes the AST more conservative (reducing very major errors) by requiring that the untreated sample have at least 1.1 fold more copies than the treated sample. P-values for digital PCR were calculated with a one-tailed $Z$ test comparing $\ln\left(\frac{FC_{ut}}{FC_t}\right)$ to $\ln(1.1)$, with $FC_{ut}$ representing the fold change in concentration of the untreated sample with respect to time = 0 and $FC_t$ representing the same quantity, but for the treated sample.

*Discussion of mechanism of action of antibiotics tested*
In addition to ciprofloxacin, we evaluated three other antibiotics used in the treatment of UTIs: (i) nitrofurantoin, which is reduced to a reactive radical inside the cell, reacting with multiple cellular targets including enzyme involved in DNA synthesis[3], which would directly affect replication; (ii) the combination of sulfamethoxazole and trimethoprim, which

synergistically inhibit folic acid biosynthesis, subsequently impairing multiple metabolic reactions including thymidine synthesis[4]; and (iii) amoxicillin, which disrupts the synthesis of the peptidoglycan layer of bacterial cell walls leading to lysis[5], but is not known to specifically affect DNA replication.

**Figures and Tables**

| Isolate Number | Specimen | AMC | CIP | NIT | SXT |
|---|---|---|---|---|---|
| 1 | urine | <=2 | <=.25 | <=16 | <=1 |
| 2 | urine | <=2 | <=.25 | <=16 | <=1 |
| 3 | urine | <=2 | <=.25 | <=16 | <=1 |
| 5 | urine | <=2 | <=.25 | <=16 | <=1 |
| 6 | urine | >16 | >2 | <=16 | <=1 |
| 8 | urine | <=2 | >2 | 64 | >8 |
| 10 | urine | 4 | >2 | <=16 | >8 |
| 11 | urine | ND | >2 | >256 | >8 |

**Table 2-S1.** Minimum inhibitory concentrations for all isolates tested, as determined by broth dilution. AMC = amoxicillin/clavulanic acid, CIP = ciprofloxacin, NIT = nitrofurantoin, SXT = sulfamethoxazole/trimethoprim. ND = not determined.

| Isolate Number | S or R | ABX | [ABX] (ug/mL) | DNA Extraction Type | Control or Treated | Fold Change (qPCR) | Upper Bound 98% CI (qPCR) | Lower Bound 98% CI (qPCR) | p-val (qPCR) | Fold Change (dPCR) | Upper Bound 98% CI (dPCR) | Lower Bound 98% CI (dPCR) | p-val (dPCR) |
|---|---|---|---|---|---|---|---|---|---|---|---|---|---|
| 1 | S | cip | 2.00 | denaturing | control | 1.41 | 0.19 | 0.19 | 0.006 | 1.15 | 0.03 | 0.03 | <0.001 |
| | | | | | treated | 0.99 | 0.02 | 0.02 | | 0.78 | 0.02 | 0.02 | |
| 5 | S | cip | 2.00 | denaturing | control | 1.83 | 0.36 | 0.36 | 0.005 | 1.60 | 0.05 | 0.05 | <0.001 |
| | | | | | treated | 0.97 | 0.18 | 0.18 | | 1.11 | 0.03 | 0.03 | |
| 10 | R | cip | 2.00 | denaturing | control | 1.81 | 0.05 | 0.05 | 0.866 | 1.39 | 0.05 | 0.05 | >0.999 |
| | | | | | treated | 1.72 | 0.24 | 0.24 | | 1.38 | 0.04 | 0.04 | |
| 2 | S | nit | 64.00 | denaturing | control | 1.38 | 0.02 | 0.02 | 0.058 | 1.48 | 0.04 | 0.04 | <0.001 |
| | | | | | treated | 1.05 | 0.34 | 0.34 | | 1.01 | 0.03 | 0.03 | |
| 3 | S | nit | 24.00 | denaturing | control | 2.93 | 0.67 | 0.67 | 0.027 | 1.58 | 0.10 | 0.10 | <0.001 |
| | | | | | treated | 1.87 | 0.09 | 0.09 | | 1.00 | 0.04 | 0.04 | |
| 11 | R | nit | 64.00 | denaturing | control | 1.27 | 0.08 | 0.08 | 0.566 | 1.38 | 0.04 | 0.04 | >0.999 |
| | | | | | treated | 1.16 | 0.05 | 0.05 | | 1.36 | 0.03 | 0.03 | |
| 3 | S | sxt | 76.00 | non-denaturing | control | 1.34 | 0.07 | 0.07 | 0.302 | 3.37 | 0.25 | 0.25 | 0.001 |
| | | | | | treated | 1.19 | 0.17 | 0.17 | | 2.67 | 0.19 | 0.19 | |
| 5 | S | sxt | 76.00 | denaturing | control | 1.63 | 0.38 | 0.38 | 0.883 | 1.31 | 0.03 | 0.03 | <0.001 |
| | | | | | treated | 1.61 | 0.10 | 0.10 | | 1.08 | 0.03 | 0.03 | |
| 8 | R | sxt | 76.00 | denaturing | control | 1.72 | 0.07 | 0.07 | 0.858 | 1.38 | 0.03 | 0.03 | >0.999 |
| | | | | | treated | 1.64 | 0.24 | 0.24 | | 1.35 | 0.03 | 0.03 | |
| 1 | S | amc | 12.00 | denaturing | control | 1.60 | 0.17 | 0.17 | 0.973 | 1.49 | 0.04 | 0.04 | >0.999 |
| | | | | | treated | 1.60 | 0.02 | 0.02 | | 1.62 | 0.05 | 0.05 | |
| 1 | S | amc | 12.00 | non-denaturing | control | 1.36 | 0.08 | 0.08 | 0.734 | 2.26 | 0.10 | 0.10 | <0.001 |
| | | | | | treated | 1.28 | 0.26 | 0.26 | | 1.33 | 0.06 | 0.06 | |
| 1 | S | amc | 12.00 | non-denaturing* | control | 3.50 | 0.72 | 0.72 | 0.463 | 3.60 | 0.19 | 0.19 | >0.999 |
| | | | | | treated | 3.14 | 1.45 | 1.45 | | 3.72 | 0.18 | 0.18 | |
| 3 | S | amc | 14.00 | non-denaturing | control | 1.60 | 0.20 | 0.20 | 0.535 | 6.56 | 0.28 | 0.28 | <0.001 |
| | | | | | treated | 1.46 | 0.55 | 0.55 | | 1.37 | 0.07 | 0.07 | |
| 6 | R | amc | 14.00 | non-denaturing | control | 1.11 | 0.13 | 0.13 | 0.920 | 1.15 | 0.04 | 0.04 | >0.999 |
| | | | | | treated | 1.14 | 0.29 | 0.29 | | 1.24 | 0.04 | 0.04 | |

**Table 2-S2.** Raw data and additional experiments performed with multiple isolates. "S or R" refers to susceptible or resistant as determined by MIC. ABX = antibiotic. * indicates samples were sheared prior to quantification (see methods section of SI). Experiment exposing isolate 1 to ciprofloxacin was performed in 1:1 media:urine, all other experiments were performed in media.
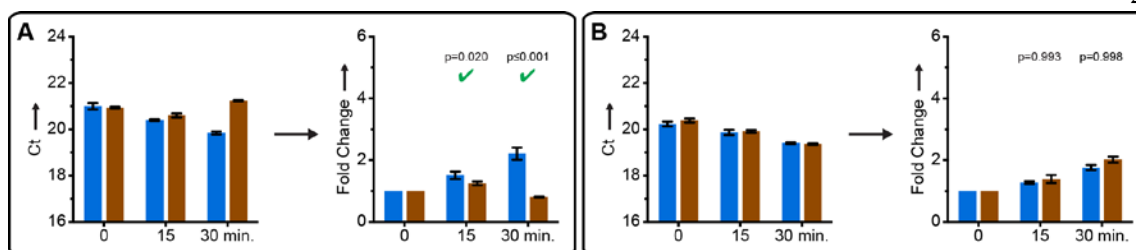
**Figure 2-S1.** qPCR time course for exposure of (A) susceptible and (B) resistant UTI *E. coli* isolates to ciprofloxacin pre-cultured in urine and exposed to antibiotics in 1:1 urine:BHI. Raw cycle thresholds represent the average of technical triplicates; error bars represent 2.8 standard deviations (see SI). Fold change values represent change from t = 0 min; error bars represent the upper and lower bounds of the 98% confidence interval. Significance was defined as a p-value <= 0.02 when comparing the fold change in 23S concentration of samples incubated without antibiotics (blue) to 1.1 times the fold change in 23S concentration of samples with antibiotics (brown) at a specific time point. Significant differences detected using the susceptible isolate are marked with a green check.
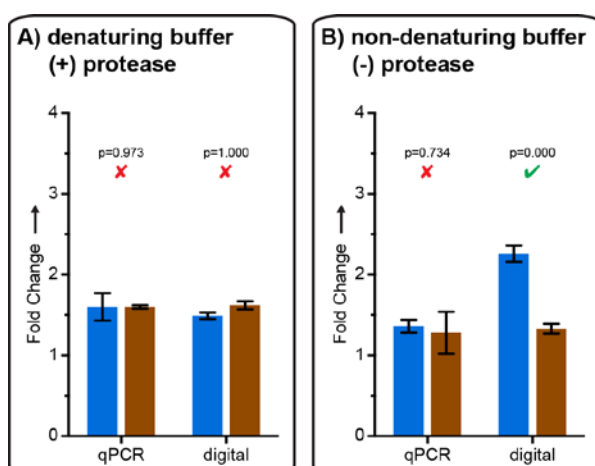


**Figure 2-S2.** Comparison of susceptible isolate analyzed by qPCR and digital PCR after a 15 min exposure to amoxicillin/clavulanic acid and extracted using a denaturing buffer with protease treatment (A) and a non-denaturing buffer without protease treatment (B). Fold change values represent change from t = 0 min; error bars are 98% confidence intervals. Significance was defined as a p-value <= 0.02 when comparing the fold change in 23S concentration of samples incubated without antibiotics (blue) to 1.1 times the fold change in

23S concentration of samples with antibiotics (brown) at a specific time point. Significant and non-significant differences are marked with a green check and red x respectively.
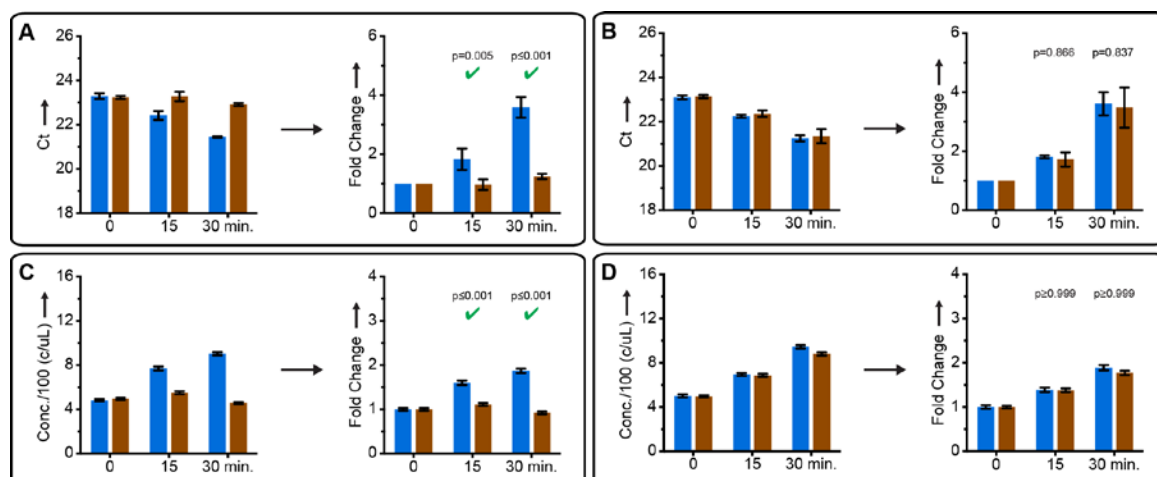


**Figure 2-S3.** Fold change plots from Figures 1 and 3 with corresponding Ct and concentration plots to demonstrate conversion from either Ct or concentration to fold change. (A, B) AST results using qPCR. Time course for exposure of (A) susceptible and (B) resistant UTI *E. coli* isolates to ciprofloxacin. For cycle thresholds (Ct) error bars are 2.8 S.D. Fold change values represent change from t = 0 min; error bars represent the upper and lower bounds of the 98% C.I. Significant differences (p-value ≤ 0.02) are marked with a green check. (C, D) AST results using dPCR. Time course for exposure of susceptible (C) and resistant (D) UTI *E. coli* isolates to ciprofloxacin. Concentrations are calculated using Poisson statistics; error bars represent the upper and lower bounds of the 98% C.I. Fold change values represent change from t = 0 min; error bars represent the upper and lower bounds of the 98% C.I. Significant (≤ 0.02) p-values for susceptible isolates are denoted with a green check.

**Contributions of non-corresponding authors**

Nathan G. Schoepp:

Major contributor to selecting DNA replication as AST marker, contributed knowledge on AST state of the art and effects of antibiotics on replication, contributed to digital resolution hypothesis, contributor to chromosome segregation hypothesis

Optimized antibiotic exposure protocols

Performed all antibiotic exposures

Maintained bacterial isolates

Performed all bulk and digital quantification experiments

Contributed all data to figures 1, 2, 3, S1, S2, S3, and table S2, contributed all non-sheared data to figure 4

Drew figures 1, 2, 3, 4, S1, S2, S3, and constructed table S2

Contributed to writing abstract, introduction, results/discussion, and conclusion sections of manuscript

Contributed to writing of supplemental information

Eugenia Khorosheva:

Major contributor to selecting DNA replication as AST marker, major contributor of knowledge on AST state of the art and effects of antibiotics on replication, contributed to selecting 23S gene as a target of choice, contributed to digital resolution hypothesis, contributed to chromosome segregation hypothesis

Selected experimental protocols for maintenance and growth of isolates

Established initial AST protocols and experimental workflow from exposure to extraction

Selected and optimized protocols for amplification with Enterobacteriaceae specific 23S primers.

Contributed to optimizing DNA shearing experiments.

Contributed to writing introduction, results/discussion, and conclusion sections of manuscript

Travis S. Schlappi:

Contributed knowledge on AST statistics, contributed to digital resolution hypothesis

Connected FDA guidelines for establishing new antimicrobial susceptibility determination methods to statistical hypothesis testing for both qPCR and dPCR.

Performed statistical analysis (p-values and error bars) for all data presented in the manuscript and supplemental information.

Performed preliminary digital PCR experiments showing that dPCR can resolve differences in concentration after 15min exposure that qPCR cannot.

Contributed to writing of supplemental information.

Matthew S. Curtis:

Contributed to selecting DNA replication as AST marker, contributed knowledge on AST state of the art and effects of antibiotics on replication, contributed to digital resolution hypothesis, major contributor to chromosome segregation hypothesis

Selected and optimized shearing protocols on extracted DNA for the analysis of chromosome structure.

Performed shearing experiments to generate data for figure 4.

Contributed to statistical analysis

Contributed to writing of the introduction, results/discussion, and conclusion of the manuscript.

Romney M. Humphries and Janet A. Hindler contributed microbiological and AST expertise.

## SI References

[1]Clinical and Laboratory Standards Institute, *M100S Performance Standards for Antimicrobial Susceptibility Testing*, 26th ed., Wayne, Penn., USA, **2016**.

[2]K. Matsuda, H. Tsuji, T. Asahara, Y. Kado, K. Nomoto, *Appl. Environ. Microbiol.* **2007**, *73*, 32-39.

[3]D. R. Guay, *Drugs* **2001**, *61*, 353-364.

[4]P. A. Masters, T. A. O'Bryan, J. Zurlo, D. Q. Miller, N. Joshi, *Arch. Intern. Med.* **2003**, *163*, 402-410.

[5]A. Tomasz, *Annu. Rev. Microbiol.* **1979**, *33*, 113-137.

*Chapter III*

# Digital Pathogen-specific Phenotypic Antibiotic Susceptibility Test Directly from Clinical Samples in as Fast as 30 Minutes Using Digital LAMP Quantification[2]

**Abstract**

Rapid antimicrobial susceptibility testing (AST) is desperately needed for informing treatment decisions and preventing the spread of antimicrobial resistance resulting from the misuse and overuse of antibiotics. To date, no phenotypic AST exists that can be performed within a single patient visit (30 min) directly from clinical samples. Here we show that AST results can be obtained by exposing clinical urine samples to an antibiotic for 15 min and using digital nucleic acid quantification to measure precisely the phenotypic response of the infecting *E. coli*. We perform this AST method using for analysis both a commercial ~2 h digital PCR assay (AUC=0.98), and an ultrafast ~7 min digital real-time loop-mediated isothermal amplification (LAMP) assay (AUC=0.96) that we developed. We also demonstrate that the rapid digital LAMP assay can be used with SlipChips to determine the phenotypic antibiotic susceptibility of *E. coli* directly from clinical urine samples in less than 30 min sample-to-answer, including all sample processing and data analysis steps. Such a rapid digital AST (dAST), once fully developed and FDA approved for additional pathogens, antibiotics, and sample types, would enable rapid clinical decision-making, improve management of infectious diseases, and increase antimicrobial stewardship.

**Introduction**

---

[2] This chapter was submitted for publication with authorship belonging to Nathan G. Schoepp[†], Travis S. Schlappi[†], Matthew S. Curtis, Slava S. Butkovich, Shelley Miller, Romney H. Humpries, and Rustem Ismagilov. "Rapid pathogen-specific phenotypic antibiotic susceptibility testing using digital LAMP quantification in clinical samples", doi: 10.1126/scitranslmed.aal3693. Specific contributions from each author are listed at the end of the chapter.

Emergence of antibiotic resistance is an impending threat to global health. It is projected to cause 10 million deaths and more than $1 trillion (USD) in total economic impact by 2050 if left unchecked (*1, 2*). In order to combat antimicrobial resistance, increase stewardship, and improve patient outcomes, healthcare providers need to be able to determine antibiotic susceptibility rapidly, and ideally directly at the point of care (POC) (*3-6*). The need for a rapid antimicrobial susceptibility test (AST) to guide antibiotic treatment is recognized by all major health organizations, including the Centers for Disease Control and Prevention and the World Health Organization (*7-11*). Urinary tract infections (UTIs) are among the most common bacterial infections, accounting for ~8 million primary care visits annually, and are almost always treated with antibiotics (*12, 13*). In the absence of a rapid AST, UTIs are among many infections that are treated with second-line antibiotics (e.g. the fluoroquinolone ciprofloxacin, cip) instead of first-line antibiotics (e.g. nitrofurantoin, nit) (*14*). This increased use of fluoroquinolones is accompanied by emergence of fluoroquinolone resistance, limiting treatment options, which is especially critical in life-threatening cases, such as when UTIs progress to sepsis. Thus, UTIs are a specific clinical scenario where an inexpensive and rapid (within the ~30 min duration of a patient visit) AST would significantly impact patient outcomes and antimicrobial stewardship. No such diagnostic currently exists.

Phenotypic AST methods based on culture of the target pathogen are the current gold standard, but are too slow (days) to support immediate treatment decisions or to be implemented at the POC (*15*). Genotypic methods, which detect known resistance genes, are faster because they do not require a culturing step (*16-18*). Genotypic methods have shown promise in select clinical settings where the presence of a single gene yields high predictive value, such as testing for mecA to detect methicillin-resistant *Staphylococcus aureus* (MRSA) (*19-21*). However, genotypic tests have not been implemented more broadly because they are not generalizable to different pathogens or mechanisms of resistance, especially in the case of Gram-negative bacteria for which more than 800 resistance genes are known for beta-lactam class antibiotics alone (*22*).

An ideal AST would test the phenotypic response of a pathogen to antibiotics (ABX) in a pathogen-specific manner and provide an AST answer in under 30 min (*23, 24*). This is a critical bar to meet because if the AST result can be obtained within the timespan of a patient visit, then the information can be used to inform treatment and increase antimicrobial stewardship at the POC. Additionally, in some infections such as sepsis, accelerated time-to-treatment is directly correlated with improved patient outcome (*25*). To achieve this speed, the AST method needs to work directly from a clinical sample. Several methods, including our previous work (*26*), have improved the speed of individual steps of the phenotypic AST workflow (such as pathogen isolation and identification, antibiotic exposure time, sample preparation, readout, etc.), but few of these papers report performing the entire workflow from start to finish using a clinical sample.

To date, no phenotypic AST has achieved a sample-to-answer result in less than 30 min directly from a clinical sample. The majority of methods under development were validated with isolates of pathogens, not with clinical samples (see Supplementary Materials Table 3-S2 for a quantitative summary of the published state of the art). Among the rapid phenotypic AST methods used with clinical samples, one microscopy-based method could detect differences in bacterial growth during antibiotic treatment after as few as 6 min of antibiotic exposure using isolates, but the total assay time for a clinical sample was 155 min (*27*). As discussed by the authors (*27*), clinical sample matrices, such as urine, present a challenge for rapid microscopy-based ASTs, affecting the speed and sensitivities (required cell concentrations) of these assays. Furthermore, identification and differentiation of target pathogens from commensal organisms can be challenging if these steps only rely on imaging, without the molecular specificity offered by other methods. A microfluidic-based microscopy method using isolates (imprecisely referred to in the abstract and the body of the paper as clinical samples) reported AST in ~3–4 hours without an identification step and this paper estimated that the total assay time from a clinical sample would be 52 hours (*28*). Another microscopy-based method in clinical testing performs identification and AST from a positive culture in 5–6 hours, with additional overnight or longer time required to first grow

the culture from a clinical sample (*29, 30*). An electrochemical method was used to determine susceptibility in as few as 25 min using non-specific redox markers for reference strains (*31*), but the workflow lacked a pathogen-identification step and the AST was not pathogen-specific. Other electrochemical methods are pathogen-specific, but required at least 45 min of assay time when using isolates (*32*). Pathogen-specific electrochemical methods have been also used to determine susceptibility from clinical samples, but assay times were on the order of hours (*33*). Methods that perform phenotypic AST by quantifying nucleic acids (NA) are promising because they provide molecular specificity, but so far most have required long antibiotic exposures (~2 h or more) in addition to the time required for measurement, which was as fast as 1.5 h using isothermal amplification (*34-36*). This promise of an NA-based AST was highlighted in a study that used RNA gene expression markers and demonstrated antibiotic exposure times as short as 10 min for isolates and as short as 30 min for clinical samples, although in that landmark study the total assay time was over 23 hours as a result of using slow quantification technology (*37*).

We have shown previously that the antibiotic exposure time in a phenotypic AST can be shortened to 15 min by measuring DNA levels in a digital format (*26*). That work was performed with bacterial UTI isolates, and required a 2 h measurement step using commercial droplet digital PCR (dPCR). As explained above, the transition from clinical isolates to clinical samples is invariably challenging for phenotypic AST methods, and previous work has highlighted these challenges (*27, 37, 38*). Therefore, in this paper, we asked and answered two salient questions: (i) For clinical samples, can digital single-molecule counting of pathogen DNA still enable phenotypic AST after a short (15 min) antibiotic exposure? and (ii) Is there a quantification strategy faster than PCR that can be used in a digital format to achieve a pathogen-specific, sample-to-answer phenotypic AST within 30 min directly from a clinical sample?

To answer these questions, we developed an ultrafast digital isothermal amplification assay to shorten the readout step, a critical requirement of rapid assays. We then demonstrated that the entire contiguous sample-to-answer workflow could enable an AST result in less than 30

min from a clinical UTI urine sample. Finally, we tested this digital antibiotic susceptibility testing (dAST) method with 51 clinical UTI urine samples using both commercial digital PCR (dPCR) and the rapid digital LAMP (dLAMP) assay we developed as a measurement method.

**Results**

*Key processes and operational space of digital AST (dAST)*

A phenotypic AST consists of two key processes: antibiotic (ABX) exposure and measurement of the AST marker (in dAST, we measure the concentration of a target NA sequence). To meet the demands of a rapid AST, these two processes, plus sample handling, must take less than 30 min. The workflow of the dAST method we used in this paper is as follows: we aliquoted and diluted a clinical urine sample into two equal volumes of media— one with an antibiotic and a control without antibiotic—then incubated at 37 °C for 15 min. After antibiotic exposure, a target NA sequence (AST marker) was quantified in each sample. Then, the ratio of the marker concentrations in the control and antibiotic-treated samples is calculated (Fig. 3-1A), defined as the control–treated (CT) ratio.

Antibiotic susceptibility was determined by comparing a CT ratio to a previously determined threshold value (susceptibility threshold). Sample pairs that yield a CT ratio that falls above this threshold are called susceptible and samples with a ratio below this threshold are called resistant. A CT ratio that is higher than the susceptibility threshold indicates that DNA replication continued in the control (-ABX) sample, but was slowed or halted in the antibiotic-treated (+ABX) sample, indicating that the sample is susceptible to the chosen antibiotic. A CT ratio that is lower than the susceptibility threshold indicates that DNA replication continued in both the control (-ABX) and antibiotic-treated (+ABX) samples at the same rate, indicating that the sample is resistant to the chosen antibiotic (Fig. 3-1A (step 4)).

The time period of the antibiotic exposure step affects the resolution requirements for the quantification step: a shorter antibiotic exposure results in a smaller difference in the concentration of the target AST marker between antibiotic-treated and control samples. Thus, at shorter exposure periods, quantification with higher resolution is required to reliably quantify an AST marker. To illustrate the interplay of antibiotic exposure time and required measurement resolution, we explored computationally the tradeoff of these three parameters (exposure time, required resolution, and DNA replication rate) and made predictions about the resolution needed to detect susceptibility. We define this combination of parameters as the operational space (Fig. 3-1B). For simplicity, we assumed that for an antibiotic-susceptible pathogen, DNA replication halts upon exposure to the antibiotic. Under this assumption, the DNA replication rate (which differs for different pathogens) directly determines the CT ratio at a given ABX exposure time. We also assumed that there was no lag phase upon transitioning from urine to liquid media; if there is a lag phase, then the requirements for resolution become even more stringent, further emphasizing the need for high-precision digital measurements. For example, if the measurement method is limited to 2-fold resolution (such as in quantitative PCR, qPCR) and the pathogen's DNA doubles every 30 min, then the minimum exposure time necessary to achieve a CT ratio of 2 is 30 min. If the measurement method can instead resolve a 1.2-fold difference in concentrations, then the minimum exposure time decreases to 8 min. Measuring changes in DNA concentration with high resolution therefore allows detection of a pathogen's response to antibiotics even faster than cell division time (*26*).
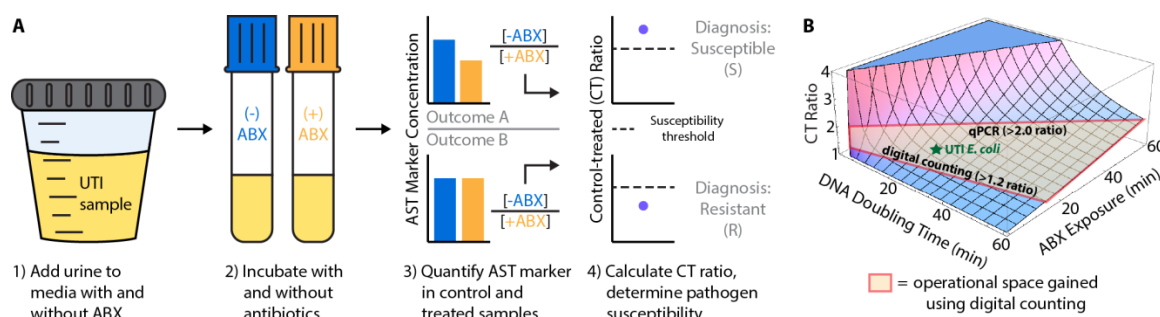


**Fig. 3-1**. Experimental workflow of the digital AST (dAST) method and computationally estimated operational space. (A) The workflow for detecting antibiotic susceptibility by

measuring the replication of a specific nucleic acid sequence (AST marker). Samples are incubated without and with antibiotics (ABX): control (-ABX) and treated (+ABX) and control–treated (CT) ratios are analyzed. (B) Theoretical model that predicts a CT ratio as a function of pathogen DNA doubling time and ABX exposure time. Digital counting is predicted to enable shorter ABX exposure times than qPCR because it can resolve smaller differences in AST marker concentrations. The operational space gained by using digital counting compared with quantitative PCR (qPCR) is outlined in red.

Compared with bulk methods (e.g. qPCR), digital quantification can resolve the difference between two concentrations with greater precision (*26, 39, 40*), which in turn has enabled shorter antibiotic exposure times (*26*). Digital quantification achieves higher resolution by partitioning target molecules into thousands of compartments such that each compartment contains a single molecule. Amplifying each partitioned molecule to a detectable level and counting the number of positive compartments at the endpoint yields precise quantification. Resolution can be increased (and antibiotic exposure time reduced) by increasing the number of digital compartments. However, the benefit of adding more digital compartments decreases beyond ~1,000 compartments and additional compartments are better utilized for multiplexing of multiple markers or antibiotics. For example, at UTI-relevant concentrations of DNA (e.g. $10^6$ copies/mL), 1,000 digital compartments with 1 nL volume each provides 1.23-fold resolution. Increasing the number of these compartments to 10,000 or 100,000 (while correspondingly reducing their volumes to 0.1 nL and 0.01 nL each to keep the same total number of target molecules) provides 1.18-fold and 1.17-fold resolution, respectively (Fig. S2A). In another example, while 10,000 of 1 nL compartments provide 1.08 resolution, 2,000 of 1 nL compartments provide 1.16 resolution each, enabling a 4-plex dAST (1 control and 4 ABX treated samples) to be performed with the same number of wells (Fig. S2C).

We have previously demonstrated that a 15 min exposure step is sufficient to generate detectable differences in DNA concentrations between the control and antibiotic-treated samples using UTI isolates and four antibiotics commonly prescribed for UTIs (*26*). For a 15 min exposure period (which is shorter than even the fastest reported uropathogenic *E. coli*

doubling time (16 min, (*41*)), we would expect the DNA concentration in the control sample to increase 1.4–1.6X (Fig. 1B, green star). Other uropathogenic organisms have doubling times of 13 min (*K. pneumoniae*) 25 min (*P. mirabilis*) and 29 min (*S. saprophyticus*) (*42, 43*). Therefore, a 15 min exposure should provide a 1.4–2.2-fold change and should also work with this method, though these theoretical estimates would need to be confirmed experimentally. These fold changes range are within the resolution of digital measurements, but such measurements in the past have taken 90 min or more (*44, 45*). If the total assay time is to remain under 30 min, digital NA quantification must be performed in less than 10 min. This assumes sample handling (including NA extraction) of at least 5 min, and antibiotic exposure of 15 min. This analysis compelled us to develop a method of digital NA quantification that can be performed in less than 10 min, which has never been accomplished before.

*Digital AST (dAST) in the presence of commensal organisms*

Next we evaluated a factor that may challenge phenotypic ASTs that are run directly on clinical samples: the presence of commensal or contaminating organisms that may respond differently to the antibiotic compared with the target pathogen. If the measurement method cannot differentiate between the response of the target pathogen and commensals, susceptibility cannot be determined accurately. NA amplification can be designed to target a sequence specific to a potential species of interest. Therefore, we hypothesized that when using a pathogen-specific NA target, the CT ratio (and AST call) would not be affected by varying levels of commensal bacteria. To test this hypothesis, dAST was performed in the presence of *Lactobacillus jensenii* (*Lj*), a common commensal bacterium found in urine. An *E. coli* culture (~$10^6$ CFU/mL) was mixed with each of three concentrations of *Lj* (0.1X, 1X, and 10X the optical density of the target pathogen) and exposed to the antibiotic ciprofloxacin (cip) for 15 min. The response was measured using droplet digital PCR (dPCR) and susceptibility of *E. coli* was determined correctly at all concentrations of the commensal organism (Fig. 3-2).
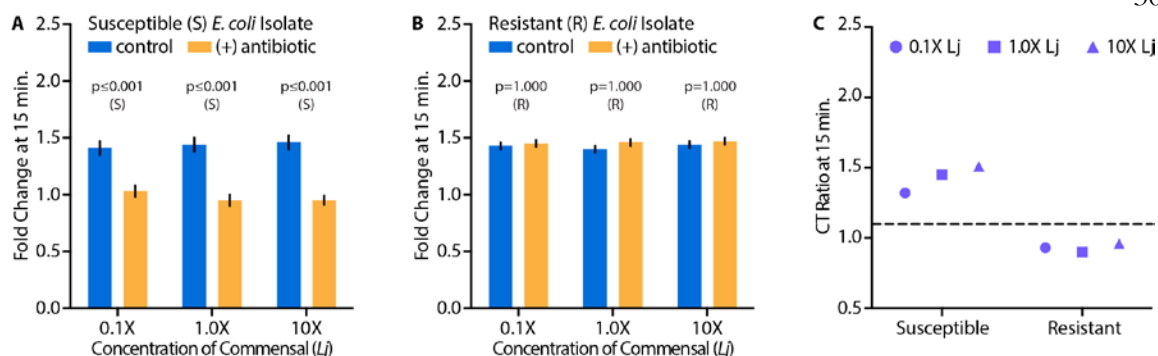
**Fig. 3-2**. Digital antimicrobial susceptibility test (dAST) using droplet digital PCR is robust to the presence of high levels of commensal bacteria due to the specificity of nucleic acid amplification. (A) A ciprofloxacin-susceptible *E. coli* isolate and (B) a ciprofloxacin-resistant *E. coli* isolate from the urine of patients diagnosed with urinary tract infections (UTIs) was exposed to 1.0 μg/mL ciprofloxacin in the presence of varying levels of *Lactobacillus jensenii* (*Lj*), a common urine commensal. Fold changes relative to time 0 were compared and used to determine susceptibility. The susceptibility calls remained unchanged at all three concentrations of commensal bacteria. (C) The calls were consistent when susceptibility was determined using control–treated (CT) ratios. N = 2 technical replicates for each single resistant and susceptible biological sample. Error bars are 98% confidence intervals.

*Optimization of isothermal amplification (LAMP)*

Having confirmed that the dAST method is capable of determining pathogen susceptibility in the presence of commensal organisms (Fig. 3-2), we next focused on shortening the measurement time from 2 h (using dPCR) to <10 min, to make the total dAST time <30 min. Digital LAMP (dLAMP) was investigated first, because it has been demonstrated previously by us and others (*39, 46-49*). However, these dLAMP assays took >45 min and were not shown to resolve small differences (~1.5X) in NA concentrations. Fast LAMP reactions often show significant background amplification in negative control treatments so we aimed to solve this problem as well.

We first designed primers and optimized real-time LAMP in bulk solutions to maximize amplification speed and specificity (initially, this was taken to mean the absence of background amplification with further testing of specificity later in the process). At very high NA concentrations, real-time bulk LAMP assays have been reported to be as fast as 5 min (*18, 50*), but at the lower concentrations of a single target molecule present in a single digital partition (~1 copy/ nL = $10^6$ copies/mL), amplification takes 10 min or more (*51-54*). To mimic the concentration of template in a single digital partition, we performed our bulk optimization experiments at ~$10^6$ copies/mL. The pathogen-specific NA sequence we chose as the dAST marker was the *E. coli* 23S rDNA gene because we showed previously that it was a reliable marker for DNA replication in the context of AST (*26*). We did not purposefully design these primers to exclude other *Enterobacteriaceae* pathogens and we expected cross-reactivity, which was observed in pilot experiments but remains to be further validated. Pan-*Enterobacteriaceae* primers would be useful for targeting other UTI pathogens. BLAST was used to evaluate primer specificity relative to the major families of bacteria found in UTIs.

The LAMP optimization process (Fig. 3-3A) consisted of four steps: 1) screening multiple LAMP primer sets for speed and specificity 2) screening multiple loop primer pairs with the selected primer set from step one for speed and specificity, 3) testing the selected LAMP + loop primers with a range of magnesium ion (Mg) concentrations, and 4) selecting the optimal amplification temperature from the data obtained in step three. Each parameter was tested using a temperature gradient, which proved to be critical to minimizing the time to positive (TTP). Of the four tested LAMP primer sets, we selected set B because it showed the fastest amplification and no background amplification (Fig. 3-3A (1)). No loop primer pair showed significantly earlier TTPs than any other pair, and no pair showed theoretical or experimental evidence of primer-dimers, so we arbitrarily chose loop A set (Fig. 3-3A (2)). Four concentrations of Mg were tested using the DNA polymerase Bst 3.0. The resulting TTPs varied by as much as 11 min depending on the amplification temperature. This optimization process resulted in TTPs as fast as ~4–5 min for ~700 target copies in a 6 μL amplification volume, with the fastest TTP (4.4 min) obtained using 6 mM Mg at 71 °C.

Once LAMP primers and protocols had been optimized, we further tested their specificity for the dAST marker. No positive signals were obtained when we ran real-time LAMP using *L. jensenii* (*Lj*) gDNA, human gDNA, or urine from healthy donors with no symptoms of UTI (Fig. 3-3B). When testing clinical UTI samples, a positive signal was only obtained when *E. coli* DNA was present. TTPs ranged from 4–5 min (Fig. 3-3C) for clinical UTI samples. We note that using this method (LAMP in a standard well-plate format) to resolve a 1.5X difference in concentration would require detecting a difference in TTP of ~8 s, which is difficult in practice to perform robustly (*39*).
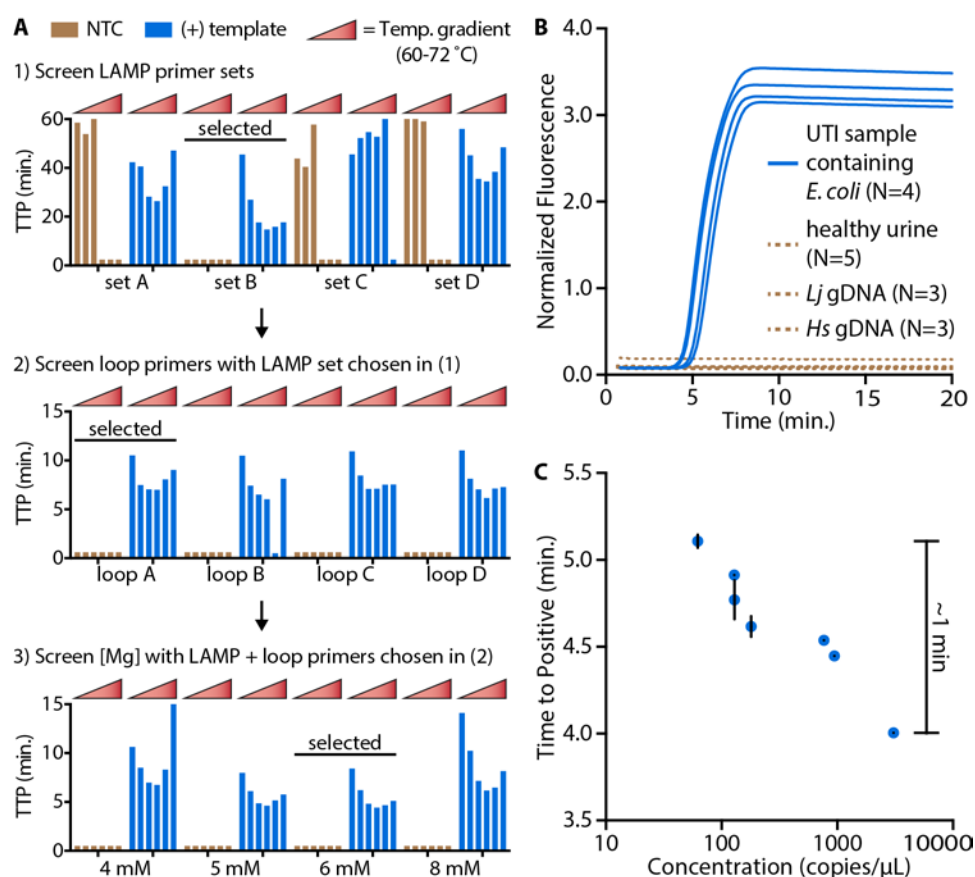


**Fig. 3-3**. Real-time LAMP optimization and compatibility with clinical samples. (A) Assay optimization protocol used to reduce the time-to-positive (TTP) from 15 min to < 5 min. Optimization was performed at a template concentration of ~700 copies/reaction or 0 copies/reaction (no template control, NTC). A value of 0.5 means no amplification was

observed. (B) Real-time fluorescence readout of amplified DNA for UTI samples containing *E. coli* (blue lines), healthy urine samples, samples containing gDNA of *Lactobacillus jensenii* (*Lj*), and samples containing human *(Hs)* gDNA (dashed brown lines). (C) TTP values for clinical UTI samples containing a range of pathogen concentrations. Error bars represent a single standard deviation from the average of technical triplicates.

*Digital AST (dAST) using ultrafast single-molecule counting (digital LAMP)*

Our next goal was to test whether using this optimized LAMP chemistry in a digital format would yield correct antibiotic susceptibility calls, while preserving the speed observed in bulk solutions. To accomplish this, the digital LAMP (dLAMP) assay must be able to resolve the small changes in NA concentrations that occur after a 15 min exposure to antibiotics, despite any heterogeneity in TTPs (the difference in amplification kinetics of individual molecules), which has been observed previously (*49, 55*). We chose to test dLAMP using clinical samples because sample matrices might increase the heterogeneity in TTPs and thus decrease resolution. Clinical urine samples can contain urea, proteins, blood (containing heme as a potent PCR inhibitor), or other cellular components that could interfere with the assay. Furthermore, we were concerned that extracellular DNA present in clinical urine may affect CT ratios. To eliminate this potential source of error, the dAST procedure that we previously developed for isolates (*26*) was modified to include DNase during the exposure step to digest any extracellular DNA (Supplementary Materials). We used the optimized LAMP assay (Fig. 3) with SlipChip microfluidic devices in a digital format (*56*). This SlipChip partitioned samples into 1,280 digital compartments. In each compartment, single molecules were amplified and counted in real time (*55*). In a clinical setting, decisions are typically made from single assay runs and thus we specifically wished to test whether differences in NA concentrations between the control and antibiotic-treated samples could be resolved reliably using a single 1,280-well SlipChip for each measurement.

Using dLAMP, most (>80%) single molecules amplified between 4–10 min, as shown by the fluorescence curves plotted in Fig. 3-4A,F. As expected, heterogeneity in TTP was

observed, likely as a result of the stochasticity of single-molecule amplification (*49, 57*).
Despite heterogeneity and matrix effects of clinical urine, we detected a significant difference
in NA concentration ($P = 0.001$) after only 5 min of amplification time for the cip-susceptible
clinical urine sample (Fig. 3-4C). For the cip-resistant sample, no significant difference in
concentration was detected during the dLAMP assay ($P > 0.05$) (Fig. 3-4H). In both samples,
the CT ratios were stable after 6 min and 40 seconds (6.7 min) of amplification (Fig. 3-4D,I),
were consistent with the ratios obtained by dPCR (Fig. 3-4E,J), and yielded the correct AST
call. We then repeated this dLAMP assay for one nit-susceptible and one nit-resistant clinical
urine sample. After 6.7 min of dLAMP amplification time, the CT ratios for both samples
were stable, and the correct antibiotic susceptibility call was determined (Figure 3-S3). This
demonstrates that the optimized dLAMP assay yields correct AST calls in only 6.7 min, well
below the 10 min limit necessary to achieve a 30 min dAST. Further, this result demonstrates
that because digital counting is ultrasensitive, individual DNA target molecules were
detected and the DNA concentration could be accurately quantified even after the dilution
that took place during antibiotic exposure and sample preparation (see Table 3-S3 for full
range of urine DNA concentrations).
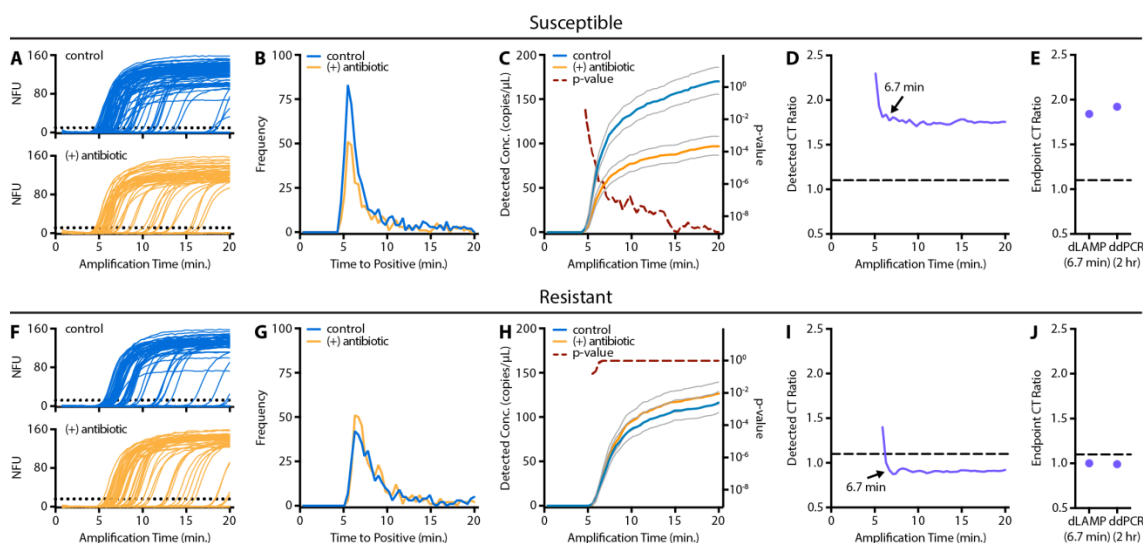


**Fig. 3-4**. High-resolution single-molecule nucleic acid amplification using ultrafast digital
LAMP (dLAMP) for digital antimicrobial susceptibility test (dAST) of clinical urinary tract
infection (UTI) urine samples with antibiotic-susceptible (A–E) and antibiotic-resistant (F–
J) *E. coli*. (A,F) Real-time fluorescence amplification traces (only 200 of 1,280 traces shown

for clarity). NFU = normalized fluorescence units; dotted line = positive threshold; when the normalized fluorescence intensity of a compartment crosses the threshold, that compartment is counted as positive. (B,G) Time Time-to-positive (TTP) distribution was determined by counting the number of compartments that crossed the positive threshold at each time point. (C,H) Detected concentrations of the target dAST marker in control and antibiotic-treated samples for successive image cycles. Note these curves are distinct from amplification curves shown in panels A and F. Grey lines represent 95% confidence intervals. (D,I) Detected control–treated (CT) ratios over time. Dashed line indicates susceptibility threshold. (E,J) Comparison of CT ratios for droplet digital PCR (dPCR) after 2 h and dLAMP (after 6.7 min of amplification).

*30 min sample-to-answer digital AST (dAST) directly from clinical urine samples*

Next, we tested whether the entire dAST workflow (antibiotic exposure, sample preparation, measurement, and data analysis) could give the correct AST call in less than 30 min. To accomplish this goal, three modifications were made to the dAST method used for Figure 3-4 (see Materials and Methods). First, the sample-preparation time was shortened from 10 min to 2 min while maintaining compatibility with dLAMP. Second, in parallel with antibiotic exposure of a clinical sample, rapid real-time LAMP was used to confirm the presence of *E. coli* and measure the approximate NA concentration of the dAST marker in the sample (Fig. 3-5B). This step provided identification of the pathogen (and could be used to select the amount of NAs loaded on the chip to maximize the performance of the digital assay), without adding time to the workflow. It also allows one to avoid the AST quantification step for samples that do not contain the pathogen, or contain it at levels too low to be of clinical significance. Third, the real-time image-analysis software we developed previously (*55*) was modified to calculate the concentrations of the dAST marker in real-time from each image, instead of after completion of amplification. After these modifications, the sum of all steps, 15 min (exposure) + 2 min (sample preparation) + 6.7 min (readout) was equal to a total of ~24 min. However, we also tested that these steps could be combined to provide a full sample-to-answer workflow (including all fluid transfer steps and data

analysis) in 30 min. We started a timer when an infected clinical urine sample was added to media with and without the antibiotic cip. After 29.8 min of total elapsed time (including 6.7 min of dLAMP amplification time), the software reported the control and treated concentrations for the cip-susceptible sample to be significantly different ($P = 1.5 \cdot 10^{-9}$), with a CT ratio of 1.59. For the cip-resistant sample, no significant difference in concentration was reported through the entirety of the dLAMP assay ($P > 0.05$). At 29.2 min (6.7 min of dLAMP amplification time) the CT ratio for the cip-resistant sample was 0.98 (Fig. 3-5D). Thus, this result shows how a combination of rapid partitioning, fast isothermal amplification, and high-resolution digital measurements enabled antibiotic susceptibility to be determined in less than 30 min.
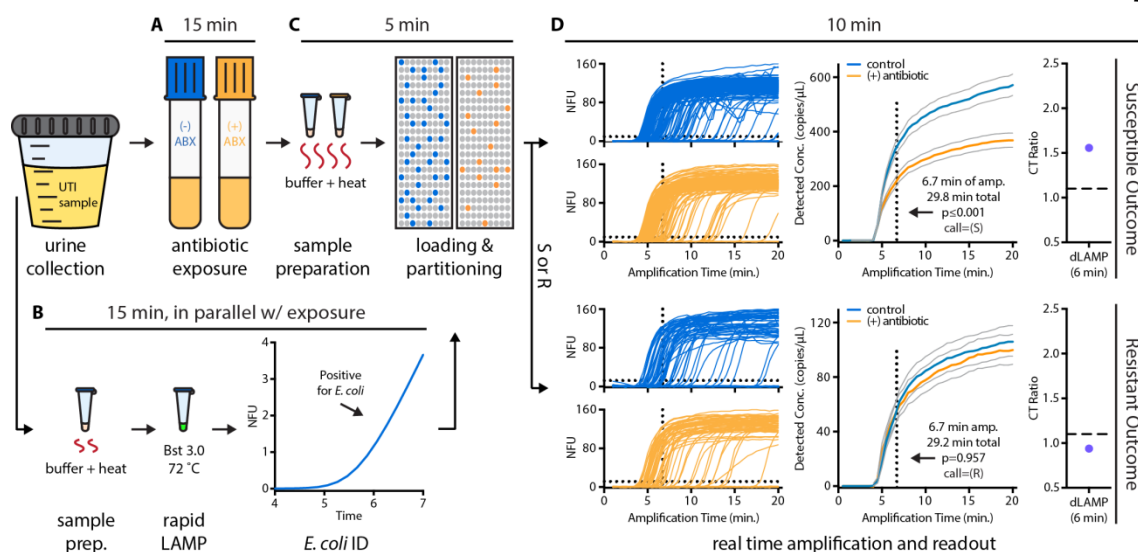
**Fig. 3-5**. Demonstration of a sample-to-answer antibiotic susceptibility test in less than 30 min using one resistant and one susceptible clinical UTI sample. (A) A clinical UTI sample was added to media with and without the antibiotic ciprofloxacin and incubated for 15 min. (B) During the antibiotic exposure step, the optimized bulk LAMP assay was performed on nucleic acids prepared from an aliquot of the urine sample. Amplification indicated the presence of *E. coli* at clinically-relevant levels. (C) Aliquots of the control and antibiotic-treated samples were added to extraction buffer; nucleic acids were prepared for quantification using digital LAMP; and samples were rapidly partitioned using SlipChips. (D) Digital LAMP was monitored in real time and a susceptibility call determined after 6.7 min of amplification; data for one resistant and one susceptible sample are shown. NFU = normalized fluorescence units. Grey lines represent 95% confidence intervals.

*Digital AST (dAST) using clinical samples*

Having established that the dAST method could be performed sample-to-answer in less than 30 min, we next tested this method with 51 clinical samples to evaluate its performance. A 15 min antibiotic exposure and NA extraction were performed on a total of 51 clinical UTI samples containing $\geq 5 \cdot 10^4$ CFU/mL *E. coli*: 17 cip-susceptible, 14 cip-resistant, 18 nit-susceptible, and 5 nit-resistant. Three clinical samples were tested separately with both cip

and nit, for a total of 54 tests. In this manuscript, we focus on categorical agreement of our binary susceptibility determination (susceptible or resistant) and did not test intermediate samples due to the variability in minimum inhibitory concentration (MIC) determination of gold-standard AST methods (*58, 59*). It is common to only challenge new AST methods against susceptible and resistant samples (*33, 34, 60*) and this excludes a small fraction of samples for cip (*61*). To ensure that there were no special issues with bacteria with intermediate MICs, we used the dAST method on a small set of cip-intermediate isolates to better understand its performance (see Supplementary Materials, Figure 3-S4).

We quantified the DNA AST marker of the control and treated extractions on all 54 samples with both dPCR and dLAMP. For each sample, the CT ratio was calculated and compared to a susceptibility threshold (1.10, determined in (*26*)) to classify samples as resistant or susceptible (Fig. 3-6A). Discordant CT ratios were observed for five samples when compared with the gold-standard broth microdilution method. As is commonly done, we re-ran discordant samples to resolve the discrepancy; however, our protocols and the potential for clinical samples to age disallowed many re-runs. Three of these five discordant samples were re-run and the second run CT ratio was averaged with the CT ratio from the first run to obtain a consensus value of the CT ratio (Samples #28, #29, #36 in Table 3-S1). We were unable to perform a second dAST assay on the other two discordant samples on the same day; rather than risk confounding effects due to aging of clinical samples on a different day, we did not rerun these samples and left them as errors that our method incurred relative to the gold-standard (Samples #22 and #30 in Table 3-S1). As a sanity check, we also reran one sample that was not discordant (Sample #122 in Table 3-S1).

With 1.10 as the susceptibility threshold for dPCR measurements, the dAST method returned 51 correct calls (94.4% categorical agreement), 2 very major errors for 19 resistant samples (10.5%), and 1 major error for 35 susceptible samples (2.9%). As 1.10 was a threshold based on experiments with isolates (*26*), we then generated a receiver operating characteristic (ROC) curve to inform the optimal threshold for clinical UTI samples (Fig. 3-6B). ROC curves show the ability of a diagnostic test to discriminate positives and negatives based on

a threshold: values below the threshold are called negative (e.g. a resistant AST call) and values above the threshold are called positive (e.g. a susceptible AST call). The area under the curve (AUC) for the generated ROC was 0.98. Using the optimal threshold given by the ROC curve (1.14), 53 of 54 dAST calls matched the gold-standard AST call (98.1% categorical agreement) with 1 very major error (5.3%) and 0 major errors (0%).

We also used digital LAMP to quantify the same samples. The CT ratios at 6.7 min were calculated and plotted in Fig. 3-6C, along with the ROC curve for digital LAMP (Fig. 3-6D). With 1.10 as the susceptibility threshold for dLAMP measurements at 6.7 min, the dAST method returned 51 correct calls (94.4% categorical agreement), 2 very major errors for 19 resistant samples (10.5%), and 1 major error for 35 susceptible samples (2.6%). The AUC for the generated ROC curve was 0.96. Using the optimal threshold given by the ROC curve (1.11), 52 of 54 dAST calls matched the gold-standard AST call (96.3% categorical agreement) with 1 very major error (5.3%) and 1 major error (2.9%).

These data show that although the optimal thresholds derived from ROC curves (1.14 for dPCR and 1.11 for dLAMP) slightly improve the categorical agreement, they are consistent with the threshold established for isolates (1.10, (26)) and are consistent with each other. It is also evident that quantifying DNA with digital LAMP at 6.7 min produces similar CT ratios and antibiotic susceptibility calls as dPCR.
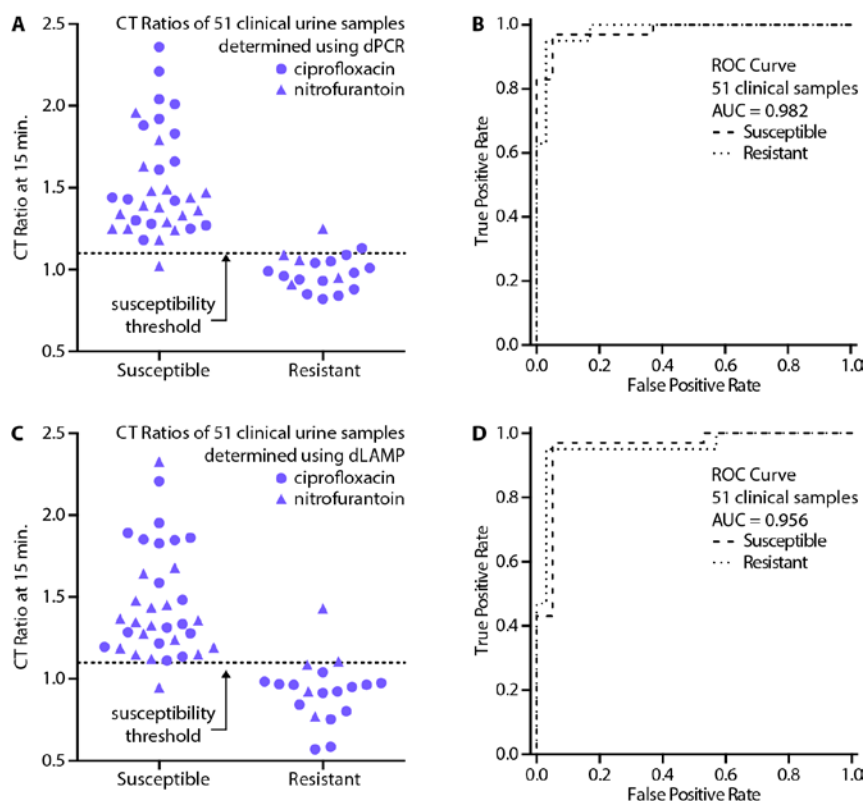
**Fig. 3-6**. Digital antimicrobial susceptibility test (dAST) directly from clinical samples using droplet digital PCR (dPCR) and digital LAMP (dLAMP) for quantification. (A/C) Antibiotic susceptibility of 51 clinical *E. coli* UTI samples was determined using the control–treated (CT) ratio after 15 min of exposure to two antibiotics, nitrofurantoin and ciprofloxacin (35 susceptible, 19 resistant, and three samples tested for both antibiotics). Nucleic acid concentrations were quantified with dPCR (A) and dLAMP (C). (B/D) Receiver operating characteristic (ROC) curves for the dAST method as measured by dPCR (B) and dLAMP (D).

**Discussion**

Here, we solved three problems that previously prevented the determination of phenotypic antibiotic susceptibility in less than 30 min from a clinical sample. First, we used digital quantification of a DNA marker to shorten the antibiotic exposure time to 15 min for clinical samples. Second, we showed that dAST is robust to the presence of commensal bacteria and

clinical urine matrices. Third, we developed and optimized a rapid, high-resolution measurement method for quantifying NA targets that shortens the measurement step to less than 10 min.

As discussed above, the introduction of commensal or contaminating organisms and clinical sample matrices to diagnostic workflows can cause major challenges in the development and translation of laboratory methods. It is therefore critical to prove that AST methods are compatible with clinical samples as soon as feasible. Here we have shown the dAST method is compatible with a wide range of urine matrices. Urine color of samples included colorless, yellow, dark yellow, and brown. pH ranged from <5.0–8.0. Protein concentrations ranged from 0.0~1.0 mg/mL (*62*). Additionally, red and white blood cell counts were as high as >$10^6$ cells/mL each in separate samples, and several samples had elevated levels of glucose. One sample contained $3 \cdot 10^4$ CFU/mL of a lactose-positive Gram-negative rod bacterium in addition to the infecting *E. coli*. While this study warrants more extensive follow-up investigation into more detailed correlations between urine composition and dAST speed, and does not establish whether or not this method would work in a more complex matrix like whole blood, this study indicates that dAST is compatible with a wide range of urine matrices and contaminants in clinical samples.

The digital LAMP assay developed here was capable of amplifying single target DNA molecules in less than 5 min. Despite the heterogeneity of single-molecule amplification times, high-resolution measurements were obtained even before all partitions with a target DNA molecule had amplified (~6.7 min). This makes dLAMP a strong tool for real-time, high-resolution, rapid measurements of NA, which increases the information gained in shorter times. Rapid, high-resolution measurements will also be invaluable for many other important assays, such as viral load measurements and genotyping (*49, 63, 64*). LAMP was chosen for translation to a digital format because it is a well-established amplification chemistry (*50, 65, 66*) with several readout methods (*67-70*). If necessary, other amplification chemistries—including NASBA, RPA, NEAR, HDA—could be tested and optimized for a digital format and used to measure a marker of interest. Additionally, we

show the LAMP assay is compatible with a rapid, one-step extraction method, which dramatically reduces sample preparation time. Due to the speed of extraction and amplification, the same LAMP assay can be used in a real-time bulk format for rapid pathogen identification in parallel with the 15 min antibiotic exposure step. This step, completed in <10 min (including sample preparation), did not extend the total assay time but provided two critical pieces of information prior to digital quantification: (i) whether a sample is infected with the pathogen of interest and (ii) whether a sample contains concentrations of the pathogen commensurate with levels found in UTI infections. UTI-positive samples gave TTP values of 4–5 min (corresponding to ~$10^5$–$10^6$ DNA copies/mL, N = 7, Fig. 3-3C), whereas clean healthy urine samples remained negative for at least 20 min (N = 5, Fig. 3-3B). This specificity is critical in working with clinical samples, because it enables the dAST to provide information specific to the pathogens of interest rather than commensals, contaminating organisms, or mixtures of pathogens (although such mixtures have not been tested here). In addition, the digital LAMP used to calculate CT ratios and determine susceptibility was informative for estimating pathogen concentration in the urine sample (see Table 3-S3).

The dAST method described herein was demonstrated with a specific scenario and thus there are inherent limitations to the extrapolations we can make to other pathogens and antibiotics. These limitations will guide future work in this area. We demonstrated dAST using a single clinical sample set of UTI urine samples infected with *E. coli* (*E. coli* causes 80% of UTIs). This is similar to other studies at this stage of technology development (*71-73*); multiple clinical sets will be run in the future. Ciprofloxacin was chosen because it has become one of the most commonly prescribed antibiotics for UTIs, despite being a second-line therapy that should be preserved for more severe cases (*12, 13, 74*). Nitrofurantoin was chosen because it is the recommended treatment for acute uncomplicated cystitis (*6*). Nit is a highly effective first-line therapy (antibiotic) that is often overlooked due to a lack of susceptibility data. The lack of AST data becomes especially important because nit is sometimes used a prophylactic treatment for recurrent UTIs and, despite its effectiveness, is not used to treat acute cases due to susceptibility concerns (*12*). Multiplexing with more pathogens and

antibiotics in a blinded study is an important next step and, if successful, would further validate and prove the clinical utility of this rapid dAST assay. Other UTI pathogens may have slower growth rates and smaller differences in control and treated concentrations (Fig. 3-1B); however, these differences are theoretically resolvable with digital NA quantification. Furthermore, alternative dAST markers might yield larger control–treated ratios after shorter antibiotic exposure times. In particular, changes in RNA in response to antibiotic exposure have been shown to be both large and fast (*37*) and should be rapidly discernable with digital methods such as the ones described here. For example, we have demonstrated quantification of viral RNA on digital SlipChips (*64, 75*), including on a 5-plex chip for multiplexed measurements. Such multiplexed measurements (with designs properly adjusted for the desired level of multiplexing and resolution, Fig. 3-S2) could be useful for analyzing combinations of RNA markers (*37*). Additionally, RNA markers (*37*) and alternative DNA markers (*26*) may be required for antibiotics with different mechanisms of action (e.g. beta lactams not tested here but described previously (*26*) to achieve a 30 min sample-to-answer dAST. Pathogen concentration is also a consideration when working with clinical samples. Quantifying NAs with high resolution is challenging if the NA concentration drops below the optimal dynamic range of the system. For example, in sepsis, the concentration of pathogens in blood can be as low as ~1–10 CFU/mL (*76*). While blood cultures (overnight or longer) are currently used to increase the concentration of pathogens, they are too slow to inform the initial treatment as each additional hour of delayed treatment in sepsis results in a 7.6% increase in mortality (*25*), emphasizing the need for rapid AST. Performing dAST in cases of sepsis therefore requires overcoming the major challenge of low concentrations of pathogens and will require alterations to the methodology, such as addition of a pathogen-concentrating step prior to antibiotic exposure, not tested here. Lastly, we have not tested dAST against heteroresistant microbial populations. While these have been documented in Gram-positive organisms (*77*), they are not common in Gram-negative organisms.

We have streamlined many aspects of the workflow for the dAST demonstration described in this paper, and believe this workflow can be performed by trained personnel in diagnostic laboratories. However, because this process requires several pipetting and handling steps,

operator error is possible. We anticipate that dAST, once developed and validated for multiple pathogens and antibiotics and cleared by regulatory agencies, would have the greatest impact on antibiotic stewardship if it can be performed by minimally trained personnel at the POC (in a CLIA-waived format in the U.S.). Therefore, the dAST workflow needs to be integrated into an inexpensive, simple-to-use device operated with inexpensive equipment. Additionally, such an integrated dAST device would increase throughput and reduce the potential biohazard risks from several open pipetting steps, which are a limitation of our current protocol. This integrated device has not been demonstrated here, but should be feasible because all steps of the dAST workflow (basic heating and mixing steps, digital quantification) are straightforward. Isothermal digital quantification can be performed using a range of technologies and amplification chemistries (*39, 46, 48, 63, 78*), including SlipChips, which are compatible with untrained users (*79*) and can be read out with optics as inexpensive as a cell phone camera (*39, 70*). Whereas reusable glass SlipChips, used by us in the past, required cleaning (*75*) disposable injection-molded SlipChips further simplify the workflow. Furthermore, the SlipChip platform supports multiplexed digital measurements (*44*), which is desired to perform AST on multiple antibiotics and/or pathogens simultaneously. Finally, the robustness of isothermal digital amplification to temperature, imaging conditions, reaction time (*39*), sample preparation methods (*80, 81*), and inhibitors (*82-84*) could further simplify the instrument requirements. This rapid digital AST (dAST), if fully developed and validated for additional microorganisms, antibiotics, and sample types, and transitioned to a CLIA-waivable POC device and FDA approved, would enable rapid clinical decision-making, improve management of infectious diseases, and increase antimicrobial stewardship.

**Materials and Methods**

*Experimental design*

The objective of this study was to develop a rapid phenotypic antibiotic susceptibility test (AST) using digital NA quantification. The two key hypotheses of this work were: i) 15 min

of antibiotic exposure can cause sufficient differences in pathogen-specific DNA concentrations between control and antibiotic-treated samples such that a high-resolution digital quantification measurement method (e.g. dPCR) can reliably detect a difference in NA concentrations for a susceptible sample and ii) a rapid digital LAMP assay can resolve these small differences in NA concentration in less than 10 min. To test the first hypothesis, 51 clinical samples were tested with the dAST method (three samples run with both antibiotics for a total of 54 antibiotic-susceptibility calls) and the results were compared to gold-standard broth microdilution. Clinical UTI samples with *E. coli* as the pathogen of interest were chosen as a test case for the dAST method using one first-line antibiotic (nitrofurantoin, nit) and one second-line antibiotic (ciprofloxacin, cip). To test the second hypothesis, the rapid digital LAMP assay we developed was compared with a commercial dPCR system for calculating CT ratios and determining antibiotic susceptibility from clinical UTI samples.

*Theoretical analysis*

To explore the tradeoffs among antibiotic exposure time, the growth rate of the bacteria in question, and the required resolution of the measurement method, we developed a simple model to inform optimal AST methods when DNA replication is used as the differentiating marker between susceptible and resistant bacteria. We assumed that i) a sample containing bacteria with an initial concentration of a specific NA sequence, $C_0$ [mol/L], has a DNA doubling time of $t_{double}$ [min] when incubated in media for $t_{inc}$ [min], ii) an antibiotic-susceptible bacteria sample incubated in media with antibiotics does not grow at all, and iii) antibiotic-resistant bacteria grow at the same rate with and without antibiotics.

Under these assumptions, the ratio of the NA concentrations of a control sample ($C_{control}$) compared to an antibiotic-treated sample ($C_{ABX}$)—the control–treated ratio (*CT ratio*)—after a certain time of antibiotic exposure ($t_{inc}$) would be:

$$CT\ ratio = \frac{C_{control}(t_{inc})}{C_{ABX}(t_{inc})} = \frac{C_0 \cdot 2^{t_{inc}/t_{double}}}{C_0} = 2^{t_{inc}/t_{double}}$$

Plotting CT ratio as a function of $t_{inc}$ and $t_{double}$ yields Fig. 3-1B. Typically, qPCR is capable of resolving 2-fold differences in concentration, whereas digital PCR (dPCR) can resolve as low as 1.2-fold differences in concentration (*40*). Due to the higher resolving power of dPCR, phenotypic AST can be performed with shorter antibiotic exposure times than if qPCR was used as the measurement method.

*Digital AST (dAST) in the presence of commensal bacteria*

Antibiotic-susceptible and antibiotic-resistant isolates of *E. coli* (*Ec*) from patients diagnosed with urinary tract infections (UTIs) were treated separately with (+ABX) and without (-ABX) antibiotics in the presence of varying concentrations of *Lactobacillus jensenii* (*Lj*), also isolated from a clinical UTI urine sample. Three concentrations of *Lj* were spiked into clinical urine samples: 0.1X, 1X, and 10X relative to the concentration of *E. coli*. Concentrations of *Ec* and *Lj* were determined by measuring optical density at 600 nm. Samples were exposed to 1 µg/mL cip for a total of 30 min under the same conditions as described previously (*26*). After 0, 15, and 30 min of exposure, a 10 µL aliquot of the sample was removed and added to 90 µL of QuickExtract DNA extraction solution (Epicentre, Madison, WI, USA). Target DNA from each extraction was quantified using droplet digital PCR (dPCR) as described previously (*26*). The fold change in the concentration of target DNA relative to time 0 in the control and antibiotic-treated samples after 15 min of antibiotic exposure was compared (Fig. 3-2A,B). The significance of this difference is measured by the p-value as described previously (*26*). The CT ratios at 15 min (Fig. 3-2C) were calculated as described in Results ("Key processes and operational space of digital AST (dAST)").

The primers used for all dPCR amplification experiments target the 23S gene of the *Enterobacteriacea* family (*26*). The concentrations of components in the dPCR mix used for these experiments and all subsequent dPCR experiments for this manuscript are as follows:

1X QX200 ddPCR EvaGreen Supermix (Bio-Rad, Hercules, CA, USA), 500 nM forward primer, and 500 nM reverse primer. The NA extraction composed 10% of the final volume in the dPCR mix. The remaining volume was nuclease-free water (NF-H$_2$O).

*Rapid loop-mediated isothermal amplification (LAMP)*

LAMP primer optimization experiments (Fig. 3-3A, steps 1–2) were performed on a Roche LightCyler 96 using the SYBR Green I channel for readout, 6 µL reaction volumes, and the following concentrations of reagents: 20 mM Tris-HCl pH 8.8, 50 mM KCl, 10 mM (NH$_4$)$_2$SO$_4$, 0.1% Tween-20, 1.4 mM dNTPs, 2 µM Syto-9, 400 U/mL Bst 2.0, ~700 copies/µL *E. coli* gDNA, and 8 mM MgSO$_4$. All samples were run across a temperature gradient spanning 60 – 72 ˚C.

The experiments optimizing magnesium concentration (Fig. 3-4A, step 3) were performed using the same protocol as above with the following concentrations of reagents: 20 mM Tris-HCl pH 8.8, 150 mM KCl, 10 mM (NH$_4$)$_2$SO$_4$, 0.1% Tween-20, 1.4 mM dNTPs, 2 µM Syto-9, 360 U/mL Bst 3.0, ~700 copies/µL *E. coli* gDNA, and variable concentrations of MgSO$_4$ (Fig. 4A). All samples were run across a temperature gradient spanning 60–74 ˚C.

Primer concentrations were kept constant in all experiments: 1.6 µM FIP/BIP, 0.2 µM FOP/BOP, and 0.4 µM loopF/loopB (when included). The final selected primer set was as follows: GGCGTTAAGTTGCAGGGTAT (FOP), TCACGAGGCGCTACCTAA (BOP), CGGTTCGGTCCTCCAGTTAGTGTTTTCCCGAAACCCGGTGATCT (FIP), TAGCGGATGACTTGTGGCTGGTTTTTCGGGGAGAACCAGCTATC (BIP), ACCTTCAACCTGCCCATG (LoopF), GTGAAAGGCCAATCAAACC (LoopB).

Identification and specificity experiments were performed using the same concentration of reagents as the experiments to optimize MgSO$_4$ concentration, but were run with 5 mM MgSO$_4$. Although 6 mM MgSO$_4$ yielded the fastest TTP, 5 mM MgSO$_4$ was used in subsequent experiments in order to minimize the risk of background amplification. We have

not observed background amplification with the primers described here, but other primer sets are sensitive to MgSO₄ concentration. The optimal TTP using 5 mM $MgSO_4$ was only 12 s slower than when using 6 mM $MgSO_4$.

BLAST was used to evaluate primer specificity against the families *Enterobacteriaciae*, *Staphylococcaceae*, and *Enterococcaceae*. The specificity of the LAMP primers targeting the *E. coli* 23S rDNA gene was tested against human genomic DNA (*Hs* gDNA), *Lactobacillus jensenii* genomic DNA (*Lj* gDNA), urine from healthy donors, and water (Fig. 4A,B). *Hs* gDNA was tested at 0.002, 0.02, and 0.2 ng/µL final reaction concentration as measured using a NanoDrop 2000c (Thermo Fisher Scientific, Waltham, MA, USA). *Lj* gDNA was tested at final reaction concentrations of 0.16, 0.8, and 1.6 ng/µL, as measured using a NanoDrop 2000c. Urine from healthy donors was run at 10% final reaction volume. Real-time LAMP amplification was performed using a range of concentrations of *E. coli* gDNA (*Ec* gDNA) prepared from clinical UTI urine samples and quantified using droplet digital PCR (Fig. 3-3C).

*Digital AST (dAST) using clinical UTI samples*

We obtained clinical urine samples under approved IRB protocols in place at the University of California Los Angeles Clinical Microbiology Laboratory (UCLA CML). Samples were de-identified before being transported to Caltech. Samples were stored in Vacutainer Plus C&S Boric Acid Sodium Borate/Formate Tubes (BD, Franklin Lakes, NJ, USA), transported at ambient temperature, and stored at 4 °C once received at Caltech. Urine samples were from otherwise healthy patients suspected of having a UTI (based on urinalysis results). The presence of *E. coli* was confirmed by the UCLA CML, and MICs determined as described previously (*26*). Urine samples were selected for dAST analysis based on the determined MIC of the infecting *E. coli*. Samples were considered cip-susceptible if the determined MIC ≤ 0.25 µg/mL and considered cip-resistant if the MIC ≥ 4 µg/mL. Samples were considered nit-susceptible if the MIC ≤ 16 µg/mL and nit-resistant if the MIC ≥ 128 µg/mL. Viable bacteria are a requirement of phenotypic ASTs. Non-viable samples were excluded if a

decrease in DNA concentration was observed (indicating digestion of DNA from non-viable cells). If the change in DNA concentration was not easily discernible by dPCR, DNA concentration at 30 min. was measured to determine whether the sample was viable (DNA concentration increased at 30 min) or non-viable (DNA concentration decreased at 30 min).

Before the start of each experiment, urine (as received, still containing boric acid) was warmed to 37 °C over 30 min to mimic the temperature of fresh urine samples. At the start of each dAST experiment (t=0), warmed urine was added to media with (+ABX) and without (-ABX) antibiotics to initiate DNA replication and begin exposure. This addition to media dilutes the boric acid present in the transport media, allowing bacterial replication to proceed. The final 500 μL sample mixture in the control and treated tubes contained 250 μL BHI (Becton Dickinson, Franklin Lakes, NJ, USA), 25 μL DNase I (New England Biolabs, Ipswich, MA, USA), 5 μL DNase buffer (100 mM Tris-HCl, 25 mM $MgCl_2$, and 5 mM $CaCl_2$), an aliquot of the urine, with the remaining volume NF-H2O. 1 μg/mL cip or 16 μg/mL nit was added to the +ABX sample, with an equal volume of NF-H2O (in the case of cip) or dimethylformamide (in the case of nit) added to the control sample (-ABX). Antibiotic concentrations were chosen based on our previous work with isolates (*26*) and are near CLSI and EUCAST breakpoints. 10 μL aliquots of urine were added to the control and treated tubes in the case of cip treatment. 25 μL aliquots were used in the case of nit treatment. This was done following the observation that higher concentrations of urine matrix sometimes showed cip-neutralizing effects (data not shown). Samples were shaken at 750 rpm at 37 °C for 30 min. After 0, 15, and 30 min of exposure, 10 μL aliquots of the control and treated samples were removed and added to 90 μL of QuickExtract DNA Extraction Solution. The extracted samples were heated according to a modified version of the manufacturer's protocol (65 °C for 6 min, 95 °C for 4 min, chilled on ice), vortexed, and centrifuged. Next, 5 μL of each extraction was added to 45 μL ddPCR mix and quantified using dPCR. If the DNA concentration of the sample was too high, template was diluted in NF-H2O and dPCR was re-run. CT ratios were then calculated (see above). If the dAST call did not match the gold-standard AST call, then the sample was re-run several hours later on the same day. For the

four samples that were re-run, only the second set of NA extractions were quantified by dLAMP.

*Rapid digital LAMP (dLAMP)*

Clinical urine samples were treated with and without 1 µg/mL cip or 16 µg/mL nit for 15 min and nucleic acids extracted as described above. The dLAMP mix consisted of 20 mM Tris-HCl pH 8.8, 150 mM KCl, 10 mM $(NH_4)_2SO_4$, 0.1% Tween-20, 1.4 mM dNTPs, 1X EvaGreen (Biotium, Fremont, CA, USA), 360 U/mL Bst 3.0, 1X RNase Cocktail (ThermoFisher, Waltham, MA, USA), 5 mM $MgSO_4$, and 1 mg/mL BSA prepared in NF-$H_2O$. Aliquots of NA extractions composed 10% or 20% of the final volume in the dLAMP mix. Two aliquots of dLAMP mix containing equal volumes of NA extractions from the control and treated samples were simultaneously loaded into two separate SlipChip devices. The top piece of each SlipChip was slipped, which partitioned the solution into 1,280 3-nL compartments (lab made glass SlipChips) or 5,376 2.4-nL compartments (injection molded plastic SlipChips) (see Supplementary Materials). The SlipChips were then placed onto the thermal cycler of a digital real-time imaging instrument and incubated at 72 °C for 20 min (*55*). Amplification time was recorded starting from when the SlipChips reached 69 °C (as measured using a temperature probe).

Images were taken either every 20 s or every 30 s and the fluorescent intensity was measured for each compartment (Fig. 3-4A). Wells that showed liquid movement or bubbles were excluded form analysis. The concentration of the target was calculated using Poisson statistics and was based on the number of "positive" compartments that exceeded the fluorescence intensity threshold (calculations were performed for time points where 13 or more compartments were positive). The concentration of the control and treated samples was calculated in real-time, along with a p-value representing the probability that the ratio of concentrations being greater than 1.10 was a result of random chance (Fig. 3-4D). If $P < 0.05$, we can be reasonably certain that the bacteria are susceptible to the antibiotic. If the p-

value remains > 0.05, we can be reasonably certain that the bacteria are resistant to the antibiotic.

*Sample-to-answer digital AST (dAST) in less than 30 min*

Clinical urine samples were treated with ("treated") and without ("control") 1 μg/mL cip for 15 min as described above. After 0 and 15 min, a 20 μL aliquot of each sample was added to 80 μL of QuickExtract DNA Extraction Solution (Epicentre). The two samples were then heated at 65 °C for 1 min followed by 98 °C for 1 min, after which they were chilled by incubation on an ice block for 30 s, vortexed, and centrifuged.

In parallel with the 15 min antibiotic exposure step, we used the semi-quantitative ability of qLAMP to predict the appropriate dilution factor for our 1,280-well digital SlipChips. A 2 μL aliquot from each of the control and treated DNA extractions from time 0 were added to 8 μL LAMP mix. The samples, along with 2 standards with known DNA concentration (S1=128.5 copies/μL and S2=766.0 copies/μL), were then incubated at 72 °C for 5 min on a Roche LightCycler 96 and fluorescent traces were monitored in real-time. If the TTP of the average of the samples was earlier than the TTP of S1, then 3 μL of the NA aliquot extracted at 15 min were added to 24 μL of dLAMP mix, along with 3 μL of NF-H$_2$O. If the TTP of the sample was between the TTPs of S1 and S2, then 6 μL of the 15-min NA extraction was added to 24 μL of dLAMP mix, with no additional NF-H$_2$O added. This step was completed within the 15 min of antibiotic exposure. In the experiments with both antibiotic-resistant and -susceptible samples (Fig. 3-5), the TTP was earlier than the TTP of S1.

After semi-quantification and mixture of the dLAMP mix with template, the dLAMP solutions were pipette-mixed, loaded into SlipChips, partitioned into 1,280 compartments, and placed on the thermal cycler of a digital real-time imaging instrument at 72 °C.

Images were taken every 30 s and the fluorescence intensity was measured for each compartment (Fig. 3-5D). The concentration of the dAST marker was calculated using

Poisson statistics and was based on the number of compartments that had exceeded a fluorescence intensity threshold. The concentration of the control and treated samples was calculated in real-time by modifying the National Instruments LabView software previously developed (*55*). We calculated a p-value representing the probability that the control concentration was greater than 1.10X the treated concentration merely by random chance in real-time as each image was processed.

*Statistical analysis*

Poisson statistics were used to calculate the 95% or 98% confidence interval of the NA concentration for each digital measurement (*44*). To calculate the error in fold change we used standard error propagation methods (*85*). With $\lambda$ as a concentration and $\sigma$ the standard deviation, the equation is:

$$\sigma_{ratio} = \sqrt{\left(\frac{\sigma_{\lambda_2}}{\lambda_1}\right)^2 + \left(\frac{\lambda_2 \cdot \sigma_{\lambda_1}}{\lambda_1^2}\right)^2}$$

P-values to compare digital NA concentrations were calculated with a one-tailed Z test asking if the control NA concentration ($\lambda_{control}$) was 1.10X higher than the treated NA concentration ($\lambda_{ABX}$) (*26, 44*):

$$Z = \frac{\ln(\lambda_{control}) - \ln(1.10 \cdot \lambda_{ABX})}{\sqrt{\sigma_{\ln(\lambda_{control})}^2 + \sigma_{\ln(\lambda_{ABX})}^2}}$$

**References**

1. R. Laxminarayan, A. Duse, C. Wattal, A. K. Zaidi, H. F. Wertheim, N. Sumpradit, E. Vlieghe, G. L. Hara, I. M. Gould, H. Goossens, C. Greko, A. D. So, M. Bigdeli, G. Tomson, W. Woodhouse, E. Ombaka, A. Q. Peralta, F. N. Qamar, F. Mir, S. Kariuki, Z. A. Bhutta, A. Coates, R. Bergstrom, G. D. Wright, E. D. Brown, O. Cars. Antibiotic resistance--the need for global solutions. *Lancet Infect Dis* **13**, 1057-1098 (2013).

2.      J. O'Neill, *Tackling Drug-Resistant Infections Globally: Final Report and Recommendations* (2016, https://amr-review.org/Publications.html)

3.      J. O'Neill, *Rapid Diagnostics: Stopping Unnecessary Use of Antibiotics* (2015, https://amr-review.org/Publications.html)

4.      S. E. Cosgrove. The relationship between antimicrobial resistance and patient outcomes: mortality, length of hospital stay, and health care costs. *Clinical infectious diseases : an official publication of the Infectious Diseases Society of America* **42 Suppl 2**, S82-89 (2006).

5.      K. K. Perez, R. J. Olsen, W. L. Musick, P. L. Cernoch, J. R. Davis, G. A. Land, L. E. Peterson, J. M. Musser. Integrating rapid pathogen identification and antimicrobial stewardship significantly decreases hospital costs. *Arch Pathol Lab Med* **137**, 1247-1254 (2013).

6.      K. Gupta, T. M. Hooton, K. G. Naber, B. Wullt, R. Colgan, L. G. Miller, G. J. Moran, L. E. Nicolle, R. Raz, A. J. Schaeffer, D. E. Soper, A. Infectious Diseases Society of, M. European Society for, D. Infectious. International clinical practice guidelines for the treatment of acute uncomplicated cystitis and pyelonephritis in women: A 2010 update by the Infectious Diseases Society of America and the European Society for Microbiology and Infectious Diseases. *Clinical infectious diseases : an official publication of the Infectious Diseases Society of America* **52**, e103-120 (2011).

7.      CDC, "Antibiotic Resistance Threats in the United States,"  (Centers for Disease Control Office of Infectious Diseases, Atlanta, GA, https://www.cdc.gov/drugresistance/pdf/ar-threats-2013-508.pdf 2013).

8.      Nesta, *Longitude Prize: How can we prevent the rise of resitance to antibiotics?* (2014, https://longitudeprize.org/challenge/antibiotics)

9.      CDDEP, "State of the World's Antibiotics,"  (Center for Disease Dynamics, Economics and Policy, Washington, D.C., http://cddep.org/sites/default/files/swa_2015_final.pdf 2015).

10.     The White House, "National Action Plan for Combating Antibiotic-Resistant Bacteria,"

(https://obamawhitehouse.archives.gov/sites/default/files/docs/national_action_plan_for_combating_antibotic-resistant_bacteria.pdf 2015).

11. WHO, "Global Antimicrobial Resistance Surveillance System - Manual for Early Implementation," (http://apps.who.int/iris/bitstream/10665/188783/1/9789241549400_eng.pdf 2015).

12. A. E. Barber, J. P. Norton, A. M. Spivak, M. A. Mulvey. Urinary tract infections: current and emerging management strategies. *Clinical infectious diseases : an official publication of the Infectious Diseases Society of America* **57**, 719-724 (2013).

13. T. M. Hooton. Uncomplicated urinary tract infection. *N Engl J Med* **366**, 1028-1037 (2012).

14. M. Kobayashi, D. J. Shapiro, A. L. Hersh, G. V. Sanchez, L. A. Hicks. Outpatient antibiotic prescribing practices for uncomplicated urinary tract infection in women in the United States, 2002-2011. *Open Forum Infect Dis* **3**, 1-7 (2016).

15. J. H. Jorgensen, M. J. Ferraro. Antimicrobial susceptibility testing: a review of general principles and contemporary practices. *Clinical infectious diseases : an official publication of the Infectious Diseases Society of America* **49**, 1749-1755 (2009).

16. T. Kostic, M. Ellis, M. R. Williams, T. M. Stedtfeld, J. B. Kaneene, R. D. Stedtfeld, S. A. Hashsham. Thirty-minute screening of antibiotic resistance genes in bacterial isolates with minimal sample preparation in static self-dispensing 64 and 384 assay cards. *Appl Microbiol Biotechnol* **99**, 7711-7722 (2015).

17. T. Ikeuchi, M. Seki, Y. Akeda, N. Yamamoto, S. Hamaguchi, T. Hirose, K. Yamanaka, M. Saito, K. Tomono, E. Tamiya. PCR-based method for rapid and minimized electrochemical detection of mecA gene of methicillin-resistant *Staphylococcus aureus* and methicillin-resistant *Staphylococcus epidermidis*. *General Medicine: Open Access* **3**, 215 (2015).

18. Y. Zboromyrska, A. Vergara, C. Cosgaya, G. Verger, N. Mosqueda, M. Almela, C. Pitart, I. Roca, F. Marco, J. Vila. Rapid detection of beta-lactamases directly

from positive blood cultures using a loop-mediated isothermal amplification (LAMP)-based assay. *Int J Antimicrob Ag* **46**, 355-356 (2015).

19. L. R. Peterson, D. M. Schora. Methicillin-Resistant Staphylococcus aureus Control in the 21st Century: Laboratory Involvement Affecting Disease Impact and Economic Benefit from Large Population Studies. *J Clin Microbiol* **54**, 2647-2654 (2016).

20. A. van der Zee, W. D. Hendriks, L. Roorda, J. M. Ossewaarde, J. Buitenwerf. Review of a major epidemic of methicillin-resistant Staphylococcus aureus: the costs of screening and consequences of outbreak management. *Am J Infect Control* **41**, 204-209 (2013).

21. M. Spencer, S. Barnes, J. Parada, S. Brown, L. Perri, D. Uettwiller-Geiger, H. B. Johnson, D. Graham. A primer on on-demand polymerase chain reaction technology. *Am J Infect Control* **43**, 1102-1108 (2015).

22. J. Davies, D. Davies. Origins and evolution of antibiotic resistance. *Microbiol Mol Biol Rev* **74**, 417-433 (2010).

23. H. D. Marston, D. M. Dixon, J. M. Knisely, T. N. Palmore, A. S. Fauci. Antimicrobial Resistance. *JAMA* **316**, 1193-1204 (2016).

24. J. M. Hicks, R. Haeckel, C. P. Price, K. Lewandrowski, A. H. B. Wu. Recommendations and opinions for the use of point-of-care testing for hospitals and primary care: summary of a 1999 symposium. *Clin Chim Acta* **303**, 1-17 (2001).

25. A. Kumar, D. Roberts, K. E. Wood, B. Light, J. E. Parrillo, S. Sharma, R. Suppes, D. Feinstein, S. Zanotti, L. Taiberg, D. Gurka, A. Kumar, M. Cheang. Duration of hypotension before initiation of effective antimicrobial therapy is the critical determinant of survival in human septic shock. *Crit Care Med.* **34**, 1589-1596 (2006).

26. N. G. Schoepp, E. M. Khorosheva, T. S. Schlappi, M. S. Curtis, R. M. Humphries, J. A. Hindler, R. F. Ismagilov. Digital Quantification of DNA Replication and Chromosome Segregation Enables Determination of

Antimicrobial Susceptibility after only 15 Minutes of Antibiotic Exposure. *Angew Chem Int Ed Engl* **55**, 9557-9561 (2016).

27. M. Fredborg, K. R. Andersen, E. Jorgensen, A. Droce, T. Olesen, B. B. Jensen, F. S. Rosenvinge, T. E. Sondergaard. Real-time optical antimicrobial susceptibility testing. *J Clin Microbiol* **51**, 2047-2053 (2013).

28. J. Choi, J. Yoo, M. Lee, E. G. Kim, J. S. Lee, S. Lee, S. Joo, S. H. Song, E. C. Kim, J. C. Lee, H. C. Kim, Y. G. Jung, S. Kwon. A rapid antimicrobial susceptibility test based on single-cell morphological analysis. *Sci Transl Med* **6**, 267ra174 (2014).

29. I. S. Douglas, C. S. Price, K. H. Overdier, R. F. Wolken, S. W. Metzger, K. R. Hance, D. C. Howson. Rapid automated microscopy for microbiological surveillance of ventilator-associated pneumonia. *Am J Respir Crit Care Med* **191**, 566-573 (2015).

30. C. Chantell. Multiplexed automated digital microscopy for rapid identification and antimicrobial susceptibility testing of bacteria and yeast directly from clinical samples. *Clinical Microbiology Newsletter* **37**, 161-167 (2015).

31. P. Ertl, E. Robello, F. Battaglini, S. R. Mikkelsen. Rapid antibiotic susceptibility testing via electrochemical measurement of ferricyanide reduction by *Escherichia coli* and *Clostridium sporogenes*. *Anal Chem* **72**, 4957-4964 (2000).

32. C. Halford, R. Gonzalez, S. Campuzano, B. Hu, J. T. Babbitt, J. Liu, J. Wang, B. M. Churchill, D. A. Haake. Rapid antimicrobial susceptibility testing by sensitive detection of precursor rRNA using a novel electrochemical biosensing platform. *Antimicrob Agents Chemother* **57**, 936-943 (2013).

33. K. E. Mach, R. Mohan, E. J. Baron, M. C. Shih, V. Gau, P. K. Wong, J. C. Liao. A biosensor platform for rapid antimicrobial susceptibility testing directly from clinical samples. *J Urol* **185**, 148-153 (2011).

34. A. Mezger, E. Gullberg, J. Goransson, A. Zorzet, D. Herthnek, E. Tano, M. Nilsson, D. I. Andersson. A general method for rapid determination of antibiotic susceptibility and species in bacterial infections. *J Clin Microbiol* **53**, 425-432 (2015).

35.    J. M. Rolain, M. N. Mallet, P. E. Fournier, D. Raoult. Real-time PCR for universal antibiotic susceptibility testing. *J Antimicrob Chemother* **54**, 538-541 (2004).

36.    I. Steinberger-Levy, O. Shifman, A. Zvi, N. Ariel, A. Beth-Din, O. Israeli, D. Gur, M. Aftalion, S. Maoz, R. Ber. A Rapid Molecular Test for Determining Yersinia pestis Susceptibility to Ciprofloxacin by the Quantification of Differentially Expressed Marker Genes. *Frontiers in Microbiology* **7**,  (2016).

37.    A. K. Barczak, J. E. Gomez, B. B. Kaufmann, E. R. Hinson, L. Cosimi, M. L. Borowsky, A. B. Onderdonk, S. A. Stanley, D. Kaur, K. F. Bryant, D. M. Knipe, A. Sloutsky, D. T. Hung. RNA signatures allow rapid identification of pathogens and antibiotic susceptibilities. *Proc Natl Acad Sci U S A* **109**, 6217-6222 (2012).

38.    M. Fredborg, F. S. Rosenvinge, E. Spillum, S. Kroghsbo, M. Wang, T. E. Sondergaard. Rapid antimicrobial susceptibility testing of clinical isolates by digital time-lapse microscopy. *Eur J Clin Microbiol Infect Dis* **34**, 2385-2394 (2015).

39.    D. A. Selck, M. A. Karymov, B. Sun, R. F. Ismagilov. Increased robustness of single-molecule counting with microfluidics, digital isothermal amplification, and a mobile phone versus real-time kinetic measurements. *Anal Chem* **85**, 11129-11136 (2013).

40.    A. S. Whale, J. F. Huggett, S. Cowen, V. Speirs, J. Shaw, S. Ellison, C. A. Foy, D. J. Scott. Comparison of microfluidic digital PCR and conventional quantitative PCR for measuring copy number variation. *Nucleic Acids Res* **40**, e82 (2012).

41.    D. Haake, B. Churchill, C. Halford, "Amdinocillin for rapid determination of susceptibility to beta-lactam antibiotics," PCT/US2014/047684, international filing date 7/22/2014.

42.    R. J. Almeida, J. H. Jorgensen. Comparison of adherence and urine growth rate properties of Staphylococcus saprophyticus and Staphylococcus epidermidis. *Eur J Clin Microbiol* **3**, 542-545 (1984).

43.    M. S. Lawlor, C. O'Connor, V. L. Miller. Yersiniabactin is a virulence factor for Klebsiella pneumoniae during pulmonary infection. *Infect Immun* **75**, 1463-1472 (2007).

44.    J. E. Kreutz, T. Munson, T. Huynh, F. Shen, W. Du, R. F. Ismagilov. Theoretical design and analysis of multivolume digital assays with wide dynamic range validated experimentally with microfluidic digital PCR. *Anal Chem* **83**, 8158-8168 (2011).

45.    S. Weaver, S. Dube, A. Mir, J. Qin, G. Sun, R. Ramakrishnan, R. C. Jones, K. J. Livak. Taking qPCR to a higher level: Analysis of CNV reveals the power of high throughput qPCR to enhance quantitative resolution. *Methods* **50**, 271-276 (2010).

46.    P. Xu, X. Zheng, Y. Tao, W. Du. Cross-Interface Emulsification for Generating Size-Tuneable Droplets. *Anal Chem* **88**, 3171-3177 (2016).

47.    F. Schuler, C. Siber, S. Hin, S. Wadle, N. Paust, R. Zengerle, F. von Stetten. Digital droplet LAMP as a microfluidic app on standard laboratory devices. *Anal Methods* **8**, 2750-2755 (2016).

48.    T. D. Rane, L. Chen, H. C. Zec, T. H. Wang. Microfluidic continuous flow digital loop-mediated isothermal amplification (LAMP). *Lab Chip* **15**, 776-782 (2015).

49.    B. Sun, J. Rodriguez-Manzano, D. A. Selck, E. Khorosheva, M. A. Karymov, R. F. Ismagilov. Measuring fate and rate of single-molecule competition of amplification and restriction digestion, and its use for rapid genotyping tested with hepatitis C viral RNA. *Angew Chem Int Ed Engl* **53**, 8088-8092 (2014).

50.    N. A. Tanner, T. C. Evans, Jr. Loop-mediated isothermal amplification for detection of nucleic acids. *Curr Protoc Mol Biol* **105**, Unit 15 14 (2014).

51.    M. Imai, A. Ninomiya, H. Minekawa, T. Notomi, T. Ishizaki, M. Tashiro, T. Odagiri. Development of H5-RT-LAMP (loop-mediated isothermal amplification) system for rapid diagnosis of H5 avian influenza virus infection. *Vaccine* **24**, 6679-6682 (2006).

52.    Y. Kurosaki, N. Magassouba, O. K. Oloniniyi, M. S. Cherif, S. Sakabe, A. Takada, K. Hirayama, J. Yasuda. Development and Evaluation of Reverse Transcription-Loop-Mediated Isothermal Amplification (RT-LAMP) Assay

Coupled with a Portable Device for Rapid Diagnosis of Ebola Virus Disease in Guinea. *PLoS Negl Trop Dis* **10**, e0004472 (2016).

53.     A. Buhlmann, J. F. Pothier, F. Rezzonico, T. H. Smits, M. Andreou, N. Boonham, B. Duffy, J. E. Frey. Erwinia amylovora loop-mediated isothermal amplification (LAMP) assay for rapid pathogen detection and on-site diagnosis of fire blight. *J Microbiol Methods* **92**, 332-339 (2013).

54.     G. P. Wu, S. H. Chen, R. E. Levin. Application of ethidium bromide monoazide for quantification of viable and dead cells of Salmonella enterica by real-time loop-mediated isothermal amplification. *J Microbiol Methods* **117**, 41-48 (2015).

55.     D. A. Selck, R. F. Ismagilov. Instrument for Real-Time Digital Nucleic Acid Amplification on Custom Microfluidic Devices. *PLoS One* **11**, e0163060 (2016).

56.     F. Shen, W. Du, J. E. Kreutz, A. Fok, R. F. Ismagilov. Digital PCR on a SlipChip. *Lab Chip* **10**, 2666-2672 (2010).

57.     D. T. Gillespie. Stochastic simulation of chemical kinetics. *Annu. Rev. Phys. Chem* **58**, 35-55 (2007).

58.     CLSI, "M100-S25 Performance Standards for Antimicrobial Susceptibility Testing,"  (Clinical Laboratory Standards Institute, 2015).

59.     J. Turnidge, D. L. Paterson. Setting and revising antibacterial susceptibility breakpoints. *Clin Microbiol Rev* **20**, 391-408, table of contents (2007).

60.     V. Ivancic, M. Mastali, N. Percy, J. Gornbein, J. T. Babbitt, Y. Li, E. M. Landaw, D. A. Bruckner, B. M. Churchill, D. A. Haake. Rapid antimicrobial susceptibility determination of uropathogens in clinical urine specimens by use of ATP bioluminescence. *J Clin Microbiol* **46**, 1213-1219 (2008).

61.     EUCAST, "Antimicrobial wild type distributions of microorganisms,"  (European Society of Clinical Microbiology and Infectious Disease, https://mic.eucast.org/Eucast2/ 2017).

62.     J. A. Simerville, W. C. Maxted, J. J. Pahira. Urinalysis: a comprehensive review. *Am Fam Physician* **71**, 1153-1162 (2005).

63.     F. Shen, E. K. Davydova, W. Du, J. E. Kreutz, O. Piepenburg, R. F. Ismagilov. Digital isothermal quantification of nucleic acids via simultaneous chemical

initiation of recombinase polymerase amplification reactions on SlipChip. *Anal Chem* **83**, 3533-3540 (2011).

64. B. Sun, F. Shen, S. E. McCalla, J. E. Kreutz, M. A. Karymov, R. F. Ismagilov. Mechanistic evaluation of the pros and cons of digital RT-LAMP for HIV-1 viral load quantification on a microfluidic device and improved efficiency via a two-step digital protocol. *Anal Chem* **85**, 1540-1546 (2013).

65. T. Notomi, Y. Mori, N. Tomita, H. Kanda. Loop-mediated isothermal amplification (LAMP): principle, features, and future prospects. *J Microbiol* **53**, 1-5 (2015).

66. N. A. Tanner, T. C. Evans, "Compositions and Methods for Reducing Background DNA Amplification," US20130323793, filing date 3/13/2013.

67. A. Martin, K. B. Grant, F. Stressmann, J.-M. Ghigo, D. Marchal, B. Limoges. Ultimate Single-Copy DNA Detection Using Real-Time Electrochemical LAMP. *ACS Sensors* **1**, 904-912 (2016).

68. N. A. Tanner, Y. Zhang, T. C. Evans, Jr. Simultaneous multiple target detection in real-time loop-mediated isothermal amplification. *Biotechniques* **53**, 81-89 (2012).

69. N. A. Tanner, Y. Zhang, T. C. Evans, Jr. Visual detection of isothermal nucleic acid amplification using pH-sensitive dyes. *Biotechniques* **58**, 59-68 (2015).

70. J. Rodriguez-Manzano, M. A. Karymov, S. Begolo, D. A. Selck, D. V. Zhukov, E. Jue, R. F. Ismagilov. Reading Out Single-Molecule Digital RNA and DNA Isothermal Amplification in Nanoliter Volumes with Unmodified Camera Phones. *ACS Nano* **10**, 3102-3113 (2016).

71. A. Courbet, D. Endy, E. Renard, F. Molina, J. Bonnet. Detection of pathological biomarkers in human clinical samples via amplifying genetic switches and logic gates. *Sci Transl Med* **7**, 289ra283 (2015).

72. T. Laksanasopin, T. W. Guo, S. Nayak, A. A. Sridhara, S. Xie, O. O. Olowookere, P. Cadinu, F. Meng, N. H. Chee, J. Kim, C. D. Chin, E. Munyazesa, P. Mugwaneza, A. J. Rai, V. Mugisha, A. R. Castro, D. Steinmiller, V. Linder, J.

E. Justman, S. Nsanzimana, S. K. Sia. A smartphone dongle for diagnosis of infectious diseases at the point of care. *Sci Transl Med* **7**, 273re271 (2015).

73. N. N. Watkins, U. Hassan, G. Damhorst, H. Ni, A. Vaid, W. Rodriguez, R. Bashir. Microfluidic CD4+ and CD8+ T lymphocyte counters for point-of-care HIV diagnostics using whole blood. *Sci Transl Med* **5**, 214ra170 (2013).

74. A. J. Kallen, H. G. Welch, B. E. Sirovich. Current antibiotic therapy for isolated urinary tract infections in women. *Arch Intern Med* **166**, 635-639 (2006).

75. F. Shen, B. Sun, J. E. Kreutz, E. K. Davydova, W. Du, P. L. Reddy, L. J. Joseph, R. F. Ismagilov. Multiplexed quantification of nucleic acids with large dynamic range using multivolume digital RT-PCR on a rotational SlipChip tested with HIV and hepatitis C viral load. *J Am Chem Soc* **133**, 17705-17712 (2011).

76. A. L. Walsh, M. D. Smith, V. Wuthiekanun, Y. Suputtamongkol, W. Chaowagul, D. A. B. Dance, B. Angus, N. J. White. Prognostic significance of quantitative bacteremia in septicemic melioidosis. *Clinical infectious diseases : an official publication of the Infectious Diseases Society of America* **21**, 1498-1500 (1995).

77. A. C. Musta, K. Riederer, S. Shemes, P. Chase, J. Jose, L. B. Johnson, R. Khatib. Vancomycin MIC plus heteroresistance and outcome of methicillin-resistant Staphylococcus aureus bacteremia: trends over 11 years. *J Clin Microbiol* **47**, 1640-1644 (2009).

78. F. Schuler, F. Schwemmer, M. Trotter, S. Wadle, R. Zengerle, F. von Stetten, N. Paust. Centrifugal step emulsification applied for absolute quantification of nucleic acids by digital droplet RPA. *Lab Chip* **15**, 2759-2766 (2015).

79. D. Witters, B. Sun, S. Begolo, J. Rodriguez-Manzano, W. Robles, R. F. Ismagilov. Digital biology and chemistry. *Lab Chip* **14**, 3225-3232 (2014).

80. K. Hayashida, K. Kajino, L. Hachaambwa, B. Namangala, C. Sugimoto. Direct blood dry LAMP: a rapid, stable, and easy diagnostic tool for Human African Trypanosomiasis. *PLoS Negl Trop Dis* **9**, e0003578 (2015).

81. J. Jevtusevskaja, K. Krolov, I. Tulp, U. Langel. The effect of main urine inhibitors on the activity of different DNA polymerases in loop-mediated isothermal amplification. *Expert Rev Mol Diagn*, 1-8 (2017).

82.     T. C. Dingle, R. H. Sedlak, L. Cook, K. R. Jerome. Tolerance of droplet-digital PCR vs real-time quantitative PCR to inhibitory substances. *Clin Chem* **59**, 1670-1672 (2013).

83.     R. H. Sedlak, J. Kuypers, K. R. Jerome. A multiplexed droplet digital PCR assay performs better than qPCR on inhibition prone samples. *Diagnostic microbiology and infectious disease* **80**, 285-286 (2014).

84.     A. S. Whale, A. S. Devonshire, G. Karlin-Neumann, J. Regan, L. Javier, S. Cowen, A. Fernandez-Gonzalez, G. M. Jones, N. Redshaw, J. Beck, A. W. Berger, V. Combaret, N. Dahl Kjersgaard, L. Davis, F. Fina, T. Forshew, R. Fredslund Andersen, S. Galbiati, A. Gonzalez Hernandez, C. A. Haynes, F. Janku, R. Lacave, J. Lee, V. Mistry, A. Pender, A. Pradines, C. Proudhon, L. H. Saal, E. Stieglitz, B. Ulrich, C. A. Foy, H. Parkes, S. Tzonev, J. F. Huggett. International Interlaboratory Digital PCR Study Demonstrating High Reproducibility for the Measurement of a Rare Sequence Variant. *Anal Chem* **89**, 1724-1733 (2017).

85.     H. H. Ku. Notes on the use of propagation of error formulas. *Journal of Research of the National Bureau of Standards, Section C: Engineering and Instrumentation* **70C**, 263-263 (1966).

**Supplementary Materials**

**Table 3-S1. Clinical samples used in this study.** Clinical urinary tract infection (UTI) urine samples tested for ciprofloxacin (cip) or nitrofurantoin (nit) susceptibility testing by gold-standard broth microdilution and by digital AST (dAST). Nucleic acids were quantified with both digital PCR (dPCR) and digital LAMP (dLAMP). Sample reruns (indicated by a "(2)") were performed several hours later on the same day when the control-treated ratio was discordant with the gold-standard AST call (CT ratio > 1.10 for a resistant sample or < 1.10 for a susceptible sample). S = antibiotic-susceptible; R = antibiotic-resistant; *major error; **very major error.

| Caltech Sample # | UCLA ID # | Description (Color, Turbidity) | ABX | MIC (μg/mL) | Gold-standard AST call | CT Ratio (dPCR) | dAST call (dPCR) | CT Ratio (dLAMP, 6.7 min) | dAST call (dLAMP) |
|---|---|---|---|---|---|---|---|---|---|

| | | | | | | | | | |
|---|---|---|---|---|---|---|---|---|---|
| 1 | 15-31A-020 | red, clear | nit | <16 | S | 1.48 | S | 1.64 | S |
| 2 | 15-31A-022 | light yellow, clear | cip | <=0.25 | S | 1.44 | S | 1.34 | S |
| 3 | 15-31A-025 | light yellow, clear | nit | <16 | S | 1.33 | S | 1.33 | S |
| 4 | 15-31A-026 | light yellow, clear | nit | <16 | S | 1.36 | S | 1.35 | S |
| 5 | 15-31A-027 | light yellow, clear | nit | <16 | S | 1.25 | S | 1.24 | S |
| 6 | 15-31A-031 | colorless, clear | cip | >=4 | R | 1.09 | R | 0.95 | R |
| 6 | 15-31A-031 | colorless, clear | nit | 256 | R | 0.95 | R | 0.77 | R |
| 7 | 15-31A-039 | light yellow, clear | cip | >=4 | R | 0.99 | R | 0.84 | R |
| 8 | 15-31A-040 | light yellow, clear | nit | 128 | R | 1.06 | R | 1.09 | R |
| 9 | 15-31A-042 | dark yellow, clear | cip | <=0.25 | S | 1.92 | S | 1.83 | S |
| 10 | 15-31A-043 | light yellow, clear | cip | <=0.25 | S | 1.66 | S | 1.85 | S |
| 10 | 15-31A-043 | light yellow, clear | nit | 128 | R | 0.91 | R | 0.92 | R |
| 11 | 15-31A-049 | light yellow, clear | cip | >=4 | R | 0.96 | R | 1.04 | R |
| 12 | 15-31A-050 | dark yellow, cloudy | cip | >=4 | R | 0.88 | R | 0.96 | R |
| 13 | 15-31A-051 | light yellow, cloudy | cip | >=4 | R | 0.98 | R | 0.97 | R |
| 14 | 15-31A-054 | light yellow, cloudy | cip | <=0.25 | S | 1.42 | S | 1.48 | S |
| 15 | 15-31A-056 | light yellow, cloudy | nit | 256 | R | 1.09 | R | 1.106 | S** |
| 16 | 15-31A-060 | light yellow, cloudy | cip | <=0.25 | S | 1.83 | S | 1.31 | S |
| 17 | 15-31A-063 | yellow, cloudy | cip | <=0.25 | S | 1.28 | S | 1.111 | S |
| 18 | 15-31A-066 | yellow, cloudy | cip | >=4 | R | 0.85 | R | 0.80 | R |
| 19 | 15-31A-067 | light yellow, cloudy | cip | >=4 | R | 0.82 | R | 0.59 | R |
| 20 | 15-31A-068 | light yellow, cloudy | cip | >=4 | R | 0.84 | R | 0.57 | R |
| 21 | 15-31A-071 | light yellow, cloudy | cip | >=4 | R | 1.04 | R | 0.92 | R |
| 22 | 15-31A-079 | light yellow, cloudy | nit | 128 | R | 1.25 | S** | 1.43 | S** |
| 23 | 15-31A-084 | yellow, clear | cip | >=4 | R | 1.01 | R | 0.96 | R |
| 24 | 15-31A-086 | yellow, cloudy | cip | <=0.25 | S | 2.01 | S | 2.21 | S |
| 25 | 15-31A-088 | yellow, cloudy | cip | <=0.25 | S | 1.25 | S | 1.22 | S |
| 26 | 15-31A-089 | light yellow, clear | cip | >=4 | R | 0.94 | R | 0.91 | R |
| 27 | 15-31A-091 | yellow, cloudy | cip | <=0.25 | S | 1.18 | S | 1.19 | S |
| 28 | 15-31A-093 | orange/red, clear | cip | <=0.25 | S | 1.08 | R | - | - |
| 28(2)† | 15-31A-093 | orange/red, clear | cip | <=0.25 | S | 1.88 | S | 1.59 | S |
| 28_avg | 15-31A-093 | orange/red, clear | cip | <=0.25 | S | 1.48 | S | - | - |
| 29 | 15-31A-096 | light yellow, cloudy | cip | >=4 | R | 1.20 | S | - | - |
| 29(2)† | 15-31A-096 | light yellow, cloudy | cip | >=4 | R | 0.93 | R | 0.98 | R |
| 29_avg | 15-31A-096 | light yellow, cloudy | cip | >=4 | R | 1.07 | R | - | - |
| 30 | 15-31A-097 | light yellow, cloudy | cip | >=4 | R | 1.13 | S** | 0.98 | R |
| 31 | 15-31A-101 | light yellow, clear | nit | <16 | S | 1.39 | S | 1.19 | S |
| 32 | 15-31A-102 | dark yellow, clear | nit | <16 | S | 1.63 | S | 1.68 | S |
| 33 | 15-31A-103 | light yellow, clear | nit | <16 | S | 1.38 | S | 1.28 | S |
| 34 | 15-31A-105 | light pink, cloudy | nit | <16 | S | 1.47 | S | 1.44 | S |
| 35 | 15-31A-108 | yellow, cloudy | nit | <16 | S | 1.29 | S | 1.37 | S |
| 36 | 15-31A-111 | yellow, clear | nit | <16 | S | 1.02 | R* | - | - |
| 36(2) | 15-31A-111 | yellow, clear | nit | <16 | S | 1.16 | S | 0.95 | R* |
| 36_avg | 15-31A-111 | yellow, clear | nit | <16 | S | 1.09 | R | - | - |
| 37 | 15-31A-112 | yellow, clear | nit | <16 | S | 1.49 | S | 1.12 | S |
| 38 | 15-31A-114 | light yellow, clear | nit | <16 | S | 1.34 | S | 1.36 | S |
| 39 | 15-31A-115 | yellow, clear | nit | <16 | S | 1.44 | S | 1.48 | S |
| 40 | 15-31A-116 | dark yellow, cloudy | cip | >=4 | R | 1.05 | R | 0.75 | R |
| 40 | 15-31A-116 | dark yellow, cloudy | nit | <16 | S | 1.96 | S | 2.33 | S |

| 41 | 15-31A-118 | yellow, clear | nit | <16 | S | 1.25 | S | 1.15 | S |
|---|---|---|---|---|---|---|---|---|---|
| 42 | 15-31A-119 | light yellow, clear | cip | <=0.25 | S | 2.21 | S | 1.95 | S |
| 43 | 15-31A-122 | light yellow, clear | nit | <16 | S | 1.17 | S | - | - |
| 43(2) | 15-31A-122 | light yellow, clear | nit | <16 | S | 1.79 | S | 1.45 | S |
| 43_avg | 15-31A-122 | light yellow, clear | nit | <16 | S | 1.48 | S | - | - |
| 44 | 15-31A-123 | yellow, cloudy | nit | <16 | S | 1.18 | S | 1.15 | S |
| 45 | 15-31A-126 | light yellow, clear | nit | <16 | S | 1.24 | S | 1.19 | S |
| 46 | 15-31A-131 | light yellow, clear | cip | <=0.25 | S | 1.61 | S | 1.28 | S |
| 47 | 15-31A-132 | dark yellow, clear | cip | <=0.25 | S | 1.27 | S | 1.14 | S |
| 48 | 15-31A-133 | dark yellow, cloudy | cip | <=0.25 | S | 1.30 | S | 1.29 | S |
| 49 | 15-31A-134 | dark yellow, clear | cip | <=0.25 | S | 2.36 | S | 1.85 | S |
| 50 | 15-31A-136 | light yellow, clear | cip | <=0.25 | S | 2.04 | S | 1.89 | S |
| 51 | 15-31A-137 | dark yellow, clear | cip | <=0.25 | S | 1.43 | S | 1.28 | S |

**Table 3-S2. Rapid phenotypic AST literature summary showing the state of the art.** Phenotypic antibiotic susceptibility tests using clinical samples, blood culture, contrived samples, clinical isolates, or reference strains with reported total assay time less than 3.5 hrs (210 min). References are sorted by sample type then by combined time of all steps. NR = not reported. Literature from 1997–present.

| Sample Type | Method | Pre-assay Enrichment Time (min) | Minimum ABX Exposure Time (min) | Combined Time of All Steps (min) | Fastest Reported Sample-to-Answer Time (min) | Reference |
|---|---|---|---|---|---|---|
| Clinical Samples | dAST (using dLAMP) | 0 | 15 | 24 | 29 | This work |
| Clinical Samples | ATP Bioluminescence | 0 | 90 | 105 | NR | (1) |
| Clinical Samples | Microscopy | 120 | 30 | 155 | NR | (2) |
| Clinical Samples | NA Quantification | 0 | 120 | 204[a] | NR | (3) |
| Clinical Samples | Microscopy | 0 | 206 | 206[b] | NR | (4) |
| Clinical Samples | Electrochemical | 0 | 150 | NR | 210 | (5) |
|  |  |  |  |  |  |  |
| Contrived Samples | Microfluidics | 0 | 60 | 60 | NR | (6) |
| Contrived Samples | Electrochemical | 0 | 60 | 100 | NR | (7) |
| Contrived Samples | Microfluidics | 0 | 120 | 120 | NR | (8) |
|  |  |  |  |  |  |  |
| Blood Culture | Microscopy | 0 | 40 | 45[c] | NR | (9) |
|  |  |  |  |  |  |  |
| Clinical Isolates | Microscopy | 0 | 40 | 40 | NR | (9) |
| Clinical Isolates | Electrochemical | 0 | 15 | 45 | NR | (10) |

| Clinical Isolates | FACS | 0 | 90 | 95 | NR | (11) |
|---|---|---|---|---|---|---|
| Clinical Isolates | Magnetic Bead Rotation | 90 | 15 | 120[d] | NR | (12) |
| Clinical Isolates | Microscopy | 120 | 6 | 126 | NR | (2) |
| Clinical Isolates | Raman Spectroscopy | 0 | 120 | 130[e] | NR | (13) |
| Clinical Isolates | Raman Spectroscopy | 0 | 120 | 130[e] | NR | (14) |
| Clinical Isolates | dAST (using dPCR) | 0 | 15 | 140 | NR | (15) |
| Clinical Isolates | FACS | 0 | 120 | 150 | NR | (16) |
| Clinical Isolates | FACS | 0 | 60 | 180 | NR | (17) |
| Clinical Isolates | Mass Spectrometry | 0 | 60 | 180 | NR | (18) |
| Clinical Isolates | Microscopy | 0 | 180 | 200[f] | NR | (19) |
| Clinical Isolates | Electrochemical | 0 | 90 | NR | NR | (5) |
|  |  |  |  |  |  |  |
| Reference Strains | Electrochemical | 0 | 10 | 25 | NR | (20) |
| Reference Strains | Raman Spectroscopy | 0 | 20 | 25[e] | NR | (14) |
| Reference Strains | Electrochemical | 0 | 20 | 42 | NR | (21) |
| Reference Strains | Microfluidics | 0 | 60 | 60 | NR | (22) |
| Reference Strains | FACS | 0 | 120 | 120[g] | NR | (23) |
| Reference Strains | Raman Spectroscopy | 0 | 120 | 130[e] | NR | (13) |

[a]time does not include washing and centrifugation steps

[b]detailed times of each step not reported, listed time is median time reported for all samples

[c]does not include time of overnight blood culture growth

[d]time does not include washing steps

[e]washing, imaging, and agarose embedding time not included

[f]reported as "clinical samples" in the abstract, but methods clearly state that all work was performed with clinical isolates: "We tested 189 clinical isolates…Before testing, each isolate was subcultured on cation-adjusted MHA for 20-24 hours"

[g]does not include time of FACS measurement

**Table 3-S3. Concentration of clinical urine samples.** Pathogen-specific 23S DNA concentration as determined by digital LAMP after 6.7 min of amplification time (Fig. 3-4C/H). Taking into account the number of rDNA copies per *E. coli* chromosome, and the efficiency of dLAMP in counting DNA in 6.7 min, the concentration of full genomes is ~6 times lower than the number reported in this table. CFU/mL was determined by plate counting at the UCLA Clinical Microbiology Laboratory.

| Caltech Sample # | 23S Conc. (cop/mL) | CFU/mL | Caltech Sample # | 23S Conc. (cop/mL) | CFU/mL |
|---|---|---|---|---|---|
| 1 | 1.59E+07 | >100,000 | 27 | 4.63E+07 | >100,000 |
| 2 | 2.52E+07 | >100,000 | 28 | 3.62E+07 | >100,000 |
| 3 | 3.94E+07 | >100,000 | 29 | 6.21E+06 | >100,000 |
| 4 | 5.63E+07 | >100,000 | 30 | 2.38E+07 | >100,000 |
| 5 | 3.14E+07 | >100,000 | 31 | 2.98E+07 | >100,000 |
| 6 | 7.86E+06 | >100,000 | 32 | 9.57E+07 | >100,000 |
| 7 | 7.07E+06 | >100,000 | 33 | 1.08E+08 | >100,000 |
| 8 | 5.08E+07 | >100,000 | 34 | 1.13E+08 | >100,000 |
| 9 | 1.72E+07 | >100,000 | 35 | 4.84E+07 | >100,000 |
| 10 | 2.64E+07 | >100,000 | 36 | 5.73E+07 | >100,000 |
| 11 | 7.44E+06 | >100,000 | 37 | 1.59E+07 | >100,000 |
| 12 | 2.75E+07 | >100,000 | 38 | 8.49E+07 | >100,000 |
| 13 | 2.07E+07 | >100,000 | 39 | 3.18E+06 | 50,000 |
| 14 | 1.55E+07 | >100,000 | 40 | 2.45E+07 | >100,000 |
| 15 | 2.12E+08 | >100,000 | 41 | 1.02E+08 | >100,000 |
| 16 | 1.59E+07 | >100,000 | 42 | 1.26E+07 | >100,000 |
| 17 | 5.12E+07 | >100,000 | 43 | 4.97E+06 | >100,000 |
| 18 | 1.44E+07 | >100,000 | 44 | 1.69E+08 | >100,000 |
| 19 | 2.62E+07 | >100,000 | 45 | 2.46E+08 | >100,000 |
| 20 | 4.52E+06 | >100,000 | 46 | 8.78E+06 | >100,000 |
| 21 | 4.25E+07 | >100,000 | 47 | 8.58E+06 | >100,000 |
| 22 | 1.30E+08 | >100,000 | 48 | 1.21E+07 | >100,000 |
| 23 | 3.04E+07 | >100,000 | 49 | 1.41E+07 | >100,000 |
| 24 | 2.38E+07 | >100,000 | 50 | 3.06E+06 | >100,000 |
| 25 | 4.19E+07 | >100,000 | 51 | 8.02E+06 | >100,000 |
| 26 | 1.92E+07 | >100,000 | | | |
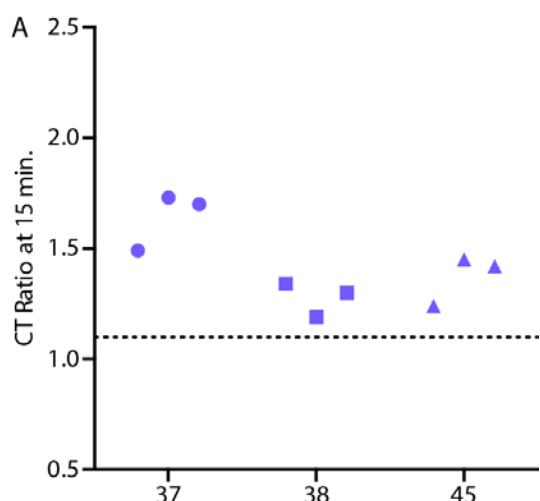
**Figure 3-S1**. **Reproducibility of dAST method with clinical urine samples.** Three ciprofloxacin-susceptible samples (#37, #38, #45) were analyzed with the dAST method in triplicate and control–treated (CT) ratios were calculated from DNA concentration measurements using digital droplet PCR.
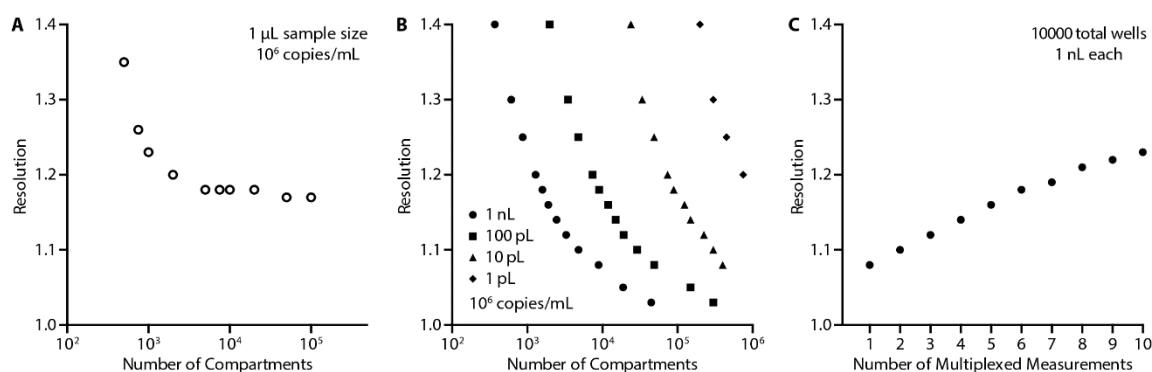


**Figure 3-S2**. **Resolution of digital devices.** The resolution of digital quantification depends on the number and volume of compartments. Simulations were performed with the methods described in (*24*). **A)** For a fixed sample size, and fixed input concentration of $10^6$ cop/mL relevant to UTIs, increasing the number of compartments (and reducing the volume of each compartment accordingly) beyond 1,000 does not improve resolution in a useful way. **B)** For fixed compartment volume, and fixed input concentration of $10^6$ copy/mL relevant to UTIs, the resolution improves with increasing number of compartments, although this increase requires a larger input of sample and amplification reagents. **C)** Dependence of resolution on

the number of multiplexed measurements made for a constant number of total wells. For example, while 10,000 of 1 nL compartments provide 1.08 resolution, 2,000 of 1 nL compartments provide 1.16 resolution each, enabling a 4-plex dAST (1 control and 4 ABX treated samples) to be performed.

## Figure 3-S3. Real-time digital LAMP DNA quantification of a UTI sample with nitrofurantoin treatment

A clinical UTI sample treated with and without 16 µg/mL nitrofurantoin. After 15 min, DNA was extracted and quantified with digital LAMP on SlipChips. The protocols followed and materials used are described in "Materials and Methods, Digital AST (dAST) using clinical UTI samples" and "Materials and Methods, Rapid digital LAMP (dLAMP)".
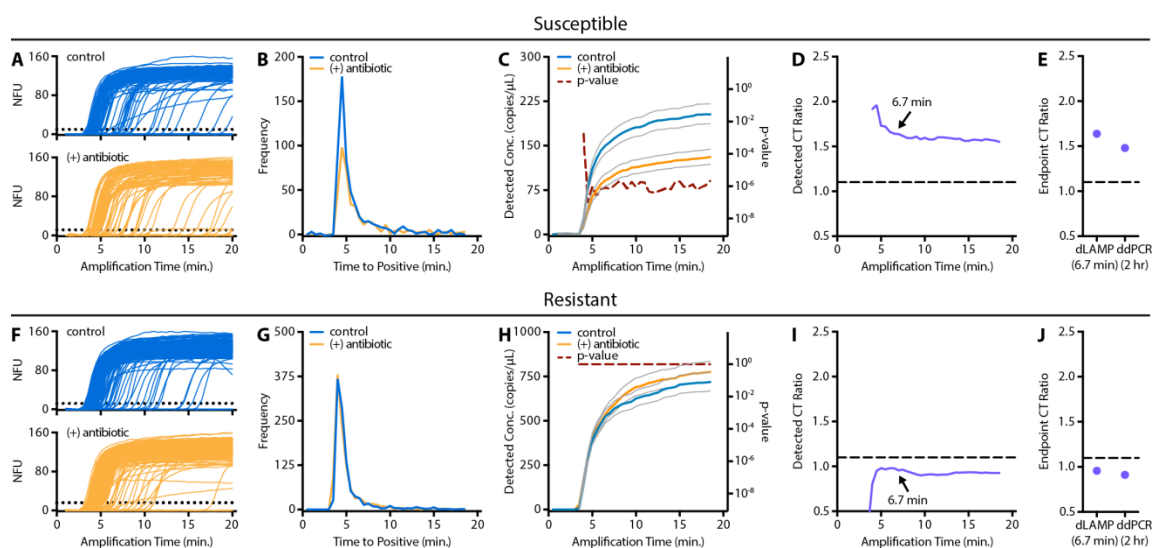


**Figure 3-S3. High-resolution single-molecule nucleic acid amplification using ultrafast digital LAMP (dLAMP) for digital antimicrobial susceptibility test (dAST) of clinical urinary tract infection (UTI) urine samples with antibiotic-susceptible (A–E) and antibiotic-resistant (F–J) *E. coli*.** (A,F) Real-time fluorescence amplification traces (only 200 of 1,280 traces shown for clarity). NFU = normalized fluorescence units; dotted line = positive threshold; when the normalized fluorescence intensity of a

compartment crosses the threshold, that compartment is counted as positive. (**B,G**) Time Time-to-positive (TTP) distribution was determined by counting the number of compartments that crossed the positive threshold at each time point. (**C,H**) Detected concentrations of the target dAST marker in control and antibiotic-treated samples for successive image cycles. Grey lines represent 95% confidence intervals. (**D,I**) Detected control–treated (CT) ratios over time. Dashed line indicates susceptibility threshold. (**E,J**) Comparison of CT ratios for droplet digital PCR (dPCR) after 2 h and dLAMP (after 6.7 min of amplification).

## Section 1. Intermediate samples

In this manuscript, we focus on categorical agreement of our binary susceptibility determination (susceptible or resistant). We chose to design our study this way and to exclude intermediate samples for the following reasons:

The current gold-standard antibiotic susceptibility testing method is broth dilution. This method, used every day in central clinical laboratories, is only accurate to +/- one dilution step. For example, *E. coli* with an initially determined ciprofloxacin MIC of 2.0 µg/mL might have an MIC of 1, 2, or 4 µg/mL if tested again using the same gold-standard method. According to the CLSI standards used in the US, 1.0 µg/mL is considered "susceptible", while 2 µg/mL is considered "intermediate" and 4.0 µg/mL is considered resistant. This is well-known in the clinical microbiology community. In fact, the CLSI manual (*25*) states that one of the roles of the intermediate category is to include a buffer zone which should prevent small, uncontrollable, technical factors from causing major discrepancies in interpretation. Furthermore, when gold standard broth dilution vs gold standard inhibition zone diameter is compared, intermediate samples do not show consistent results (see FIG. 4 of (*26*); of the five samples tested with intermediate MICs (as determined by the gold-standard), the inhibition zone method called one of them resistant, two intermediate, and two susceptible (*26*)).
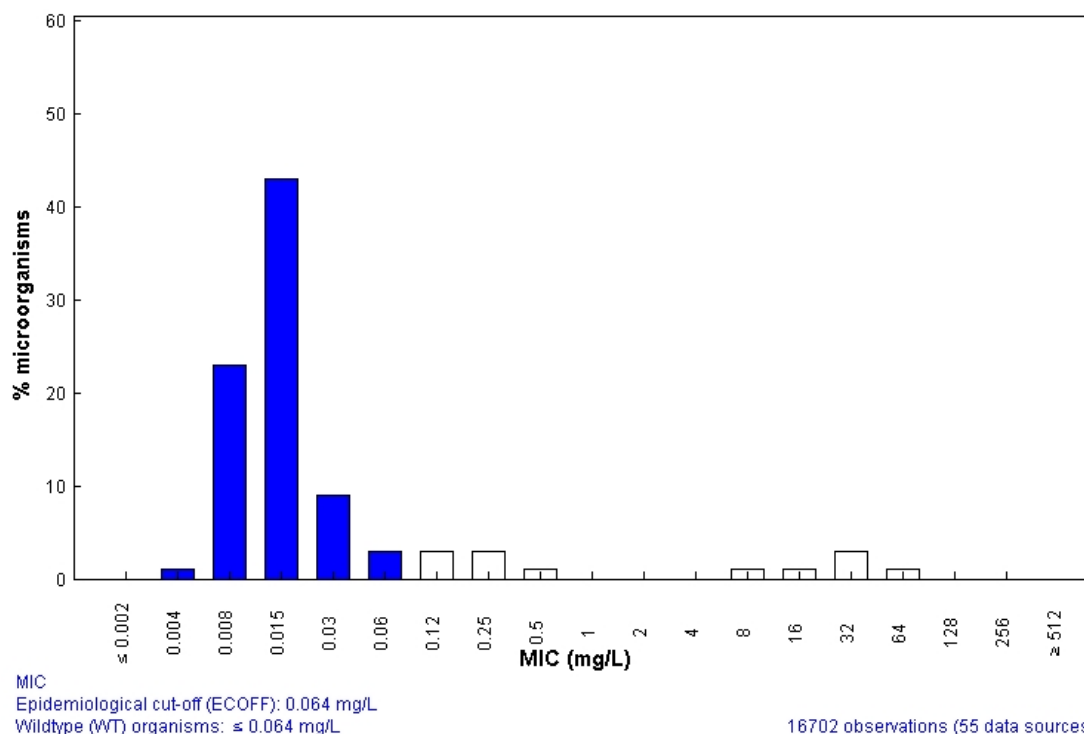
A further issue is the discrepancy of the meaning "resistant and susceptible" around these concentrations. For example, using The European Committee on Antimicrobial Susceptibility Testing – (EUCAST) standards, susceptible isolates are those with ciprofloxacin MIC of 0.25 µg/mL and below, while intermediate isolates have MIC of 0.5 µg/mL and resistant isolates are 1.0 µg/mL and above.

We chose to exclude samples with MICs of 0.5, 1.0, and 2.0 µg/mL to ensure that the gold standard method would not frequently switch between a susceptible and resistant call if repeated.

Importantly, this approach is still applicable to "real world" samples and does not correspond to only looking at extremes of MIC. Excluding these samples only eliminates a small percentage of *E. coli* samples based on epidemiological data (see Figure below), with the caveat that these distributions may change at different times in different locations.

**Ciprofloxacin / Escherichia coli**
**International MIC Distribution - Reference Database 2017-04-17**

MIC distributions include collated data from multiple sources, geographical areas and time periods and can never be used to infer rates of resistance

MIC
Epidemiological cut-off (ECOFF): 0.064 mg/L
Wildtype (WT) organisms: ≤ 0.064 mg/L

16702 observations (55 data sources)

*Ciprofloxacin MIC distribution for E. coli. Note that a broader range of antibiotic concentrations is tested when generating epidemiological data than is tested in clinical microbiology laboratories. Also note that the cut-off MIC for defining resistant and susceptible organisms is different between the epidemiological and clinical microbiological data. Epidemiological cut off is defined relative to the wild-type susceptibility while the clinical cut off is defined relative to clinically relevant susceptibility. Finally, note that these data should not be used to infer the rates of resistance in a particular geographical location at a particular time (27).*

For nitrofurantoin (nit), MIC of >=128 is considered resistant and MIC of <= 32 is considered susceptible. Similarly, we chose to exclude the minimal possible number of samples with MICs that might switch between a susceptible or resistant call when repeated. For this reason, we excluded samples with MICs of 32 and 64 µg/mL.

Therefore, it should not be surprising that when validating a new AST method with <u>clinical samples</u>, it is common to challenge the method only against susceptible and resistant samples that are above or below the MIC breakpoints, while avoiding intermediate samples (*1, 3, 5*).

To test whether intermediate or near-intermediate samples provide any unexpected results, we did run a small separate study of 8 clinical <u>isolates</u> (2 operators with 4 isolates each) with intermediate and near-intermediate MICs using dPCR readout. We exposed these isolates with (1.0 µg/mL ciprofloxacin) and without antibiotics for 15 min and measured the nucleic acid concentrations with dPCR. Isolates with MIC of 1.0 µg/mL are clustering very close to the threshold and slightly below, while isolates with MIC of 0.5 µg/mL are comfortably above the threshold and would be read as susceptible (Figure 3-S4).
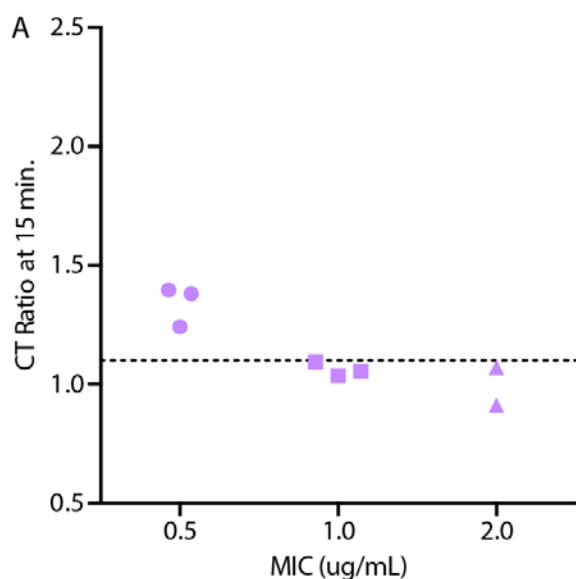


**Figure 3-S4**. The digital AST (dAST) method with clinical isolates from urinary tract infections using a 15 min treatment of 1 µg/mL ciprofloxacin. Three isolates with different MICs were analyzed with the dAST method in triplicate or duplicate (two operators with four samples each). Control–treated (CT) ratios were calculated from dPCR DNA concentration measurements.

**Section 2. Supplementary Materials and Methods**

*Materials and reagents*

All reagents purchased from commercial sources were used as received unless otherwise stated. BBL trypticase soy agar (TSA) plates with 5% sheep blood and Bacto brain heart infusion (BHI) media were purchased from BD Biosciences (Franklin Lakes, NJ, USA). All antibiotic stock solutions and nucleic acid amplification reactions were prepared using sterile, nuclease-free water (NF-H$_2$O) purchased from Thermo Fisher (Waltham, MA, USA). Ciprofloxacin was purchased from Sigma-Aldrich (St. Louis, MO, USA) and prepared as a 1 mg/mL stock solution in NF-H$_2$O. Nitrofurantoin was purchased from Sigma-Aldrich (St. Louis, MO, USA) and prepared as a 10 mg/mL stock solution in NF-H$_2$O. QuickExtract DNA Extraction was purchased from Epicentre (Madison, WI, USA). QX200 ddPCR EvaGreen Supermix was purchased from Bio-Rad Laboratories (Hercules, CA, USA). Bst 3.0 and 10 mM dNTPs were purchased from NEB (Ipswich, MA, USA). Pooled healthy human urine was obtained from Lee Biosolutions (Maryland Heights, MO, USA). Primer sequences were ordered as dried stocks from IDT (Coralville, IA, USA).

*Digital quantification with dPCR*

Droplet digital PCR reactions were carried out as described previously (*15*).

*Design, fabrication and preparation of SlipChips*

Details of the design, fabrication, preparation, and assembling of the single-volume 1,280-well SlipChip glass devices are described in previous work (*28*). For this manuscript, the workflow in Figure 3-5 was performed with lab-made reusable glass microfluidic chips (Samples 28-29,48-51). To run the rest of the 54 samples with the rapid dLAMP assay, we obtained a set of disposable injection molded chips (5,376 2.4-nL compartments) from

SlipChip Corp, which enabled shorter turnaround times between experiments (Samples 1-27,30-47).

*Clinical sample handling and gold-standard broth microdilution AST*

Urine from patients suspected of having urinary tract infections (UTIs) was collected and transported in a BD Vacutainer Urine Collection Tube containing formate and borate as preservatives. Next, pathogens from the urine samples were isolated and identified using mass spectrometry. Broth microdilution AST was performed on samples positive for *E. coli*.

*dAST with clinical samples*

One modification to our original dAST protocol (*15*) is the addition of DNase to digest extracellular DNA. We did this to eliminate the confounding effect that extracellular DNA could have on the CT ratio. Consider an antibiotic-susceptible sample with 500 cop/μL of cell-free DNA and 300 cop/μL DNA inside cells. If the genomes replicate 1.5X over a 15 min exposure time, then the CT ratio in the case where cell-free DNA is also detected would be 950 cop/uL ÷ 800 cop/uL = 1.19; in the case where cell-free DNA is digested by DNase and not detected, the CT ratio would be 450 cop/uL ÷ 300 cop/uL = 1.50.

If discordant AST calls (compared to the gold-standard) were noticed on the same day, we re-ran that sample to resolve the discordancy. Some reruns are accepted even in the FDA submissions of diagnostic AST devices, so rerunning samples in itself is not a problem.  It would have been better to rerun the samples twice, to get a third measurement as a tie-breaker.  Unfortunately, we could not do so due to the limitations of our protocols and the concern for aging of clinical samples over time (and we were not able to rerun all of the samples).

Because our data provide a quantitative measurement (CT ratio), we averaged the two runs to obtain a consensus value of the CT ratio. When we do this (using dPCR values as an

example), we find that three samples (#28, #29, #43) returned average CT ratios (1.48, 1.07, 1.48) that were in agreement with the gold standard (S, R, S). For a fourth sample (#36), the average CT ratio (1.09) was also discordant with the gold standard (S) and we recorded it as an error in our analysis for both dPCR and dLAMP (see Table 3-S1).

*Isolate maintenance and exposure experiments.*

For all experiments involving isolates (Fig. 3-2), isolates were maintained and antibiotic exposure carried out as described in previous work (*15*). All *E. coli* isolates were maintained on solid or liquid BHI media (BD, Franklin Lakes, NJ, USA), all *Lactobacillus jensenii* isolates were maintained on solid or liquid MRS media (BD, Franklin Lakes, NJ, USA).

**Contributions of non-corresponding authors**

Co-first authorship order was determined by a coin flip.

Nathan G. Schoepp:

Major contributor to Figures 1A, 4, 5, 6

Sole contributor to Figure 2, Figure 3 A/B

Contributor to Figure 3C

Major contributor to Figure S1, Figure S3, Figure S4

Major contributor to Table S1, Table S2, Table S3

Major contributor to writing manuscript and supplementary materials

Travis S. Schlappi:

Major contributor to Figures 1A, 4, 5, 6

Sole contributor to Figure 1B

Contributor to Figure 3C

Major contributor to Figure S1, Figure S3, Figure S4; sole contributor to Figure S2

Major contributor to Table S1, Table S3; minor contributor to Table S2

Major contributor to writing manuscript and supplementary materials

Matthew S. Curtis:

Sole contributor to the adaptation of custom imaging systems for real-time analysis described in Figure 5.

Contributor to Figure 4, Figure 5, Figure 6, Figure S3

Slava S. Butkovich:

Major contributor to Figure 3C.

Contributor to Figure 6

Romney M. Humphries and Shelley Miller contributed microbiological and AST expertise, as well as providing de-identified clinical UTI samples and testing those samples with gold-standard broth microdilution.

**References**

1.  V. Ivancic, M. Mastali, N. Percy, J. Gornbein, J. T. Babbitt, Y. Li, E. M. Landaw, D. A. Bruckner, B. M. Churchill, D. A. Haake. Rapid antimicrobial susceptibility determination of uropathogens in clinical urine specimens by use of ATP bioluminescence. *J Clin Microbiol* **46**, 1213-1219 (2008).

2.  M. Fredborg, K. R. Andersen, E. Jorgensen, A. Droce, T. Olesen, B. B. Jensen, F. S. Rosenvinge, T. E. Sondergaard. Real-time optical antimicrobial susceptibility testing. *J Clin Microbiol* **51**, 2047-2053 (2013).

3.  A. Mezger, E. Gullberg, J. Goransson, A. Zorzet, D. Herthnek, E. Tano, M. Nilsson, D. I. Andersson. A general method for rapid determination of antibiotic susceptibility and species in bacterial infections. *J Clin Microbiol* **53**, 425-432 (2015).

4.  T. Stenholm, A. J. Hakanen, E. Hakanen, H. Harma, M. Osterblad, J. Vuopio, P. E. Hanninen, P. Huovinen, K. Rankakokko-Jalava, P. Kotilainen. High-

throughput screening of colonization samples for methicillin-resistant Staphylococcus aureus. *Scand J Infect Dis* **45**, 922-929 (2013).

5.  K. E. Mach, R. Mohan, E. J. Baron, M. C. Shih, V. Gau, P. K. Wong, J. C. Liao. A biosensor platform for rapid antimicrobial susceptibility testing directly from clinical samples. *J Urol* **185**, 148-153 (2011).

6.  Y. Lu, J. Gao, D. D. Zhang, V. Gau, J. C. Liao, P. K. Wong. Single cell antimicrobial susceptibility testing by confined microchannels and electrokinetic loading. *Anal Chem* **85**, 3971-3976 (2013).

7.  J. D. Besant, E. H. Sargent, S. O. Kelley. Rapid electrochemical phenotypic profiling of antibiotic-resistant bacteria. *Lab Chip* **15**, 2799-2807 (2015).

8.  C. H. Chen, Y. Lu, M. L. Sin, K. E. Mach, D. D. Zhang, V. Gau, J. C. Liao, P. K. Wong. Antimicrobial susceptibility testing using high surface-to-volume ratio microchannels. *Anal Chem* **82**, 1012-1019 (2010).

9.  M. Fredborg, F. S. Rosenvinge, E. Spillum, S. Kroghsbo, M. Wang, T. E. Sondergaard. Rapid antimicrobial susceptibility testing of clinical isolates by digital time-lapse microscopy. *Eur J Clin Microbiol Infect Dis* **34**, 2385-2394 (2015).

10. C. Halford, R. Gonzalez, S. Campuzano, B. Hu, J. T. Babbitt, J. Liu, J. Wang, B. M. Churchill, D. A. Haake. Rapid antimicrobial susceptibility testing by sensitive detection of precursor rRNA using a novel electrochemical biosensing platform. *Antimicrob Agents Chemother* **57**, 936-943 (2013).

11. M. A. Broeren, Y. Maas, E. Retera, N. L. Arents. Antimicrobial susceptibility testing in 90 min by bacterial cell count monitoring. *Clin Microbiol Infect* **19**, 286-291 (2013).

12. I. Sinn, P. Kinnunen, T. Albertson, B. H. McNaughton, D. W. Newton, M. A. Burns, R. Kopelman. Asynchronous magnetic bead rotation (AMBR) biosensor in microfluidic droplets for rapid bacterial growth and susceptibility measurements. *Lab Chip* **11**, 2604-2611 (2011).

13. C. Y. Liu, Y. Y. Han, P. H. Shih, W. N. Lian, H. H. Wang, C. H. Lin, P. R. Hsueh, J. K. Wang, Y. L. Wang. Rapid bacterial antibiotic susceptibility test

based on simple surface-enhanced Raman spectroscopic biomarkers. *Sci Rep* **6**, 23375 (2016).

14.     T. T. Liu, Y. H. Lin, C. S. Hung, T. J. Liu, Y. Chen, Y. C. Huang, T. H. Tsai, H. H. Wang, D. W. Wang, J. K. Wang, Y. L. Wang, C. H. Lin. A high speed detection platform based on surface-enhanced Raman scattering for monitoring antibiotic-induced chemical changes in bacteria cell wall. *PLoS One* **4**, e5470 (2009).

15.     N. G. Schoepp, E. M. Khorosheva, T. S. Schlappi, M. S. Curtis, R. M. Humphries, J. A. Hindler, R. F. Ismagilov. Digital Quantification of DNA Replication and Chromosome Segregation Enables Determination of Antimicrobial Susceptibility after only 15 Minutes of Antibiotic Exposure. *Angew Chem Int Ed Engl* **55**, 9557-9561 (2016).

16.     N. K. Shrestha, N. M. Scalera, D. A. Wilson, G. W. Procop. Rapid differentiation of methicillin-resistant and methicillin-susceptible Staphylococcus aureus by flow cytometry after brief antibiotic exposure. *J Clin Microbiol* **49**, 2116-2120 (2011).

17.     I. Faria-Ramos, M. J. Espinar, R. Rocha, J. Santos-Antunes, A. G. Rodrigues, R. Canton, C. Pina-Vaz. A novel flow cytometric assay for rapid detection of extended-spectrum beta-lactamases. *Clin Microbiol Infect* **19**, E8-E15 (2013).

18.     C. Lange, S. Schubert, J. Jung, M. Kostrzewa, K. Sparbier. Quantitative matrix-assisted laser desorption ionization-time of flight mass spectrometry for rapid resistance detection. *J Clin Microbiol* **52**, 4155-4162 (2014).

19.     J. Choi, J. Yoo, M. Lee, E. G. Kim, J. S. Lee, S. Lee, S. Joo, S. H. Song, E. C. Kim, J. C. Lee, H. C. Kim, Y. G. Jung, S. Kwon. A rapid antimicrobial susceptibility test based on single-cell morphological analysis. *Sci Transl Med* **6**, 267ra174 (2014).

20.     P. Ertl, E. Robello, F. Battaglini, S. R. Mikkelsen. Rapid antibiotic susceptibility testing via electrochemical measurement of ferricyanide reduction by *Escherichia coli* and *Clostridium sporogenes*. *Anal Chem* **72**, 4957-4964 (2000).

21.     T. S. Mann, S. R. Mikkelsen. Antibiotic susceptibility testing at a screen-printed carbon electrode array. *Anal Chem* **80**, 843-848 (2008).

22. Y. Tang, L. Zhen, J. Liu, J. Wu. Rapid antibiotic susceptibility testing in a microfluidic pH sensor. *Anal Chem* **85**, 2787-2794 (2013).

23. B. L. Roth, M. Poot, S. T. Yue, P. J. Millard. Bacterial viability and antibiotic susceptibility testing with SYTOX green nucleic acid stain. *Appl Environ Microbiol* **63**, 2421-2431 (1997).

24. J. E. Kreutz, T. Munson, T. Huynh, F. Shen, W. Du, R. F. Ismagilov. Theoretical design and analysis of multivolume digital assays with wide dynamic range validated experimentally with microfluidic digital PCR. *Anal Chem* **83**, 8158-8168 (2011).

25. CLSI, "M100-S25 Performance Standards for Antimicrobial Susceptibility Testing," (Clinical Laboratory Standards Institute, 2015).

26. J. Turnidge, D. L. Paterson. Setting and revising antibacterial susceptibility breakpoints. *Clin Microbiol Rev* **20**, 391-408, table of contents (2007).

27. EUCAST, "Antimicrobial wild type distributions of microorganisms," (European Society of Clinical Microbiology and Infectious Disease, https://mic.eucast.org/Eucast2/ 2017).

28. B. Sun, J. Rodriguez-Manzano, D. A. Selck, E. Khorosheva, M. A. Karymov, R. F. Ismagilov. Measuring fate and rate of single-molecule competition of amplification and restriction digestion, and its use for rapid genotyping tested with hepatitis C viral RNA. *Angew Chem Int Ed Engl* **53**, 8088-8092 (2014).

*Chapter IV*

Flow-through capture and in situ amplification can enable rapid detection of a few single molecules of nucleic acids from several milliliters of solution[3]

**Abstract**

Detecting nucleic acids (NAs) at zeptomolar concentrations (few molecules per milliliter) currently requires expensive equipment and lengthy processing times to isolate and concentrate the NAs into a volume that is amenable to amplification processes, such as PCR or LAMP. Shortening the time required to concentrate NAs and integrating this procedure with amplification on-device would be invaluable to a number of analytical fields, including environmental monitoring and clinical diagnostics. Microfluidic point-of-care (POC) devices have been designed to address these needs, but they are not able to detect NAs present in zeptomolar concentrations in short time frames because they require slow flow rates and/or they are unable to handle milliliter-scale volumes. In this paper, we theoretically and experimentally investigate a flow-through capture membrane that solves this problem by capturing NAs with high sensitivity in a short time period, followed by direct detection by amplification. Theoretical predictions guided the choice of physical parameters for a chitosan-coated nylon membrane; these predictions can also be applied generally to other capture situations with different requirements. The membrane is also compatible with *in situ* amplification, which, by eliminating an elution step enables high sensitivity and will facilitate integration of this method into sample-to-answer detection devices. We tested a wide range of combinations of sample volumes and concentrations of DNA molecules using

a capture membrane with 2 mm radius. We show that for nucleic acid detection, this approach can concentrate and detect as few as ~10 molecules of DNA with flow rates as high as 1 mL/min, handling samples as large as 50 mL. In a specific example, this method reliably concentrated and detected ~25 molecules of DNA from 50 mL of sample.

**Introduction**

Detection of nucleic acids (NAs) at ultra-low concentrations (few molecules per milliliter of sample) in short time intervals is invaluable to a number of analytical fields, including environmental monitoring and clinical diagnostics[1-6]. Pathogens in aqueous environmental samples are frequently present at or below zeptomolar concentrations (~1000 microorganisms per liter), requiring laborious filtration and concentration procedures before detection is possible.[7,8] In many clinical applications, including minimal residual diseases[9] and latent Hepatitis C viral (HCV) or HIV infections, target NAs are also present at < 10 molecules/mL.[10,11] Blood bank donations are typically pooled before screening, so targets may be diluted by several orders of magnitude before being screened for pathogens, generating a sample where ultra-sensitive detection is critical.[12,13] Each of these examples requires the processing of large volumes (mLs) of extremely dilute samples, and therefore the ability to concentrate NAs on the order of 1000X to reach PCR-suitable volumes (μLs). Additionally, the entire concentration process must be done within minutes and not rely on expensive equipment to be directly applicable to limited-resource settings (LRS) and at the point-of-care (POC).[14,15]

Commercial systems for the purification and concentration of nucleic acids typically involve solid phase extraction (SPE), which uses chaotropic agents to control the absorption and release of NAs on silica.[16,17] While this method is widely used, most available protocols require centralized laboratories for centrifuging samples or manipulating beads.[18] NA precipitation[19] methods are also commonly used to extract and concentrate NAs from clinical and environmental samples; however these methods are laborious and involve the use of hazardous reagents.[20] These methods are challenging to deploy for LRS, where

instrumentation is limited, or for use at the POC, where diagnostics must be rapid and require minimal sample handling.[18] To address these needs, several charge-based methods have been developed, which typically include a charged polymer matrix including chitosan, poly-L-lysine, and so on for NA capture (we are building on that work in this paper).[21-25] To increase sensitivity, these and other systems concentrate NAs and then either elute before amplification[21,22,24,25] or perform amplification *in situ.*[23,26-29] Concentration factors up to $15X$[21,30] and limits-of-detection as sensitive as $10^4$ copies/mL[23] or 500 cells/mL[26] have been reported. While these methods have clear advantages over traditional solid-phase extraction methods, processing time and lowest detectable concentration are still limited by their inability to handle large sample volumes ($>1$ mL)[26-28,31] and/or their slow processing rates, which range from $\mu$L/min to $\mu$L/hr.[18,21,22,24,32,33] Thus, current methods—whether commercialized or from literature—lack the required combination of sensitivity, speed and ease of implementation, leaving a gap in the current NA detection workflow.

We hypothesized that pressure-driven flow and capture in a porous matrix could facilitate the handling of large samples, while retaining many of the characteristics needed for both LRS and POC. Here, we analyze this approach theoretically and experimentally to determine a regime in which rapid, convection-driven capture is possible. Using a theoretical framework to predict capture efficiency as a function of flow-through conditions, we determined the parameters necessary for a detection matrix to capture a few nucleic acid molecules ($<10$) from several mLs of volume in short times ($<10$ minutes). We tested our predictions experimentally with respect to capture efficiency, lowest detectable concentration, processing time, and total sample volume. Furthermore, we demonstrated that the capture matrix is compatible with direct amplification, eliminating the need for an elution step. The ability to amplify *in situ* makes this approach amenable to integration into sample-to-answer devices, and preserves the high concentration factors achieved during capture by preventing loss of target to the capture matrix during elution.

**Experimental Section**

**Capture Simulations**. The fraction of nucleic acid molecules captured in a membrane pore compared to the amount flowed through (capture efficiency) was simulated at steady-state using the *Transport of Diluted Species* module of *Comsol Multiphysics (version 4.4)*. A complete description of the model geometry, transport parameters, kinetics, boundary conditions, mesh, and calculations performed is included in Supporting Information.

**Chitosan Membrane Fabrication**. A nylon membrane (LoProdyne LPNNG810S, Pall Corp., New York City, NY) was used as a porous matrix support. Two methods were employed for chitosan functionalization of the membrane, summarized below as "Method A" and "Method B."

*Method A:* The LoProdyne membrane has hydroxyl surface chemistry and was functionalized with N,N carbonyldiimidazole (CDI) in methylene chloride according to the manufacturer's protocol (http://www.pall.com; Supporting Information S-VII).

Chitosan oligosaccharide lactate (No. 523682, Sigma-Aldrich, St. Louis, MO) was purified by dissolving 1.2 g chitosan in 40 mL nuclease-free (NF) water, then precipitated by adding 3 mL 1M NaOH. This solution was mixed and filtered through Whatman paper #8 (12 cm). It was then rinsed with MilliQ water until the eluant was neutral. Washed chitosan was dried for 2 h under vacuum, then a rotary evaporator was used to remove residual moisture.

The optimal pH at which to cross-link chitosan with CDI was determined to be pH 5.0. Based on the pKa of chitosan (pKa = 6.3), ~5% of the chitosan's amines will be deprotonated and able to react. At pH > 5, a larger percentage of the chitosan amines will be deprotonated, resulting in a higher degree of crosslinking to the support surface, and fewer available amines to interact with nucleic acids. At a pH of 5.0, the chitosan polymer should crosslink to the support at either one or two positions, leaving the bulk of the polymer free in solution.

To prepare chitosan-coated supports, a 6 mg/mL solution of purified chitosan was prepared in 34 mM HCl. This solution was vortexed for 10 min until the chitosan was fully dissolved,

then sonicated to remove bubbles. The pH was then raised to 5.0 by addition of NaOH while vortexing. A CDI-functionalized LoProdyne membrane was then saturated with this chitosan solution. The membrane and chitosan solution were sandwiched between two glass slides, and pressed to remove excess chitosan solution. The wet membrane was blot-dried and placed in a desiccator to dry under vacuum for 20–30 min. After drying, the membrane was placed in a 50 mL Falcon tube and rinsed with NF water. The water was poured out, 0.1 M HCl was added to quench any remaining CDI and remove non-crosslinked chitosan, and the membrane and HCl vortexed for 2 min. The HCl was poured out and the membrane was rinsed with NF water again. Next, the membrane was placed in a fresh Falcon tube, rinsed more with NF water, washed in NF water for 25 min while agitated, rinsed with NF water three more times, blot dried, then air dried in a desiccator.

*Method B:* To prepare hydrogel coated membranes, a 0.5% (w/v) solution of chitosan (TCI OBR6I) was prepared in 150 mM HCl. A 25% (v/v) solution of glutaraldehyde was added to this solution to a final concentration of 4 mM. The solution was rapidly mixed, and added to the LoProdyne membrane in excess. The saturated membranes were then spun on a Laurel WS-400-6NNP/Lite spin coater at 500 rpm for 5 s with an acceleration setting of 410, followed by 15 s at 2000 rpm with an acceleration setting of 820. Membranes were allowed to crosslink for 2 h in air, washed 3 times with NF water, and dried under vacuum.

**Binding Capacity Measurements**. 1000 ng of salmon sperm DNA (Invitrogen, Carlsbad CA) in 100 µL of 10 mM MES buffer (pH ~5) was sequentially flushed through a chitosan membrane (radius = 2 mm, fabricated with Method A) five times via a syringe/luer lock system (Figure 4-S4). The inlet and eluate DNA concentration of each flush was measured with PicoGreen dye (Invitrogen); subtracting the eluate from the inlet and converting to mass of DNA yielded the plot in Figure 4-3.

**Capture and *In Situ* Amplification**. λ-phage DNA stocks were quantified via digital PCR.[34] This DNA was spiked into varying volumes of 10 mM MES buffer (pH ~5) to create concentrations ranging from 0.2 to 20 copies/mL (Table 4-S4). The solutions were flowed

through chitosan-coated nylon membranes (radius = 2 mm) using syringes and luer locks (Figure 4-S4), followed twice by 100 μL MES buffer.  The membranes were then removed from the syringe/luer lock system, placed in an Ilumina Eco™ well plate, and 5–10 μL of PCR mix was added to each membrane. The well plate was inserted into an Ilumina Eco™ real time PCR system (EC-101-1001, Ilumina, San Diego, CA) and thermal cycled; correct λ-phage product was verified with a gel and melt curve analysis (Figure 4-S5).

The PCR mixture used for amplification of λ-phage DNA on the chitosan-coated nylon membranes contained the following: 5 μL 2X SsoFast Evagreen SuperMix (BioRad, Hercules, CA), 1 μL of BSA (20 mg/mL), 2 μL of 10 ng/uL salmon sperm DNA (Invitrogen), 1 μL of 5 μM primers (SI-VI), and 1 μL of NF water. The PCR amplification was performed with an initial 95 °C step for 3 min and then followed by 40 cycles of: (i) 20 s at 95 °C, (ii) 20 s at 62 °C, (iii) 15 s at 72 °C.

## Results and Discussion

**Theoretical Analysis.** To predict a regime that would enable rapid flow-through capture of nucleic acids present at low concentrations, we developed a theoretical model that takes into account the convection, diffusion, and adsorption of nucleic acid molecules onto a capture agent layered within a porous matrix (Figure 4-1a and S-I). Although the structure of the nylon membrane is spongy and non-uniform, approximating the pores as cylinders is an appropriate simplification to estimate the transport processes and has been done previously.[35,36] The parameters governing capture dynamics in a cylindrical pore are superficial velocity $U$ [m/s], pore radius $R_p$ [m], membrane radius $R_m$ [m], membrane thickness (or, equivalently, pore length) $\delta_m$ [m], diffusivity of nucleic acid molecules[37] $D$ [m$^2$/s], association rate constant[38] $k_{on}$ [m$^3$/(mol·s)], surface concentration of the capture agent $\gamma$ [mol/m$^2$], and mass transfer coefficient $k_c$ [m/s]. Instead of analyzing every relevant parameter individually, we condensed them into two dimensionless numbers:[39,40] Damköhler ($Da$) and Péclet ($Pe$). $Da$ characterizes the balance between adsorption rate and transport rate

(Eq. 1) while *Pe* characterizes the balance between convection rate and diffusion rate (Eq. 2).

$$Da = \frac{adsorption\ rate}{transport\ rate} = \frac{k_{on}\gamma}{k_c}, k_c = 1.62\left(\frac{UD^2}{2\delta_m R_p}\right)^{\frac{1}{3}} \quad (2)$$

$$Pe = \frac{convection\ rate}{diffusion\ rate} = \frac{U/\delta_m}{D/R_p^2} \quad (2)$$

*Da* > 1 indicates that the rate of DNA binding to the capture agent is faster than the rate of DNA transport to the pore wall; *Pe* < 1 means the rate at which molecules diffuse to the pore wall is faster than the rate at which they are convected through the pore. To capture dilute nucleic acids from large volumes in short times, two conditions must be met: i) efficient capture (*Da* >> 1), and ii) fast flow rates (*Q* ~ 1 mL/min) while maintaining *Pe* < 1.
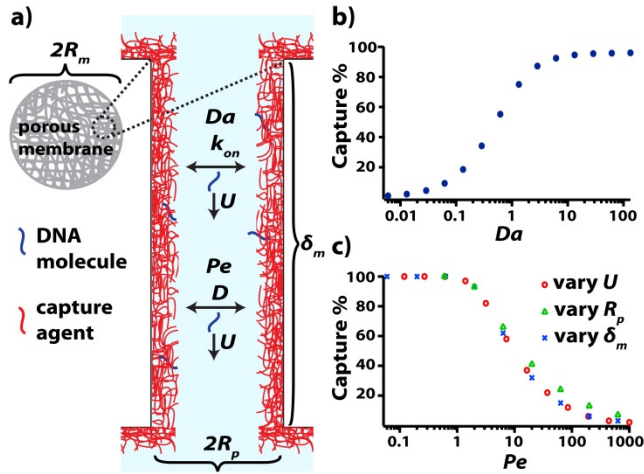


**Figure 4-1. Theoretical model and numerical simulations for flow-through capture. a) A schematic drawing showing the process of capturing nucleic acids from a sample flowing through a porous membrane (which has been functionalized with a capture agent). b) Predictions for the percentage of molecules captured at the pore wall as a function of the Damköhler number (*Da*). c) Predictions for the percentage of molecules captured at the pore wall as a function of the Péclet number (*Pe*). *Pe* is changed by**

**varying the velocity ($U$), pore length ($\delta_m$), or pore diameter ($R_p$); all result in a similar dependence of capture percentage on $Pe$.**

Capture efficiency is a factor of binding kinetics (time for the nucleic acid molecule to bind to the capture agent) and transport (time for the nucleic acid molecule to travel from the bulk solution to the pore wall coated with capture agent). High capture efficiency occurs when the transport rate is slower than the binding reaction rate (i.e., $Da \gg 1$), which can occur with fast reactions or slow transport. Many passive capture processes—such as wicking through a porous matrix or mixing with beads—rely on slow transport rates to achieve high $Da$. These processes capture efficiently at small length scales in microliter volumes;[21-23,33] however, for milliliter volumes and large length scales, passive capture processes would require impractical amounts of capture agent or time for $Da$ to be greater than 1. A fast binding reaction with diffusion-limited kinetics would enable higher transport rates (and thus faster flow rates) without adversely affecting capture efficiency. Electrostatic binding and silica adsorption in the presence of $Ca^{2+}$ are examples of diffusion-limited chemical reactions[41,42] that would maintain high $Da$ without relying on slow transport rates to ensure efficient capture. Our simulations show that when a capture agent coated on a pore wall has fast binding kinetics, $Da > 10$ ensures $> 95\%$ capture of nucleic acids flowing through the pore (Figure 4-1b and S-I). To scale up efficient capture processes to larger volumes, the mass transport rate can be increased. One way to increase mass transport rate is actively forcing fluid through a porous matrix,[43] which has been used for protein capture[44] and is well established in membrane chromatography[35,36]. However, flow-through capture has not been analyzed theoretically nor tested experimentally for rapid capture and detection of zeptomolar nucleic acids.

In general, high flow rates increase the transport rate, decrease $Da$, and thus reduce capture efficiency. However, the transport rate can be maintained below the adsorption rate (keeping $Da \gg 1$) by manipulating other transport parameters, thus counteracting the high flow rate. These transport parameters can be analyzed together by simulating the capture efficiency as a function of $Pe$ (S-I): simulations show that keeping $Pe < 1$ ensures $> 90\%$ capture efficiency (Figure 4-1c). To achieve a high convection rate and maintain $Pe < 1$, a relatively high

diffusion rate is required, which ensures that the molecules don't leave the pore before having a chance to diffuse to the wall and bind. To maintain this balance of a high convection rate with an even higher diffusion rate, the membrane radius, pore radius, and membrane thickness can be adjusted. Setting $Pe < 1$ in Eq. 2 provides the following constraint on flow rate through the membrane ($Q$) as a function of $\delta_m$, $R_m$, and $R_p$, where $\phi$ represents the porosity of the membrane (see S-II for derivation).

$$Q < \frac{\pi \phi D \delta_m R_m^2}{R_p^2} \quad (3)$$

Plotting Eq. 3 at different membrane thicknesses explores the relationship of these parameters (Figure 4-2a); trends favoring $Pe < 1$ and flow rates $> 1$ mL/min are decreasing pore radius, increasing membrane radius, and increasing membrane thickness. Decreasing the pore size enables faster diffusion rates and lower $Pe$, but it also increases the resistance to flow. Figure 4-2b considers this tradeoff, showing the pressure drop required for a sample to flow through the membrane at 1 mL/min at different membrane and pore radii. The overlap of the green triangles ($Pe < 1$) with red color ($\Delta P < 1$ atm) represents an ideal combination of parameters wherein $Pe$ is low enough and a reasonable pressure drop is achieved to flow at 1 mL/min.

a) when *Pe* < 1

$\delta_m$ = 100 μm

$\delta_m$ = 500 μm

$\delta_m$ = 1000 μm

b) when *Q* = 1 mL/min

$\delta_m$ = 100 μm
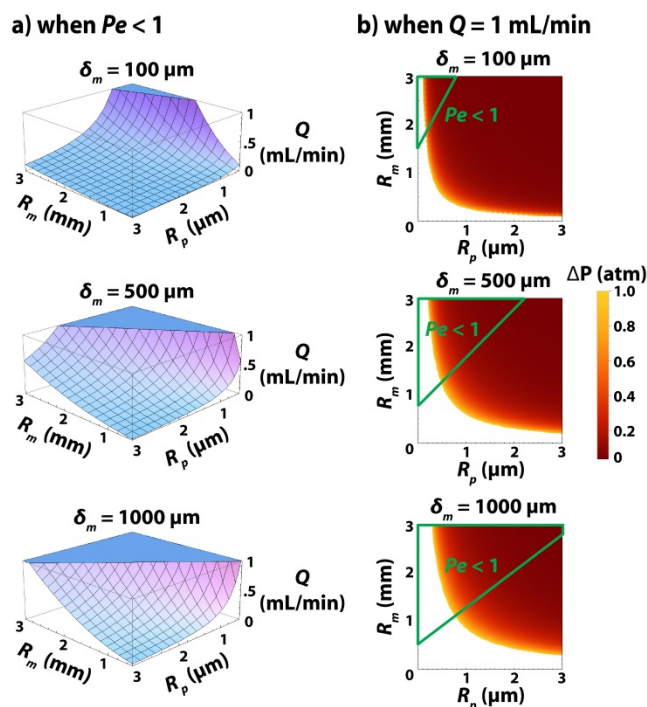
$\delta_m$ = 500 μm

$\delta_m$ = 1000 μm

**Figure 4-2. Predictions of membrane radius, pore radius, and membrane thickness tradeoffs for achieving high flow rates while also maintaining reasonable pressure drop (ΔP) and a low Péclet number (*Pe*). a) Combinations of membrane radius, pore radius, and flow rate that maintain *Pe* < 1 for different membrane thicknesses. Any point below the surface curvature has *Pe* < 1. b) The influence of membrane and pore radius on pressure drop with the flow rate through the membrane held constant at 1 mL/min. The overlap of the green triangle (*Pe* < 1) and red colored area represents efficient and rapid capture with a reasonable pressure drop (ΔP < 1 atm). The white area signifies a combination of membrane and pore radius that results in prohibitively large pressure drops (ΔP > 1 atm) necessary to achieve 1 mL/min.**

**Experimental Analysis.** Based on these predictions, we chose an appropriate experimental system to evaluate the ability of a flow-through matrix to rapidly capture zeptomolar concentrations of nucleic acids. This matrix should be compatible with *in situ* amplification, so glass fiber, silica, and other common capture materials that inhibit amplification reactions were not considered.[45,46] Nylon membranes do not prevent nucleic acid amplification and can be purchased in various pore sizes and thicknesses. The membrane thickness for a

LoProdyne nylon membrane from Pall Corporation ranges from 127.0-190.5 μm (see **Experimental Section**); at this thickness, a membrane radius of 2 mm is flexible and easily placed in a well plate for nucleic acid amplification. For a membrane thickness of 160 μm, flow rate of 1 mL/min, and membrane radius of 2 mm, Eq. 3 predicts that pore radii less than 0.76 μm would maintain $Pe < 1$. Therefore, we chose LoProdyne membranes with a pore radius of 0.6 μm; coating the membrane pores with a capture agent makes the pore size even smaller, ensuring that we were well below the 0.76 μm requirement. As described, the capture agent must have diffusion-limited kinetics. Because electrostatic binding is very fast and can easily be used for nucleic acid capture utilizing a cationic polymer to attract the negatively charged phosphate backbone of DNA, we chose chitosan as the capture agent, which has previously been used for NA capture.[21-25] Chitosan is an inexpensive biocompatible polymer with amine groups on its backbone that become positively-charged when the pH is below 6.3.[22,47] We functionalized chitosan onto the nylon membrane as described in **Experimental Section**. To verify that functionalizing the membrane with chitosan does not reduce the pore size such that the pressure drop becomes untenable (Figure 4-2b), we measured the capture efficiency at different flow rates. This experiment showed that the chitosan-functionalized nylon membrane captures > 90% of nucleic acids when solution is flowed through at 1 mL/min (see Figure 4-S2 of the Supporting Information).

To test the predictions from our analysis, we evaluated the capture efficiency as a function of Pe by flowing 500 ng/mL solutions of DNA through chitosan membranes at five different flow rates. Each flow rate was tested with three replicates and the capture efficiency along with one standard deviation is plotted in Figure 4-S2. These experiments confirmed that the chitosan membranes capture efficiently over a range of $Pe$, with > 90% capture of DNA when $Pe < 1$ (Figure 4-S2). We also measured the DNA binding capacity of chitosan-functionalized nylon membranes and found that they have a capacity of 1000 ng or more (Figure 4-3). This capacity is much greater than needed for our target application of zeptomolar concentrations ($10^{-21}$ M ~ 0.6 fg/mL for a bacterial genome). However, researchers in other fields may find this matrix useful in capturing large amounts of genetic material for other applications.
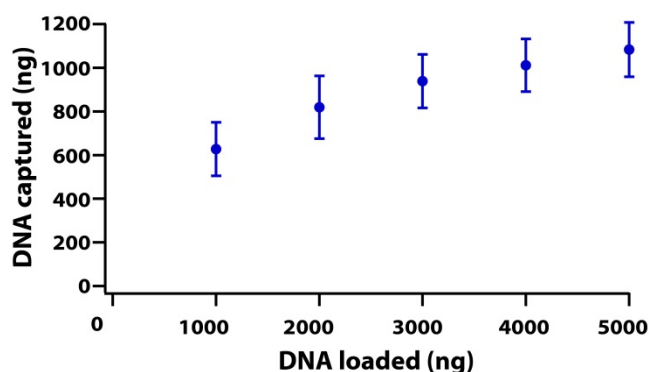
**Figure 4-3. DNA binding capacity of chitosan-functionalized membranes fabricated with Method A.**

Next, we tested whether *in situ* amplification would be chemically compatible with the nylon membrane that had been functionalized with chitosan. We added serial dilutions of DNA to the membrane, then submerged in amplification mix and amplified DNA via PCR. The chitosan membrane was compatible with *in situ* PCR amplification down to ~2 copies per reaction (Figure 4-S3a). We also tested the chitosan membrane compatibility with *in situ* LAMP and showed successful amplification at 20 copies per reaction (Figure 4-S3b[48]).

In this paper we did not study the location at which amplification occurs (i.e. whether amplification is initiated on the target molecules still attached to the surface of the membrane, or on the molecules released from the surface into the membrane pores, or on the molecules diffusing out of the pores). Further, we did not study the spatiotemporal mechanism of propagation of amplification once it is initiated. Such studies could provide interesting information in subsequent research.

The final step was to use chitosan's charge-switch capability to couple rapid capture with direct amplification without eluting the nucleic acids. A sample flows through the chitosan-coated membrane at pH ~5 and the negatively-charged phosphate backbone of DNA will electrostatically bind to the positively-charged amine groups on the chitosan. Following capture of NAs, the addition of amplification mix at pH ~8 deprotonates the amine groups and releases the captured nucleic acids for amplification (Figure 4-4).
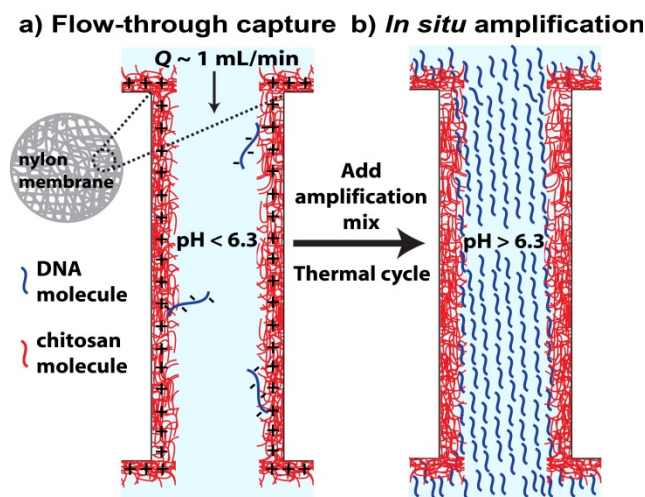
**a) Flow-through capture  b) *In situ* amplification**

**Figure 4-4. Schematic of capture and *in situ* amplification. a) Nucleic acids in a solution with pH < 6.3 will electrostatically bind to the protonated chitosan pore wall. b) Addition of amplification mix (pH ~8) deprotonates the chitosan and releases nucleic acids. Thermal cycling amplifies DNA.**

We then tested this idea (combining rapid capture and *in situ* amplification via charge-switch) at ultra-low concentrations (~1 copy/mL) and fast flow rates. Various amounts of λ DNA were spiked into volumes ranging from 1 to 50 mL with 100 ng or less background DNA (Table 4-S4); the solution was then flowed through a 2 mm radius chitosan-functionalized membrane at ~1 mL/min. After capture, the amplification was performed *in situ* with small volumes of PCR reagents (5–10 µL), as opposed to the traditional method of eluting from a capture matrix and using larger volumes of PCR reagents. DNA product was detected after thermal cycling using EvaGreen dye (see SI-V for details). This methodology detected a DNA target at concentrations as low as 0.5 copies/mL from as many as 50 mL (Figure 4-5b). Compiling data from replicate experiments run on different days, pre-concentration using the chitosan-functionalized membrane allowed detection down to 1 copy/mL over 85% of the time. Using any concentration above 10 copies/mL, detection results for the capture and amplification matrix were positive 100% of the time. No amplification was detected when flowing through buffer without DNA (see Figure 4-5a and Table 4-S4), ensuring that the λ DNA product detected is indeed from the sample flowed

through the membrane and not contamination of the membrane, lab materials, or PCR reagents with λ-phage DNA.
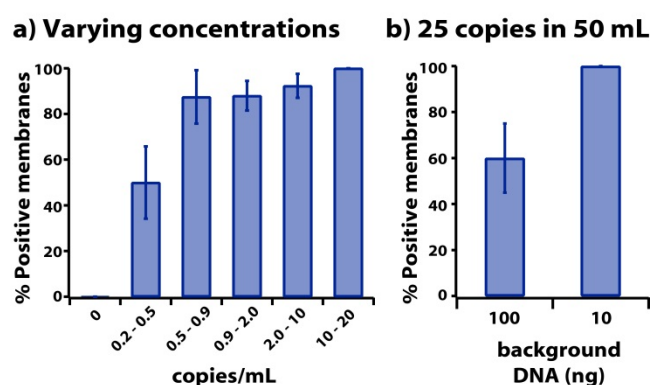


**Figure 4-5. Nucleic acid detection via flow-through capture and *in situ* amplification on chitosan membranes. a) Percent of membranes that were positive for λ DNA product over different experiments on different days for varying concentrations (0.2–20 copies/mL). The volume flowed through ranged from 1 to 50 mL (Table 4-S4) and the flow rate was ~1 mL/min. Each bin of the histogram has 6–26 samples for a total of 82 samples. b) Percent of membranes that were positive for λ DNA product over different experiments on different days. 50 mL solutions with 25 copies of target DNA and 10 or 100 ng background DNA were flowed through membranes at ~0.3 mL/min. The number of replicates are N = 10 for 100 ng and N = 9 for 10 ng. All error bars are 1 S.D.**

We observed that the chitosan membrane performance appeared to decrease slightly as larger volumes were flowed through (e.g., >10 mL volumes were 77% positive (23 out of 30 tests) and >20 mL volumes were 60% positive (9 out of 15 tests), see Table 4-S4). This decreased performance at higher volumes could be due to chitosan shedding off the membrane during flow or the fact that larger volumes have longer residence times and therefore more opportunity for the DNA molecule to release from its binding site and be flushed out of the membrane with the eluate. A thicker membrane with longer pores or a chitosan-functionalization method that more strongly attaches chitosan to the nylon membrane could

potentially improve its performance at larger volumes; however, these parameters were not tested and are outside of the scope of this study.

Our experiments have been using stringent conditions with high flow rate (~1 mL/min) and high level of added background DNA. For some applications, these conditions might be too stringent, and high sensitivity of detection may be more valuable. For example, drinking water samples do not always have the high level of background DNA we used. The presence of high levels of background DNA can affect capture efficiency of the target molecule during flow-through and can affect amplification efficiency during PCR. We therefore also tested detection of ultra-low concentrations of nucleic acids from large volumes with reduced background DNA at 10 ng and slower flow rates at 0.3 mL/min. We compared 50 mL solutions with 100 ng background DNA to 50 mL solutions with 10 ng background DNA. These experiments showed that 25 copies in 50 mL could be consistently detected under these conditions (Figure 4-5b). We have not yet further investigated how the performance of this method depends on the interplay of flow rate, pore geometry, level of DNA background, and the details of fabrication of the chitosan coating.To test whether salts in solution could interfere with electrostatic binding and decrease the ability of chitosan membranes to capture and detect nucleic acids, we performed six preliminary experiments. The experiments were identical to those performed for Figure 4-5, but instead of using 10 mM MES buffer as the medium comprising nucleic acids, various salt solutions were used (see S-VIII for details): i) Ringer's solution (10 and 20 copies λ DNA in 1 mL), Ringer's solution with 5 mM EDTA (10 and 20 copies λ DNA in 1 mL) and 5 mM EDTA alone (10 and 20 copies λ DNA in 1 mL). All six experiments resulted in positive amplification, indicating that the presence of salts does not disrupt capture of nucleic acids on the chitosan membrane nor their subsequent amplification.

**Conclusion**

We evaluated an approach for ultrasensitive detection of nucleic acids using chitosan as a charge-switch matrix that enables concentration factors up to 5000X (defined as the ratio of

final detection volume to the starting sample volume, e.g., DNA from 50 mL of solution was detected in 10 µL of PCR mix) and subsequent *in situ* amplification. A theoretical model guided the parameters chosen for flow rate, membrane radius, and pore radius. Based on model predictions, membranes with specific pore and membrane radii were functionalized to capture low copy numbers of nucleic acids from large volumes in short times. Using this approach, we were able to capture zeptomolar concentrations of nucleic acids from up to 50 mL of solution at a flow rate of 1 mL/min with $\Delta P < 1$ atm. In applications with different requirements for flow rate, pressure drop, or membrane size, this theory can be applied to guide choices of membrane parameters that meet those requirements.

In addition, flowing through a matrix that is compatible with *in situ* amplification obviates the need for centrifugation or bead manipulation and simplifies the purification process by eliminating an elution step. Chitosan-functionalized nylon membranes are sturdy, flexible, and small enough to be incorporated into integrated devices for complete sample-to-answer diagnostics. In this study, we focused on the theory and the proof-of-principle experiments using solutions of purified nucleic acids in clean matrixes. However, more complex matrices are encountered in many applications. Ultrasensitive measurements of viral, bacterial, and cancer-associated nucleic acids provide important diagnostic information to clinicians, but require the extraction and detection of NAs from milliliters of plasma and in some cases cell lysis. Combining this approach with lysis buffers and/or sample pretreatment should be tested next to evaluate the efficacy of this methodology for detection from a variety of sample matrices, such as blood, plasma, urine, and water. Additional work on integration of this approach with isothermal amplification would enable rapid and ultra-sensitive nucleic acid measurements for point-of-care and limited-resource settings.

**References**

(1) Fearon, M.; Scalia, V.; Lane, D.; Bigham, M.; Hawes, G.; O'Brien, S.; Kadkhoda, K. *Transfusion* **2016**, *56*, 994-995.
(2) Fong, T.-T.; Lipp, E. K. *Microbiol. Mol. Biol. Rev.* **2005**, *69*, 357-371.

(3) Hodgson, S. H.; Douglas, A. D.; Edwards, N. J.; Kimani, D.; Elias, S. C.; Chang, M.; Daza, G.; Seilie, A. M.; Magiri, C.; Muia, A. *Malar. J.* **2015**, *14*, 33.

(4) World Health Organization. *Guidelines for Drinking-water Quality: Recommendations*; World Health Organization, Geneva, **2004**; Vol. 1, 3rd ed..

(5) Raboud, J. M.; Montaner, J. S.; Conway, B.; Rae, S.; Reiss, P.; Vella, S.; Cooper, D.; Lange, J.; Harris, M.; Wainberg, M. A. *AIDS* **1998**, *12*, 1619-1624.

(6) Sarmati, L.; D'Ettorre, G.; Parisi, S. G.; Andreoni, M. *Curr. HIV Res.* **2015**, *13*, 250.

(7) Jiang, S.; Noble, R.; Chu, W. *Appl. Environ. Microbiol.* **2001**, *67*, 179-184.

(8) Haramoto, E.; Kitajima, M.; Katayama, H.; Ohgaki, S. *Water Res.* **2010**, *44*, 1747-1752.

(9) Campana, D.; Pui, C.-H. *Blood-* **1995**, *85*, 1416-1434.

(10) Maggiolo, F.; Callegaro, A.; Cologni, G.; Bernardini, C.; Velenti, D.; Gregis, G.; Quinzan, G.; Soavi, L.; Iannotti, N.; Malfatto, E. *JAIDS* **2012**, *60*, 473-482.

(11) Castillo, I.; Bartolome, J.; Quiroga, J.; Barril, G.; Carreño, V. *Aliment. Pharmacol. Ther.* **2009**, *30*, 477-486.

(12) Keys, J. R.; Leone, P. A.; Eron, J. J.; Alexander, K.; Brinson, M.; Swanstrom, R. *J. Med. Virol.* **2014**, *86*, 473-477.

(13) Abubakar, A.; Ozumba, P.; Buttner, P.; Winter, J.; Abimiku, A. *Journal of Antivirals & Antiretrovirals* **2015**, *2015*.

(14) Yager, P.; Domingo, G. J.; Gerdes, J. *Annu. Rev. Biomed. Eng.* **2008**, *10*, 107-144.

(15) Urdea, M.; Penny, L. A.; Olmsted, S. S.; Giovanni, M. Y.; Kaspar, P.; Shepherd, A.; Wilson, P.; Dahl, C. A.; Buchsbaum, S.; Moeller, G. *Nature* **2006**, *444*, 73-79.

(16) Boom, R.; Sol, C.; Salimans, M.; Jansen, C.; Wertheim-van Dillen, P.; Van der Noordaa, J. *J. Clin. Microbiol.* **1990**, *28*, 495-503.

(17) Wen, J.; Legendre, L. A.; Bienvenue, J. M.; Landers, J. P. *Anal. Chem.* **2008**, *80*, 6472-6479.

(18) Dineva, M. A.; Mahilum-Tapay, L.; Lee, H. *Analyst* **2007**, *132*, 1193-1199.

(19) Chomczynski, P.; Sacchi, N. *Anal. Biochem.* **1987**, *162*, 156-159.

(20) Miller, D.; Bryant, J.; Madsen, E.; Ghiorse, W. *Appl. Environ. Microbiol.* **1999**, *65*, 4715-4724.

(21) Byrnes, S. A.; Bishop, J. D.; Lafleur, L.; Buser, J.; Lutz, B.; Yager, P. *Lab on a Chip* **2015**, *15*, 2647-2659.

(22) Cao, W.; Easley, C. J.; Ferrance, J. P.; Landers, J. P. *Anal. Chem.* **2006**, *78*, 7222-7228.

(23) Pandit, K. R.; Nanayakkara, I. A.; Cao, W.; Raghavan, S. R.; White, I. M. *Anal. Chem.* **2015**, *87*, 11022-11029.

(24) Hagan, K. A.; Meier, W. L.; Ferrance, J. P.; Landers, J. P. *Anal. Chem.* **2009**, *81*, 5249-5256.

(25) Kendall, E. L.; Wienhold, E.; DeVoe, D. L. *Biomicrofluidics* **2014**, *8*, 044109.

(26) Connelly, J. T.; Rolland, J. P.; Whitesides, G. M. *Anal. Chem.* **2015**, *87*, 7595-7601.

(27) Rodriguez, N. M.; Linnes, J. C.; Fan, A.; Ellenson, C. K.; Pollock, N. R.; Klapperich, C. M. *Anal. Chem.* **2015**, *87*, 7872-7879.

(28) Liu, C.; Geva, E.; Mauk, M.; Qiu, X.; Abrams, W. R.; Malamud, D.; Curtis, K.; Owen, S. M.; Bau, H. H. *Analyst* **2011**, *136*, 2069-2076.

(29) Rodriguez, N. M.; Wong, W. S.; Liu, L.; Dewar, R.; Klapperich, C. M. *Lab on a Chip* **2016**.

(30) Reedy, C. R.; Bienvenue, J. M.; Coletta, L.; Strachan, B. C.; Bhatri, N.; Greenspoon, S.; Landers, J. P. *Forensic science international: genetics* **2010**, *4*, 206-212.

(31) Jangam, S. R.; Yamada, D. H.; McFall, S. M.; Kelso, D. M. *J. Clin. Microbiol.* **2009**, *47*, 2363-2368.

(32) Breadmore, M. C.; Wolfe, K. A.; Arcibal, I. G.; Leung, W. K.; Dickson, D.; Giordano, B. C.; Power, M. E.; Ferrance, J. P.; Feldman, S. H.; Norris, P. M. *Anal. Chem.* **2003**, *75*, 1880-1886.

(33) Shim, S.; Shim, J.; Taylor, W. R.; Kosari, F.; Vasmatzis, G.; Ahlquist, D. A.; Bashir, R. *Biomedical microdevices* **2016**, *18*, 1-8.

(34) Shen, F.; Du, W.; Kreutz, J. E.; Fok, A.; Ismagilov, R. F. *Lab on a Chip* **2010**, *10*, 2666-2672.

(35) Thömmes, J.; Kula, M. R. *Biotechnol. Prog.* **1995**, *11*, 357-367.

(36) Unarska, M.; Davies, P.; Esnouf, M.; Bellhouse, B. *J. Chromatogr. A* **1990**, *519*, 53-67.

(37) Lukacs, G. L.; Haggie, P.; Seksek, O.; Lechardeur, D.; Freedman, N.; Verkman, A. *J. Biol. Chem.* **2000**, *275*, 1625-1629.

(38) Wink, T.; de Beer, J.; Hennink, W. E.; Bult, A.; van Bennekom, W. P. *Anal. Chem.* **1999**, *71*, 801-805.

(39) Hansen, R.; Bruus, H.; Callisen, T. H.; Hassager, O. *Langmuir* **2012**, *28*, 7557-7563.

(40) Koyayashi, T.; Laidler, K. J. *Biotechnol. Bioeng.* **1974**, *16*, 99-118.

(41) Nguyen, T. H.; Elimelech, M. *Biomacromolecules* **2007**, *8*, 24-32.

(42) Minehan, D. S.; Marx, K. A.; Tripathy, S. K. *Macromolecules* **1994**, *27*, 777-783.

(43) Chung, Y.-C.; Jan, M.-S.; Lin, Y.-C.; Lin, J.-H.; Cheng, W.-C.; Fan, C.-Y. *Lab on a Chip* **2004**, *4*, 141-147.

(44) Bhattacharjee, S.; Dong, J.; Ma, Y.; Hovde, S.; Geiger, J. H.; Baker, G. L.; Bruening, M. L. *Langmuir* **2012**, *28*, 6885-6892.

(45) Wang, W.; Wang, H. B.; Li, Z. X.; Guo, Z. Y. *J. Biomed. Mater. Res. A* **2006**, *77*, 28-34.

(46) Linnes, J.; Rodriguez, N.; Liu, L.; Klapperich, C. *Biomedical Microdevices* **2016**, *18*, 1-12.

(47) Kyung-Hee, C.; Kwang-hee, K. P. *Bulletin of the Korean Chemical Society* **1983**, *4*, 68-72.

(48) Nagamine, K.; Hase, T.; Notomi, T. *Mol. Cell. Probes* **2002**, *16*, 223-229.

**Supporting Information**

*Flow-through capture simulations*

The fraction of nucleic acid molecules captured in a membrane pore compared to the amount flowed through (capture efficiency) is a function of pore geometry, flow parameters, and adsorption kinetics (Figure 4-S1). The concentration of nucleic acids at any position in the pore, $C(r, z)$, was simulated at steady-state using the *Transport of Diluted Species* module of *Comsol Multiphysics (version 4.4)* with the parameters listed in Table 4-S1. To generate the data for Figure 4-1b-c, a parametric sweep was performed with various values of $k_{on} \cdot \gamma$, $U$,

$R_p$, and $\delta_m$ (Table 4-S2 and Table 4-S3). Then, the inlet flux ($J_{in} = J|_{z = \delta m}$) and outlet flux ($J_{out} = J|_{z = 0}$) were evaluated and used in Eq. S-1 to calculate capture efficiency.

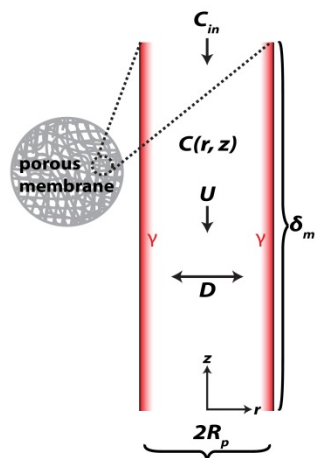$$Capture\ \% = 1 - \frac{J_{out}}{J_{in}} \qquad \text{(S-3)}$$



Figure 4-S6. Schematic of flow-through simulation geometry. Red represents the capture agent ($\gamma$) coated on the surface of the pore wall.

Table 4-S1. Parameters used in the flow-through capture simulations.

| Parameter | Description | Value |
|---|---|---|
| $R_p$ | Pore radius | $0.56 - 17.78$ μm |
| $\delta_m$ | Pore length (thickness of membrane) | $0.316 - 3162$ μm |
| $U$ | Flow velocity | $0.118 - 1000$ mm/s |
| $D$ | Diffusivity of nucleic acid molecule | $10\ \mu m^2 \cdot s^{-1}$ |
| $k_{on}$ | Nucleic acid binding rate constant | $10^6\ L \cdot mol^{-1} \cdot s^{-1}$ |
| $\gamma$ | Surface concentration of capture agent | $10^{-7}\ mol \cdot m^{-2}$ |
| $C_{in}$ | Inlet concentration of nucleic acids | $1$ μM |

Table 4-S2. The product of $k_{on} \cdot \gamma$ was varied to generate Capture % as a function of Damköhler number ($Da$) (Figure 4-1b). $R_p$ (1 μm), $\delta_m$ (100 μm), $U$ (2 mm/s), $D$ (10 μm$^2 \cdot$s$^{-1}$), and $C_{in}$ (1 μM) were held constant.

| $k_{on} \cdot \gamma$ (m/s) | $k_c$ (m/s) | *Da* | $J_{in}$ (mol/s) | $J_{out}$ (mol/s) | Capture % |
|---|---|---|---|---|---|
| 1.00E-07 | 1.62E-05 | 0.01 | -3.92E-18 | -3.88E-18 | 1.0 |
| 2.15E-07 | 1.62E-05 | 0.01 | -3.92E-18 | -3.83E-18 | 2.1 |
| 4.64E-07 | 1.62E-05 | 0.03 | -3.92E-18 | -3.74E-18 | 4.5 |
| 1.00E-06 | 1.62E-05 | 0.06 | -3.92E-18 | -3.55E-18 | 9.3 |
| 2.15E-06 | 1.62E-05 | 0.13 | -3.92E-18 | -3.19E-18 | 18.5 |
| 4.64E-06 | 1.62E-05 | 0.29 | -3.92E-18 | -2.58E-18 | 34.2 |
| 1.00E-05 | 1.62E-05 | 0.62 | -3.92E-18 | -1.75E-18 | 55.2 |
| 2.15E-05 | 1.62E-05 | 1.33 | -3.92E-18 | -9.77E-19 | 75.0 |
| 4.64E-05 | 1.62E-05 | 2.87 | -3.92E-18 | -5.03E-19 | 87.2 |
| 1.00E-04 | 1.62E-05 | 6.17 | -3.92E-18 | -2.94E-19 | 92.5 |
| 2.15E-04 | 1.62E-05 | 13.3 | -3.92E-18 | -2.11E-19 | 94.6 |
| 4.64E-04 | 1.62E-05 | 28.7 | -3.92E-18 | -1.78E-19 | 95.5 |
| 1.00E-03 | 1.62E-05 | 61.7 | -3.92E-18 | -1.63E-19 | 95.8 |
| 2.15E-03 | 1.62E-05 | 133 | -3.92E-18 | -1.57E-19 | 96.0 |

Table 4-S3. $U$, $\delta_m$, or $R_p$ was varied to generate Capture % as a function of Péclet number ($Pe$) (Figure 4-1c). $C_{in}$ (1 μM), $k_{on} \cdot \gamma$ ($10^{-4}$ m/s), and $D$ (10 $\mu m^2 \cdot s^{-1}$) were held constant.

| U (m/s) | $\delta_m$ (μm) | $R_p$ (μm) | *Pe* | $J_{in}$ (mol/s) | $J_{out}$ (mol/s) | Capture % |
|---|---|---|---|---|---|---|
| 1.18E-04 | 100 | 1 | 0.12 | -2.46E-19 | -2.32E-36 | 100.0 |
| 2.68E-04 | 100 | 1 | 0.27 | -5.32E-19 | -1.00E-26 | 100.0 |
| 6.11E-04 | 100 | 1 | 0.61 | -1.20E-18 | -4.11E-22 | 100.0 |
| 1.39E-03 | 100 | 1 | 1.39 | -2.72E-18 | -7.21E-20 | 97.4 |
| 3.16E-03 | 100 | 1 | 3.16 | -6.19E-18 | -1.11E-18 | 82.0 |
| 7.20E-03 | 100 | 1 | 7.20 | -1.41E-17 | -5.92E-18 | 58.0 |
| 1.64E-02 | 100 | 1 | 16.4 | -3.21E-17 | -2.02E-17 | 37.0 |
| 3.73E-02 | 100 | 1 | 37.3 | -7.30E-17 | -5.70E-17 | 22.0 |
| 8.48E-02 | 100 | 1 | 84.8 | -1.66E-16 | -1.46E-16 | 12.3 |
| 1.93E-01 | 100 | 1 | 193 | -3.78E-16 | -3.54E-16 | 6.5 |
| 4.39E-01 | 100 | 1 | 439 | -8.60E-16 | -8.32E-16 | 3.2 |
| 1.00E+00 | 100 | 1 | 1000 | -1.96E-15 | -1.93E-15 | 1.6 |
| 2.00E-03 | 3162 | 1 | 0.06 | -3.90E-18 | 8.30E-39 | 100.0 |

| 2.00E-03 | 1000 | 1 | 0.20 | -3.90E-18 | -1.15E-28 | 100.0 |
|---|---|---|---|---|---|---|
| 2.00E-03 | 316 | 1 | 0.63 | -3.90E-18 | -1.72E-21 | 100.0 |
| 2.00E-03 | 100 | 1 | 2.00 | -3.90E-18 | -2.90E-19 | 92.6 |
| 2.00E-03 | 31.6 | 1 | 6.32 | -3.90E-18 | -1.50E-18 | 61.5 |
| 2.00E-03 | 10.0 | 1 | 20.0 | -3.90E-18 | -2.65E-18 | 32.1 |
| 2.00E-03 | 3.16 | 1 | 63.2 | -3.90E-18 | -3.30E-18 | 15.4 |
| 2.00E-03 | 1.00 | 1 | 200 | -3.90E-18 | -3.65E-18 | 6.4 |
| 2.00E-03 | 0.316 | 1 | 632 | -3.90E-18 | -3.80E-18 | 2.6 |
| 2.00E-03 | 100 | 0.56 | 0.63 | -1.23E-18 | -1.60E-21 | 99.9 |
| 2.00E-03 | 100 | 1.00 | 2.00 | -3.90E-18 | -2.90E-19 | 92.6 |
| 2.00E-03 | 100 | 1.78 | 6.32 | -1.23E-17 | -4.20E-18 | 65.9 |
| 2.00E-03 | 100 | 3.16 | 20.0 | -3.90E-17 | -2.30E-17 | 41.0 |
| 2.00E-03 | 100 | 5.62 | 63.2 | -1.23E-16 | -9.40E-17 | 23.6 |
| 2.00E-03 | 100 | 10.00 | 200 | -3.90E-16 | -3.40E-16 | 12.8 |
| 2.00E-03 | 100 | 17.78 | 632 | -1.23E-15 | -1.15E-15 | 6.5 |

Geometry: The model was assembled using a cylindrical geometry drawn in 2D axially symmetric space, with $r$ as the radial component and $z$ the axial component (Figure 4-S1). The radius of the cylinder ($R_p$) varied from 0.56 μm to 17.78 μm; the length of the cylinder ($\delta_m$) varied from 0.316 μm to 3162 μm (Table 4-S3).

Transport: In a porous matrix, fluid flow can be approximated with a uniform velocity ($U$) independent of radius[1]. The flow velocity varied from $1.18 \cdot 10^{-4}$ m/s to 1 m/s (Table 4-S3). The top boundary of the cylinder ($z = \delta_m$) was an inlet and the bottom boundary ($z = 0$) was an outlet. The diffusion coefficient used was for DNA[2], $10^{-11}$ m²/s.

Kinetics: The binding rate between nucleic acids and the capture agent was assumed to be second order with respect to nucleic acid concentration and capture agent surface concentration. We assumed the surface concentration of capture agent ($\gamma$) was in excess (and therefore unchanging during the course of the adsorption reaction) and estimated it to be $10^{-7}$ mol/m². With a kinetic rate constant estimated from nucleic acid-cationic polymer kinetics[3], the adsorption rate occurring at the pore wall is shown in Eq. S-2.

$$R_{ads} = k_{on} \cdot \gamma \cdot C(R_p, z) \qquad \text{(S-4)}$$

Normally, adsorption kinetics include both an on and off rate. However, in this situation, we excluded the off rate from analysis because it was insignificant compared to the on rate ($k_{on}$ ~ 107 M$^{-1}$s$^{-1}$, $k_{off}$ ~ 10-3 s-1, reference 38 from the manuscript).

Boundary conditions: The inlet concentration of nucleic acid molecules ($C_{in}$ = 10$^{-6}$ mol/L) represents a normal nucleic acid concentration in human blood plasma[4]. Axial symmetry was imposed at $r = 0$, and a flux boundary condition (Eq. S-3) was imposed at $r = R_p$ to represent the adsorption of nucleic acid molecules to the surface of the pore wall.

$$R_{ads} = D \left. \frac{\partial C(r,z)}{\partial r} \right|_{r=R_p} \qquad \text{(S-5)}$$

Mesh and solver settings: The geometry was meshed using a Free Triangular mesh with a maximum element size of 0.0525 $\mu$m. The Direct Stationary Solver (PARDISO) was used with a nested dissection multithreaded preordering algorithm and an auto scheduling method.

*Equation 3 and Figure 4-2b*

The number of pores in a membrane ($n_p$) can be calculated from the porosity ($\phi$) as in Eq. S-4.

$$\phi = \frac{n_p \pi R_p^2}{\pi R_m^2} \rightarrow n_p = \frac{\phi R_m^2}{R_p^2} \qquad \text{(S-6)}$$

The flow rate through the entire membrane ($Q$) is the flow rate through each pore ($Q_p$) multiplied by the number of pores ($Q = n_p Q_p$). Using Eq. S-4 for $n_p$ and solving for $Q_p$ gives the following:

$$Q_p = \frac{Q R_p^2}{\phi R_m^2} \qquad \text{(S-7)}$$

Eq. S-6 results from plugging Eqn S-5 into the relationship between pore flow rate and flow velocity ($Q_p = U \pi R_p^2$).

$$U = \frac{Q_p}{\pi R_p^2} = \frac{Q}{\pi \phi R_m^2} \qquad \text{(S-8)}$$

Then, using Eq. S-6 in Eq. 2 and setting the condition that $Pe < 1$ yields Eq. S-7.

$$Pe = \frac{UR_p^2}{D\delta_m} = \frac{QR_p^2}{\pi\phi R_m^2 D\delta_m} < 1 \tag{S-9}$$

Solving Eq. S-7 for $Q$ yields Eq. 3. $\phi = 0.6$ and $D = 10^{-11}$ m$^2$/s were assumed for all calculations.

To calculate the pressure drop as a function of pore radius ($R_p$) and membrane radius ($R_m$), Pouiselle flow was assumed (Eq. S-8). Flow rate through the pore ($Q_p$) was replaced with flow rate through the entire membrane ($Q$) using Eq. S-5. $Q$ (1 mL/min), $\mu$ ($10^{-3}$ Pa·s), and $\phi$ (0.6) were held constant; $R_p$ and $R_m$ were varied from 1 to 3 μm and 1 to 3 mm, respectively. The results, along with regimes of $Pe < 1$ calculated from Eq. 2, are plotted in Figure 4-2b.

$$\Delta P = \frac{8\mu Q_p \delta_m}{\pi R_p^4} = \frac{8\mu Q \delta_m}{\pi\phi R_p^2 R_m^2} \tag{S-10}$$

*DNA binding efficiency as a function of* Pe

100 ng of salmon sperm DNA (Invitrogen, CA) in 200 μL of 10 mM MES buffer (pH ~5) was flushed through a chitosan membrane with a radius of 2 mm at different flow rates via the syringe/luer lock system shown in Figure 4-S4. The inlet and eluate DNA concentration of each flush was measured with PicoGreen dye (Invitrogen, CA); converting to mass ($m_{DNA}$), Eq. S-9 was then used to calculate the capture efficiency.

$$Capture\ \% = \left(1 - \frac{m_{DNA,out}}{m_{DNA,in}}\right) \cdot 100 \tag{S-11}$$

$Pe$ was calculated via Eq. 2 and the results are plotted in Figure 4-S2. This agrees with theoretical predictions that $Pe > 1$ results in reduced capture. Also, layering the nylon membrane with chitosan does not significantly hinder flow rate or require untenable pressure drops to achieve flow rates of ~ 1 mL/min and efficient capture.
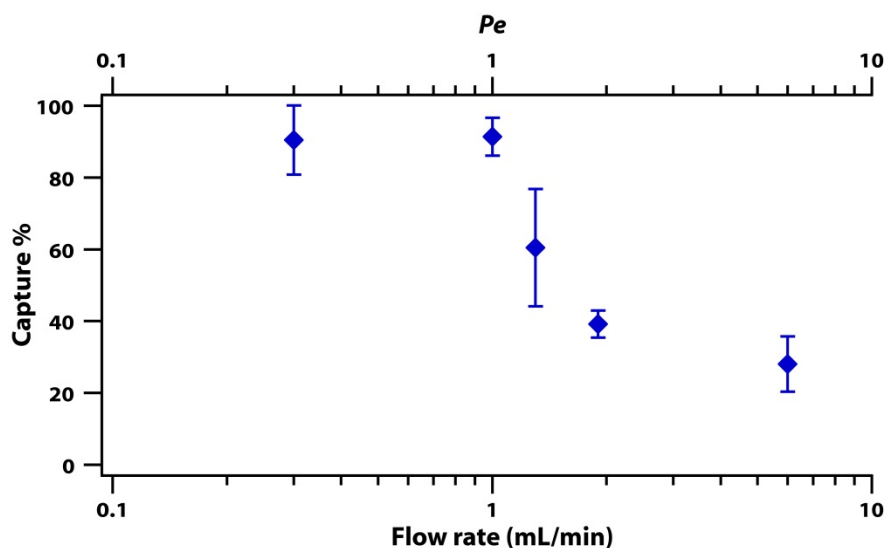
Figure 4-S7. Capture efficiency depends on flow rate.

We clarify that capture efficiencies > 90% are only possible when the capture agent is in excess of the target DNA molecule and $Pe < 1$, which is the case for 100 ng of input DNA (Figure 4-S2). On the other hand, the purpose of the experiments in Figure 4-3 was to measure the total binding capacity of the chitosan membrane (i.e., occupy all the cationic binding sites). To accomplish this, larger quantities of DNA (1000 ng) were flowed through the membrane and the capture efficiency was not expected to be high; in fact, with each successive load, it should decrease to 0% until all binding sites are occupied. Indeed, we observed that the capture efficiency in Figure 4-3 varied from 60% in the first run to 20% in the fifth run—by the time the fifth load of 1000 ng DNA was flowed through the membrane, there were fewer binding sites available and thus the recovery was much lower than the first load when all binding sites were available.

*Compatibility of chitosan membrane with* in situ *amplification*

To test the compatibility of chitosan membranes with *in situ* PCR amplification, 1 μL of varying concentrations of λ DNA was wetted into chitosan membrane with a radius of 2 mm. The membrane was then placed in a well plate and 10 μL PCR mix was added to the well. Replicates containing 10 μL PCR mix with the same amount of λ DNA and no membrane present were also included. The well plate was inserted into an Ilumina Eco™ real-time PCR

System (EC-101-1001) and thermal cycled; correct λ-phage DNA product was verified with melt curve analysis. The PCR mix and thermal cycling conditions used were the same as described in the Experimental Section. Figure 4-S3a shows that chitosan membranes are compatible with *in situ* PCR amplification down to ~2 copies/reaction.

To test compatibility with *in situ* LAMP amplification, 20 copies of λ DNA were wetted into a chitosan membrane with a radius of 2 mm. The membrane was then placed in a well plate and 10 μL LAMP mix was added to the well. Replicates containing 10 μL LAMP mix with 20 copies of λ DNA and no membrane present were also included as solution controls. The well plate was inserted into an Ilumina Eco$^{TM}$ real-time PCR System and incubated for 40 min at 68 °C. Figure 4-S3b shows the real-time fluorescent traces representing DNA product.
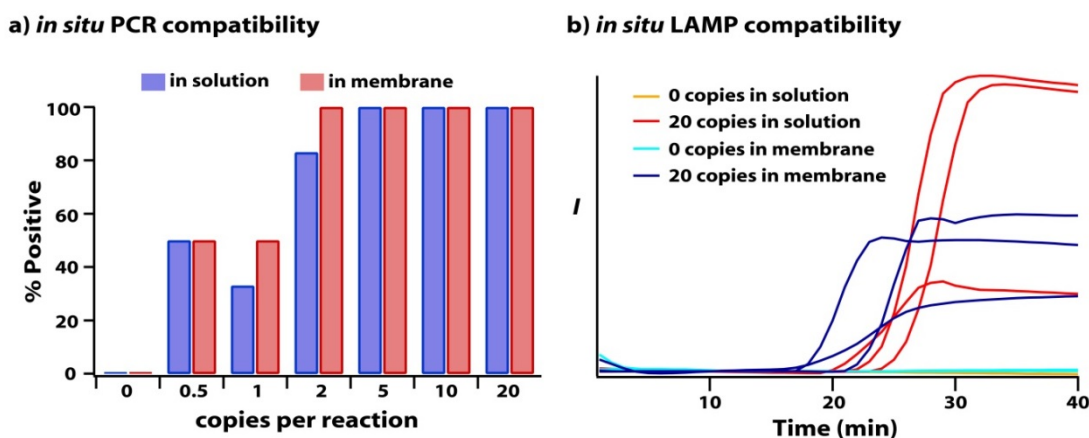


Figure 4-S8. Compatibility of chitosan membranes with PCR and LAMP amplification. a) Dilutions of λ DNA were wetted onto chitosan membranes or placed into a well plate without a membrane; PCR mix was added and amplification was detected via melt curve analysis. Six replicates were run at each dilution; the percent of replicates positive for λ DNA product is shown (n = 6). b) 20 copies of λ DNA were wetted onto chitosan membranes within a well plate, or placed into a well plate without a membrane; LAMP mix was added and amplification was detected via real-time fluorescence. Three replicates were run for each sample; the fluorescent traces as a function of time are plotted.

LAMP reagents were purchased from Eiken Chemical (Tokyo, Japan), product code LMP207. The LAMP mixture used for amplification of λ-phage DNA contained the following: 5 µL Reaction Mixture, 0.4 µL of Enyzme Mixture, 0.5 µL of 20X LAMP primer mixture (Table 4-S6), 0.25 µL of Calcein (Fd), and 3.85 µL of nuclease-free water.

*Details of capture and* in situ *amplification (Figure 4-5)*

Figure 4-S4 is a schematic of the syringe/luer lock system used to flow mL-scale volumes through chitosan membranes with a radius of 2 mm. Syringes were purchased from BD (Franklin Lakes, NJ) and luer locks (Catalog #LC78-J1A) were purchased from Nordson Medical (Westlake, Ohio). Table 4-S4 shows all the quantities of λ DNA, volumes of 10 mM MES buffer, and amounts of background DNA used to generate Figure 4-5. Salmon sperm DNA from Invitrogen (Carlsbad, CA) was used as "background DNA".
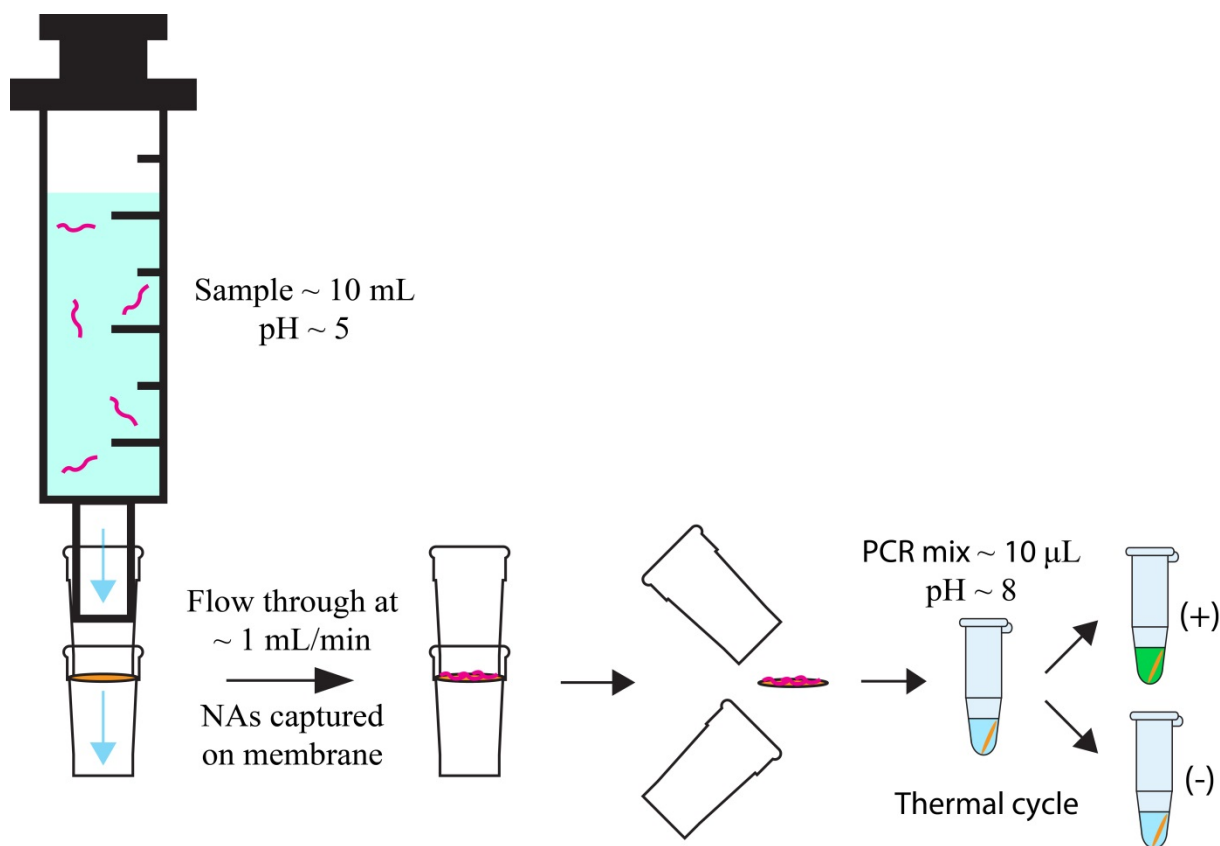
Figure 4-S9. Schematic of syringe/luer lock system used to flow mL-scale volumes through the chitosan membrane with a radius of 2 mm. A chitosan membrane is placed in between two luer locks. A syringe containing a nucleic acid sample is connected to the top luer lock and the plunger is compressed to flush the sample through the membrane. Then, the luer locks are disconnected from the syringe, and taken apart, and the membrane containing captured nucleic acids is placed in a PCR tube along with amplification mix for thermal cycling.

Table 4-S4. Volumes of 10 mM MES (2-(N-morpholino)ethanesulfonic acid) buffer and final concentrations of λ DNA used for Figure 4-5a. The two fabrication methods are described in the Experimental Section.

| Copies of λ DNA | Volume of 10 mM MES buffer (mL) | λ DNA Concentration (cop/mL) | Background DNA added to MES buffer (ng) | Positive membranes | Total membranes tested | Fabrication Method |
|---|---|---|---|---|---|---|
| 0 | 1 | 0 | 100 | 0 | 3 | A |
| 0 | 3 | 0 | 100 | 0 | 3 | B |
| 10 | 50 | 0.2 | 100 | 1 | 1 | B |
| 10 | 50 | 0.2 | 100 | 1 | 4 | A |
| 5 | 15 | 0.3 | 100 | 2 | 2 | A |
| 10 | 30 | 0.3 | 100 | 1 | 2 | A |
| 10 | 25 | 0.4 | 100 | 1 | 2 | A |
| 5 | 10 | 0.5 | 100 | 2 | 2 | A |
| 10 | 20 | 0.5 | 100 | 3 | 4 | A |
| 25 | 50 | 0.5 | 100 | 1 | 1 | B |
| 25 | 50 | 0.5 | 0 | 1 | 1 | B |
| 9 | 10 | 0.9 | 10 | 6 | 6 | B |
| 5 | 5 | 1.0 | 100 | 2 | 2 | A |
| 10 | 10 | 1.0 | 100 | 1 | 2 | A |
| 10 | 10 | 1.0 | 50 | 3 | 3 | B |
| 9 | 5 | 1.8 | 0 | 6 | 6 | B |
| 6 | 3 | 2.0 | 100 | 2 | 3 | B |
| 10 | 5 | 2.0 | 50 | 2 | 3 | B |
| 12 | 5 | 2.4 | 100 | 3 | 3 | A |
| 10 | 4 | 2.5 | 100 | 2 | 2 | A |

| | | | | | | |
|---|---|---|---|---|---|---|
| 5 | 1 | 5.0 | 100 | 5 | 5 | A |
| 10 | 2 | 5.0 | 100 | 4 | 4 | A |
| 6 | 1 | 6.0 | 100 | 3 | 3 | B |
| 10 | 1 | 10.0 | 100 | 3 | 4 | A |
| 20 | 2 | 10.0 | 100 | 2 | 2 | A |
| 10 | 1 | 10.0 | 0 | 2 | 3 | B |
| 20 | 1 | 20.0 | 100 | 5 | 5 | A |
| 20 | 1 | 20.0 | 0 | 3 | 3 | B |

To detect λ DNA product after *in situ* amplification, two methods were used. i) After thermal cycling the membrane with PCR mix in a well plate, an appropriate amount of 6x gel loading dye and TE buffer was added to each well and pipette mixed. Then, 5 μL of this solution was removed from the well, placed in a 1.2% agarose gel, and run for 50 min at 80V. Samples with DNA product at the same length as the λ PCR amplicon (322 base pairs) were considered positive. An example of a gel image is shown in Figure 4-S5a. ii) After thermal cycling, the PCR reaction mixture was transferred to an empty well and an appropriate amount of 20X Evagreen dye (Biotium) and 10X TE buffer was added. A continuous melt curve was then obtained from 65–95 ˚C; samples with a peak around ~85 ˚C (the melting temperature of the λ PCR amplicon) were considered positive. (Figure 4-S5b).
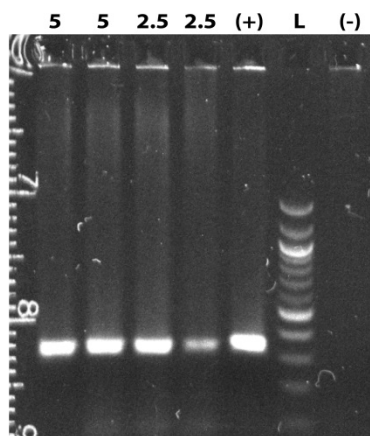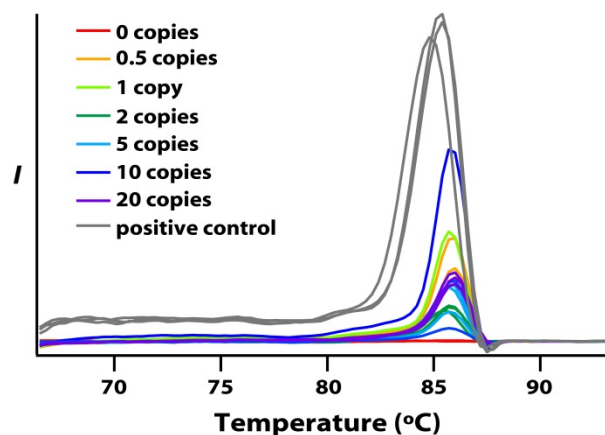


Figure 4-S10. DNA detection after *in situ* amplification. a) Varying concentrations of λ DNA in 10 mM MES buffer were flowed through chitosan membranes. The membranes

were then placed in a well plate and thermal cycled. After thermal cycling, each sample was run on a gel. Lanes 1–2: 5 copies/mL; Lanes 3–4: 2.5 copies/mL; Lane 5: positive control (10 copies of λ DNA in PCR mix, no membrane); Lane 6: negative control (0 copies of λ DNA in PCR mix, no membrane). b) Dilutions of λ DNA were wetted onto chitosan membranes; PCR mix was added and melt curve fluorescent traces are plotted. Three replicates were run at each dilution.

It is important to note that while Table 4-S4 includes experiments done on multiple batches of membranes over 8 months, it does not include all experiments that we performed with chitosan-coated nylon membranes. Using binding capacity measurements (described in Experimental Section) and DNA capture experiments (described in S-IV), we determined that there was batch-to-batch variation in the fabrication process. Therefore, only those batches with consistent performance were analyzed and other batches that did not meet our standards were excluded from analysis.

Table 4-S5 summarizes Table 4-S4 by binning the various experiments into concentration ranges and reporting a "% Positive membranes" along with the standard error. This data is then plotted in Figure 4-5a of the manuscript.

Table 4-S5. Histogram of Table 4-S4 with concentration bins and standard error.

| Concentration (cop/mL) | positive | total | positive/total | SE |
|---|---|---|---|---|
| 0 | 0 | 6 | 0.00 | 0.00 |
| 0.2 - 0.5 | 5 | 10 | 0.50 | 0.16 |
| 0.5 - 0.9 | 6 | 7 | 0.86 | 0.13 |
| 0.9 - 2.0 | 22 | 25 | 0.88 | 0.06 |
| 2.0 - 10.0 | 24 | 26 | 0.92 | 0.05 |
| 10.0 - 20.0 | 8 | 8 | 1.00 | 0.00 |

To reliably detect ultra-low concentrations of nucleic acids from large volumes, we reduced the background DNA amount to 10 ng and relaxed the constraint imposed on the experiments

for Figure 4-5a that the solution be flowed through the membrane at 1 mL/min. We instead flowed through at ~0.3 mL/min and compared 50 mL solutions with 100 ng background DNA to 50 mL solutions with 10 ng background DNA. These experiments showed that 25 copies in 50 mL can be consistently detected when the flow rate and background DNA are reduced from the previous constraints of 1 mL/min and 100 ng. The data is shown in Table 4-S6 below and summarized in the manuscript with Figure 4-5b.

Table 4-S6. Volumes of 10 mM MES (2-(N-morpholino)ethanesulfonic acid) buffer and final concentrations of λ DNA used for Figure 4-5b. The two fabrication methods are described in the Experimental Section.

| Copies of λ DNA | Volume of 10 mM MES buffer (mL) | λ DNA Concentration (cop/mL) | Background DNA added to MES buffer (ng) | Positive membranes | Total membranes tested | Fabrication Method |
|---|---|---|---|---|---|---|
| 25 | 50 | 0.5 | 100 | 6 | 10 | B |
| 25 | 50 | 0.5 | 10 | 9 | 9 | B |

Primer sequences for *λ*-phage DNA PCR amplification and *λ*-phage DNA LAMP amplification

A mixture of primers from Table 4-S7 was made at 5 μM each in nuclease-free water and used for the PCR amplification reactions described in this manuscript.

Table 4-S7. Sequences for λ-phage DNA PCR primers.

| | |
|---|---|
| forward | CGTTGCAGCAATATCTGGGC |
| reverse | TATTTTGCATCGAGCGCAGC |

A mixture of each primer from Table 4-S8 was made in nuclease-free water and used for the LAMP amplification reactions described in S-IV. The concentration of each primer in the 20X mixture is also listed.

Table 4-S8. Sequences for λ-phage DNA LAMP primers[5] and their concentration in the 20X primer mix.

| Name | Sequence | Conc. |
|------|----------|-------|
| FOP | GGCTTGGCTCTGCTAACACGTT | 4 μM |
| BOP | GGACGTTTGTAATGTCCGCTCC | 4 μM |
| FIP | CAGCCAGCCGCAGCACGTTCGCTCATAGGAGATATGGTAGAGCCGC | 32 μM |
| BIP | GAGAGAATTTGTACCACCTCCCACCGGGCACATAGCAGTCCTAGGGACAGT | 32 μM |
| LOOPF | CTGCATACGACGTGTCT | 8 μM |
| LOOPR | ACCATCTATGACTGTACGCC | 8 μM |

*CDI functionalization of nylon membrane*

Before coating with chitosan, the LoProdyne membrane was functionalized with N,N carbonyldiimidazole (CDI) in methylene chloride according to the manufacturer's protocol. The protocol is found at this website (http://www.pall.com/main/oem-materials-and-devices/literature-library-details.page?id=4765) and is also copied below:

LoProdyne LP membrane has hydroxyl surface chemistry. The membrane binds very little protein in standard binding tests using IgG or BSA. The membrane can be activated for covalent attachment using N, N® carbonyldiimidazole (CDI) in methylene chloride as follows:

Dissolve 0.49 g CDI in 45 mL MeCl2.

Add to a glass dish under a fume hood.

Immerse sheet of LoProdyne LP membrane in this solution for 15 minutes, RT.

Wash membrane 4X with 40 mL per wash MeCl2, 5 minutes per wash.

Air dry at 60 °C for 3 minutes.

Store in vacuum desiccator until use.

*Complex solutions*

To test whether salts in solution could interfere with electrostatic binding and decrease the ability of chitosan membranes to capture and detect nucleic acids, we performed preliminary experiments in complex solutions. Ringer's solution was used to mimic the salt concentration of plasma and was made according to the instructions at the following website: http://cshprotocols.cshlp.org/content/2008/1/pdb.rec11273.full?text_only=true. The information from the website is also pasted below:

Ringer's solution (pH 7.3-7.4)

Reagent (amount to add): NaCl (7.2 gm), CaCl2 (0.17 gm), KCl (0.37 gm).

Dissolve all reagents into reagent-grade H2O, and bring the final volume to 1 L. Adjust the pH to 7.3-7.4. Once thoroughly dissolved, filter through a 0.22-μm filter, aliquot into single-use volumes (25-50 mL), and autoclave.

The final salt concentration of the Ringer's solution is ~125 mM. 5 mM EDTA was also tested because plasma is often processed and stored in an anticoagulant such as EDTA.

*References*

(1) Thömmes, J.; Kula, M. R. *Biotechnol. Prog.* 1995, *11*, 357-367.

(2) Lukacs, G. L.; Haggie, P.; Seksek, O.; Lechardeur, D.; Freedman, N.; Verkman, A. *J. Biol. Chem.* 2000, *275*, 1625-1629.

(3) Wink, T.; de Beer, J.; Hennink, W. E.; Bult, A.; van Bennekom, W. P. *Anal. Chem.* 1999, *71*, 801-805.

(4) Kamm, R. C.; Smith, A. G. *Clin. Chem.* 1972, *18*, 519-522.

(5) Nagamine, K.; Hase, T.; Notomi, T. *Mol. Cell. Probes* 2002, *16*, 223-229.

*Author Contributions*

Contributions of non-corresponding authors:

Travis S. Schlappi:

Contributor to method/protocol development for capture experiments and in situ amplification experiments.

Major contributor to simulation and theory development.

Performed all simulations for Figures 1 and 2.

Developed protocol for DNA capacity measurements and performed all experiments for Figure 3.

Contributed to experiments and data accumulation for Figure 5.

Major contributor to outline, manuscript, and supporting information writing.

Major contributor to figure and manuscript revisions.

Made all figures and tables in the manuscript and supporting information.

Stephanie E. McCalla:

Major contributor to concept of chitosan-based flow-through capture and in situ amplification for low concentration detection.

Major contributor to method/protocol development for chitosan functionalization (hydrogel and monolayer), capture experiments, and in situ amplification experiments.

Major contributor to simulation and theory development.

Performed preliminary experimental work on in situ amplification and flow-through capture.

Performed preliminary simulations for Figure 1c.

Contributed to outline writing.

Contributed to manuscript revisions.

Nathan G. Schoepp:

Major contributor to method/protocol development for chitosan hydrogel synthesis.

Contributor to method/protocol development for capture experiments, and in-situ amplification.

Contributor to experiments and data accumulation for Figure 5.

Minor contributor to manuscript writing.

Minor contributor to manuscript revisions.

*Chapter V*

# Digital, ultra-sensitive, end-point protein measurements with large dynamic range via Brownian trapping with drift[4]

## Abstract

This paper shows that the concept of Brownian trapping with drift can be applied to improve quantitative molecular measurements. It has the potential to combine the robustness of end-point spatially-resolved readouts, the ultra-sensitivity of digital single-molecule measurements, and the large dynamic range of qPCR; furthermore, at low concentrations of analytes, it can provide a direct comparison of the signals arising from the analyte and from the background. It relies on the finding that molecules simultaneously diffusing, drifting (via slow flow) and binding to an array of non-saturable surface traps have an exponentially decreasing probability of escaping the traps over time, and therefore give rise to an exponentially decaying distribution of trapped molecules in space. This concept was tested with enzyme and protein measurements in a microfluidic device.

## Introduction

Digital single-molecule measurements,[1] such as digital PCR (dPCR)[2] and digital immunoassays,[3] compartmentalize molecules of the target analyte, and perform a detection reaction providing an "on" or "off" signal for each compartment (digital unit). Analyte concentration is then quantified by counting the signals and using a Poisson distribution. This methodology has been used in a wide range of applications to detect nucleic acids and proteins with ultra-sensitivity.[4]

---

One limitation of digital measurements is that the dynamic range (i.e. the range between the lowest and highest concentrations in a sample that can be measured) is limited by the number of digital units in the assay. Quantitative real-time PCR (qPCR), has a much wider dynamic range because input concentration is calculated as an exponential function of the qPCR output, however this method is less convenient than an end-point measurement. Dynamic range in dPCR can be increased by introducing very large numbers of digital units (compartments),[5] or using digital units of multiple sizes,[6] which increases the dynamic range by more than ~ 100 fold. However, the multivolume strategy is not as effective for digital immunoassays that lack the exponential amplification of PCR. One strategy to improve dynamic range for digital immunoassays involves combining the digital readout with the analog readout, which has increased the dynamic range from 2.5 logs to 4.1 logs.[7] Such improvement is desired, for example, in assays for the biomarker glial fibrillary acidic protein (GFAP) in traumatic brain injury.[8]

**Results and Discussion**

Our goal was to test whether it would be possible to combine into a single measurement (i) the high sensitivity of digital assays, in which individual molecules give rise to on/off signals (ii) the broad dynamic range (~ $10^8$) characteristic of a technique like qPCR, in which large changes in the input concentration give rise to logarithmically smaller changes in the output (Cq); in other words, input concentration is calculated as an exponential function of the output; and (iii) a readout in which the input number of molecules is quantified by an end-point spatial signal, which is more robust than the temporal signal from kinetic real time assays.[9]
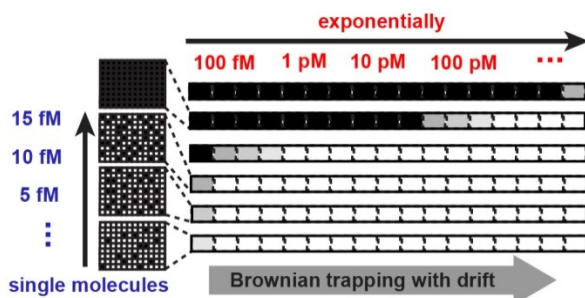
Figure 5-1. A conceptual schematic of a digital measurement using Brownian trapping with drift. This concept aims to combine the ultra-sensitivity of digital detection (shown in blue) with the broad dynamic range inherent in real-time PCR assays, in which large changes in the input concentration give rise to logarithmically smaller changes in the output (shown in red).

Here, we tested whether our goal could be reached by implementing the concept of Brownian trapping with drift[10] in a microfluidic device (Fig. 5-1). In Brownian trapping, target objects move by diffusion and are captured by traps of radius $\rho$ and trap density $v$. When Brownian trapping is combined with directional drift $U$ of the target objects[10], the probability of a target object eluding the traps, $P(t; U, v, \rho)$, decays exponentially at long times with decay rate $\lambda(U, v, \rho)$, a function of $U$, $v$, and $\rho$ (Eq. 1).[10c]

Eq. 1 $$P(t; U, v, \rho) \sim \exp(-\lambda(U, v, \rho) \cdot t)$$

This exponential decay only occurs when traps are not saturated by the targets during the experiment. This phenomenon has been analyzed mathematically in the context of charge carriers in semiconductors,[10a] diffusion-controlled reactions in the presence of a biasing field,[10d] and photoluminescence in the presence of electrical bias,[10b] but has not been applied to molecular analyses.

To test Brownian trapping in a digital immunoassay (Fig. 5-1), we envisioned the target object was a protein analyte molecule, and the traps were areas containing a capture reagent, such as an antibody. Traps were distributed on the channel surface, configured to act as

digital units, and grouped into regions (Fig. 5-2). We envisioned introducing drift using a gentle advective flow of solution through the microfluidic channel. Under these conditions, each trap provides a digital on/off readout (Fig. 5-2). At low concentrations, we hypothesized that most analyte molecules would be trapped at the beginning of the channel and concentration could be estimated using the conventional Poisson statistics of digital immunoassays.[3c] However, at high concentrations, we hypothesized that analyte concentration could be estimated using a spatial analogue of Eq. 1 (see S1).
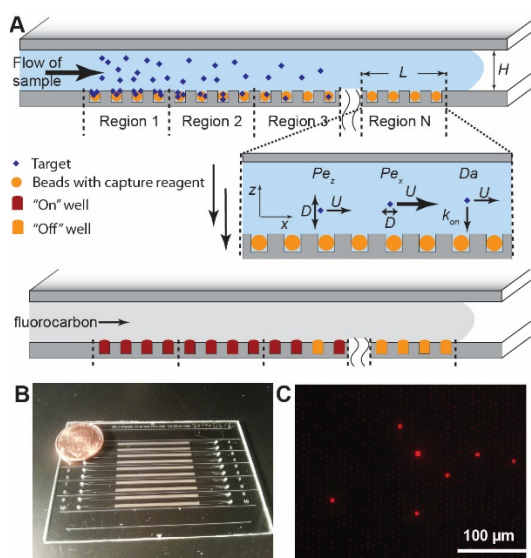


Figure 5-2. An experimental design to test the concept of digital measurements based on Brownian trapping with advective drift. (A) Schematic of the design, which features a shallow channel (50 µm) on top of an array of microwells. A bead (orange) coated with a capture reagent (e.g. an antibody), is placed in each microwell. The channel guides the flow of the sample over the microwells, and target molecules (blue) are captured by the beads. After labeling, the microwells are compartmentalized by fluorocarbon for digital readout. (B) A photograph of an assembled device with 10 parallel arrays. (C) A fluorescent image of the digital readout.

Our experimental design (Fig 5-2) satisfied four criteria arising from the concept of Brownian trapping with drift[10] (we have not optimized experimental parameters, instead choosing one experimentally convenient combination; see SI). (i) Drift should dominate over

diffusion of the protein target (diffusion coefficient $D \sim 10^{-11}$ m$^2$/s) along the flow direction $x$ (here, Péclet number $Pe_x = UL/D \sim 10^3$), with each region sufficiently long ($L \sim 10^{-3}$ m) and flow sufficiently high ($U \sim 10^{-5}$ m/s). Under these conditions, the exponential decay over time (Eq. 1) would be manifested as an exponential decay over space (Fig. 5-1), effectively converting temporal distribution into spatial distribution. (ii) At the same time, flow should be slow enough that diffusion of the protein from the top to the bottom of the channel ($H$) is not slower than flow over one region ($Pe_z = (U/L)/(D/H^2) \sim 2.5$); (iii) Each trap should have high binding capacity so it is not saturated by the targets during the experiment. Beads used for digital immunoassays[3,4a,4c,4d] satisfy this criterion. This criterion has not been met previously in innovative quantification approaches that flow a sample through a microfluidic channel to generate a density gradient on the channel surface.[11] In such experiments, the protein signal decayed linearly over channel length instead of exponentially. (iv) The Damköhler number $Da \sim k_{on}[Ab]L/U$, (estimated to be $\sim 1$, [Ab] is the concentration of the capture reagent) should be close to or greater than 1 to enable rapid capture of the target molecules once they diffuse to the traps.

We tested this concept experimentally using a glass SlipChip device[12] (Fig. 5-2B), which contained 10 parallel arrays created by dry-etching with C$_4$F$_8$, each containing 540,000 microwells grouped into regions. Each well was loaded with a single bead coated with a capture antibody. We took advantage of the relative movement of the two plates of the SlipChip to achieve uniform and near-complete bead loading. As the sample passed over the wells, the protein targets were trapped on the beads, rapidly depleting the target analyte from the flowing solution.
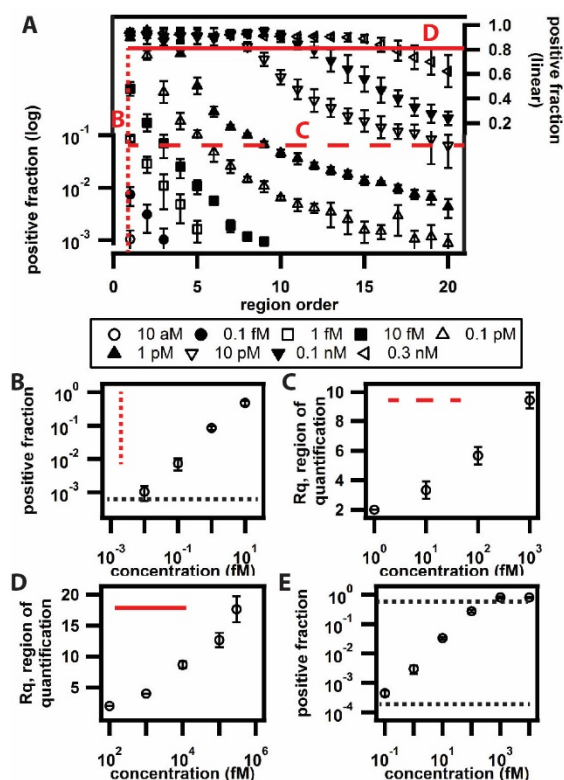
Figure 5-3. Experimental evaluation of the digital protein measurement with Brownian trapping with drift. A) Capture curves of biotinylated β-galactosidase with concentrations ranging from 10 aM to 0.3 nM. The red lines indicate data re-plotted in panels B, C, and D. B) A plot of the positive fraction of beads at the first region vs low analyte concentrations, from 9 aM to 20 fM. The dotted horizontal line represents the lower limit of quantification. C) A plot of Rq (region of quantification, threshold of 0.07 positive fraction) vs the logarithm of analyte concentration ranging from 1 fM to 1 pM. D) A plot of Rq (threshold of 0.8 positive fraction) vs the logarithm of analyte concentration ranging from 0.1 pM to 0.3 nM. E) A plot of the positive fraction of beads in the entire array in a standard digital protein assay at concentrations ranging from 0.1 fM to 10 nM. The dotted horizontal lines represent the upper and lower limits of quantification.

We first used a simple model system with biotin-modified β-galactosidase as the target analyte (3 μL samples in a range of concentrations) and streptavidin-coated beads as the capture agents. First, the enzyme solution was flown over the beads through the channel at a

velocity of 17 μm/s for 1 h. Then a solution of fluorogenic substrate resorufin β-D-galactopyranoside (RGP) was injected into the channel, immediately followed by a flow of FC40 to compartmentalize the beads in the microwells. Analyte concentration was estimated using the fraction of beads that captured at least one molecule (positive fraction of beads) [3,4a,4c,4d] (Fig. 5-3A). Analyte molecules were preferentially captured in the upstream regions, so low analyte concentrations were quantified by the positive fraction of wells located in the first capture region (Fig. 5-3B). We calculated the limit of detection (LOD) from three times the standard deviation of the experimentally measured background signal to be 9 aM. At higher concentrations, as is established,[7] we used a fraction of 0.8 as the practical upper limit, corresponding to 20 fM (Fig. 5-3B).

At high analyte concentrations, beads in the upstream regions contained many analyte molecules, precluding end-point digital quantification using those regions (we emphasize that beads, which could bind ~$10^5$ analyte molecules, were not expected to be fully saturated with analyte under those conditions). Analyte molecules were also captured in the downstream regions. As predicted, we observed that exponentially increasing analyte concentration gave rise to an approximately linear shift in the region where the capture curve crossed a threshold value of positive fraction (Figs. 5-3A, 5-3C, 5-3D). We refer to this region as Rq (region of quantification), analogous to Cq used in qPCR; its position depends on the value of the chosen threshold. Using a low threshold of 0.07 positive fraction (Fig. 5-3C) provided a dynamic range that overlapped well with the digital calibration curve (Fig. 5-3B) while extending it by ~ $10^2$ (above 1 pM). Using a high threshold of 0.8 positive fraction (Fig. 5-3D) further extended the dynamic range above 0.3 nM. The combined dynamic range was ~ 4 x $10^7$-fold, with a sensitivity of ~ 20 molecules in 3 μL.

For comparison, in an identical SlipChip device we performed a standard digital protein assay in which the whole solution was injected into the device rapidly and kept stationary during a 1 h incubation, followed by detection as described above. The calculated dynamic range in this stationary assay ranged from 0.02 fM to 0.5 pM, demonstrating a range of ~ 20,000-fold, and a sensitivity of ~ 30 molecules (Fig. 5-3E). Therefore, the digital

measurement based on Brownian trapping with drift showed similar sensitivity but a more than 1,000-fold improvement in dynamic range relative to the stationary digital assay in the same device.

We then tested how this approach performs in a more complex, clinically relevant immunoassay for a human protein target, TNF-α in a 25% serum. To streamline the multi-step ELISA protocol, we adopted a cartridge-with-spacers approach in which all reagents were loaded into a cartridge as plugs separated by FC40 fluorocarbon and air, then delivered into the channel[13] (Fig. 5-S3). We performed calibrations with 8 μL samples containing known TNF-α concentrations in buffered 25% bovine serum. The captured TNF-α molecules were then incubated with 6.5 nM biotinylated detection antibody for 1 h, followed by a 0.5 h incubation with 400 pM streptravidin-galactosidase conjugate and compartmentalization with fluorocarbon.
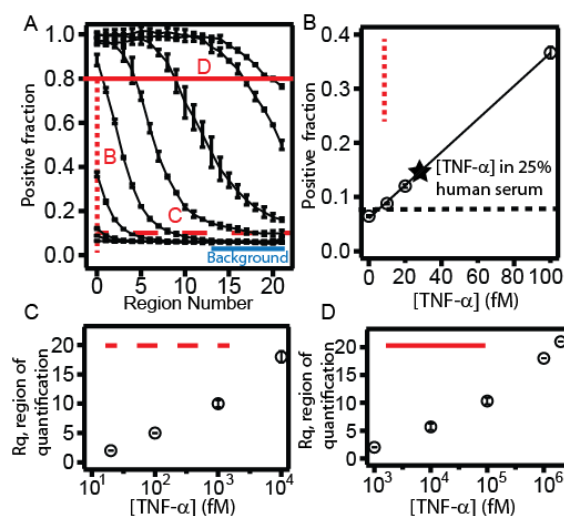


Figure 5-4. A test of digital measurements based on Brownian trapping with advective drift using human TNF-α. (A) Capture curves obtained from 25% bovine serum samples spiked with increasing concentrations of recombinant TNF-α. From bottom to top, curves represent TNF-α concentrations of 0 pM, 0.01 pM, 0.02 pM, 0.1 pM, 1 pM, 10 pM, 100 pM, 1,000 pM, and 2,000 pM. The blue line underlies the background signal level directly measured in the assays at low concentrations  (B) A plot of positive bead fraction at low concentration of

TNF-α corresponding to the vertical dotted red line in A. The dotted horizontal line represents the background signal + 3 S.D. The endogenous [TNF-α] in 25% pooled human serum is shown by the star symbol. C) A plot of Rq (region of quantification, threshold of 0.11 positive fraction) vs the logarithm of TNF-α concentration ranging from 20 fM to 10 pM.  D) A plot of Rq (threshold of 0.8 positive fraction) vs the logarithm of TNF-α concentration ranging from 1 pM to 2 nM.

The measurement preserved ultra-sensitivity, with an LOD of 6 fM (Fig. 5-4B). We used this measurement to determine the endogenous concentration of TNF-□ in pooled human serum, which is below the detection limit of a conventional ELISA.[14] The measured concentration was 0.031 ± 0.001 pM in 25% serum (Fig. 5-4B), which translates to 0.125 ± 0.004 pM in pure serum. This value is consistent with those determined previously using other single-molecule approaches.[4a,15] At higher concentrations, using a low threshold of 0.11 positive fraction (Fig. 5-4C) provided a dynamic range of ~$10^3$, and using a high threshold of 0.8 positive fraction (Fig. 5-4D) extended it to 2 nM, for a total dynamic range of ~300,000 fold. While this is wider than the dynamic range achieved previously by digital readout alone (~ 316-fold)[3c] or the digital and analog readouts combined (~ 13,000-fold),[7] it is smaller than the dynamic range obtained under the more ideal conditions with enzymes (Fig. 5-3).

**Conclusion**

We conclude that the concept of Brownian trapping with drift can be used for digital measurements of proteins that combine high sensitivity of digital assays with large dynamic range of qPCR but with an end-point readout. This combination of features has not been demonstrated previously and may be advantageous even for nucleic acid quantification. These findings justify performing future work to understand how combinations of values (and their variability) of $Pe_x$, $Pe_z$, $Da$, capture efficiency, flow control,[16] device design and assay chemistry impact assay performance, and enable the design of optimal assays for a given analyte. For example, given the similarity to qPCR, we anticipate lower resolution at higher concentrations where errors in determining the Rq parameter would lead to

exponentially larger errors in quantification. It remains to be tested whether methods analogous to those used in qPCR (e.g. the use of spatial or color multiplexing to introduce quantification controls and/or introduce parallel assays targeting multiple epitopes of the same target) could be used with this approach. The low sample consumption and the use of smaller numbers of wells per measurement with a given dynamic range (see S8) would make this approach compatible with spatial multiplexing and single-cell analysis.[17] Finally, we emphasize that at low concentrations of analyte the downstream regions provide a direct measurement of the background signal of the assay (Fig. 5-4A). This feature should be useful to improve assay fidelity.

**References**

(1) (a) Li, Z. H.; Hayman, R. B.; Walt, D. R. *J. Am. Chem. Soc.* **2008**, *130*, 12622. (b) Rissin, D. M.; Gorris, H. H.; Walt, D. R. *J. Am. Chem. Soc.* **2008**, *130*, 5349. (c) Rissin, D. M.; Walt, D. R. *J. Am. Chem. Soc.* **2006**, *128*, 6286. (d) Rondelez, Y.; Tresset, G.; Tabata, K. V.; Arata, H.; Fujita, H.; Takeuchi, S.; Noji, H. *Nat. Biotechnol.* **2005**, *23*, 361.

(2) (a) Vogelstein, B.; Kinzler, K. W. *Proc. Natl. Acad. Sci. U. S. A.* **1999**, *96*, 9236. (b) Sykes, P. J.; Neoh, S. H.; Brisco, M. J.; Hughes, E.; Condon, J.; Morley, A. A. *Biotechniques* **1992**, *13*, 444.

(3) (a) Walt, D. R. *Anal. Chem.* **2013**, *85*, 1258. (b) Chang, L.; Rissin, D. M.; Fournier, D. R.; Piech, T.; Patel, P. P.; Wilson, D. H.; Duffy, D. C. *J. Immunol. Methods* **2012**, *378*, 102. (c) Rissin, D. M.; Kan, C. W.; Campbell, T. G.; Howes, S. C.; Fournier, D. R.; Song, L.; Piech, T.; Patel, P. P.; Chang, L.; Rivnak, A. J.; Ferrell, E. P.; Randall, J. D.; Provuncher, G. K.; Walt, D. R.; Duffy, D. C. *Nat. Biotechnol.* **2010**, *28*, 595. (d) Shim, J. U.; Ranasinghe, R. T.; Smith, C. A.; Ibrahim, S. M.; Hollfelder, F.; Huck, W. T. S.; Klenerman, D.; Abell, C. *ACS Nano* **2013**, *7*, 5955. (e) Witters, D.; Knez, K.; Ceyssens, F.; Puers, R.; Lammertyn, J. *Lab Chip* **2013**, *13*, 2047. (f)  Kim, S. H.; Iwai, S.; Araki, S.; Sakakihara, S.; Iino, R.; Noji, H. *Lab Chip* **2012**, *12*, 4986.

(4) (a) Song, L. N.; Hanlon, D. W.; Chang, L.; Provuncher, G. K.; Kan, C. W.; Campbell, T. G.; Fournier, D. R.; Ferrell, E. P.; Rivnak, A. J.; Pink, B. A.; Minnehan, K. A.; Patel, P.

P.; Wilson, D. H.; Till, M. A.; Faubion, W. A.; Duffy, D. C. *J. Immunol. Methods* **2011**, *372*, 177. (b) Shen, F.; Davydova, E. K.; Du, W. B.; Kreutz, J. E.; Piepenburg, O.; Ismagilov, R. F. *Anal. Chem.* **2011**, *83*, 3533. (c) Chang, L.; Song, L. N.; Fournier, D. R.; Kan, C. W.; Patel, P. P.; Ferrell, E. P.; Pink, B. A.; Minnehan, K. A.; Hanlon, D. W.; Duffy, D. C.; Wilson, D. H. *J. Virol. Methods* **2013**, *188*, 153. (d) Randall, J.; Mortberg, E.; Provuncher, G. K.; Fournier, D. R.; Duffy, D. C.; Rubertsson, S.; Blennow, K.; Zetterberg, H.; Wilson, D. H. *Resuscitation* **2013**, *84*, 351. (e) Shen, F.; Du, W. B.; Kreutz, J. E.; Fok, A.; Ismagilov, R. F. *Lab Chip* **2010**, *10*, 2666.

(5) (a) Heyries, K. A.; Tropini, C.; VanInsberghe, M.; Doolin, C.; Petriv, O. I.; Singhal, A.; Leung, K.; Hughesman, C. B.; Hansen, C. L. *Nat. Methods* **2011**, *8*, 649. (b) Hatch, A. C.; Fisher, J. S.; Tovar, A. R.; Hsieh, A. T.; Lin, R.; Pentoney, S. L.; Yang, D. L.; Lee, A. P. *Lab Chip* **2011**, *11*, 3838.

(6) (a) Shen, F.; Sun, B.; Kreutz, J. E.; Davydova, E. K.; Du, W. B.; Reddy, P. L.; Joseph, L. J.; Ismagilov, R. F. *J. Am. Chem. Soc.* **2011**, *133*, 17705. (b) Kreutz, J. E.; Munson, T.; Huynh, T.; She, F.; Du, W.; Ismagilov, R. F. *Anal. Chem.* **2011**, *83*, 8158.

(7) Rissin, D. M.; Fournier, D. R.; Piech, T.; Kan, C. W.; Campbell, T. G.; Song, L. A.; Chang, L.; Rivnak, A. J.; Patel, P. P.; Provuncher, G. K.; Ferrell, E. P.; Howes, S. C.; Pink, B. A.; Minnehan, K. A.; Wilson, D. H.; Duffy, D. C. *Anal. Chem.* **2011**, *83*, 2279.

(8) Mayer, C. A.; Brunkhorst, R.; Niessner, M.; Pfeilschifter, W.; Steinmetz, H.; Foerch, C. *PLoS One* **2013**, *8*(4):e62101.

(9) Selck, D. A.; Karymov, M. A.; Sun, B.; Ismagilov, R. F. *Anal. Chem.* **2013**, *85*, 11129.

(10) (a) Grassberger, P.; Procaccia, I. *Phys. Rev. A* **1982**, *26*, 3686.(b) Dulea, M.; Aldea, A. *J Non-Cryst Solids* **1987**, *90*, 461. (c) Eisele, T.; Lang, R. *Probab. Th. Rel. Fields* **1987**, *74*, 125. (d) Sanchez, A. D. *Physica A* **2000**, *284*, 1.

(11) (a) Zhong, M.; Lee, C. Y.; Croushore, C. A.; Sweedler, J. V. *Lab Chip* **2012**, *12*, 2037. (b) Alino, V. J.; Sim, P. H.; Choy, W. T.; Fraser, A.; Yang, K. L. *Langmuir* **2012**, *28*, 17571. (c) Xue, C. Y.; Khan, S. A.; Yang, K. L. *Adv. Mater.* **2009**, *21*, 198. (d) Fosser, K. A.; Nuzzo, R. G. *Anal. Chem.* **2003**, *75*, 5775. (e) Wagner, P.; Zaugg, F.; Mitchink, M. U.S. Patent 20110124130A1, 2011.

(12) (a) Du, W. B.; Li, L.; Nichols, K. P.; Ismagilov, R. F. *Lab Chip* **2009**, *9*, 2286. (b) Huynh, T.; Sun, B.; Li, L.; Nichols, K. P.; Koyner, J. L.; Ismagilov, R. F. *J. Am. Chem. Soc.* **2013**, *135*, 14775. (c) Liu, W.; Chen, D.; Du, W.; Nichols, K. P.; Ismagilov, R. F. *Anal. Chem.* **2010**, *82*, 3276. (d) Sakakihara, S.; Araki, S.; Iino, R.; Noji, H. Lab Chip 2010, 10, 3355.

(13) (a) Zheng, B.; Tice, J. D.; Ismagilov, R. F. *Adv. Mater.* **2004**, *16*, 1365. (b) Linder, V.; Sia, S. K.; Whitesides, G. M. *Anal. Chem.* **2005**, *77*, 64. (c) Zheng, B.; Ismagilov, R. F. *Angew. Chem.-Int. Edit.* **2005**, *44*, 2520. (d) Chen, D. L.; Ismagilov, R. F. *Curr. Opin. Chem. Biol.* **2006**, *10*, 226.

(14) Martinez-Borra, J.; Lopez-Larrea, C.; Gonzalez, S.; Fuentes, D.; Dieguez, A.; Deschamps, E. M.; Perez-Pariente, J. M.; Lopez-Vazquez, A.; de Francisco, R.; Rodrigo, L. *Am J Gastroenterol* **2002**, *97*, 2350.

(15) Todd, J.; Simpson, P.; Estis, J.; Torres, V.; Wub, A. H. B. *Cytokine* **2013**, *64*, 660.

(16) Begolo, S.; Zhukov, D. V.; Selck, D. A.; Li, L.; Ismagilov, R. F. *Lab Chip* **2014,** published online Sept. 18, 2014, 10.1039/C4LC00910J.

(17) Han, Q.; Bagheri, N.; Bradshaw, E. M.; Hafler, D. A.; Lauffenburger, D. A.; Love, J. C. *Proc. Natl. Acad. Sci. U. S. A.* **2012**, 109, 1607.

**Supporting Information**

*Theoretical description and analysis*

Drift dominates the transport of analytes along a channel when the ratio of advection rate to diffusion rate is much greater than 1. The Péclet number characterizes this balance and is defined in the longitudinal direction as follows:

Eq. S1
$$Pe_x = \frac{advection\ rate\ in\ x}{diffusion\ rate\ in\ x} = \frac{U/L}{D/L^2} = \frac{UL}{D}.$$

In our experiment, the target analyte (protein) had a diffusion coefficient $D \sim 10^{-11}$ m$^2$/s, drift velocity $U \sim 10^{-5}$ m/s, and was flown past capture regions of length $L \sim 10^{-3}$ m, resulting in

$Pe_x \sim 10^3$. Thus, longitudinal transport of an analyte molecule and its distance traveled as a function of time, $x(t)$, can be formulated to ignore diffusion effects and depends only on drift velocity: $x(t) \approx Ut$. Replacing $t \approx x/U$ in Eq 1 converts the exponential decay over time into an exponential decay over space.

At the same time, flow should be slow enough that diffusion of the protein from the top to the bottom of the channel ($H$) is comparable relative to flow over one capture region. This ensures that analyte molecules aren't advected away before they have a chance to diffuse down to the capture beads. Again, the Péclet number formulates this comparison:

Eq. S2
$$Pe_z = \frac{advection\ rate\ in\ x}{diffusion\ rate\ in\ z} = \frac{U/L}{D/H^2}.$$

In our experimental setup, $H = 50$ µm, resulting in $Pe_z \sim 2.5$.

Finally, for trapping to be effective and give rise to an exponential decay in space, the capture rate of analyte molecules onto the beads must be comparable to the transport rate away from the beads, as shown by the Damköhler number:

Eq. S3
$$Da = \frac{capture\ rate}{transport\ rate\ in\ x} = \frac{k_{on}[Ab]}{U/L}.$$

In our experimental setup, $k_{on} \sim 10^5$ M$^{-1}$ s$^{-1}$, [Ab] $\sim 10^{-7}$ M, resulting in $Da \sim 1$.

*Origin of the exponential decay in space*

Exponential decay in space is reasonable because if capture efficiency in each region is constant, then connecting the regions in series will result in an exponential relationship between analyte molecules captured and region number

Replacing $t = n \cdot \Delta t$ in Eq. 1, Eq. S4 represents the number of free analyte molecules in solution that survive up until the exit of region $n$ ($n = 1,2,3 \dots$), where $\Delta t$ is the residence time over each region and $C_0$ is the initial amount of analytes.

Eq. S4
$$N_{free}(n) = C_0 e^{-\lambda n \Delta t}$$

Because the amount of captured molecules is simply the free molecules exiting the region subtracted from the free molecules entering the region, the capture efficiency can be calculated according to Eq. S5.

Eq. S5
$$\beta = \frac{\text{captured molecules in region } n}{\text{surviving molecules entering region } n}$$
$$= \frac{C_0 e^{-\lambda(n-1)\Delta t} - C_0 e^{-\lambda n \Delta t}}{C_0 e^{-\lambda(n-1)\Delta t}} = 1 - e^{-\lambda \Delta t}$$

Because $\lambda$ and $\Delta t$ are both constant for this assay, the capture efficiency is constant in each region.

If the capture efficiency is constant in each region and the regions are connected together in series, one would expect an exponential decay for the free analytes in solution because they are reduced by a factor of $\beta$ after each region. As long as there is an excess of capture antibodies, the capture process will only depend on the amount of free analytes in solution; thus, we also expect to see an exponential decay in captured analytes. In fact, solving Eq. S5 for the amount of captured analyte molecules in region $n$ directly reveals this exponential relationship between captured analyte molecules ($N_{captured}$) and region number $n$.

Eq. S6
$$N_{captured}(n) = \beta C_0 e^{-\lambda(n-1)\Delta t}$$

*Materials*

The paramagnetic beads for enzyme were Agilent LodeStar 2.7 Streptavidin (Agilent Technologies, Santa Clara, CA). The magnetic beads for TNF-α assays were Agilent

LodeStar 2.7 Carboxyl (Agilent Technologies), covalently attached to the antibody by standard coupling chemistry. β-galactosidase from *Escherichia coli* (G3153, Sigma-Aldrich, St. Louis, MO) was biotinylated using the Chromalink biotinylation reagent and diluted in Starting Block T20 PBS (Thermo Scientific, Waltham, MA ). Monoclonal anti-TNF-α antibody, recombinant TNF-α calibrator, and detection anti-TNF-α antibody were purchased from R&D Systems (Minneapolis, MN). The Streptavidin-β-galactosidase (SβG) conjugate and the enzyme substrate RGP were purchased from Life Technologies (Grand Island, NY). Pooled human serum was purchased from ValleyBiomedical (Winchester, VA). Bovine serum was purchased from Thermo Scientific (Waltham, MA). Fluorocarbon oils FC40 and FC3283 were obtained from 3M (St. Paul, MN). RfOEG (triethyleneglycol mono[1*H*,1*H*-perfluorooctyl]ether) was synthesized in the lab.

*Device fabrication*

Sodalime and borofloat glass plates coated with Cr and photoresist (Telic company, Valencia, CA) were used to fabricate the device. Standard photolithographic methods were used to transfer the designed pattern, including the microwells and channels, onto the glass plates. The photomask was designed using Autocad and then printed on a transparent film (CAD/Art Services, Bandon, OR) or a Cr mask (Photo sciences, Torrance, CA) (Figure 5-S1). A PDMS/glass adapter was used to connect the tubing to the device.

To fabricate the channels in the top plate of the device, we used a wet-etching method with hydrofluoric acid. Briefly, the back and side of the plate were taped to protect the bare glass from HF etching. Then the glass plates were immersed in HF etching solution at 40° C with continuous shaking. Photoresist/chrome served as the etching mask. All channels were etched to a depth of 50 µm. Typical etching rate under these conditions was 1.3 µm/min. After etching, plates were rinsed thoroughly with water to remove residual HF and blown dry with nitrogen. Remaining photoresist and the chromium layer were removed by acetone and chrome etchant. Through holes were drilled at both ends of the channels and then the plate was thoroughly cleaned with piranha solution. Finally, the plate was air plasma treated

for 100 s and subjected to gas-phase silanization using trichlorosilane (Tridecafluoro-1,1,2,2 –tetrahydrooctyl; Gelest Inc., Morrisville, PA) . Briefly, the vacuum in a glass desiccator was pumped down to 0.4 Torr at room temperature to facilitate the vaporization of fluorosilane, and then the chamber was closed for 1 h. Next, the plate was baked at 95° C overnight and rinsed by FC3283 to remove unbound silane. The plate was further baked for at least 30 min to complete the fluorosilanization procedure.

To fabricate microwells in the bottom half of the device for single-bead confinement, we used borofloat glass plates and a fluorine-based dry etching method with C4F8-based plasma. Briefly, the photoresist was removed from the glass plate following the photolithography step using acetone. The remaining Cr layer served as the dry-etching mask. The glass plate was mounted on a 6-in carrier wafer using thermogrease fomblin and subject to C4F8-based plasma etching (plasmalab 100, oxford instrument) under the following conditions: chamber pressure 10 mT, C4F8 flow rate 40 sccm, and ICP power 3000w. Typical etching rate under these conditions was 0.2–0.3 µm/min. Uniform single-bead loading per microwell is important for downstream digital readout and data interpretation using Poisson statistics. To improve etching uniformity across the plate, a two-step etching protocol was adopted. At the end of the first half of the etching step, the plate was removed from the chamber and subjected to a sonication-assisted wash to remove non-volatile residuals, such as sodium fluoride. Then the plate was rinsed by isopropanol and blown dry using nitrogen. The second half the etching step was performed with the plate rotated 180º to increase etching uniformity.

A hydrophilic surface chemistry in the microwell is also important for successful bead loading, as hydrophobic wells fail to load beads. We chose to functionalize the microwell surface with PEG-silane both to render it hydrophilic and prevent non-specific protein adsorption. To fabricate PEGlated microwells on a hydrophobic surface, the dry-etched plate was first briefly etched with diluted HF in a sonication batch to regenerate the glass surface in the etched microwells. Then, the microwells were PEG-silanized. Briefly, 150 µL silane were dissolved in 100 mL toluene and then 80 µL HCl was added in a dropwise manner while the mixture was sonicated. The mixture was further sonicated for 10 min before use.

The plate was immersed in this mixture and subjected to brief sonication to ensure wetting of the microwells. The plate was incubated at room temperature on a shaker for 1 h and washed sequentially by toluene and ethanol. Next, the plate was baked at 150° C for 30 min to finish the PEG silanization procedure. To protect the PEG chemistry in the etched microwells from downstream fluorosilanization, sacrificial resist was used to preserve the surface chemistry. The plate was spin-coated with a negative photoresist NR9-3000PY (Futurrex, Franklin, NJ) and baked. Then the plate was flipped and exposed to UV light using the Cr as an embedded mask. The photoresist was developed according to manufacturer's protocol. Next, the chrome layer was removed using chrome etchant. The plate was thoroughly rinsed by water and baked at 95° C for 30 min to dry. The plate was then air plasma treated and fluorosilanized using the protocol outlined above. Finally, the sacrificial photoresist was removed in hot DMSO (110° C, 10 min). The surface outside of the microwells functionalized with fluorinated silane is fluorophilic. This combination of hydrophilic and fluorophilic surface chemistry allows the microwells to be easily compartmentalized for downstream digital readout by simply flowing fluorocarbon oils over the microwells.

To fabricate the PDMS/glass adapter, access holes were first drilled on a sodalime glass plate to match the inlet ports on the top half the device. A PDMS slab with matching access holes was then plasma-bonded to the glass plate. The complete adapter was plasma treated for 100 sec and fluorosilanzed following the procedure outlined above.

*Device operation and bead loading*

The bottom half of the device was briefly sonicated in water to pre-wet the microwells. A wet cleanroom wipe was used to cover the regions of microwells. Then 100 µL of FC40 containing 0.4 mg/ml fluoro-surfactant RfOEG was applied to the plate along the cloth edge and the top half of the device was assembled. The wipe was gently pulled out from the gap and the additional FC40 was injected into the channels using manual pipettes. At this stage, the device is ready for bead loading.

Capture reagent-coated magnetic beads were stored in starting block PBS solution at 4° C. Prior to use, the beads were concentrated to 75 mg/ml in the same buffer and then 2-3 µL of the bead slurry was injected to the channel. Next, the device was held on the edge of a magnet so that the channel axis aligned with the magnet edge and the beads in the channel were pulled uniformly toward the channel side. While held on the magnet, the top glass plate was gently slipped away from the magnet and the beads were physically scraped against the magnetic pulling force. As a result, the beads were actively pulled into the well while the unloaded beads were removed from the surface.  By using concentrated bead slurry and repeating the loading procedure, both high loading efficiency and uniformity in bead loading across the chip were obtained. Typical loading efficiency was >90%. The unloaded beads were collected, washed, and stored in TPBS for future use. Next, the device was manually aligned under a stereoscope so that the channels on the top plate aligned with the microwell features on the bottom. A PDMS/glass adapter was then used to connect Teflon tubing to the device inlets. The tubing contained the following solution sequence: FC40, 0.5 µL air, 2 µL FC40 and then 5 µL washing buffer (PBS with 0.05 % Tween-20). The solution sequence was pumped through the channel at a rate of 0.5ul/min to remove any loose beads. The microwells were finally resealed by FC40 and the device was stored on ice until use.

*Digital measurements of enzyme*

Test solutions of biotinylated β-galactosidase were prepared by diluting in TPBS with 1 mM MgCl$_2$. The solutions of 3 µL are either (i) directly pipetted into the device and incubated for an hour; or (ii) gently aspirated into Teflon tubings and then delivered to the channels at 0.05 µL/min for 1 h, controlled by a syringe pump equipped with a multi-syringe rack. The device is then washed with 30 µL PBS with 0.05 % Tween-20 per channel. The device then is loaded with 100 mM RGP in PBS with 0.05 % Tween-20 and 1 mM MgCl$_2$, and digitized by flowing FC40 into the channels. The device was imaged after 15 minutes.

*Digital measurements of TNF-α*

Standard ELISA procedure was followed to perform the on-chip digital immunoassay for TNF-α. Syringe pump and Teflon tubing preloaded with washing buffer and other reagent solution were used to deliver the solution to the device. In addition, the assay was performed on a magnet to minimize bead loss.

Specifically, the calibrator sample were prepared in 25% bovine serum to 75% TPBS buffer. 25% pooled human serum sample was similarly prepared to measure the endogenous concentration of TNF-α. The antibody and β-galactosidase -streptavidin conjugate was diluted in TPBS. The washing buffers were 1x and 5x PBS containing 0.1% Tween-20 (1x PBST and 5x PBST). The solutions was preloaded into Teflon tubing and delivered to the 10 channels on the device simultaneously using a syringe pump equipped with a multi-syringe rack. The flow rate was 2 µL/min except at 0.1 µL/min for the sample plug. Throughout the assay, as multiple air-aqueous, air-oil and aqueous-oil interfaces migrated through the bead-loaded regions, the device was kept on a magnet to minimize bead loss. Solution sequence was stopped during incubation with detection antibody and enzyme conjugate and then resumed subsequently. The second (b) and third (c) solution sequences were pumped through the device from the opposite direction of the first solution sequence (a) to avoid potential cross-contamination of target analytes between regions. Details of the solution sequences were as follows (also see Fig. 5-S3):

a. FC40, 0.5 µL air, 2 µL FC40, 2 µL 5x PBST, 0.5 µL air, 4 µL 5x PBST, 0.5 µL air, 2 µL 1x PBST, 0.5 µL air, and 8 µL serum sample.

b. FC40, 0.5 µL air, 2 µL FC40, 3 µL 5x PBST, 0.5 µL air, 3 µL 5x PBST, 0.5 µL air, 4 µL biotinylated detection antibody, 0.5 µL air, 4 µL 1x PBST.

c. FC40, 0.5 µL air, 2 µL FC40, 2 µL enzyme substrate, 0.5 µL air, 3 µL 1x PBST, 0.5 µL air, 5 µL 5x PBST (total 5 repeats), 4 µL streptavidin-galactosidase conjugate, 0.5 µL 1x PBST. All aqueous solutions were supplemented with 1 mM $MgCl_2$ to enhance the enzyme activity of β-galactosidase.

The total assay time takes ~ 6 h. Specifically, it takes ~0.5 h for bead loading, ~2 h for sample delivery for a volume of 8 µL, 1 h for incubation with a detection antibody, 0.5 h for incubation with streptavidin-galactosidase, ~0.5 h for washing, and ~1.5 h for incubation with substrate and subsequent imaging.

*Image acquisition and analysis*

Fluorescence images were acquired in TexasRed and GFP channels on an inverted microscope equipped with a 0.63x camera adapter and a digital CCD camera using the autofocus function to enhance quality. Positive bead count and total bead count were analyzed based on threshold fluorescence intensity and morphological criteria. The image acquisition, processing, and analysis were all performed using MetaMorph software (Molecular Devices, Sunnyvale, CA).

Specifically, the acquired images were digitally processed and analyzed using the following sequence in Metamorph: (a) subtract the uniform background arising from the dark current of the camera; (b) flatten the field of view to remove the bias in fluorescent intensity resulting from non-uniform illumination; (c) apply "No Neighbors" function in Metamorph to reduce the haze effect and improve contrast.

Next, the selection and quantification of positive beads were automatically performed using the Metamorph function of "threshold image" and "integrated morphometry analysis" based on the following criteria: (a) Fluorescence intensity > 500 (Figure 5-S5A); (b) "Area" range for inclusion: 2-50 pixels; (c) "Shape factor" range for inclusion: 0.9-1 inch. Finally, the correct selection of positive beads was confirmed visually.

*Achieving a given dynamic range with fewer wells in digital assay with drift relative to a standard digital assay*

The Brownian trapping with drift format achieves a larger dynamic range with fewer wells than a standard digital format. This can potentially be useful in single cell analysis, and in multiplexed assays, where one wants each cell to use as few wells as possible in order to fit them all onto a chip. As an example, consider the theoretical calculation of dynamic ranges for a standard digital assay with 5000 wells compared to a digital assay with drift as described in this manuscript, but only containing 150 wells. The volume of sample analyzed is 5 $\mu L$ and each well in both formats has a volume of 1 nL. Labeling efficiencies and background effects are ignored as this is a simplified model intended to compare the dynamic ranges, not predict actual outcomes.

*Standard digital assay*

LDL is the lower detection limit and is defined as the concentration which would have a 95% chance of generating a least one positive well and equals the concentration calculated from three positive wells [1]. To calculate the concentration from three positive wells, one uses Eq. 2 from Reference [1], which is derived from the Poisson distribution.

$$\text{Eq. S7} \qquad LDL = -\frac{\ln\left(\frac{w-3}{w}\right)}{v}$$

For $w = 5000$ wells and a well volume $v = 1$ nL, $LDL = 0.6$ molecules/$\mu$L.

ULQ is the upper limit of quantification and is defined as the concentration which would have a 95% chance of generating at least one negative well and equals the concentration calculated on the basis of three negative wells [1].

$$\text{Eq. S8} \qquad ULQ = -\frac{\ln\left(\frac{3}{w}\right)}{v}$$

For $w = 5000$ wells and a well volume $v = 1$ nL, $UQL = 7.42 \cdot 10^3$ molecules/$\mu$L. Thus, the dynamic range, $ULQ/LDL$, is $10^{4.09}$.

*Digital assay with drift*

The dynamic range of a digital assay with drift depends on how many regions there are, the capture efficiency of each region ($\beta$), and the number of wells in each region. Consider a microfluidic chip with 15 regions, 10 wells in each region, and a capture efficiency of 25%. The LDL for the drift assay can be calculated by asking what concentration one must start with in order to have three positive wells in the whole device. At the completion of the assay, the total amount of captured analyte molecules is simply the analyte molecules escaping region 15 (calculated with Eq. S4) subtracted from the initial amount, $C_0$.

Eq. S9 $$N_{captured} = C_0 - C_0 e^{-15\lambda\Delta t}$$

Setting Eq. S9 equal to Eq. S7 with $w = 150$ and $v = 1$ nL yields $C_0 = LDL = 20.5$ molecules/$\mu$L.

The ULQ for the drift assay can be calculated by asking what concentration one must start with in order to have three negative wells in the final region (the preceding regions will all be saturated). The amount of captured analyte molecules in the 15$^{th}$ region is found from Eq. S6.

Eq. S10 $$N_{captured}(15) = \beta C_0 e^{-\lambda\Delta t(15-1)}$$

Setting Eq. S10 equal to Eq. S8 with $w = 10$ and $v = 1$ nL yields $C_0 = UQL = 2.70 \cdot 10^5$ molecules/$\mu$L. Thus, the dynamic range is $10^{4.12}$, which is comparable to the dynamic range of the standard digital assay, but with only 150 wells instead of 5000.

*Author contributions*

W.L., S.G., and R.F.I. designed the SlipChip experiments. W.L., S.G. performed experiments and data analysis. T.S., W.L., S.G. performed theoretical analysis. W.L., S.G., T.S. and R.F.I. wrote the paper.

S.G. performed the dry-etching.

S.G. and W.L. fabricated devices.

W.L. performed the measurements for Fig. 3.

S.G. performed the measurements for Fig. 4.

W.L. and T.S. performed the COMSOL simulation for plots in Figure S6.

*Reference*

[1] Jason E. Kreutz, Todd Munson, Toan Huynh, Feng Shen, Wenbin Du, and Rustem F. Ismagilov, "Theoretical Design and Analysis of Multivolume Digital Assays with Wide Dynamic Range Validated Experimentally with Microfluidic Digital PCR," Analytical Chemistry 2011 83: 8158-8168.

A. Photomask for microwells
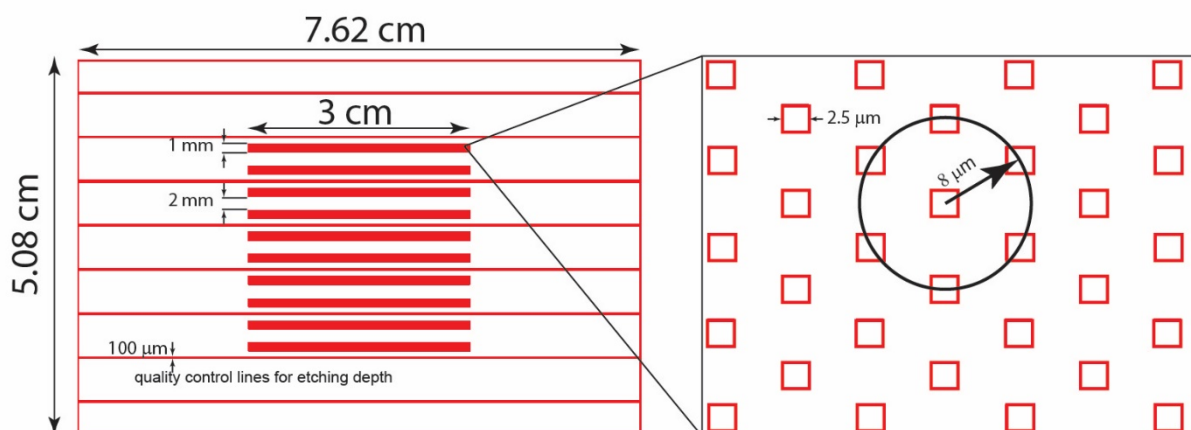


B. Photomask for channels
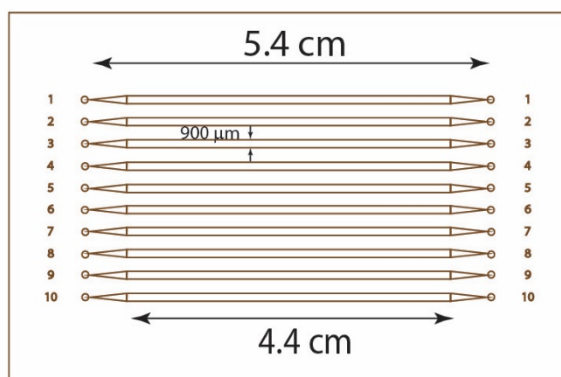


Figure 5-S1. Photomask design. (A) Each channel contains a total of 541,250 microwells (125 vertical x 4330 horizontal), arranged in a hexagonal pattern with a center-to-center spacing of 8 µm. Channels were divided into 22 regions, each of which consisted of 24,604 microwells. Horizontal stripes with a width of 100 µm were included to control the etching depth and uniformity across the chip. (B) Channels were arranged to precisely match the microwell features. An etching depth of 50 µm by isotropic HF etching yields an actual channel width of 1,000 µm."

A.

B.

C.

D.
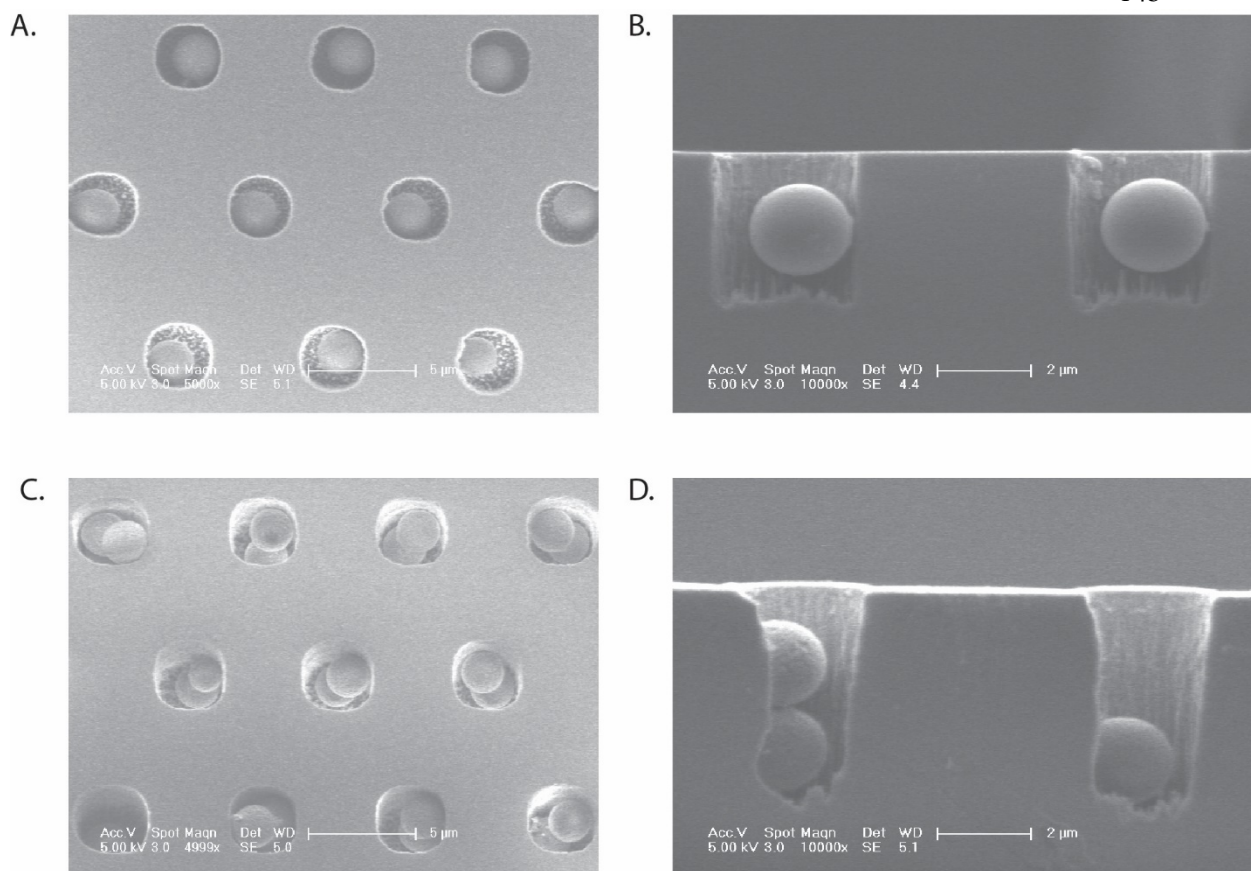
Figure 5-S2. Etching profile examined by SEM. Etching depth needs to be precisely controlled to confine single beads (A and B). The dimension for the etched microwells is approximately 3 µm in diameter and 3 µm in depth, just enough to accommodate a single 2.7 µm bead. Over-etched microwells (C and D) can load more than one bead and thus were not used in the experiment.

A.



FC40    Air         5x PBST    1x PBST         Serum sample

B.



Biotinylated
detection Ab

C.



substrate                          5x         Streptavidin-
                                              galactosidase
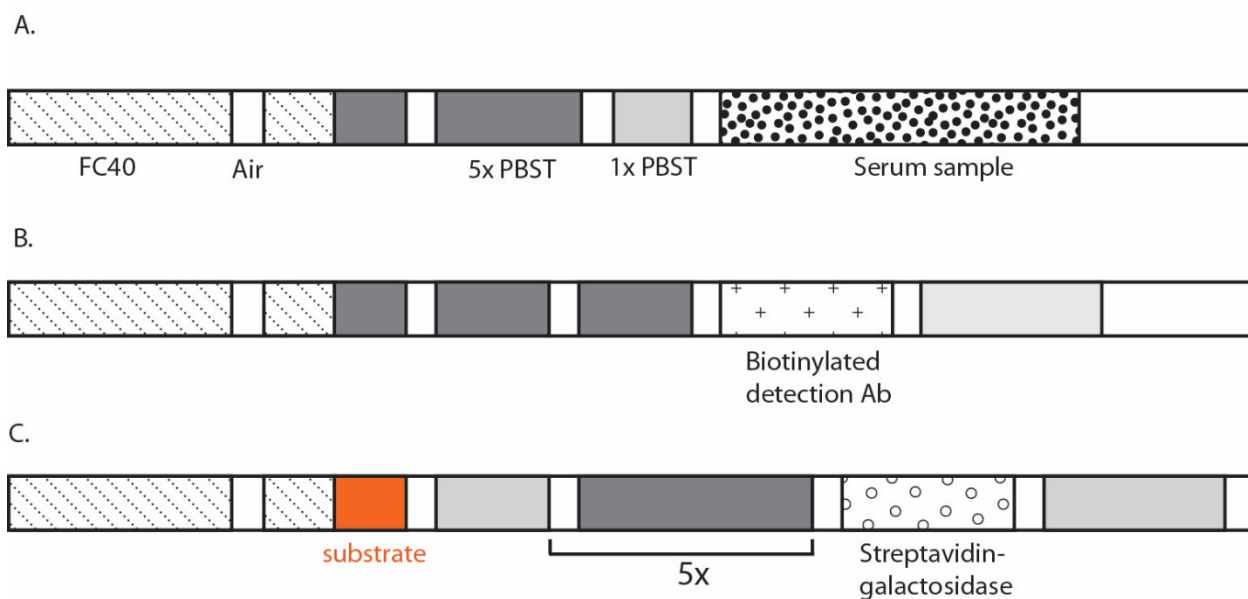
Figure 5-S3. Solution sequences used for on-chip immunoassays. Solutions were loaded in Teflon tubing with air spacers and infused into channels using a syringe pump at a controlled flow rate. See experimental section for solution volumes.
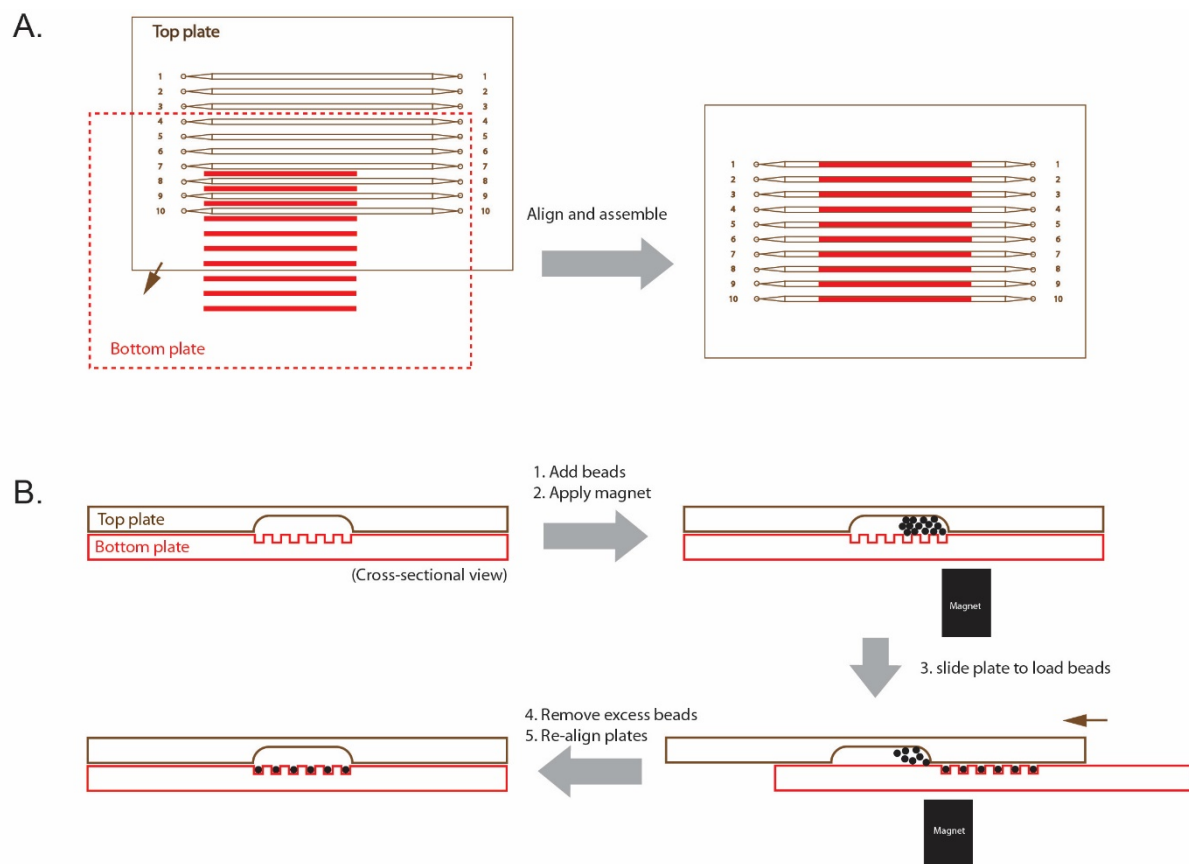
Figure 5-S4. Device assembly and operation to perform the on-chip digital assay. (A) Two complementary microfluidic plates were assembled and aligned with the etched features facing each other. (B) The bead slurry was injected into the channels and then loaded into the microwells using a magnet and a slipping motion. Excess beads were removed and the plates were realigned.
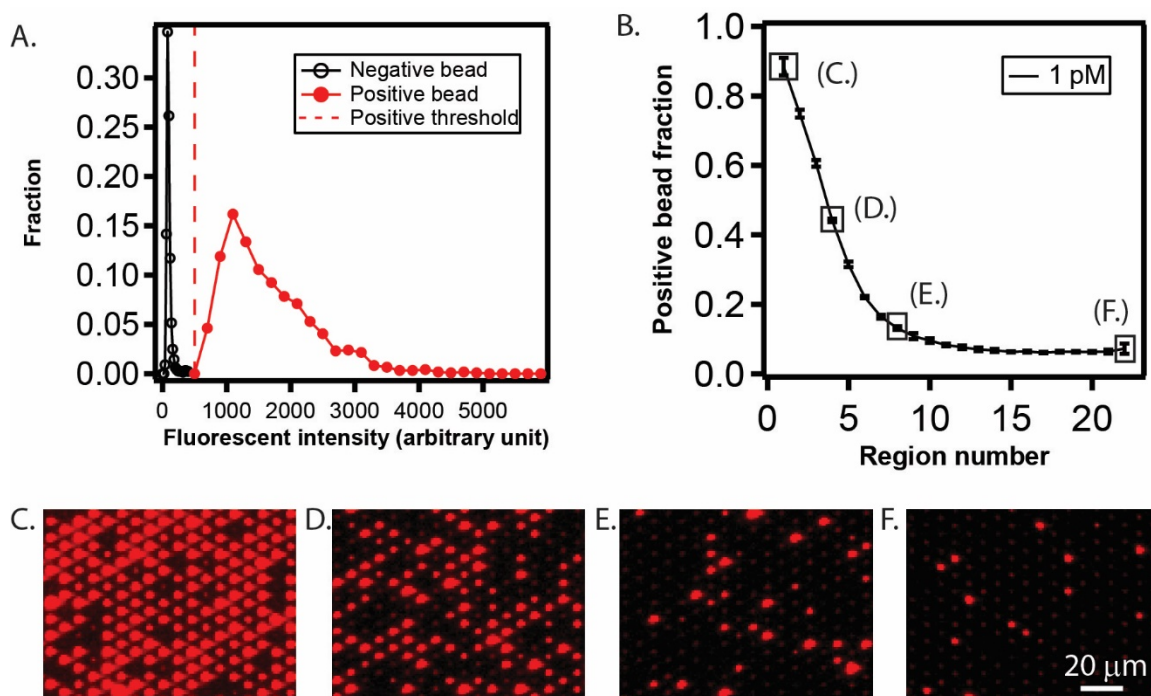
Figure 5-S5. Experimental results and analysis. (A) Histogram of average fluorescence intensity for negative and positive bead fractions. Fluorescence signals ("positive" beads) that arise from enzymatic activities are clearly differentiated from the background fluorescence signal ("negative" beads) and provides the justification of a fluorescence intensity threshold of 500 a.u. (red dashed line). (C-F) Characteristic readout images acquired at different positions (region numbers) along the channel for the 1.0 pM curve from Figure 5-4.
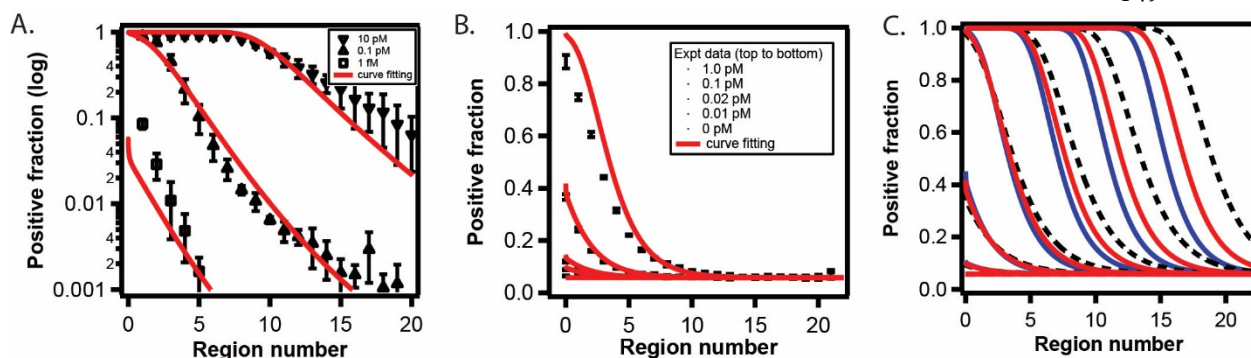
Figure 5-S6. (A) Curves of best fit for Figure 5-3. The surface concentration of the captured enzyme molecules was simulated using COMSOL Multiphysics, based on a transport-and-adsorption model. A 2D channel was built and meshed with a height of 50 μm and a length of 4 cm. The surface concentration of the capture agent was $1.4 \times 10^{-9}$ mol/m$^2$; the diffusion coefficient was $0.25 \times 10^{-10}$ m$^2$/s; the flow velocity was 17 μm/s; and the reaction time was 3600 seconds. The $k_{on}$ for a mono-biotin-labeled enzyme and the streptavidin coated on beads was assumed to be $1.6 \times 10^5$ M$^{-1}$ s$^{-1}$; and it was assumed that the total $k_{on}$ is proportional to the number of biotin labeled to the enzyme, which follows a Poisson distribution with an average labeling ratio of 7.9. The $k_{off}$ was assumed to be $5 \times 10^{-9}$ s$^{-1}$. The surface concentration of the captured enzyme molecules was converted to positive fraction of beads assuming 625,000 beads were loaded. (B) Curves of best fit for the data in Figure 5-4. Simulation for the concentration of the target molecules was performed similarly as above, with parameters as follows: channel height was 50 μm; channel length was 3 cm; surface concentration of capture antibody was $3.75 \times 10^{-9}$ mol/m$^2$; $k_{on}$ was $2 \times 10^5$ M$^{-1}$ s$^{-1}$; $k_{off}$ was $8 \times 10^{-7}$ s$^{-1}$; the diffusion coefficient was $0.9 \times 10^{-10}$ m$^2$/s; flow velocity was 33 μm/s; and reaction time was 4800 seconds. The surface concentration of the captured target molecules was multiplied by a labeling efficiency of 4%, converted to a positive fraction of beads assuming 540,000 beads, then added to the experimental measured background of 0.06 (positive fraction of beads). Given the complexity in the experiment including the matrix effect in the serum, heterogeneous activities of molecules, and non-specific binding, the theoretical fit to experimental data ranging from 0 pm to 1.0 pM was remarkable. The fits deviate from experimental data for the high concentration range (>1.0 pM, not shown) and the origin of the deviation will be a subject for future investigation. (C) Impact of drift velocity, and thus

capture efficiency, on assay performance. The concentration series from bottom to top is 0 pM, 0.01 pM, 0.1 pM, 1 pM, 10 pM, 100 pM and 1000 pM. For each concentration condition, three drift velocities were simulated, represented by the blue (30 µm/s for 5400 s), red (as in B, 33 µm/s for 4800 s), and dashed lines (38 µm/s for 4200 s). The impact of the drift velocity on the position of the curves, thus the spatial distribution of the trapped analytes along the channel, is more substantial for the high concentration conditions. As a result, the drift velocity will have a more pronounced effect on the dynamic range of the assay than the sensitivity.

*Chapter VI*

# Localization of Short-Chain Polyphosphate Enhances its Ability to Clot Flowing Blood Plasma[5]

**Abstract**

Short-chain polyphosphate (polyP) is released from platelets upon platelet activation, but it is not clear if it contributes to thrombosis. PolyP has increased propensity to clot blood with increased polymer length and when localized onto particles, but it is unknown whether spatial localization of short-chain polyP can accelerate clotting of flowing blood. Here, numerical simulations predicted the effect of localization of polyP on clotting under flow, and this was tested *in vitro* using microfluidics. Synthetic polyP was more effective at triggering clotting of flowing blood plasma when localized on a surface than when solubilized in solution or when localized as nanoparticles, accelerating clotting at 10–200 fold lower concentrations, particularly at low to sub-physiological shear rates typical of where thrombosis occurs in large veins or valves. Thus, sub-micromolar concentrations of short-chain polyP can accelerate clotting of flowing blood plasma under flow at low to sub-physiological shear rates. However, a physiological mechanism for the localization of polyP to platelet or vascular surfaces remains unknown.

**Introduction**

PolyP is an activator of blood coagulation through its ability to accelerate the activation of coagulation factors XII, XI, and V1,2, and by abrogating tissue factor pathway inhibitor

---

(TFPI) function3,4. Long-chain polyP (hundreds to thousands of residues long) appears to be a much more potent activator of clotting, via activation of factor XII and the contact pathway, than short-chain polyp5–7. Short-chain polyP (60–100 phosphate residues long) is found in dense granules of human platelets and granules of mast cells (acidocalcisomes) and released upon their activation, while long-chain polyP occurs in microbes and some mammalian cells, such as in prostate cancer7–10. A characteristic of long-chain polyP is its ability to aggregate into particles, and this spatial localization may possibly contribute to its propensity to accelerate clotting11. It is less clear if there is a pathophysiological role for polyP released from human cells in thrombosis3. Short-chain endogenous polyP facilitates activation of FXII *in vitro*, albeit at supraphysiological concentrations12. It can also contribute to clotting *in vitro* under flow when tissue factor (TF) is present13. It is well-known that the local concentration of activators can profoundly influence their ability to initiate the clotting of blood14. Localization of polyP onto particles also accelerates coagulation under stagnant conditions15. Thus, we hypothesized that short-chain polyP may be a more effective activator when spatially

localized onto surfaces, capable of accelerating clotting of flowing blood *in vitro* without participation of TF.

Initiation of blood coagulation is triggered when the local concentration of activators reaches a critical threshold, upon which the proteolytic cascade amplifies the local concentration of active enzymes to form a cross-linked fibrin mesh16,17. The spatial localization of activators to surfaces effectively increases their local concentration, allowing coagulation to be triggered with less total amount of activator18,19. Several activators have displayed this effect of spatial localization in microfluidic models of clotting, including TF, glass, and bacteria that activate prothrombin and factor X20. Flow influences coagulation in a variety of ways and enhances the effects of spatial localization21. Flow continuously strips clotting factors from catalytic surfaces, preventing activators from achieving a critical threshold and ultimately preventing clot initiation22,23. To accelerate clotting of flowing blood, greater amounts of activator need to be localized in order to achieve a higher local concentration24. In this study, we used numerical

simulations and a microfluidic model of thrombosis to investigate whether the ability

of localization to enhance clotting extends to short-chain polyP *in vitro* under flow. The

shear rates used in this study range from low to sub-physiological (i.e. pathological) shear.

These low shear rates mimic those typical of where thrombosis

occurs in large veins and valves, such as in deep vein thrombosis (DVT) or those associated

with airplane economy class syndrome[25–30]. This microfluidic model of thrombosis

enabled clotting of plasma, or lack thereof, to be monitored over many hours in the absence

of TF. In contrast to coagulation that occurs from acute injury to vessels, such as from

puncture that exposes large amounts of TF, thrombosis may initiate over longer periods of

time and can be potentiated by factor XII[2,31–35]. Our experiments were designed to

determine if localization of physiologically-relevant concentrations of platelet-length

polyP could contribute to coagulation *in vitro* at low to sub-physiological shear, but they

do not validate whether or not localization of platelet-length polyP contributes to

thrombosis *in vivo*.


**Results**


**Numerical simulations predict the localization of polyP will increase its coagulability at low shear rates.** To initially examine how localizing polyP onto surfaces affects thrombin generation, we used a two-dimensional numerical simulation that considered diffusion, convection, and the rates of 41 reactions of the coagulation cascade (Supplementary Tables 6-S1–3). An established kinetic model for the coagulation cascade was used with the addition of polyP>1000 in three reactions that were previously characterized in kinetic assays[1,4,5,7,20]. PolyP was either spatially localized onto the surface of a cylindrical channel or dispersed throughout its volume. Shear rates were from $1 \text{ s}^{-1}$ to $120 \text{ s}^{-1}$, a range that encompasses sub-physiological shear rates ($< \sim 10 \text{ s}^{-1}$) and shear rates in the inferior vena cava, venous valves, and large veins[25–27,36]. When polyP was localized onto the surface of the channel with a shear rate of $1 \text{ s}^{-1}$, the local thrombin burst was 782-fold higher than when an equal amount of polyP was dispersed throughout the volume ($1.83 \times 10^{-8}$ M versus $2.34 \times 10^{-11}$ M) (Fig. 6-1A). The amount of polyP in

the simulations was $7.54 \times 10{-}9$ mol, which equates to 30 μ M (with respect to phosphate monomer) when the total volume of the simulation was considered. The resulting thrombin burst was a consequence of the higher local concentration of polyP, which led to increased positive feedback from the coagulation cascade. Simulations showed that differences in thrombin generation persisted over various shear rates, up to 60 s−1 (Fig. 6-1B). However, at a set distance, the difference decreased as shear rate increased, because thrombin was rapidly transported down-stream.
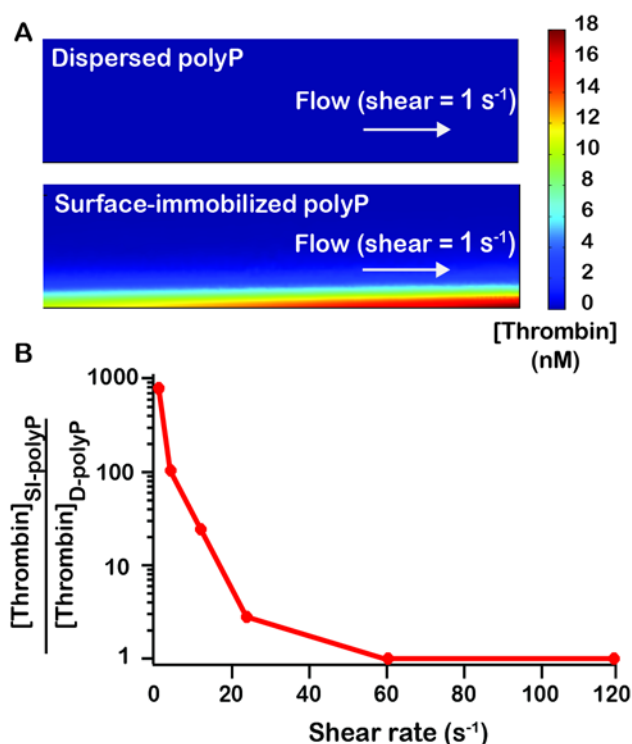


**Figure 6-1. Numerical simulations predict localization of polyP accelerates thrombin production at low shear rates.** Two-dimensional numerical simulations of the human blood coagulation cascade, comparing the generation of thrombin by polyP dispersed throughout a cylindrical channel versus polyP immobilized on the channel surface. The channel was 20 mm long with a radius of 2 mm. The overall number of polyP molecules was the same in all simulations ($7.54 \times 10{-}9$ moles). (**A**) Plots show [thrombin], which is the sum of concentrations of thrombin and meizothrombin, for a two-dimensional longitudinal cut of the cylinder at 500 s into the simulation. (**B**) The fold difference in the

maximum [thrombin] generated in the channel when polyP was surface-immobilized (SI-polyP) versus dispersed (D-polyP) at varying shear rates.

**Surface-immobilized polyP accelerates clotting of flowing blood plasma.** To determine if SI-polyP was able to accelerate clotting of flowing blood plasma, synthetic polyP400 was immobilized onto the walls of microfluidic channels (Fig. 6-2A). Half of each chamber was patterned with biotinylated lipids followed by an excess of streptavidin (Fig. 6-2B). Biotinylated-polyP400 was then flowed through the channel, becoming immobilized onto streptavidin. The surface concentration of SI-polyP400 was varied by diluting biotinylated-polyP400 in a solution of biotin-PEG before coating the channel. The concentration of polyP was determined by DAPI staining.

Fluorescence intensities from known concentrations of stained D-polyP, which was soluble and dispersed throughout the channel, were used to generate a standard curve and used to calculate the surface concentration of SI-polyP (Fig. 6-2C). The surface concentration of SI-polyP was 300 nmol/m2, and could be decreased to 60 nmol/m2 by diluting with biotin-PEG. To test the ability of patterned polyP to induce clotting, platelet-poor human plasma was flowed through the chambers. Based on the simulation data, we tested the lowest shear (1 s−1) as it was predicted to have the largest effect on thrombin generation and therefor clotting. A range of shear rates are explored in later experiments. The plasma clotted selectively on areas with immobilized polyP400 (300 nmol/m2) in 50–70 min at a shear rate of 1 s−1. No clotting was observed over 5 hr in channels without polyP400 (Fig. 6-2D). All polyP concentrations are reported in terms of phosphate monomer.
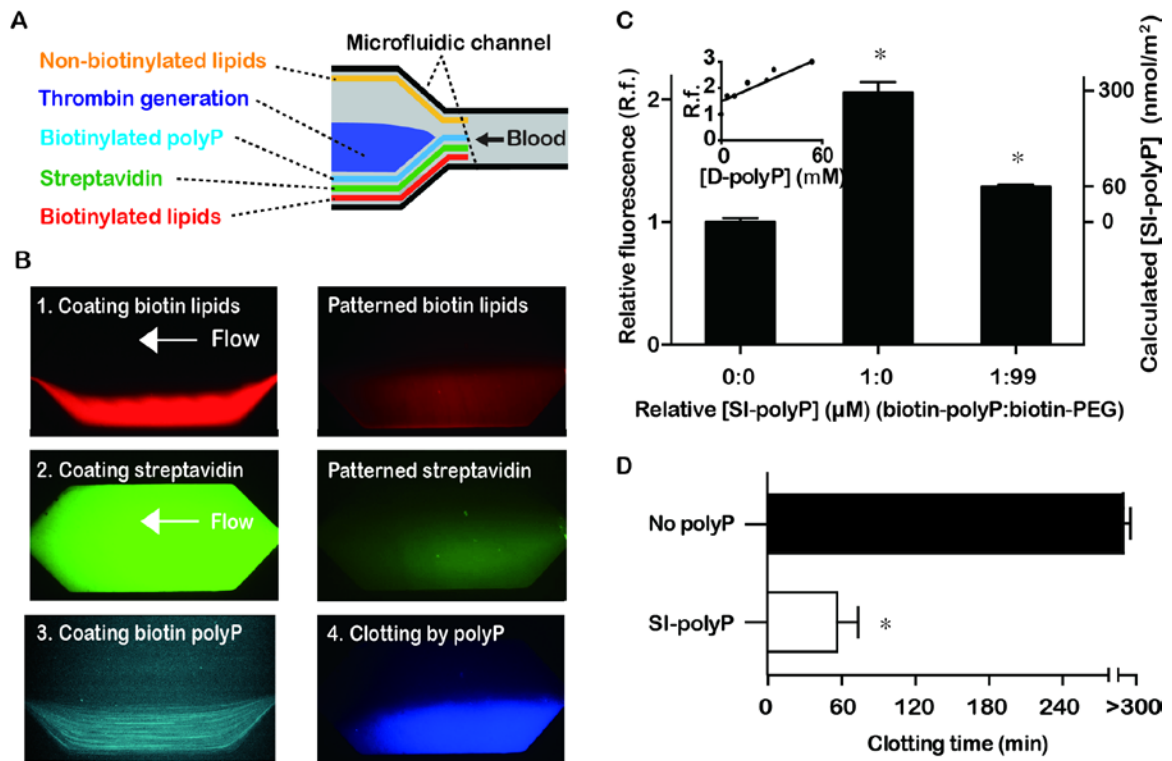
**Figure 6-2. PolyP induces clotting of flowing blood plasma when localized on a surface at sub-physiological shear.** (**A**) Schematic of biotinylated synthetic polyP (cyan) patterned onto the surface of half of a microfluidic channel, which induces production of thrombin and clotting (blue) of flowing blood plasma (grey). (**B**) Images of fluorescent-labeled agents flowing and patterned along one side of a microfluidic channel. Biotinylated lipids (tagged red) self-assembled on the channel wall. Non-biotinylated lipids (not tagged in these images) were simultaneously flowed and patterned on the other side of the chamber using laminar flow patterning. Then, streptavidin (tagged green) was flowed through and bound to the biotinylated lipids, followed by flowing biotinylated polyP labeled with DAPI (cyan), which bound streptavidin. A substrate (blue) for thrombin was activated, indicating initiation of clotting, selectively on patterned polyP400 (300 nmol/m2). Scale bar is 250 μm. (**C**) Quantifying of the amount of SI-polyP by measuring the fluorescence of DAPI bound to it. Channels with SI-polyP were compared to channels without polyP and to channels treated with polyP diluted with biotinylated PEG. Inset is a standard curve of known concentrations of solubilized D-polyP, which was used to calculate the surface

concentration of SI-polyP in coated channels. (**D**) The clotting times of normal human plasma flowing through channels coated with polyP400 at a shear rate of 1 s−1. *$p$ = < 0.01 compared to controls without polyP. Data indicate mean ± SEM, $n$ = 3.

**Measuring clot times simultaneously at various shear rates.** A microfluidic system containing six regions with varying shear rates was used to measure clot times of flowing blood plasma (Fig. 6-3A). The range of shear rates was 1–110 s−1, which encompasses physiological shear rates which occur in the inferior vena cava, venous valves, and large veins; as well as, sub-physiological shear rates (< ~10 s−1) that occur in pathological contexts25–28,36. These calculated shear rates were within 3–8% of the values obtained by measuring the flow velocity of micro particles by florescence microscopy. Clotting was monitored by visualizing the movement of fluorescent tracer beads specifically in the shear chambers, which became immobilized in clotted regions, and by a fluorogenic peptide substrate, which fluoresced when cleaved by thrombin during clotting (Fig. 6-3B). To characterize and determine the range of clot times of flowing blood plasma in the microfluidic system, coagulation factor VIIa (FVIIa) was used, and added to plasma at a range of concentrations (Fig. 6-3C). FVIIa does not circulate in plasma in appreciable amounts physiologically (~1% of total FVII circulates as FVIIa)37, but is administered during severe hemorrhage in some cases to aid in hemostasis at doses of 90 to 270 μ g/kg, which roughly corresponds to 1 to 4 μ g/mL in plasma38,39. In the device, plasma containing 16 μ g/mL of FVIIa clotted in approximately 20–40 min, plasma containing 4 μ g/mL of FVIIa clotted in approximately 60 min, and plasma containing 4 ng/mL did not clot within 6 hr. Intermediate clotting times occurred with concentrations of 400 ng/mL and 40 ng/mL and were dependent on shear rate. Clot formation always occurred from the channel wall, crudely mimicking how physiological thrombus formation occurs from the walls of blood vessels and is shear-dependent40.
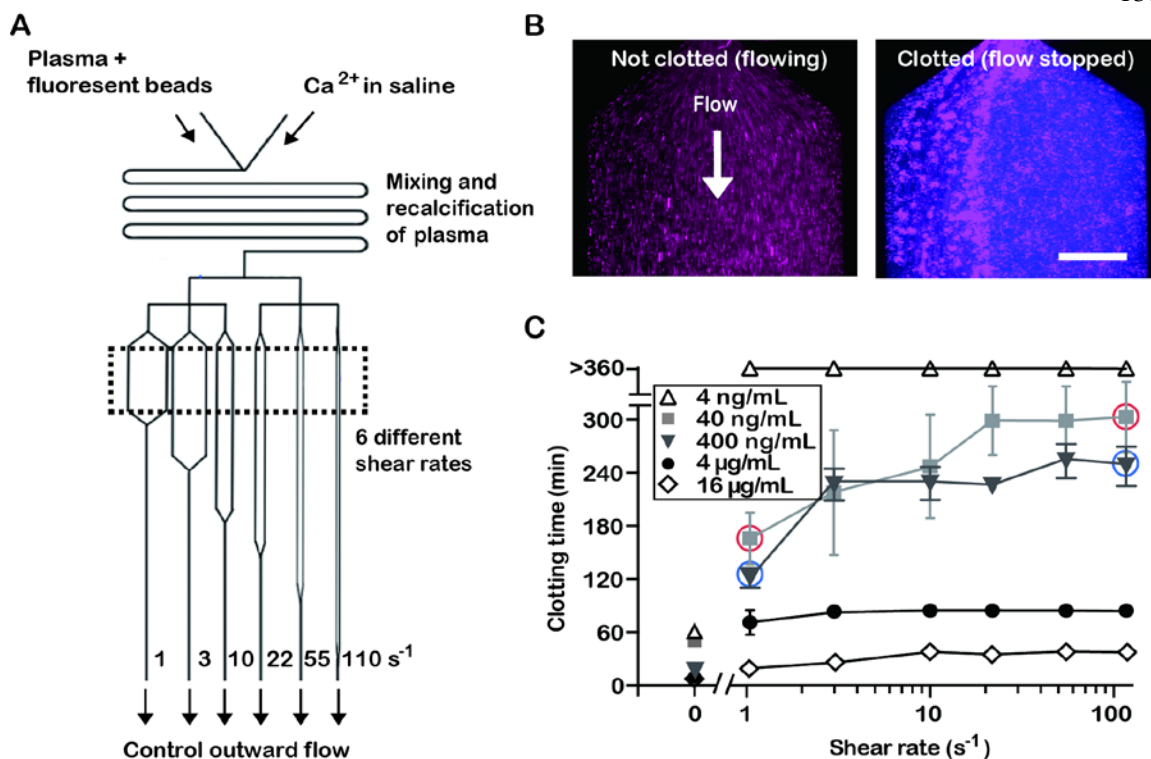
**Figure 6-3. The microfluidic system used to measure clotting over a range of shear rates.** (**A**) Schematic of the microfluidic system. Box (dashed lines) indicates the region where shear rates were varied and clot times were measured. (**B**) Fluorescence images showing that clotting was detected by the cessation of flow of tracer beads (pink) and by the cleavage of a substrate for thrombin (blue). Scale bar is 250 $\mu$ m. (**C**) Assessing the range of clotting times in this flow system by adding various concentrations of FVIIa to the plasma. Data points indicate mean $\pm$ SEM, $n = 3$–4. Red circles indicate $p = < 0.05$ between the data points, and blue circles indicate $p = < 0.01$ between the data points.

**Short-chain polyP accelerates clot formation faster when surface-localized than when dispersed in nanoparticles or in solution.** PolyP160 was previously demonstrated to be a weak initiator of the contact pathway, but we examined the hypothesis that spatially localizing polyP160 onto a surface (SI-polyP160) would enhance its ability to contribute to clot formation compared to polyP160 dispersed as nanoparticles (NP-polyP160) or in solution (D-polyP160, Fig. 6-4A). With NP-polyP160 (1 $\mu$ M, 250 nm diameter,

Supplementary Fig. 6-S1), clotting occurred in approximately 170 min and 200 min at a shear rate of 1 s−1 and 22 s−1 respectively. When a similar amount of polyP160 was localized onto the channel surface, clotting occurred significantly faster than both NP-polyP160 and D-polyP160. Clotting initiated from the parallel channel shear chamber walls, or in areas where the channel expanded from high to very low shear, and progressively grew outwards (Fig. 6-4B). Clotting with D-polyP160 (1 μ M) was 4- to 2.8-fold slower than SI-polyP160 and 1.6- to 0-fold slower than NP-polyP160 at all shear rates. Overall, clotting occurred fastest with SI-polyP160 than dispersed polyP160 in either soluble or NP forms, even with 6–43 fold less SI-polyP160 in the channels.

**Platelet-length polyP can accelerate clotting when surface-localized.** The concentration of polyP is approximately 1.1 mM in platelets, where it is stored in platelet dense granules, and can reach up to 2–7 μM in blood upon platelet activation[41,42]. To test whether synthetic polyP similar in length to those found in human platelets can clot flowing blood at physiological concentrations, polyP70 was tested (Fig. 6-4C). Soluble polyP70 (D-polyP70) at 400 nM did not accelerate clotting of flowing blood plasma at the shear rates tested. In contrast, an equivalent amount of SI-polyP70 substantially accelerated clotting, to 70 min and 160 min at shear rates of 1 s−1 and 110 s−1 respectively. The amount of SI-polyP70 used corresponded to a surface concentration of 24 nmol/m2 and a total concentration of around 400 nM in the volume of the channel. Initiation time of clotting by SI-polyP70 was dependent on FXII (Supplementary Fig. 6-S2).
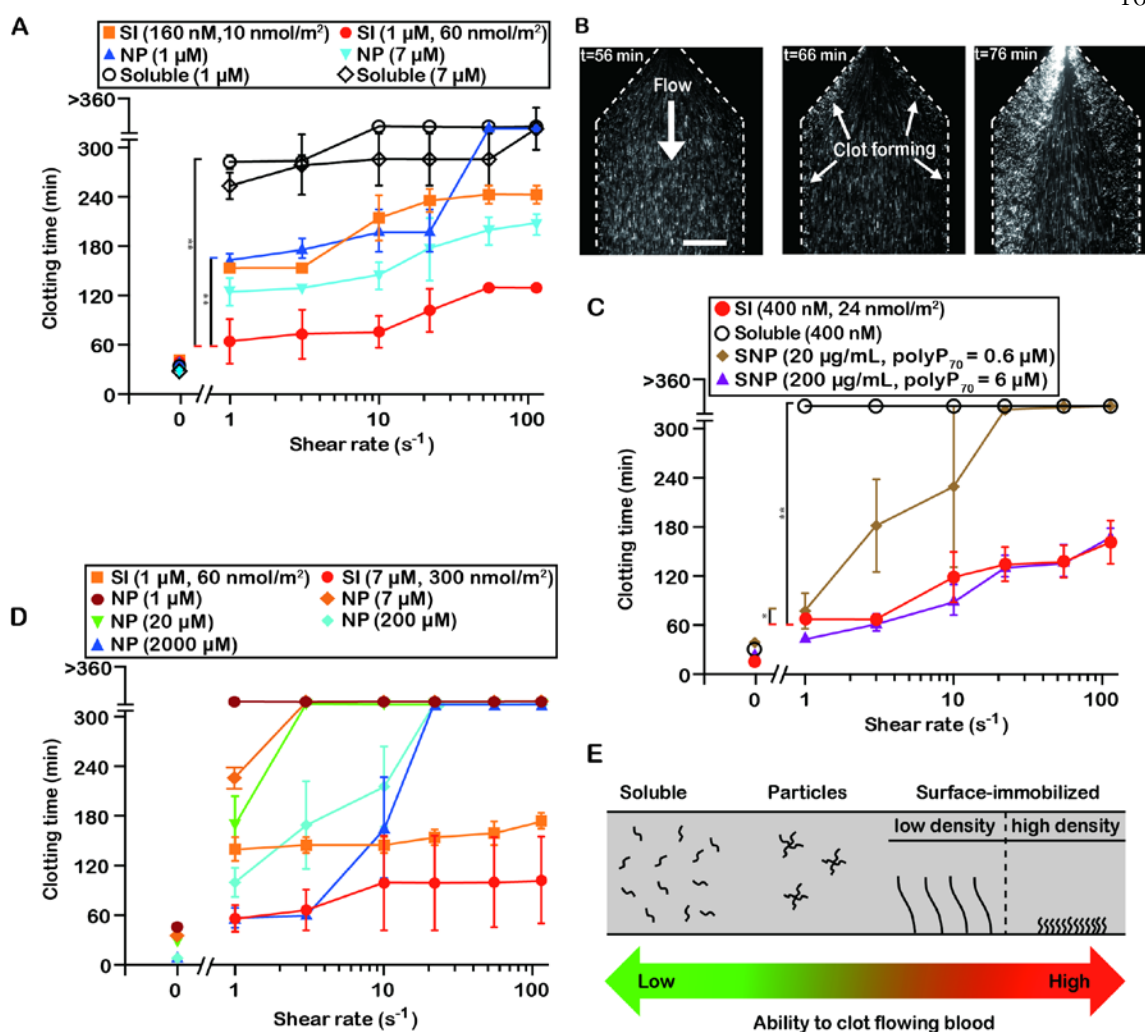
**Figure 6-4. PolyP accelerates clotting best when spatially localized onto surfaces, compared to soluble polyP and nanoparticles of polyP.** (**A**) Clotting times of plasma by polyP160 at varying shear rates, comparing three states of polyP160: solubilized, self-assembled nanoparticles, and surface-immobilized. (**B**) Time-lapse images showing SI-polyP160 initiating clotting (detected by non-flowing beads) from the channel wall (dashed lines). Scale bar is 250 μ m. (**C**) Comparing three states of polyP70: solubilized, surface-immobilized onto the microfluidic channels, and immobilized onto silica nanoparticles. Clotting tendencies of plasma containing silica nanoparticles coated with polyP70 (SNP-polyP70) compared to soluble and surface-immobilized polyP70 under shear in the microfluidic device. (**D**) Comparing two states of long-chain polyP: surface immobilized

polyP400 and nanoparticles of self-assembled polyP>1000. (**E**) Schematic summarizing the relationship between spatial distribution of polyP and the acceleration of clotting in the above experiments. Data points indicate mean $\pm$ SEM, *p < 0.001, **p < 0.0001, $n$ = 3–4. Statistical analysis represents comparisons between whole curves.

SI-polyP70 and D-polyP70 could not be directly compared to self-assembled nanoparticles of polyP70 (NP-polyP70), because the solubility of polyP70 is greater than longer chain polyP, and NP-polyP70 was not stable. Alternatively, we tested a second formulation of polyP nanoparticles, where polyP70 was coated on silica nanoparticles (SNP-polyP70)43. When SNP-polyP70 was added to plasma at varying shear, clotting occurred in approximately 70 min to 160 min at 200 µ g/mL and 80 min to > 360 min at 20 µ g/mL. These masses of SNP-polyP70 corresponded to concentrations of polyP70 of 6 µ M and 0.6 µ M, respectively, but include both polyP70 and silica. Silica is also an activator of factor XII, so an equal comparison between SI-polyP70 and SNP-polyP70 cannot be made. Nevertheless, the clotting times of SI-polyP70 (400 nM) were significantly faster than 20 µ g/mL of aSNP-polyP70, and were nearly identical to 200 µ g/mL of a SNP-polyP70 even though there was a 15-fold lower concentration of polyP70.

**Clotting by long-chain polyP is also enhanced by surface localization.** To understand if the effect of surface localization extends to long-chain polyP, we tested a range of concentrations of long-chain polyP either surface localized (SI-polyP400) or dispersed as nanoparticles (NP-polyP>1000). PolyP>1000 naturally self-assembles, localizing into nanoparticles of 150 □} 30 nm in diameter in solutions containing Ca2+ at low millimolar concentrations11. It is a known activator of clotting under static conditions when dispersed throughout plasma3. We compared NP-polyP>1000 to SI-polyP400, rather than SI-polyP>1000, because surface patterning of polyP requires biotinylation of the polyP chains, and the biotinylation procedure caused degradation of long chain-lengths of polyP. When plasma was flowed over SI-polyP400, clotting occurred in approximately 60 min to 100 min at 7 µM and 140 min to 170 min at 1 µ M at the shear rates examined (Fig. 6-4D). The clot times using NP-polyP>1000 demonstrated robust shear- and concentration-

dependence at 2000, 200, 20, 7 and 1 μ M. NP-PolyP>1000 was most potent at 2000 μ M, initiating clotting at 60 min at 1 and 3 s−1, although requiring 285-fold more phosphate to match the propensity of SI-polyP400 to clot flowing plasma under the same conditions.

**Discussion**

Together, these data show that the spatial localization of synthetic polyP onto surfaces affects its ability to activate clotting under flow (Fig. 6-4E). Short-chain polyP polymers (polyP160 and polyP70) greatly accelerated clotting of flowing blood plasma at low to sub-physiological shear when surface-localized onto the walls of microfluidic chambers compared to when they are dispersed (nanoparticle or soluble forms). Soluble short-chain polyP only clotted stagnant blood (near-zero flow) in our experiments, and clotting did not occur within a span of hours even at sub-physiological shear rates. Localization of polyP onto the surface of channels showed the greatest activity overall. The concentration at which SI-polyP70 accelerated clotting *in vitro* is well-within the range of amounts of polyP released into plasma following platelet activation. Although it is not known if polyP localizes to cell surfaces or thrombi, or to the extent polyP contributes to physiological or pathophysiological coagulation, it is important to identify scenarios in which polyP could potentially elicit a role. These results propose that if polyP can surface-localize it may contribute to clotting at sub-physiological shear following platelet activation, but further *in vitro* and *in vivo* experiments are necessary to verify that this is a potential mechanism.

Remarkably, comparing SI-polyP70, SI-polyP160, and SI-polyP400, to each other shows that short-chain polyP could match the propensity of longer chain polyP to accelerate clotting under flow. SI-polyP70 accelerated clotting to a similar extent as SI-polyP160 and SI-polyP400 with a lower concentration of phosphate. Although clotting times were similar between them with respect to surface coverage of full-length polymers, this is likely because shorter chains have high surface coverage relative to the amount of monomer. Thus, clotting occurred faster with both increasing surface concentration of phosphate and increasing surface coverage.

The simulations predicted the trend observed *in vitro*. Localization creates high local concentrations of polyP, and in the numerical simulations this led to larger thrombin bursts due to increased positive feedback from the coagulation cascade. The simulations included polyP binding and inhibiting TFPI and accelerating activation of factors V and XI, which all occur in plasma. The mechanism is likely contact system mediated as under stagnant conditions FXII contributed to initiation of clotting by polyP, but we did not test this further in flow experiments. It was recently shown that short-chain polyP could complex with FXII *in vitro* to allostericly induce its activation at high polyP concentrations of 70–130 μ M12. This polyP-induced activation of FXII was enhanced in the presence of zinc ions, which is known to bind robustly to both FXII and PolyP3,12. Short-chain polyP can also contribute to clotting independently of FXII when TF is present13. The results here, without TF, indicate that localization can further increase the propensity of short-chain polyP to clot blood plasma.

In these microfluidic experiments, shear rate and concentrations of either FVIIa or polyP influenced the clotting times over several hours. The shear rates mimicked the shear rates that are typical in large veins and valves; as well as, pathological shear which occurs it the context of thrombosis. The reported clotting times appear very long compared to clotting times in most *in vitro*, stagnant clotting assays, which occur in seconds to minutes. However, residence time of plasma in the microfluidic chambers was only ~10 sec, with plasma being continuously transported into and out of the chamber, and thus the rate of clotting cannot be directly compared to stagnant clotting assays. Long clot times were possible in this device, compared to most other flow systems, because platelet-poor plasma was recalcified on the device and because TF was not included44. The observed clotting times were much slower than what is typical in acute hemostasis and at high concentrations of TF, but they were within the time-frame that formation and growth of thrombi occurs inside veins and regions of low shear31–33. Thrombosis, in contrast to hemostasis, can involve progressive and gradual clot growth, where there is much less TF but increased contribution of factors XI and XII2,45. The clotting times measured in this microfluidic

system are more representative of clotting times that would occur during thrombosis inside intact veins, rather than punctured vessels or stagnant clotting assays. In addition, the shear rates used in our microfluidic model include the rates which occur in large veins. Though platelets appear to contribute more to arterial thrombi than venous thrombi, they also contribute to venous thrombosis[46,47]. For example, antiplatelet drugs have also been beneficial in treating venous thrombosis[47–49].

For several concentrations and chain-lengths of polyP, it was not possible to make equivalent comparisons between SI-polyP, NP-polyP, SNP-polyP, and D-polyP, because the chain-length and concentration are important determinants of whether polyP self-assembles into particles or remains soluble. The solubility of short-chain polyP is greater than long-chain polyP, but solubility also depends on the concentration of polyP and $Ca^{2+}$. For example, polyP160 can be formulated to be soluble or to form NP-polyP by varying the concentration of polyP and $Ca^{2+}$ [11]. We used concentrations of polyP160 well below its limit of solubility. PolyP160 was first dissolved into water and then diluted into plasma. When added to citrated plasma, soluble polyP likely remained dissolved, as plasma has insufficient free divalent cations to facilitate nanoparticle formation[11]. Once plasma is recalcified, polyP likely remains protein-bound even in the presence of low millimolar amounts of ionic calcium, at least for the 35 sec that it is present in the microfluidic devices (Supplementary Fig. 6-S3)[11,50]. In contrast, NP-polyP were formed by precipitating polyP160 in 5 mM $Ca^{2+}$, generating nanoparticles that were stable for over 6 hr, as measured by dynamic light scattering. NP-polyP was diluted in the calcium-saline solution that mixed with blood plasma inside the microfluidic devices to keep the nanoparticles intact. The stability of NP-polyP in plasma is unknown; however, NP-polyP was initially prepared under supersaturated conditions, and the solubility of NP-polyP displays hysteretic behavior[11]. Thus, a large portion of NP-polyP, once formed, likely remained as NPs in the microfluidic devices. Although synthetic polyP was used in these experiments, natural polyP is also typically bound to calcium[51].

In summary, this work shows that spatial localization of synthetic polyP, including short-chain polyP, increases its propensity to accelerate clotting of blood plasma at low to sub-physiological shear. The observed clotting times were much slower than what is typical in hemostasis, but they were within the time-frame that thrombosis occurs inside veins, particularly post-operative deep vein thrombi, which form over a period of days[32,33,52]. The experiments were designed solely to test if surface-localization of short-chain polyP accelerates clot formation under flow, at venous and sub-physiological shear rates. An important observation from this was that when localized, short-chain polyP could match the ability of long-chain polyP to accelerate clotting. The concentration required to accelerate clotting is markedly reduced when polyP is spatially localized onto surfaces, and to a lesser extent, into particles, even under flow and without TF. These biophysical insights provide a potential biophysical mechanism by which platelet-length polyP could contribute to thrombosis in regions of low shear, but further work is required to validate if this mechanism could indeed extend to *in vivo* scenarios. This effect of localization may potentially contribute to clotting at higher shear when TF is present[13]. Although these *in vitro* results, in an artificial flow system, support the notion that platelet-derived polyP could contribute to coagulation *in vivo*, the flow system used here does not include many factors that normally regulate clotting, such as platelets, platelet-derived polyP, red blood cells, immune cells, endothelium and other soluble factors. For these reasons, appropriate *in vivo* models are necessary to verify whether platelet-derived polyP and its spatial localization contributes to clot formation and thrombosis.

**Materials and Methods**

**Numerical Simulations.** Thrombin generation was modeled with the *Transport of Diluted Species* module of Comsol Multiphysics 4.4 by adding diffusion and convection to a previously reported kinetic model[20]. Changes to the model included the addition of three rate equations to describe the activity of polyP: 1) the binding and inhibition of TFPI; TFPI + polyP $\leftrightarrow$ TFPI-polyP; kon = $4.0 \times 10^5$ M$^{-1}$s$^{-1}$, koff = $1.0 \times 10^{-2}$s$^{-1}$, 2) the activation of factor V; V + Xa + polyP $\rightarrow$ Va + Xa + polyP; k = $8.0 \times 10^{12}$ M$^{-2}$s$^{-1}$, 3) the activation of

factor XI; XI + IIa + polyP → XIa + IIa + polyP; k = 8.8 × 10$^9$ M$^{-2}$s$^{-1}$ 1,4,5,7,20. The diffusion coefficient for all soluble species was 5 × 10$^{-11}$ m$^2$/s and the velocity profile varied with the shear rate, $v_z(r) = \frac{\gamma_w R}{2}\left(1 - \frac{r}{R}\right)^2$, where $v_z$ is the velocity in the axial directionat each radial coordinate $r$, $R$ is the cylinder radius, and $\gamma_w$ is the shear rate at the cylinder wall. The chemical species were flowed into a cylindrical geometry of radius 2 mm and length 20 mm. For each shear rate, [thrombin] was sampled after the incoming flow had displaced the channel volume 12.5 times. Both the experiments and simulations were performed in the same mass-transfer regime (*Pe* ≫ 1 and *Gz* > 3000).

**Preparing soluble polyP (D-polyP), self-assembled polyP nanoparticles (NP-polyP), polyP-coated silica nanoparticles (SNP-polyP), and surface-immobilized polyP (SI-polyP).** To make D-polyP, polyP was solubilized and diluted first in water and then added to citrated plasma (frozen citrated normal control plasma, Affinity Biologicals Inc.) prior to entering the microfluidic device. NP-polyP was generated as described previously11. Briefly, soluble polyP was added to a calcium solution (10 mM polyP, 5 mM CaCl$_2$, 8 mM Tris, pH 6.0) followed by vortexing, during which polyP self-assembled into nanoparticles tightly bound to Ca2+ cations11. The formation and size of the nanoparticles were verified after adding them to this calcium solution by observing the scattering intensity and hydrodynamic diameter, as measured by dynamic light scattering (Zetasizer Nano ZSP, Malvern Instruments). NP-polyP formulations were added and diluted in calcium-saline solution, rather than the citrated-plasma, prior to entering the microfluidic device. The NP-polyP were stable for over 6 hr in these solutions. SNP-polyP70 were made by covalently attaching polyP70 onto silica nanoparticles as previously described43. Synthetic PolyP was generated by solubilization from Maddrell salts and biotinylated as previously described7,50. Synthetic polyP has been previously characterized, including its chain length, counterions, and clotting activity7,11. Long-chain NP-polyP contained a heterogeneous preparation of very long,

non-biotinylated polyP polymers ranging from around 200 mers to 1300 mers, referred to here as NP-PolyP>1000. Some experiments with SI-polyP employed heterogeneous long-

chain biotinylated polyP consisting of chains 50 to 400 units in length, referred to here as biotin-polyP400. Some experiments employed fractionated material of narrower sizes (polyP70 and polyP160)[7]. All polyP concentrations are stated with respect to the concentration of phosphate monomer.

**Preparing microfluidic devices with SI-polyP.** Microfluidic devices were prepared from polydimethylsiloxane (PDMS) as previously described[53]. Channel dimensions are listed as follows (length × width, 125 μm height for all channels): 1.67 mm × 1000 μm (1 s$^{-1}$), 3.33 mm × 500 μm (3 s$^{-1}$), 5.83 mm × 286 μm (10 s$^{-1}$), 8.33 mm × 200 μm (22 s$^{-1}$), 12.50 mm × 133 μm (55 s$^{-1}$), 16.67 mm, 100 μm (110 s$^{-1}$). The devices were incubated in saline and kept under vacuum overnight to hydrate and remove air from the channels. Devices remained soaked in saline throughout the experiment to aid in coating the surfaces with lipids, and to reduce convective flow during experiments in the absence of flow. The devices were coated with phosphatidylcholine (PC) vesicles to prevent activation of clotting on the PDMS surface. In devices that were not coated withSI-polyP, vesicles were prepared with egg PC (Avanti Polar Lipids, Alabaster, USA) and fluorescent Texas Red 1,2-Dihexadecanoyl-*sn*-Glycero-3-Phosphoethanolamine (DHPE) (Invitrogen) in a 99.5:0.5 molar ratio. Lipids were extruded through a 100 nm membrane using a Lipex Thermobarrel Extruder (Northern Lipids, Burnaby, Canada). The vesicle solution (10 mg/mL in dH2O) were flowed through microfluidic channels at a rate of 1 μL/min for 15 min and rinsed out with saline. The coating of PC on the channels was stable for at least 10 hours (Supplementary Fig. 6-S4). For devices where polyP was surface-immobilized, the channel was first coated with biotinylated lipids (1 μL/min, 15 min) and rinsed out with saline. To prepare biotinylated vesicles, 1-oleoyl-2-[12[biotinyl(aminododecanoyl)]-sn-glycero-3-phosphocholine (biotinylated-PC, Avanti Polar Lipids) was mixed with Egg PC and Texas Red DHPE in a molar ratio of 5.0:94.5:0.5 and extruded. Next, streptavidin (100 μg/mL) conjugated to Alexa Fluor® 488 (Molecular Probes, Inc.) was flowed through the device (1 μL/min, 40 min) and then rinsed with saline to wash away the unbound, excess streptavidin. Finally, a solution of

biotin-polyP (50 µg/mL) and biotinylated-polyethylene glycol (biotin-PEG) (either 0 or 99 molar equivalents to biotin-polyP) was flowed through the device (1 µL/min, 40 min), binding to the patterned streptavidin followed by a saline rinse, which resulted in SI-polyP being selectively patterned on the walls of the microfluidic device shear chambers. Liposomes and saline were flowed into the device through a combination of inlet and outlet channels to achieve laminar flow patterning, such that the parallel streams of fluids were at low Reynolds number ($\ll$ 1) and maintained sharp boundaries and excluded the possibility of turbulent flow54,55. This patterning allowed specific channel walls of the device to be coated, either all channels in the device, the channels in the shear chambers, or one wall of the chambers. To measure the amount of polyP, it was stained by flowing DAPI (40 µg/mL in 15 mM Tris acetate, 300 mM NaCl, 30 mM EDTA, and 0.02% NaN3) into the device. Thrombin generation during clotting was detected by adding 125 µ g/mL of fluorescent peptide substrate for thrombin (Boc-Val-Pro-Arg-4-methylcoumaryl-7-amide, Peptide Institute Inc.) into normal plasma.

**Flowing plasma and calcium into devices and measuring clotting.** Flow rates were controlled using a syringe pump (Harvard Apparatus PHD 2000) by withdrawing solutions out of the outlets of the device at a rate of 1 µl/min. Shear rates in different channels were controlled by the width of each channel, while the residence time of plasma within the shear chambers were kept constant (~10 sec) by varying their respective lengths. Tubing connected to the outlets of the device were charged with 50 µ l of Egg PC vesicles to prevent clotting from initiating in the tubing or syringes. A solution of sodium citrate (10 mM in dH2O) was initially pulled into both inlet channels to wash out the device and further charge the outlet tubing. Normal citrated human plasma (7 mM citrate) and calcium-saline solution (40 mM CaCl2 and 90 mM NaCl) were simultaneously pulled into the device and mixed at a ratio of 3:1 to recalcify the plasma, yielding a final free calcium concentration of 4–5 mM56. To measure clotting times, fluorescent beads (2.5 µ g/mL, Fluoresbrite Plain YG 1.0 Micron Microsphere, Polysciences Inc.), and in some experiments 125 µ g/mL fluorescent thrombin substrate, were mixed into the plasma and time-course imaging of each channel was performed using an epifluorescence microscope

(Leica DMI6000B). The fluorescent beads did not influence clotting times (Supplementary Fig. 6-S5). Clotting was determined by the immobilization of the fluorescent beads and in some experiments also by the generation of blue fluorescence upon cleavage of the thrombin substrate. In experiments where the effect of nanoparticle polyP (NP-polyP) on clotting was tested, the activators were mixed with the calcium solution prior to entering the device. For experiments with soluble polyP (D-polyP), polyP was added to the plasma instead to prevent nanoparticle formation. For experiments at zero shear, normal or congenital FXII-deficient plasma (Geroge King Bio-Medical, Inc.) and calcium were mixed together immediately before flowing them into the device and blocking all outlets to create stagnant plasma.

**References**

1. Muller, F. *et al.* Platelet Polyphosphates Are Proinflammatory and Procoagulant Mediators *In Vivo*. *Cell* **139,** 1143–1156, doi: 10.1016/j.cell.2009.11.001 (2009).

2. Renne, T., Schmaier, A. H., Nickel, K. F., Blomback, M. & Maas, C. *In vivo* roles of factor XII. *Blood* **120,** 4296–4303, doi: 10.1182/blood-2012-07-292094 (2012).

3. Morrissey, J. H., Choi, S. H. & Smith, S. A. Polyphosphate: an ancient molecule that links platelets, coagulation, and inflammation. *Blood* **119,** 5972–5979, doi: 10.1182/blood-2012-03-306605 (2012).

4. Smith, S. A. *et al.* Polyphosphate modulates blood coagulation and fibrinolysis. *Proc. Natl. Acad. Sci. USA* **103,** 903–908, doi: 10.1073/pnas.0507195103 (2006).

5. Choi, S. H., Smith, S. A. & Morrissey, J. H. Polyphosphate is a cofactor for the activation of factor XI by thrombin. *Blood* **118,** 6963–6970, doi: 10.1182/blood-2011-07-368811 (2011).

6. Puy, C. *et al.* Factor XII promotes blood coagulation independent of factor XI in the presence of long-chain polyphosphates. *J. Thromb. Haemost.* **11,** 1341–1352, doi: 10.1111/jth.12295 (2013).

7. Smith, S. A. *et al.* Polyphosphate exerts differential effects on blood clotting, depending on polymer size. *Blood* **116,** 4353–4359, doi: 10.1182/blood-2010-01-266791 (2010).

8. Kumble, K. D. & Kornberg, A. Inorganic Polyphosphate in Mammalian-Cells and Tissues. *J Biol Chem* **270,** 5818–5822 (1995).

9. Moreno-Sanchez, D., Hernandez-Ruiz, L., Ruiz, F. A. & Docampo, R. Polyphosphate Is a Novel Pro-inflammatory Regulator of Mast Cells and Is Located in Acidocalcisomes. *J Biol Chem* **287,** 28435–28444, doi: 10.1074/jbc.M112.385823 (2012).

10. Nickel, K. F. *et al.* The polyphosphate-factor XII pathway drives coagulation in prostate cancer-associated thrombosis. *Blood* **126,** 1379–1389, doi: 10.1182/blood-2015-01-622811 (2015).

11. Donovan, A. J., Kalkowski, J., Smith, S. A., Morrissey, J. H. & Liu, Y. Size-Controlled Synthesis of Granular Polyphosphate Nanoparticles at Physiologic Salt Concentrations for Blood Clotting. *Biomacromolecules* **15,** 3976–3984, doi: 10.1021/bm501046t (2014).

12. Engel, R., Brain, C. M., Paget, J., Lionikiene, A. S. & Mutch, N. J. Single-chain factor XII exhibits activity when complexed to polyphosphate. *J. Thromb. Haemost.* **12,** 1513–1522, doi: 10.1111/jth.12663 (2014).

13. Zhu, S., Travers, R. J., Morrissey, J. H. & Diamond, S. L. FXIa and platelet polyphosphate as therapeutic targets during human blood clotting on collagen/tissue factor surfaces under flow. *Blood* **126,** 1494–1502, doi: 10.1182/blood-2015-04-641472 (2015).

14. Kastrup, C. J., Runyon, M. K., Lucchetta, E. M., Price, J. M. & Ismagilov, R. F. Using chemistry and microfluidics to understand the spatial dynamics of complex biological networks. *Accounts Chem. Res*. **41,** 549–558, doi: 10.1021/ar700174g (2008).

15. Szymusiak, M. *et al.* Colloidal Confinement of Polyphosphate on Gold Nanoparticles Robustly Activates the Contact Pathway of Blood Coagulation. *Bioconjug Chem* **27,** 102–109, doi: 10.1021/acs.bioconjchem.5b00524 (2016).

16. Okorie, U. M., Denney, W. S., Chatterjee, M. S., Neeves, K. B. & Diamond, S. L. Determination of surface tissue factor thresholds that trigger coagulation at venous and arterial shear rates: amplification of 100 fM circulating tissue factor requires flow. *Blood* **111,** 3507–3513, doi: 10.1182/blood-2007-08-106229 (2008).

17. Balandina, A. N. *et al.* Positive Feedback Loops for Factor V and Factor VII Activation Supply Sensitivity to Local Surface Tissue Factor Density During Blood Coagulation. *Biophys. J.* **101,** 1816–1824, doi: 10.1016/j.bpj.2011.08.034 (2011).

18. Kastrup, C. J., Runyon, M. K., Shen, F. & Ismagilov, R. F. Modular chemical mechanism predicts spatiotemporal dynamics of initiation in the complex network of hemostasis. *Proc. Natl. Acad. Sci. USA* **103,** 15747–15752, doi: 10.1073/pnas.0605560103 (2006).

19. Kastrup, C. J. *et al.* Spatial localization of bacteria controls coagulation of human blood by 'quorum acting'. *Nat. Chem. Biol.* **4,** 742–750, doi: 10.1038/nchembio.124 (2008).

20. Chatterjee, M. S., Denney, W. S., Jing, H. Y. & Diamond, S. L. Systems Biology of Coagulation Initiation: Kinetics of Thrombin Generation in Resting and Activated Human Blood. *PLoS Comput. Biol.* **6,** 24, doi: 10.1371/journal.pcbi.1000950 (2010).

21. Rana, K. & Neeves, K. B. Blood flow and mass transfer regulation of coagulation. *Blood Rev*, doi: 10.1016/j.blre.2016.04.004 (2016).

22. Fogelson, A. L., Hussain, Y. H. & Leiderman, K. Blood Clot Formation under Flow: The Importance of Factor XI Depends Strongly on Platelet Count. *Biophys. J.* **102,** 10–18, doi: 10.1016/j.bpj.2011.10.048 (2012).

23. Haynes, L. M., Dubief, Y. C., Orfeo, T. & Mann, K. G. Dilutional Control of Prothrombin Activation at Physiologically Relevant Shear Rates. *Biophys. J.* **100,** 765–773, doi: 10.1016/j.bpj.2010.12.3720 (2011).

24. Runyon, M. K., Kastrup, C. J., Johnson-Kerner, B. L., Van Ha, T. G. & Ismagilov, R. F. Effects of shear rate on propagation of blood clotting determined using microfluidics and numerical simulations. *J. Am. Chem. Soc.* **130,** 3458–3464, doi: 10.1021/ja076301r (2008).

25. Cheng, C. P., Herfkens, R. J. & Taylor, C. A. Inferior vena caval hemodynamics quantified *in vivo* at rest and during cycling exercise using magnetic resonance imaging. *Am J Physiol-Heart C* **284,** H1161–H1167, doi: 10.1152/ajpheart.00641.2002 (2003).

26. Karino, T. & Motomiya, M. Flow through a Venous Valve and Its Implication for Thrombus Formation. *Thromb Res* **36,** 245–257, doi: 10.1016/0049-3848(84)90224-X (1984).

27. Papaioannou, T. G. & Stefanadis, C. Vascular wall shear stress: basic principles and methods. *Hellenic journal of cardiology: HJC=Hellenike kardiologike epitheorese* **46,** 9–15 (2005).

28. Hathcock, J. J. Flow effects on coagulation and thrombosis. *Arterioscler Thromb Vasc Biol* **26,** 1729–1737, doi: 10.1161/01. ATV.0000229658.76797.30 (2006).

29. Goel, M. S. & Diamond, S. L. Adhesion of normal erythrocytes at depressed venous shear rates to activated neutrophils, activated platelets, and fibrin polymerized from plasma. *Blood* **100,** 3797–3803, doi: 10.1182/blood-2002-03-0712 (2002).

30. Gallus, A. S. Travel, venous thromboembolism, and thrombophilia. *Seminars in thrombosis and hemostasis* **31,** 90–96, doi: 10.1055/s-2005-863810 (2005).

31. Casa, L. D. C., Deaton, D. H. & Ku, D. N. Role of high shear rate in thrombosis. *J. Vasc. Surg.* **61,** 1068–1080, doi: 10.1016/j.jvs.2014.12.050 (2015).

32. Aghourian, M. N., Lemarie, C. A. & Blostein, M. D. *In vivo* monitoring of venous thrombosis in mice. *J. Thromb. Haemost.* **10,** 447–452, doi: 10.1111/j.1538-7836.2011.04615.x (2012).

33. Wilson, J. S., Virag, L., Di Achille, P., Karsaj, I. & Humphrey, J. D. Biochemomechanics of Intraluminal Thrombus in Abdominal Aortic Aneurysms. *J. Biomech. Eng.-Trans. ASME* **135,** 14, doi: 10.1115/1.4023437 (2013).

34. Stavrou, E. & Schmaier, A. H. Factor XII: What does it contribute to our understanding of the physiology and pathophysiology of hemostasis & thrombosis. *Thromb Res* **125,** 210–215, doi: 10.1016/j.thromres.2009.11.028 (2010).

35. Yau, J. W. *et al.* Selective depletion of factor XI or factor XII with antisense oligonucleotides attenuates catheter thrombosis in rabbits. *Blood* **123,** 2102–2107, doi: 10.1182/blood-2013-12-540872 (2014).

36. Sakariassen, K. S., Orning, L. & Turitto, V. T. The impact of blood shear rate on arterial thrombus formation. *Future Sci. OA* **1** (2015).

37. Morrissey, J. H., Macik, B. G., Neuenschwander, P. F. & Comp, P. C. Quantitation of Activated Factor-Vii Levels in Plasma Using a Tissue Factor Mutant Selectively Deficient in Promoting Factor-Vii Activation. *Blood* **81,** 734–744 (1993).

38. Riddell, A., Abdul-Kadir, R., Pollard, D., Tuddenham, E. & Gomez, K. Monitoring low dose recombinant factor VIIa therapy in patients with severe factor XI deficiency undergoing surgery. *Thromb. Haemost.* **106,** 521–527, doi: 10.1160/Th10-12-0816 (2011).

39. Hendriks, H. G. D. *et al.* An effective treatment of severe intractable bleeding after valve repair by one single dose of activated recombinant factor VII. *Anesth. Analg.* **93,** 287–289, doi: 10.1097/00000539-200108000-00009 (2001).

40. Mackman, N. New insights into the mechanisms of venous thrombosis. *J. Clin. Invest.* **122,** 2331–2336, doi: 10.1172/jci60229 (2012).

41. Ruiz, F. A., Lea, C. R., Oldfield, E. & Docampo, R. Human platelet dense granules contain polyphosphate and are similar to acidocalcisomes of bacteria and unicellular eukaryotes. *J Biol Chem* **279,** 44250–44257, doi: 10.1074/jbc.M406261200 (2004).

42. Smith, S. A. *et al.* Inhibition of polyphosphate as a novel strategy for preventing thrombosis and inflammation. *Blood* **120,** 5103–5110, doi: 10.1182/blood-2012-07-444935 (2012).

43. Kudela, D. *et al.* Clotting Activity of Polyphosphate-Functionalized Silica Nanoparticles. *Angew. Chem.-Int. Edit.* **54,** 4018–4022, doi: 10.1002/anie.201409639 (2015).

44. Colace, T. V., Tormoen, G. W., McCarty, O. J. & Diamond, S. L. Microfluidics and coagulation biology. *Annu Rev Biomed Eng* **15,** 283–303, doi: 10.1146/annurev-bioeng-071812-152406 (2013).

45. Geddings, J. E. & Mackman, N. New players in haemostasis and thrombosis. *Thromb. Haemost.* **111,** 570–574, doi: 10.1160/th13-10-0812 (2014).

46. von Bruhl, M. L. *et al.* Monocytes, neutrophils, and platelets cooperate to initiate and propagate venous thrombosis in mice *in vivo*. *J Exp Med* **209,** 819–835, doi: 10.1084/jem.20112322 (2012).

47. Becattini, C. & Agnelli, G. Aspirin for prevention and treatment of venous thromboembolism. *Blood Rev* **28,** 103–108, doi: 10.1016/j.blre.2014.03.003 (2014).

48. Mekaj, Y. H., Daci, F. T. & Mekaj, A. Y. New insights into the mechanisms of action of aspirin and its use in the prevention and treatment of arterial and venous thromboembolism. *Ther Clin Risk Manag* **11,** doi: 10.2147/Tcrm.S92222 (2015).

49. Collaborative Overview of Randomized Trials of Antiplatelet Therapy. 3. Reduction in Venous Thrombosis and Pulmonary-Embolism by Antiplatelet Prophylaxis among Surgical and Medical Patients. *Brit Med J* **308,** 235–246 (1994).

50. Choi, S. H. *et al.* Phosphoramidate End Labeling of Inorganic Polyphosphates: Facile Manipulation of Polyphosphate for Investigating and Modulating Its Biological Activities. *Biochemistry* **49,** 9935–9941, doi: 10.1021/bi1014437 (2010).

51. Jensen, T. E., Baxter, M., Rachlin, J. W. & Jani, V. Uptake of Heavy-Metals by Plectonema-Boryanum (Cyanophyceae) into Cellular-Components, Especially Polyphosphate Bodies - an X-Ray-Energy Dispersive Study. *Environ Pollut A* **27,** 119–127, doi:10.1016/0143-1471(82)90104-0 (1982).

52. Yamaguchi, T., Hasegawa, M., Niimi, R. & Sudo, A. Incidence and time course of asymptomatic deep vein thrombosis with fondaparinux in patients undergoing total joint arthroplasty. *Thromb Res* **126,** E323–E326, doi: 10.1016/j.thromres.2010.03.018 (2010).

53. Whitesides, G. M., Ostuni, E., Takayama, S., Jiang, X. Y. & Ingber, D. E. Soft lithography in biology and biochemistry. *Annu. Rev. Biomed. Eng.* **3,** 335–373, doi: 10.1146/annurev.bioeng.3.1.335 (2001).

54. Kenis, P. J. A., Ismagilov, R. F. & Whitesides, G. M. Microfabrication inside capillaries using multiphase laminar flow patterning. *Science* **285,** 83–85, doi: 10.1126/science.285.5424.83 (1999).

55. Colace, T. V., Tormoen, G. W., McCarty, O. J. T. & Diamond, S. L. Microfluidics and Coagulation Biology. *Annu Rev Biomed Eng* **15,** 283–303, doi: 10.1146/annurev-bioeng-071812-152406 (2013).

56. Mann, K. G., Whelihan, M. F., Butenas, S. & Orfeo, T. Citrate anticoagulation and the dynamics of thrombin generation. *J. Thromb. Haemost.* **5,** 2055–2061, doi: 10.1111/j.1538-7836.2007.02710.x (2007).

**Supplementary Information**

*Numerical Simulations*

Table 6-S1: Reactions and rate constants used in the simulations for Figure 6-1.

| Rxn | Model Expressions | $k_1$ | $k_{-1}$ | $k_{cat}$ | References |
|---|---|---|---|---|---|
| 1 | $Xa + VII \rightarrow Xa + VIIa$ | $1.3 \cdot 10^7$ $M^{-1}s^{-1}$ | | | (1) |
| 2 | $IIa + VII \rightarrow IIa + VIIa$ | $2.3 \cdot 10^4$ $M^{-1}s^{-1}$ | | | (1) |
| 3 | $II + Xa \rightarrow IIa + Xa$ | $7.5 \cdot 10^3$ $M^{-1}s^{-1}$ | | | (1) |
| 4 | $IIa + VIII \rightarrow IIa + VIIIa$ | $2.0 \cdot 10^7$ $M^{-1}s^{-1}$ | | | (1) |
| 5 | $VIIIa + IXa \leftrightarrow IXaVIIa$ | $1.0 \cdot 10^7$ $M^{-1}s^{-1}$ | $5.0 \cdot 10^{-3}$ $s^{-1}$ | | (1) |
| 6 | $IXaVIIa + X \leftrightarrow IXaVIIaX \rightarrow IXaVIIa + Xa$ | $1.0 \cdot 10^8$ $M^{-1}s^{-1}$ | $1.0 \cdot 10^{-3}$ $s^{-1}$ | $8.2$ $s^{-1}$ | (1) |
| 7 | $VIIIa \leftrightarrow VIIIa1L + VIIIa2$ | $6.0 \cdot 10^{-3}$ $s^{-1}$ | $2.2 \cdot 10^4$ $M^{-1}s^{-1}$ | | (1) |
| 8 | $IXaVIIIaX \rightarrow VIIIa1L + VIIIa2 + X + IXa$ | $1.0 \cdot 10^{-3}$ $s^{-1}$ | | | (1) |
| 9 | $IXaVIIIa \rightarrow VIIIa1L + VIIIa2 + IXa$ | $1.0 \cdot 10^{-3}$ $s^{-1}$ | | | (1) |
| 10 | $IIa + V \rightarrow IIa + Va$ | $2.0 \cdot 10^7$ $M^{-1}s^{-1}$ | | | (1) |
| 11 | $Xa + Va \leftrightarrow XaVa$ | $7.5 \cdot 10^3$ $M^{-1}s^{-1}$ | $0.2$ $s^{-1}$ | | (1) |
| 12 | $XaVa + II \leftrightarrow XaVaII \rightarrow XaVa + mIIa$ | $1.0 \cdot 10^8$ $M^{-1}s^{-1}$ | $103$ $s^{-1}$ | $63.5$ $s^{-1}$ | (1) |
| 13 | $XaVa + mIIa \rightarrow XaVa + IIa$ | $1.5 \cdot 10^7$ $M^{-1}s^{-1}$ | | | (1) |
| 14 | $Xa + TFPI \leftrightarrow XaTFPI$ | $9.0 \cdot 10^5$ $M^{-1}s^{-1}$ | $3.6 \cdot 10^{-4}$ $s^{-1}$ | | (1) |
| 15 | $Xa + ATIII \rightarrow XaATIII$ | $1.5 \cdot 10^{-3}$ $M^{-1}s^{-1}$ | | | (1) |
| 16 | $mIIa + ATIII \rightarrow mIIaATIII$ | $7.1 \cdot 10^3$ $M^{-1}s^{-1}$ | | | (1) |
| 17 | $IXa + ATIII \rightarrow IXaATIII$ | $4.9 \cdot 10^2$ $M^{-1}s^{-1}$ | | | (1) |
| 18 | $IIa + ATIII \rightarrow IIaATIII$ | $7.1 \cdot 10^3$ $M^{-1}s^{-1}$ | | | (1) |
| 19 | $XIIa + XII \leftrightarrow XIIaXII \rightarrow XIIa + XIIa$ | $1.0 \cdot 10^8$ $M^{-1}s^{-1}$ | $750$ $s^{-1}$ | $3.3 \cdot 10^{-2}$ $s^{-1}$ | (1) |
| 20 | $XIIa + PK \leftrightarrow XIIaPK \rightarrow XIIa + K$ | $1.0 \cdot 10^8$ $M^{-1}s^{-1}$ | $3.6 \cdot 10^3$ $s^{-1}$ | $40$ $s^{-1}$ | (1) |
| 21 | $XII + K \leftrightarrow XIIK \rightarrow XIIa + K$ | $1.0 \cdot 10^8$ $M^{-1}s^{-1}$ | $45.3$ $s^{-1}$ | $5.7$ $s^{-1}$ | (1) |
| 22 | $PK + K \rightarrow K + K$ | $2.7 \cdot 10^4$ $M^{-1}s^{-1}$ | | | (1) |
| 23 | $K \rightarrow KInhibited$ | $1.1 \cdot 10^{-2}$ $s^{-1}$ | | | (1) |
| 24 | $XIIa + C1inh \rightarrow XIIaC1inh$ | $3.6 \cdot 10^3$ $M^{-1}s^{-1}$ | | | (1) |
| 25 | $XIIa + ATIII \rightarrow XIIaATIII$ | $21.6$ $M^{-1}s^{-1}$ | | | (1) |
| 26 | $XI + IIa \leftrightarrow XIIIa \rightarrow XIa + IIa$ | $1.0 \cdot 10^8$ $M^{-1}s^{-1}$ | $5.0$ $s^{-1}$ | $1.3 \cdot 10^{-4}$ $s^{-1}$ | (1) |
| 27 | $XIIa + XI \leftrightarrow XIIaXI \rightarrow XIIa + XIa$ | $1.0 \cdot 10^8$ $M^{-1}s^{-1}$ | $200$ $s^{-1}$ | $5.7 \cdot 10^{-4}$ $s^{-1}$ | (1) |
| 28 | $XIa + XI \rightarrow XIa + XIa$ | $3.19 \cdot 10^6$ $M^{-1}s^{-1}$ | | | (1) |

| 29 | XIa + ATIII → XIaATIII | $3.2 \cdot 10^2$ M$^{-1}$s$^{-1}$ | | | (1) |
|---|---|---|---|---|---|
| 30 | XIa + C1inh → XIaC1inh | $1.8 \cdot 10^3$ M$^{-1}$s$^{-1}$ | | | (1) |
| 31 | XIa + a1AT → XIaa1AT | $1.0 \cdot 10^2$ M$^{-1}$s$^{-1}$ | | | (1) |
| 32 | XIa + a2AP → XIaa2AP | $4.3 \cdot 10^3$ M$^{-1}$s$^{-1}$ | | | (1) |
| 33 | XIa + IX ↔ XIaIX → XIa + IXa | $1.0 \cdot 10^8$ M$^{-1}$s$^{-1}$ | 41 s$^{-1}$ | 7.7 s$^{-1}$ | (1) |
| 34 | IXa + X ↔ IXaX → IXa + Xa | $1.0 \cdot 10^8$ M$^{-1}$s$^{-1}$ | 0.64 s$^{-1}$ | $7.0 \cdot 10^{-4}$ s$^{-1}$ | (1) |
| 35 | Xa + VIII ↔ XaVIII → Xa + VIIIa | $1.0 \cdot 10^8$ M$^{-1}$s$^{-1}$ | 2.1 s$^{-1}$ | 0.023 s$^{-1}$ | (1) |
| 36 | VIIa + IX ↔ VIIaIX → VIIa + IXa | $1.0 \cdot 10^8$ M$^{-1}$s$^{-1}$ | 0.9 s$^{-1}$ | $3.6 \cdot 10^{-5}$ s$^{-1}$ | (1) |
| 37 | VIIa + X ↔ VIIaX → VIIa + Xa | $1.0 \cdot 10^8$ M$^{-1}$s$^{-1}$ | 210 s$^{-1}$ | $1.6 \cdot 10^{-6}$ s$^{-1}$ | (1) |
| 38* | polyP + TFPI ↔ polyPTFPI | $4.0 \cdot 10^5$ M$^{-1}$s$^{-1}$ | $1.0 \cdot 10^{-2}$ s$^{-1}$ | | (2),(3) |
| 39* | V + Xa + polyP → Va + Xa + polyP | $8.0 \cdot 10^{12}$ M$^{-2}$s$^{-1}$ | | | (1),(2) |
| 40* | XI + IIa + polyP → XIa + IIa + polyP | $8.8 \cdot 10^9$ M$^{-2}$s$^{-1}$ | | | (3) |

*Reactions 38-40 are bulk reactions for dispered polyP simulations (D-polyP) and surface reactions for the surface-immobilized polyP simulations (SI-polyP).

Reaction 38: polyP abrogates TFPI function (2).

For polyP binding to TFPI, similar rate constants were used as when polyP binds and releases from other plasma proteins. The association rate constant for the polyP reaction with IIa, XI, and XIa ranges from $1.64 \cdot 10^6$ M$^{-1}$s$^{-1}$ to $5.12 \cdot 10^6$ M$^{-1}$s$^{-1}$ (3); thus, $1.0 \cdot 10^6$ M$^{-1}$s$^{-1}$ was chosen for $k_{1,38}$. The disassociation rate constant for the polyP reaction with IIa, XI, and XIa ranges from $1.05 \cdot 10^{-2}$ s$^{-1}$ to $7.71 \cdot 10^{-2}$ s$^{-1}$ (3); thus, $1.0 \cdot 10^{-2}$ s$^{-1}$ was chosen for $k_{-1,38}$.

Reaction 39: polyP accelerates V activation by Xa (2).

The activation of V to Va by IIa occurs with a rate constant ($k_{1,10}$) of $2.0 \cdot 10^7$ M$^{-1}$s$^{-1}$ (see Reaction 10 in Table 6-S1) (1). The reaction is $V + IIa \rightarrow Va + IIa$ and the rate law is:

$$\frac{d[Va]}{dt} = k_{1,10}[V][IIa]$$

PolyP accelerates the activation of V by Xa; we assume this occurs with a similar rate as that of V activation by IIa. The reaction would be $V + Xa + polyP \rightarrow Va + Xa + polyP$ and the rate law would be:

$$\frac{d[Va]}{dt} = k_{1,39}[V][Xa][polyP]$$

To approximate the rate constant, we assume that $k_{1,10} \sim k_{1,39}[polyP]$. With a typical $[polyP] \sim 1\mu M$, this means that $k_{1,39} \sim 2.0 \cdot 10^{13} M^{-2} s^{-1}$.

Reaction 40: polyP enhances XI activation by thrombin (3).

A simple reaction for polyP enhancing XI activation by thrombin would be $XI + IIa + polyP \rightarrow XIa + IIa + polyP$. The rate law would be:

$$\frac{d[XIa]}{dt} = k_{1,39}[XI][IIa][polyP]$$

For an estimate of the reaction rate constant for polyP enhancing XI activation, Figure 6-1A from Reference shows a XI activation rate of ~1 nM/min when ~5μM polyP is present. The concentrations used in this figure were $[XI] = 30 \; nM$ and $[IIa] = 5 \; nM$. Therefore,

$$k_{1,40} \sim \frac{1\frac{nM}{min}}{(30 \; nM)(5 \; nM)(5 \; \mu M)} \sim 2.2 \cdot 10^{10} \frac{1}{M^2 s^1}$$

For all polyP reactions, elementary mass action kinetics was assumed. Also, the experiments that the rate constants were based on happened in test tubes, whereas the experiments performed for this paper happened in microfluidic devices. To account for this, a factor $\eta$ was multiplied to each polyP forward rate constant ($k_{1,38}$, $k_{1,39}$, $k_{1,40}$) and simulations were run to match the clotting time in the microfluidic device. $\eta$ was found to be ~0.4, so the final rate constants used are as appears in Table 6-S1 ($k_{1,38} = 4.0 \cdot 10^5$ M⁻¹s⁻¹, $k_{1,39} = 8.0 \cdot 10^{12}$ M⁻²s⁻¹, $k_{1,40} = 8.8 \cdot 10^9$ M⁻²s⁻¹).

Table 6-S2: Chemical species and their initial concentrations used in the simulations for Figure 6-1. All initial concentrations were taken from Reference (1).

| Species | Initial Concentration (M) |
|---------|---------------------------|
| VII | $1 \cdot 10^{-8}$ |
| VIIa | $1 \cdot 10^{-10}$ |
| Xa | 0 |
| IIa | 0 |
| X | $1.6 \cdot 10^{-7}$ |
| IX | $9 \cdot 10^{-8}$ |
| II | $1.4 \cdot 10^{-6}$ |
| VIII | $7 \cdot 10^{-10}$ |
| VIIIa | 0 |
| IXaVIIIa | 0 |
| IXaVIIIaX | 0 |
| VIIIa1L | 0 |
| VIIIa2 | 0 |
| V | $2 \cdot 10^{-8}$ |
| Va | 0 |
| XaVa | 0 |
| XaVaII | 0 |
| mIIa | 0 |
| TFPI | $2.5 \cdot 10^{-9}$ |
| XaTFPI | 0 |
| ATIII | $3.4 \cdot 10^{-6}$ |
| XaATIII | 0 |
| mIIaATIII | 0 |
| IXaATIII | 0 |

| | |
|---|---|
| IIaATIII | 0 |
| XII | $3.4 \cdot 10^{-7}$ |
| XIIa | 0 |
| XIIaXII | 0 |
| PK0 | $4.5 \cdot 10^{-7}$ |
| XIIaPK | 0 |
| XIIK | 0 |
| K | 0 |
| C1inh | $2.5 \cdot 10^{-6}$ |
| XIIaC1inh | 0 |
| XIIaATIII | 0 |
| XI | $3.1 \cdot 10^{-8}$ |
| XIIIa | 0 |
| XIa | 0 |
| XIIaXI | 0 |
| XIaATIII | 0 |
| XIaC1inh | 0 |
| a1AT | $4.5 \cdot 10^{-5}$ |
| a2AP | $1 \cdot 10^{-6}$ |
| XIaa1AT | 0 |
| XIaa2AP | 0 |
| XIaIX | 0 |
| IXaX | 0 |
| XaVIII | 0 |
| VIIaIX | 0 |
| VIIaX | 0 |
| KInhibited | 0 |
| polyP | |

For the polyP concentration, the same number of polyP molecules ($7.5 \cdot 10^{-9}$ moles) was either i) localized to the surface of the cylinder, or ii) dispersed throughout the volume of the cylinder. This corresponds to a surface polyP concentration of $3 \cdot 10^{-5}$ mol/m$^2$ in the SI-polyP simulations and a dispersed polyP concentration of $3 \cdot 10^{-2}$ mol/m$^3$ in the D-polyP simulations.

Table 6-S3: Shear rates used in the simulations for Figure 6-1b and the resulting thrombin concentration for dispersed and localized polyP

| Shear rate | [thrombin]$_{SI\text{-}polyP}$ (mol/m$^3$) | [thrombin]$_{D\text{-}polyP}$ (mol/m$^3$) | [thrombin]$_{SI\text{-}polyP}$ / [thrombin]$_{D\text{-}polyP}$ |
|---|---|---|---|
| 1 | $1.83 \cdot 10^{-5}$ | $2.34 \cdot 10^{-8}$ | 782.1 |
| 4 | $1.72 \cdot 10^{-9}$ | $1.65 \cdot 10^{-11}$ | 104.2 |
| 12 | $4.70 \cdot 10^{-12}$ | $1.93 \cdot 10^{-13}$ | 24.4 |
| 24 | $8.40 \cdot 10^{-14}$ | $2.98 \cdot 10^{-14}$ | 2.8 |
| 60 | $1.87 \cdot 10^{-15}$ | $1.95 \cdot 10^{-15}$ | 1.0 |
| 120 | $2.40 \cdot 10^{-16}$ | $2.36 \cdot 10^{-16}$ | 1.0 |

*References*

1. Chatterjee MS, Denney WS, Jing H, Diamond SL. Systems biology of coagulation initiation: kinetics of thrombin generation in resting and activated human blood. PLoS computational biology. 2010;6(9).

2. Smith SA, Mutch NJ, Baskar D, Rohloff P, Docampo R, Morrissey JH. Polyphosphate modulates blood coagulation and fibrinolysis. Proceedings of the National Academy of Sciences of the United States of America. 2006;103(4):903-8.

3. Choi S, SA S, JH M. Polyphosphate is a cofactor for the activation of factor XI by thrombin. Blood. 2011;118(26):6963-70.

*Microfluidic Experiments*
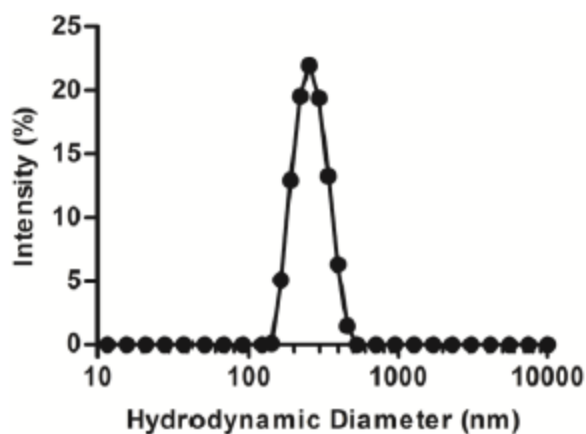
**Supplementary Figure 6-S1. Size distribution of NP-polyP160.** Representative DLS data demonstrating NP-polyP160 consisting of particles with an average hydrodynamic diameter of $250 \pm 65$ nm.
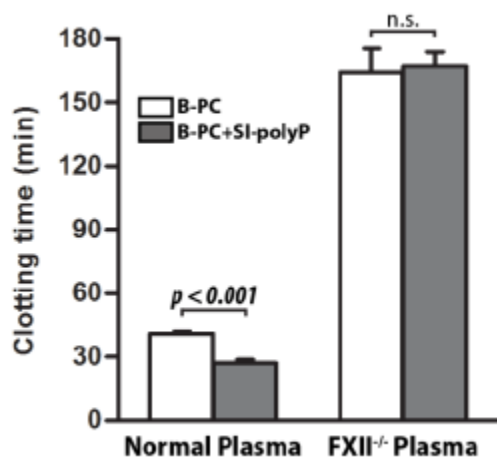


**Supplementary Figure 6-S2. polyP facilitates clotting through activation of Factor XII.** Clotting times of normal plasma and FXII-deficient plasma at zero-shear with SI-polyP70 or without (biotinylated-PC alone). Data indicate mean $\pm$ SEM, n=3.
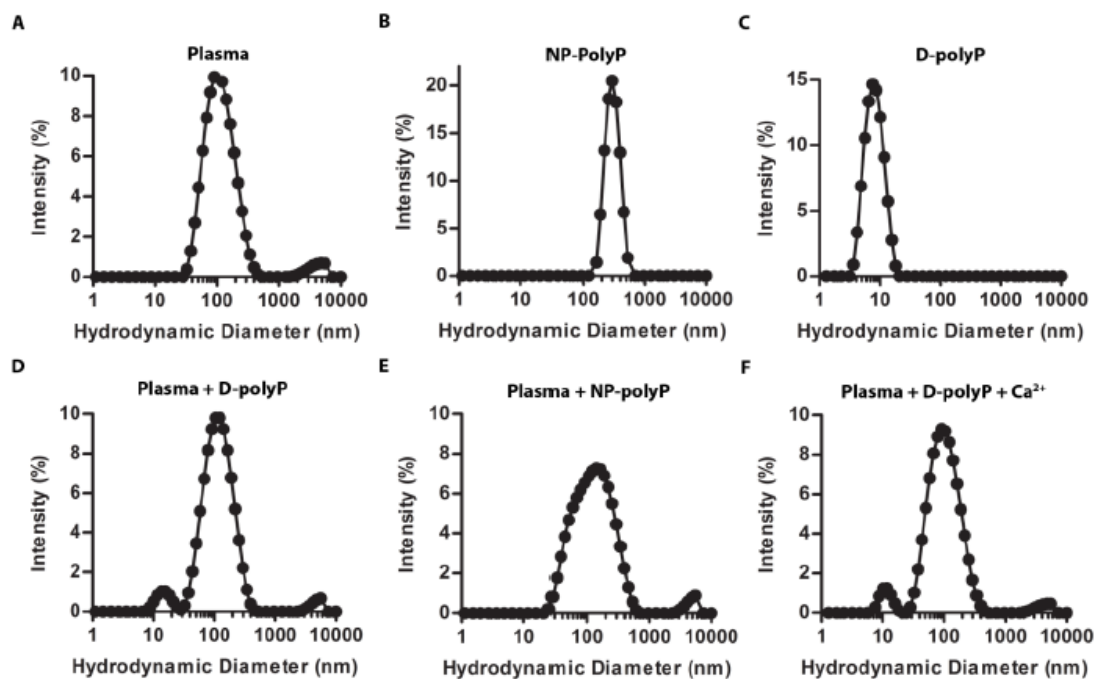
**Supplementary Figure 6-S3. DLS size distribution of soluble D-polyP160 and NP-polyP160 in buffer and plasma.** (A) Normal citrated plasma without polyP, which contains background intensity from components normally in plasma. (B-C) Aggregated and soluble polyP160 respectively in HEPES buffered saline. (D) Soluble polyP160 added to citrated plasma. (E) Preformed NP-polyP160 added to citrated plasma. (F) Soluble polyP160 was added to citrated plasma and recalcified; the graph of panel F resembles panel D (D-polyP) rather than panel E (NP-polyP).
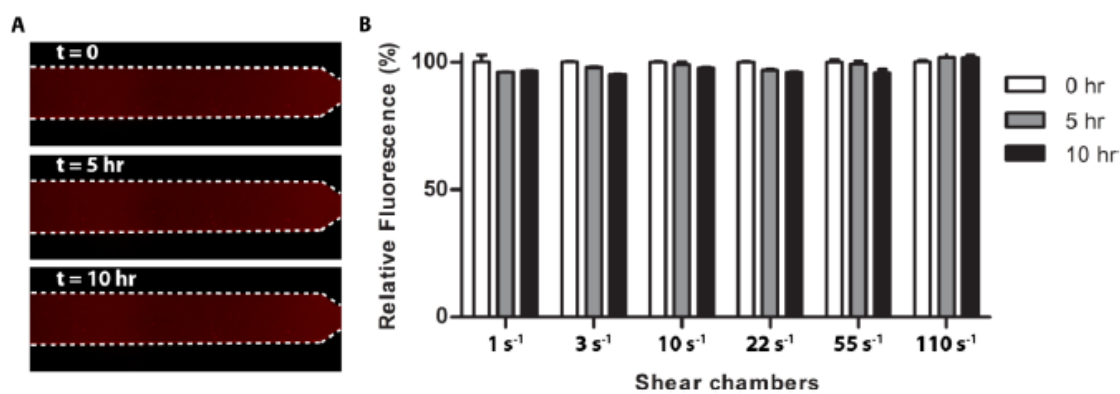
**Supplementary Figure S4. PC channel coverage and stability.** (A) Representative time lapse images of a channel (white dashed lines) coated with PC/Texas Red DHPE (red) with citrated normal plasma flowing through it. (B) Fluorescence intensities in different regions of each shear chamber. Data indicate mean ± SEM.

*Author Contributions*

J.H.Y and N.M. contributed equally to this work. J.H.Y., N.M., K.Y.T.C., J.R.B., S.A.S., A.J.D., and D.K., performed experiments and analyzed data; T.S.S. performed simulations and analyzed data described in Figure 6-1 and Tables 6S-1, 6S-2, 6S-3; J.H.Y., N.M., T.S.S., C.J.K., J.H.M., Y.L., and G.D.S. conceptualized and planned experiments; J.H.Y., N.M., and C.J.K. wrote the manuscript; and all authors reviewed and edited the manuscript before submission.